Lehrstuhl für Biomedizinische Physik
Physik Department
Technische Universität München

High-Sensitivity Grating-Based Phase-Contrast Computed Tomography with Incoherent Sources

Lorenz Birnbacher

July 2018

Supervisors:
Prof. Dr. Julia Herzen
Prof. Dr. Franz Pfeiffer

Technische Universität München

Technische Universität München
Physik Department
Lehrstuhl für Biomedizinische Physik

High-sensitivity grating-based phase-contrast computed tomography with incoherent sources

Lorenz Johann Benedikt Birnbacher

Vollständiger Abdruck der von der Fakultät für Physik der Technischen Universität München zur Erlangung des akademischen Grades eines

Doktors der Naturwissenschaften (Dr. rer. nat.)

genehmigten Dissertation.

Vorsitzender:	Prof. Dr. Martin Zacharias
Prüfer der Dissertation:	1. Prof. Dr. Franz Pfeiffer
	2. Prof. Dr. Wolfgang Weber

Die Dissertation wurde am 05.07.2018 bei der Technischen Universität München eingereicht und durch die Fakultät für Physik am 07.12.2018 angenommen.

Abstract

Several novel X-ray imaging techniques have been developed over the last decades to access phase-contrast information aside the conventional X-ray attenuation contrast. One of those methods is X-ray grating interferometry or Talbot interferometry, which is an X-ray imaging technique highly sensitive to soft tissue differences. The method, which was developed at highly coherent synchrotron sources, is also compatible with X-ray sources of limited coherence enabling the use of high-flux laboratory X-ray sources. Additionally, grating interferometry provides access to the so-called dark-field signal, which is an imaging contrast related to small-angle scattering. In combination with computed tomography, grating-based phase-contrast computed tomography (GBPC-CT) and grating-based dark-field computed tomography (GBDF-CT) can be performed.

This work entitled "High-sensitivity grating-based phase-contrast computed tomography with incoherent sources" addresses several challenges of GBPC-CT that occur when going from monochromatic, high-flux synchrotron sources to polychromatic laboratory X-ray sources.

One of the main goals of X-ray phase-contrast imaging is to achieve high angular sensitivity necessary for high soft tissue contrast, which relates to resolving subtle differences in electron density. We could show that high angular sensitivity and thus electron density resolution comparable to results from synchrotron sources is possible with laboratory GBPC-CT.

In comparison to other phase-contrast techniques, GBPC-CT provides the advantage to perform quantitative imaging, which renders the method highly interesting for increased comparability of the data. In this work, we present not only how to achieve highly reliable electron density values, but also how to use the attenuation coefficient to determine the effective atomic number with polychromatic GBPC-CT.

When performing high sensitivity GBPC-CT, the method gets more prone to streak artifacts reducing the quality of the phase-contrast data. The solution that we present in this work is tilting the gratings by $\pi/4$ around the optical axis in combination with statistical iterative reconstruction to utilize the two-dimensional phase-contrast information. In doing so, the extent of streak artifacts could be enormously reduced and the reliability of the quantitative values could be improved.

Furthermore, we used laboratory GBPC-CT for several biomedical studies within the range of this work to assess the potential of GBPC-CT as a biomedical imaging method. The results of phase-contrast studies covering breast cancer and renal cell carcinoma samples using the high soft tissue contrast of GBPC-CT, as well as the visualization of microcalcifications in specimens containing atherosclerotic plaque with grating-based dark-field tomography render GBPC-CT and respectively GBDF-CT promising preclinical imaging methods.

Zusammenfassung

In den letzten Jahrzehnten wurden diverse neuartige Röntgenbildgebungsmethoden entwickelt, um die Phasenkontrastinformation jenseits des allseits bekannten Röntgenabsorptionskontrasts zugänglich zu machen. Eine dieser Methoden ist gitterbasierte Röntgeninterferometrie oder Röntgen-Talbot-Interferometrie, eine Technik, die hochsensitive Gewebedifferenzierung ermöglicht. Diese Methode, die an Synchrotronanlagen mittels äußerst kohärenter Röntgenstrahlung entwickelt wurde, ist dadurch charakterisiert, dass sie sich auch mit inkohärenten Röntgenquellen, wie sie vornehmlich im Labor auftreten, realisieren lässt. Zusätzlich erhält man mit Röntgengitterinterferometrie das so genannte Dunkelfeldsignal, welches einer Art Kleinwinkelstreuung entspricht. In Kombination mit Computertomographie ist es zudem möglich, gitterbasierte Phasenkontrastcomputertomographie (GBPC-CT) und gitterbasierte Dunkelfeldcomputertomographie (GBDF-CT) anzuwenden.

Die vorliegende Arbeit „High-sensitivity grating-based phase-contrast computed tomography with incoherent sources" liefert einen Beitrag zu den Herausforderungen von GBPC-CT, die durch die Translation von monoenergetischen Synchrotronquellen mit hohem Fluss zu polychromatischen Laborquellen entstehen.

Ein Hauptziel von Röntgenphasenkontrastbildgebung ist das Erreichen von möglichst hoher Winkelsensitivität für maximalen Gewebekontrast, was dem Erreichen einer hohen Elektronendichteauflösung entspricht. In dieser Arbeit konnte gezeigt werden, dass eine Winkelsensitivität und dementsprechend eine Elektronendichteauflösung auf einem vergleichbaren Level von Ergebnissen, die an Synchrotronquellen erzielt wurden, auch mit Laborquellen erreicht werden kann.

Ein großer Vorteil von GBPC-CT gegenüber anderen Röntgenphasenkontrasttechniken ist die quantitative Art der Bildgebung, was GBPC-CT zu einer besonders bedeutsamen Methode aufgrund der hohen Vergleichbarkeit der Daten macht. In dieser Arbeit wird nicht nur gezeigt, dass mit GBPC-CT verlässliche Elektronendichtewerte bestimmt werden können, sondern auch, dass die Absorptionsmodalität in Kombination mit der Elektronendichte dazu verwendet werden kann, die effektive Atomzahl zu bestimmen.

Bei hochsensitiver GBPC-CT reduziert das erhöhte Auftreten von Streifenartefakten die Qualität der Phasenkontrastdaten. Eine Methode, die in dieser Arbeit präsentiert wird, um diese Artefakte zu minimieren, ist das Drehen der Gitter um $\pi/4$ um die Strahlachse in Kombination mit statistischer iterativer Rekonstruktion. Mit der dadurch erhaltenen zweidimensionalen Phasenkontrastinformation gelang es, Streifenartefakte deutlich zu reduzieren und damit die quantitativen Werte zu verbessern.

Desweiteren wurde in mehreren GBPC-CT Studien im Rahmen dieser Arbeit das Potential von GBPC-CT in Verwendung von Laborquellen als biomedizinische Bildgebungsmethode untersucht. Die Phasenkontrastergebnisse von hochaufgelösten, quantitativen Brustkrebs- und Nierenkrebsmessungen sowie die Visualisierung von Mikroverkalkungen von Proben mit atherosklerotischer Plaque in der Dunkelfeldcomputertomographie machen GBCT-CT bzw. GBDF-CT zu vielversprechenden vorklinischen Bildgebungsmethoden.

Dedicated to my parents

Contents

CHAPTER 1

Introduction to X-ray phase-contrast imaging

X-ray phase-contrast imaging combines two originally different fields of imaging: X-ray imaging and phase-contrast microscopy. While phase-contrast techniques were developed with light microscopy, similar contrast modalities are difficult to achieve with X-rays aside from the commonly known conventional absorption imaging.

1.1 Phase-contrast imaging

Light microscopy emerged in the 17th century with the development of bright-field microscopy by Robert Hooke and Anton van Leeuwenhoek (Hooke, 1665; Schierbeek, 1959). Technical progress and the use of staining techniques continuously improved the image contrast. In the early 1930's the Danish scientist Frits Zernike developed phase-contrast microscopy (Zernike, 1942, 1955; Murphy and Davidson, 2013), which enabled the first visualization of internal structures of living cells without the need for staining. For his invention using a combination of a condenser annulus and phase plates, Frits Zernike was awarded with the Nobel Prize in Physics in 1953. A similar phase-contrast microscopy technique developed by Georges Nomarski in 1955 is differential interference contrast (DIC) microscopy, which leads to the optical path difference induced by optical prisms (Nomarski, 1955; Murphy and Davidson, 2013). The third classical microscopy concept is dark-field microscopy, which visualizes only light scattered by the sample, whereas the image remains mainly dark if no scattering occurs (Gage, 2009). The difference between dark-field, phase-contrast, and bright field microscopy is illustrated in Fig. 1.1 by way of example for a tissue paper.

While the recent developments in light microscopy focus primarily on superresolution methods like stimulated emission depletion (STED) fluorescence microscopy, for which the Nobel Prize in Chemistry was awarded in 2014 overcoming Abbe's resolution limit (Vonesch et al., 2006), new imaging methods have emerged in combination with X-ray imaging.

1.2 X-ray phase-contrast imaging

X-rays were discovered 1895 by Wilhelm C. Röntgen and became shortly thereafter indispensable for medical and industrial X-ray imaging (Röntgen, 1898). For his breakthrough discovery, Röntgen received the first Nobel Prize in Physics in 1901.

But it was not until 1965 that only absorption contrast was used as X-ray imaging contrast, when Ulrich Bonse and Michael Hart performed first experiments at a synchrotron showing X-ray phase-contrast images. Three silicon crystals were used to

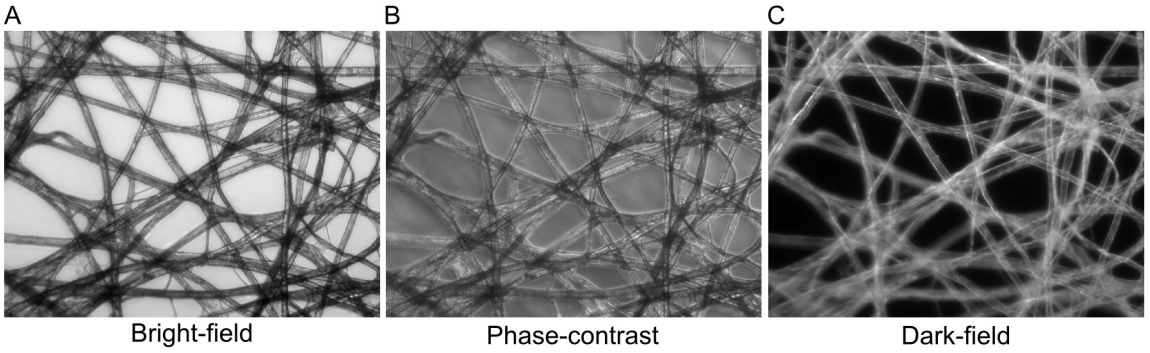

Fig. 1.1 | Micrograph of a lens tissue paper. Subfigure (A) shows the bright-field image, subfigure (B) the phase-contrast image, and subfigure (C) the dark-field image. The pixel size is 1.6 µm at 10x magnification. Figure adapted from Wheeler (2010).

visualize phase changes that coherent, monochromatic X-rays undergo when penetrating matter similarly to visible light. The interference of the beam with and without the object allowed to directly measure the phase of the object Φ (Bonse and Hart, 1965; Momose et al., 1996; Fitzgerald, 2000; Bravin et al., 2012).

In the 1990's, analyzer based phase-contrast (or diffraction enhanced) imaging, which is based like the previous method on Bragg reflection, was developed. Thereby, a single crystal is used to visualize the phase change when an object is inserted into the X-ray beam. The sample is scanned under different angles leading to an intensity rocking curve related to the phase shift. Only one analyzer crystal is needed to measure the one-dimensional gradient of the object $\nabla\Phi$ (Davis et al., 1995; Chapman et al., 1997). Another method to access phase-contrast is single or multi distance propagation imaging. The method utilizes free-space propagation of the sample wave-front to the detector. This technique needs a detector system with small pixel size next to a coherent X-ray source to resolve the edge-enhancement corresponding to the second derivative of the phase $\nabla^2\Phi$. The method does not use any additional optical elements in the beam rendering it quite popular for high resolution phase-contrast imaging at synchrotron facilities (Snigirev et al., 1995; Wilkins et al., 1996).

With the development of grating interferometry in the late 1990's, a further important step in phase-contrast imaging was achieved (Momose et al., 2003). In detail, a so-called phase grating creates a periodically reappearing interference pattern due to Fresnel propagation (Cloetens et al., 1999). This phenomenon is described by the so-called Talbot effect, which is originally known from experiments with visible light (Talbot, 1836). Samples in the beam cause changes in the interference pattern, which can be resolved by the use an analyzer grating (David et al., 2002; Momose et al., 2003; Weitkamp et al., 2005). With this Talbot interferometer, one does not only obtain the differential phase-contrast (DPC) signal related to the gradient of the phase $\nabla\Phi$, but also the dark-field contrast (DFC) signal related to small-angle scattering next to the conventional attenuation signal (Pfeiffer et al., 2008).

1.3 Grating-based phase-contrast computed tomography

Conventional computed tomography provides the distribution of the attenuation information in a non-destructive manner and is besides magnetic resonance imaging (MRI) and positron-emission tomography (PET) one of the most successful three-dimensional imaging techniques in medicine. Although the concept of computed tomography is rather old, it took until the 1960's and 1970's to develop first clinical scanners by Godfrey N. Hounsfield and Allan M. McCormack. For their work on computed tomography, Godfrey N. Hounsfield and Allan M. McCormack were awarded with the Nobel Prize in Medicine in 1979 (Buzug, 2008).

However, CT suffers from low soft tissue contrast or limited functional imaging in comparison to MRI and PET. Combining now CT with grating interferometry allows for a new range of potential applications: grating-based phase-contrast CT (GBPC-CT) does not only provide high three-dimensional soft tissue sensitivity in comparison to equivalent attenuation data (Momose, 2003; Weitkamp et al., 2005; Pfeiffer et al., 2007a, 2013), GBPC-CT enables quantitative imaging related to the electron density (Herzen et al., 2009; Qi et al., 2010; Willner et al., 2014). Moreover, the grating-based dark-field computed tomography (GBDF-CT) signal enables the visualization of small-angle scattering structures below the physical pixel size like in the case of microcalcifications (Pfeiffer et al., 2008; Malecki et al., 2012; Wolf et al., 2014). First GBPC-CT results from synchrotron sources include for example high resolution rat brain imaging without the need of contrast agents (Pfeiffer et al., 2007a; Schulz et al., 2010), breast cancer imaging (Sztrókay et al., 2012b), or microtomography of human testicle samples (Zanette et al., 2013b).

1.4 Laboratory grating-based phase-contrast computed tomography

Although grating-based phase-contrast imaging requires coherent X-ray sources, introducing an additional source grating enabled the use of grating interferometry with limited coherence X-ray sources (Pfeiffer et al., 2006). The latter step has provided laboratory access to the method increasing the range of potential applications in medicine and material science.

With all the promising GBPC-CT results and applications from high-flux, monochromatic synchrotron sources, the central question is what level of performance can be achieved with laboratory GBPC-CT setups due to the limited coherence and the polychromatic spectrum. The respective performance parameter is the angular sensitivity, which describes the minimum resolvable refraction angle of the Talbot-Lau interferometer (Modregger et al., 2011). High angular sensitivity is essential for high soft tissue contrast related to high electron density resolution. One goal of this work is to investigate what level of angular sensitivity can be reached with optimized polychromatic, laboratory GBPC-CT in comparison to synchrotron sources.

Moreover, in comparison to other phase-contrast techniques GBPC-CT provides the

advantage to perform quantitative imaging (Pfeiffer et al., 2007b; Herzen et al., 2009; Qi et al., 2010; Willner et al., 2014), which renders the method highly interesting for increased comparability of the data. The extent of the accuracy of quantitative imaging using a polychromatic X-ray source is of current interest using state-of-the-art GBPC-CT with incoherent sources. In this work, not only how to achieve reliable electron density values is presented, but also how to utilize the attenuation coefficient to determine the effective atomic number with polychromatic GBPC-CT. This allows to access two in general absolute physical quantities.

When performing high sensitivity GBPC-CT, the method gets prone to streak artifacts reducing the quality of the phase-contrast data. One promising method is to tilt the gratings by $\pi/4$ in combination with additional processing (Rutishauser et al., 2011). However, this approach is not applicable for laboratory GBPC-CT setups due to the cone beam geometry. This work presents a novel approach which combines the tilted gratings with statistical iterative reconstruction to use the two-dimensional phase-contrast information. In doing so, the extent of streak artifacts could be enormously reduced and the quality of the quantitative values could be improved.

In the last years not only methodical advances were made, first relevant applications in medical phase-contrast radiography and GBPC-CT were studied. Concerning phase-contrast and dark-field radiography, highly promising results were achieved for example in phase-contrast mammography (Stampanoni et al., 2011; Grandl et al., 2015; Scherer et al., 2015b; Hauser et al., 2014; Köhler et al., 2015). Also, dark-field radiography with focus on characterization of chronic obstructive pulmonary diseases (COPDs) and lung carcinomas turned out to be of great interest (Bech et al., 2013; Yaroshenko et al., 2013; Meinel et al., 2014; Yaroshenko et al., 2015, 2016; Hellbach et al., 2015, 2016, 2017; Scherer et al., 2017). Just recently, the first DFC radiography of living pigs was successfully accomplished as a further milestone towards clinical application (Gromann et al., 2017). Furthermore, first studies of laboratory GBPC-CT based on the work described in Willner et al. (2016) include phase-contrast tomography of breast (Grandl et al., 2013, 2014), atherosclerotic plaque (Hetterich et al., 2014, 2015a,b) and kidney (Fingerle et al., 2014). The potential of GBPC-CT as a biomedical imaging method is further intensified within the range of this work. Results of studies covering phase-contrast results of breast cancer imaging and renal cell carcinoma using the high soft tissue contrast of GBPC-CT, as well as the visualization of microcalcifications in atherosclerotic plaque with grating-based dark-field tomography render GBPC-CT and respectively GBDF-CT promising preclinical imaging methods.

1.5 Outline

In **Chapter 2** of this work entitled "High-sensitivity grating-based phase-contrast computed tomography with incoherent sources" the underlying theory covering the basic concept of the utilized laboratory grating-based phase-contrast CT setup is outlined. The first aspects presented are X-ray interaction and the complex index of refraction. Next, the Talbot effect and grating interferometry with incoherent sources leading to the three image signals X-rat attenuation contrast, differential phase-contrast, and dark-field contrast are described. The last part of the first chapter illustrates

the basics of tomographic reconstruction including filtered backprojection (FBP) and statistical iterative reconstruction (SIR).

Chapter 3 presents the experimental Talbot-Lau type interferometer setup at hand. The setup components, namely the X-ray source, the detector, and the gratings, lead to the setup design and performance. Processing and postprocessing of the data as well as the workflow for tomographic experiments at this setup and the setup characterization are completing **Chapter 3**.

For high quality GBPC-CT results, the essential parameter is the angular sensitivity besides other performance parameters like the spatial resolution and the measurement duration. In **Chapter 4**, the main parameters how to achieve high angular resolution defined by the minimum resolvable refraction angle are derived. The latter leads to high electron density resolution and thus subtle soft tissue differentiation.

In **Chapter 5**, quantitative imaging with determination of the electron density and the effective atomic number is investigated. After the theoretical presentation how to calculate the electron density and the effective atomic number using effective energy calibration with polychromatic GBPC-CT setup, experimental results showing the performance of the method are discussed.

A special case of artifacts arising with high sensitivity GBPC-CT are streak artifacts. Using the tilted grating method being topic of **Chapter 6**, one can elegantly reduce streak artifacts using the full three-dimensional phase-contrast information. First, an analytical method using two-dimensional phase integration and subsequent phase-contrast computed tomography is introduced. Next, the novel approach combining the tilted grating configuration with statistical iterative reconstruction (SIR) is illustrated.

Chapter 7 presents exemplary biomedical applications of GBPC-CT. In several preclinical studies the diagnostic value of preclinical, ex-vivo GBPC-CT was investigated. In the first study presented within the range of this work, phase-contrast CT results of breast tumor samples – intraductal carinoma in situ (DCIS) – are shown. Thereby, dilated ducts related to breast cancer could be visualized. Further, an ex-vivo study investigating the potential of GBPC-CT imaging of renal cell carcinomas (RCC) enabled improved quantitative characterization of tumor tissue in comparison to clinical CT and clinical MRI. In this case, especially the potential to avoid the use of contrast agents, which can for example cause renal failure, promotes the effort to apply clinically GBPC-CT. The last study shown in **Chapter 7** deals with the dark-field signal (GBDF-CT) of atherosclerotic plaque in coronary arteries. As a result, GBDF-CT leads to an improved detection of microcalcifications of plaques due to small-angle scattering, which cannot be resolved in conventional CT with the same pixel size.

CHAPTER 2

Theoretical background

Short summary

This chapter covers the theoretical background of grating-based phase-contrast computed tomography with incoherent X-ray sources. First, basic X-ray interaction with matter and attenuation imaging will be explained. The chapter continues with X-ray wave-front propagation necessary for the understanding of phase-contrast imaging. The next chapter will introduce the principles of the Talbot-Lau interferometer and especially the Talbot effect used in this work. Eventually, the basics of filtered back-projection and statistical iterative reconstruction as approaches for reconstruction in computed tomography will be presented. The references used here for the following chapter are D. Attwood (1999), D. Paganin (2006), T. Buzug (2008) J. Als-Nielsen & D. MacMarrow (2011), and P. Willmott (2011).

2.1 X-ray interaction with matter

X-rays are electromagnetic waves with energies mainly in the keV to MeV regime, which corresponds to wavelengths from approximately 1 nm to 1 pm. Although, the overlap between X-rays and ultraviolet radiation on the lower energetic side and gamma rays on the higher energetic part of the electromagnetic spectrum is continuous. In this energy range, X-rays interact mainly with electrons. Thereby, X-rays are either absorbed photoelectrically or scattered. The latter happens either elastically or inelastically.

Additional effects, which are not further considered in the following chapter, are X-ray fluorescence, emission of Auger electrons, and pair-production. X-ray fluorescence describes the emission of a photon with specific, almost discrete energy after an electron transition from a higher to a lower shell. Auger electrons are formed when the energy released after ejecting an inner shell electron directly causes an ejection of secondary electrons in higher shells. Excess energy with respect to the binding energy leads to more kinetic energy of the electron. Pair production occurs at energies above 1.022 MeV when an X-ray photon decays into an electron and a positron traveling in opposite directions.

2.1.1 Cross sections

Photoelectric absorption, elastic, and inelastic scattering are the primary interaction effects in the X-ray energy regime used for X-ray imaging and form the total scattering cross section

$$\sigma_{\mathrm{tot}}(E,Z) = \sigma_{\mathrm{ph}}(E,Z) + \sigma_{\mathrm{incoh}}(E,Z) + \sigma_{\mathrm{coh}}(E,Z), \tag{2.1}$$

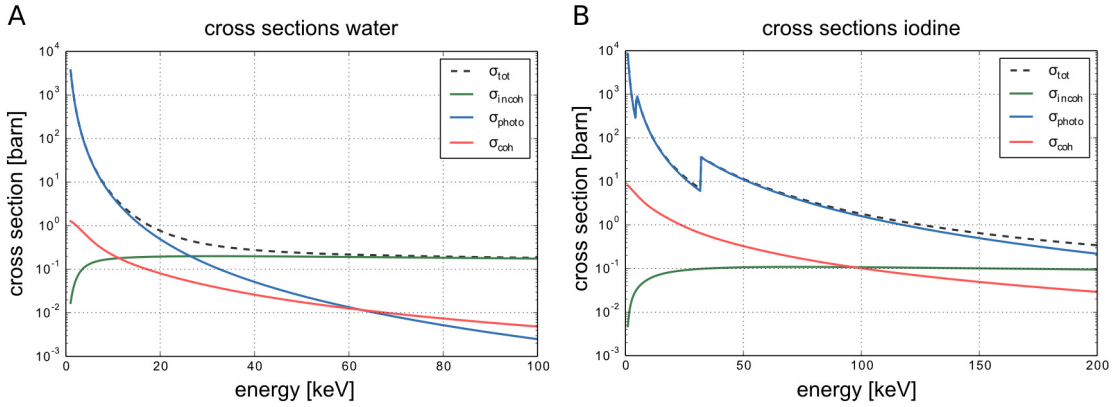

Fig. 2.1 | Cross sections in dependency of the energy. The different parts of the interaction cross section are shown by way of example for water (A) and iodine (B). The photoelectric effect, elastic, and inelastic interaction are the major contributions in this energy range. The data can be found in Berger et al. (2010).

with σ_{ph} denoting the photoelectric cross section, σ_{incoh} the incoherent cross section, and σ_{coh} the coherent cross section contribution.

Photoelectric absorption

Photoelectric absorption describes the complete absorption of an incident photon by the atom ejecting an electron, primarily of the inner ones, and causes a vacancy in the atomic shell. For this process the energy of the photon must match the binding energy of the electron.

The cross section of the photoelectric absorption $\sigma_{\mathrm{ph}}(E, Z)$ can be approximated as

$$\sigma_{\mathrm{ph}}(E, Z) \propto \frac{Z^{4-5}}{E^{2.5-3.5}}, \tag{2.2}$$

as shown in White (1977). The variation in the proportionalities for both the atomic number Z and the photon energy E originate from the different absorption edges of the atoms.

Inelastic scattering

Inelastic scattering – also known as Compton scattering – describes scattering processes in which the photon with initial energy E_0 loses part of its energy ejecting an electron, preferably weaker bound electrons. Applying conservation of energy and momentum leads to

$$\frac{E_0}{E} = \frac{\lambda}{\lambda_0} = \frac{k_0}{k} = 1 + \lambda_{\mathrm{C}} k_0 (1 - \cos\theta), \tag{2.3}$$

with E being the final energy of the photon, $\lambda_{\mathrm{C}} = h/m_{\mathrm{e}}c = 2.43\,\mathrm{pm}$ being the Compton length including the electron rest mass m_{e}, the vacuum speed of light c, and Planck's constant h (or its reduced version $\hbar$) (Compton, 1923). θ is the scattering angle of the photon. The often needed relation between the energy E and the wave vector k, the

wavelength λ, or the photon frequency ν is

$$E = \hbar kc = hc/\lambda = h\nu. \tag{2.4}$$

The Compton cross section can be approximated by the Klein-Nishina formula (Klein and Nishina, 1929), which equals for scattering at one single electron

$$\sigma_{incoh} = 2\pi r_0^2 \left[\left(\frac{1+\tilde{E}}{\tilde{E}^2} \right) \left(2\frac{1+\tilde{E}}{1+2\tilde{E}^2} - \frac{\ln(1+2\tilde{E})}{\tilde{E}} \right) + \frac{\ln(1+2\tilde{E})}{2\tilde{E}} - \frac{1+3\tilde{E}}{(1+2\tilde{E})^2} \right], \tag{2.5}$$

with

$$\tilde{E} = \frac{h\nu}{m_e c^2} \tag{2.6}$$

being the reduced photon energy (Buzug, 2008). In good approximation, the proportionality of the Compton cross section $\sigma_{\text{incoh}}(E, Z)$ depends only on the atomic number

$$\sigma_{\text{incoh}}(Z) \propto Z. \tag{2.7}$$

Elastic scattering

Elastic X-ray scattering, which is also known as Thomson or Rayleigh scattering, occurs when only the direction of the incident photon is changed, not its energy or its momentum, respectively (Buzug, 2008). The latter corresponds to wavelengths of the X-ray photon λ being much larger than the diameter d of the object

$$\lambda \gg d, \tag{2.8}$$

which is usually the case for electrons and X-rays. Generally, elastic photon scattering at an electron can be described by the Thomson cross section

$$\sigma_{\text{coh,e}} = \frac{8\pi}{3} r_0^2 \frac{\omega^4}{(\omega^2 - \omega_0^2)^2}, \tag{2.9}$$

with the natural frequency of bound electrons ω_0 (Buzug, 2008). At the high photon energy limit corresponding to $\omega \gg \omega_0$, the Thomson cross section at a single electron becomes constant with

$$\sigma_{\text{coh,e}} = \frac{8\pi}{3} r_0^2, \tag{2.10}$$

which equals the Klein-Nishina cross section (Eq. 2.5) in its low energy limit $E \to 0$. Scattering now at an atom with Z electrons leads to

$$\sigma_{\text{coh}} = Z\sigma_{\text{coh,e}}. \tag{2.11}$$

In classical electromagnetic description, the elastic scattering cross section should be independent of the energy and show only a proportionality to the atomic number

$$\sigma_{\text{coh}}(Z) \propto Z. \tag{2.12}$$

However, quantum mechanical effects lead to an energy dependency, which can be observed in Fig. 2.1, where the total cross section with its individual components is shown by way of example for water and iodine.

2.1.2 Atomic scattering factor

The total atomic scattering factor $f(\vec{Q})$ with scattering vector $\vec{Q}$ describes wave-optical properties of materials when going from photon scattering at a single electron to a cloud of assumed free electrons. Multiple scattering occurs in phase, when the scattering process happens in forward direction $\vec{Q} \approx 0$. However, when scattering happens at a different angle, the relative phase and the amplitudes between two scattering waves will differ from zero. The strength of this interaction is described by the total scattering factor $f(\vec{Q})$, which is the Fourier transform of the charge distribution $\rho(\vec{r})$

$$f(\vec{Q}) = \int \mathrm{e}^{2\pi i \vec{Q}\cdot\vec{r}}\, \rho(\vec{r}) \mathrm{d}\vec{r}. \tag{2.13}$$

The atomic scattering factor equals the atomic number $f(0) = Z$ when scattering in forward direction with $\vec{Q} = 0$ occurs (Willmott, 2011).

Considering now bound electrons in an atom or molecule, the response of the electrons to the electromagnetic wave of X-rays is dampened and reduces the atomic scattering factor by an additional factor f', if the X-ray energy is below the electron binding energy. Above the binding energy, the electron can be described as a free electron. Moreover, close to absorption edges, partial absorption will occur causing delayed re-emission leading to a change of phase and amplitude of the driving X-ray wave. The latter leads to an additional imaginary part of the atomic scattering factor corresponding to the absorption. In combination, those two effects form the total atomic scattering factor

$$f_{\mathrm{tot}} = f_1 + i f_2, \tag{2.14}$$

which is a complex quantity with f_1 being the real part and f_2 being the imaginary part. The real part can be expressed as

$$f_1 = f - f'. \tag{2.15}$$

If the electrons are free, $f' = 0$ and f_1 equals the unaltered scattering factor of Eq. (2.13). The imaginary part f_2 in forward direction can be formulated as

$$f_2(\vec{Q} = 0) = \frac{\sigma_{\mathrm{ph}}}{2 r_0 \lambda} = \frac{\sigma_{\mathrm{ph}} E}{2 r_0 h c}, \tag{2.16}$$

with the photoelectric cross section σ_{ph} described in Eq. (2.2) (Willmott, 2011).

2.1.3 Complex index of refraction

On a more macroscopic level of interaction, scattering and photoelectric absorption lead to reflection, refraction, and absorption of X-rays. The quantity describing those

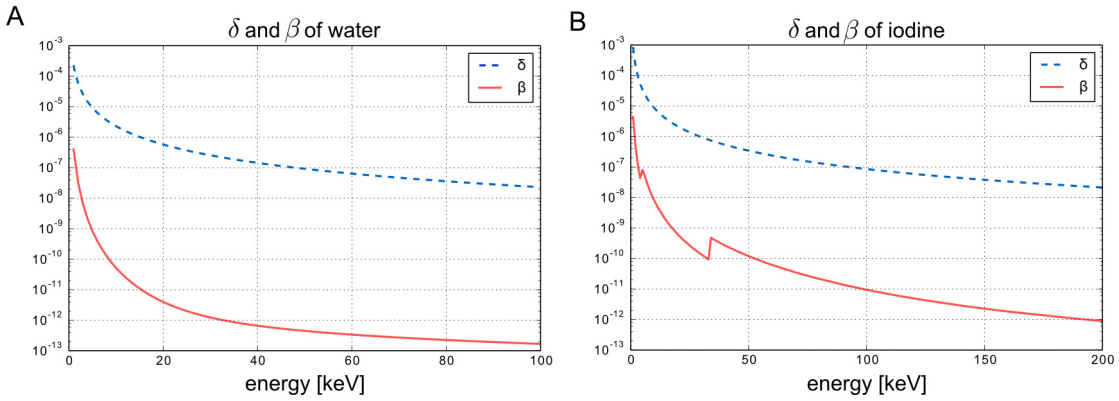

Fig. 2.2 | Comparison of delta and beta The refractive index decrement δ is compared to the imaginary part of the refractive index β, shown by way of example for water (A) and iodine (B). Iodine shows an absorption edge at 31 keV. The data can be found in Berger et al. (2010).

effects in the X-ray regime is the complex index of refraction

$$n(E) = 1 - \frac{r_0}{2\pi}\frac{(hc)^2}{E^2}\sum_i N_i f_i(\vec{Q}), \tag{2.17}$$

related to the atomic scattering factors with N_i being the number of atoms of type i per volume and $f_i(\vec{Q})$ being the atomic scattering factor of atom i (Willmott, 2011). Grouping Eq. (2.17) in real and imaginary part leads to

$$n(E) = 1 - \delta(E) + i\beta(E), \tag{2.18}$$

with δ being the refractive index decrement relevant for phase changes and β being the imaginary part related to absorption. Far from absorption edges and considering only scattering in forward direction, the scattering factor equals

$$\sum_i N_i f_{1,i}(\vec{Q} \approx 0) = \rho_\mathrm{e} \tag{2.19}$$

with ρ_e being the electron density according to Eqs. (2.13)–(2.16). Eventually, this results in the refractive index decrement

$$\delta = \frac{r_0}{2\pi}\lambda^2\rho_\mathrm{e} = \frac{2\pi r_0 \hbar^2 c^2}{E^2}\rho_\mathrm{e}. \tag{2.20}$$

Comparing the imaginary part of Eq. (2.18) with Eqs. (2.16) and (2.17) leads to the imaginary part of the refractive index

$$\beta = \frac{r_0}{2\pi}\lambda^2 f_2 = \frac{\lambda}{4\pi}\sum_i N_i\sigma_{i,\mathrm{ph}} = \frac{\hbar c}{2E}\sum_i N_i\sigma_{i,\mathrm{ph}}, \tag{2.21}$$

where $\sigma_{i,\mathrm{ph}}$ is the photoelectric cross section of atom i as illustrated in Fig. 2.2.

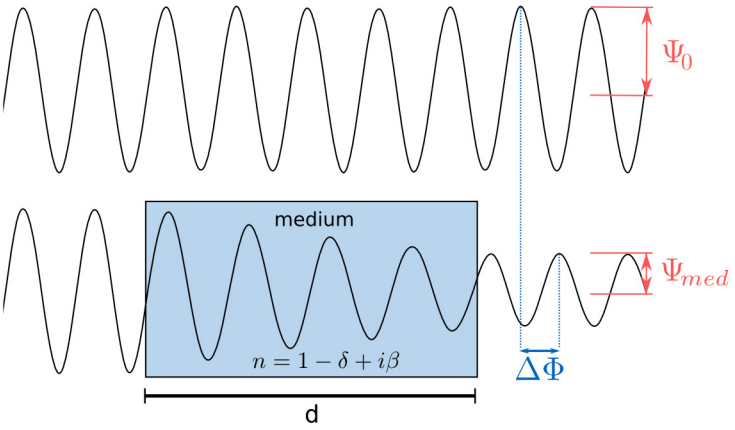

Fig. 2.3 | Comparison of a monochromatic wave propagating through vacuum and through an object with refractive index n. The object with thickness d induces both a phase shift $\Delta\Phi$ (blue) and a reduction of the amplitude from Ψ_0 to Ψ_{med} (red).

In the wave optical model, an electromagnetic wave can be described as

$$\Psi(\vec{r}, t) = \Psi_0 \, \mathrm{e}^{i(\vec{k}\cdot\vec{r} - \omega t)}, \tag{2.22}$$

where Ψ_0 is the initial amplitude at $\vec{r} = (0, 0, 0)^{\mathrm{T}}$, $\vec{k}$ is the wave vector with $|\vec{k}| = \frac{2\pi}{\lambda}$, and the angular frequency ω is defined by the energy $E = \hbar\omega$. If the wave is propagating in matter, the complex index of refraction is added in Eq. (2.22) changing its group velocity. Assuming a one-dimensional direction of the wave propagation with $\vec{r} = (0, 0, z)^{\mathrm{T}}$, Eq. (2.22) results in

$$\Psi(z, t) = \Psi_0 \, \mathrm{e}^{i(nkz - \omega t)} = \Psi_0 \underbrace{\mathrm{e}^{i(kz - \omega t)}}_{\text{propagation}} \cdot \underbrace{\mathrm{e}^{-i\delta kz}}_{\text{phase shift}} \cdot \underbrace{\mathrm{e}^{-\beta kz}}_{\text{attenuation}}, \tag{2.23}$$

where the first term describes the undisturbed wave propagation, the second term the phase shift, and the last term describes the attenuation of the initial wave as shown in Fig. 2.3.

Attenuation and the Lambert-Beer law

When X-rays interact with matter, the wave amplitude is reduced and the phase is shifted as indicated in Eq. (2.23). The amplitude is related to the intensity, which is the experimental quantity that can be directly accessed. Squaring Eq. (2.23) results in the intensity

$$I(z) = |\Psi(z, t)|^2 = \Psi_0^2 \, \mathrm{e}^{-2\beta kz}. \tag{2.24}$$

Based on this equation, the linear attenuation coefficient is defined as the exponential proportionality $\mu = 2k\beta$. In a simplified case, the exponential decay – also known as Lambert-Beer law – is

$$I(z) = I_0 \, \mathrm{e}^{-\mu z}, \tag{2.25}$$

with a linear mono-energetic attenuation coefficient μ and a homogeneous object with thickness z. In the polychromatic case with an heterogeneous object, Lambert-Beer law is denoted as

$$I(z) = \int_{E_{\min}}^{E_{\max}} I_0(E)\, \mathrm{e}^{-\int_0^z \mu(E,Z,z')\mathrm{d}z'}\, \mathrm{d}E. \tag{2.26}$$

The total attenuation coefficient $\mu(E, Z)$ for a material depends on both the energy E and the atomic number Z and relates to the scattering cross section $\sigma_{\mathrm{tot}}(E, Z)$ from Eq. (2.1) as

$$\mu(E, Z) = \left(\frac{\rho N_A}{A}\right) \sigma_{\mathrm{tot}}(E, Z), \tag{2.27}$$

with ρ being the mass density, N_A being Avogadro's constant, and A being the atomic mass number. When dealing with molecules with N atoms, the total energy-dependent attenuation coefficient is

$$\mu(E) = \sum_i^N w_i \mu_i(E), \tag{2.28}$$

with the mass fraction w_i of atom i and the respective attenuation coefficient $\mu_i(E)$. Attenuation coefficients and β-values by way of example for water ($Z \approx 7.5$) and iodine ($Z = 53$) are shown in Figs. 2.1 and 2.2.

Snell's law for X-rays

Snell's law known from geometrical optics is also valid for X-rays

$$n_1 \sin\alpha_1 = n_2 \sin\alpha_2, \tag{2.29}$$

with the complex indices of refraction n_i and the refraction angles α_i. Assuming an X-ray wave transversing a purely phase shifting object with $n_2 = 1-\delta$ in air, Eq. (2.29) results in

$$\sin\alpha_1 = (1-\delta)\sin\alpha_2, \tag{2.30}$$

with the complex index of refraction of air n_1 approximated to 1. The electron density is thereby the essential parameter, which is in air approximately $3.62\times10^{-1}\,\mathrm{e/nm^3}$ and about three orders of magnitude below the electron density of water ($3.34\times10^{2}\,\mathrm{e/nm^3}$). Using the approximation $\sin x \approx x$, Eq. (2.30) simplifies to

$$\alpha_1 \approx (1-\delta)\alpha_2. \tag{2.31}$$

The difference of those two angles $\Delta\alpha = \alpha_2 - \alpha_1$ is then

$$\Delta\alpha \approx \delta\alpha_2. \tag{2.32}$$

Due to the higher energy of X-rays in comparison to visible light (cf. Eq. 2.20), the refractive index decrement δ is in the order of $10^{-5} - 10^{-8}$ depending on the material and energy (Als-Nielsen and McMorrow, 2011). Visualizing such small differences in the refractive index and thus in the refraction angle α is one central difficulty of

phase-contrast imaging. Refractive index decrement values by way of example for water ($Z \approx 7.5$) and iodine ($Z = 53$) are shown in Fig. 2.2 (A) and (B).

2.2 Talbot effect

In order to derive the Talbot effect necessary for the understanding of grating interferometry, one has to consider Fresnel diffraction in the near-field. An object in the beam distorts the wave front and – depending on the distance between the object and the interaction – the distorted wave propagates further in free space until the detector system is reached (Talbot, 1836; Paganin, 2006).

2.2.1 Wave front propagation

The Fresnel integral is an approximation of the Kirchhoff-Fresnel diffraction integral for spherical waves using the paraxial approximation $|k_z| \gg |k_\perp|$ for either relatively small objects or large propagation distances in beam direction. The total distance is then $r \approx z + \frac{x^2+y^2}{2z}$. If one assumes a monochromatic and time-independent wave front with a refractive index $n = 1$, one can formulate the Fresnel integral as

$$\Psi(x, y, z) = \frac{\mathrm{e}^{ikz}}{i\lambda z} \iint \Psi_0(x', y', z = 0)\, \mathrm{e}^{\frac{ik}{2z}((x-x')^2+(y-y')^2)}\, \mathrm{d}x'\mathrm{d}y', \tag{2.33}$$

based on the Huygens-Fresnel principle stating that at each wave can be formed by a sum of spherical point waves. This equation is equivalent to a convolution of the initial wave front $\Psi(x, y, z = 0)$ with a propagator function

$$\mathcal{P}(x, y, z) = \frac{\mathrm{e}^{ikz}}{i\lambda z}\, \mathrm{e}^{ik(x^2+y^2)/2z}\,. \tag{2.34}$$

resulting in

$$\Psi(x, y, z) = \mathcal{P}(x, y, z) \star \Psi(x, y, z = 0), \tag{2.35}$$

with $\star$ being the convolution operator. Using the convolution theorem

$$\mathcal{F}\{A \star B\} = \mathcal{F}\{A\} \cdot \mathcal{F}\{B\}, \tag{2.36}$$

where $\mathcal{F}$ denotes the Fourier transform, one can express the convolution in the two-dimensional case as

$$\Psi(x, y, z) = \mathcal{F}_{2\mathrm{D}}^{-1}\{\mathcal{F}_{2\mathrm{D}}\{\mathcal{P}(x, y, z)\} \cdot \mathcal{F}_{2\mathrm{D}}\{\Psi_0(x', y', z = 0)\}\}, \tag{2.37}$$

turning the Fresnel integral into a multiplication in frequency space.
The two-dimensional Fourier transform of the propagator $\mathcal{P}(x, y, z)$ in Eq. (2.34) is simply

$$\tilde{\mathcal{P}}(k_\mathrm{x}, k_\mathrm{y}, z) \equiv \mathrm{e}^{ikz}\, \mathrm{e}^{-iz(k_\mathrm{x}^2+k_\mathrm{y}^2)/2k}, \tag{2.38}$$

with k_x and k_y being the components of the wave vector in x- and y-direction.

A periodical structure in the beam with period p results in frequency components

$k_\mathrm{x} = 2\pi m/p$ and $k_\mathrm{y} = 2\pi n/p$ after Fourier transform with m, n being positive integers. Added to Eq. (2.38) at distance $z = d$, the propagator yields

$$\tilde{\mathcal{P}}(k_\mathrm{x} = 2\pi m/p, k_\mathrm{y} = 2\pi n/p, z = d) = \mathrm{e}^{ikd}\,\mathrm{e}^{-\frac{id}{2k}[(\frac{2\pi m}{p})^2+(\frac{2\pi n}{p})^2]} \tag{2.39}$$

$$= \mathrm{e}^{ikd}\,\mathrm{e}^{-id\frac{\lambda}{4\pi}(\frac{2\pi}{p})^2[m^2+n^2]} \tag{2.40}$$

$$= \mathrm{e}^{ikd}\,\mathrm{e}^{-2\pi id\frac{\lambda}{2p^2}[m^2+n^2]}, \tag{2.41}$$

and if the distance d matches the Talbot distance

$$d_\mathrm{T} = \frac{2p^2}{\lambda}, \tag{2.42}$$

this leads to

$$\tilde{\mathcal{P}}(k_\mathrm{x} = 2\pi m/p, k_\mathrm{y} = 2\pi n/p, z = d_\mathrm{T}) = \mathrm{e}^{ikd_\mathrm{T}}\,. \tag{2.43}$$

This equation signifies that the propagator at the Talbot distance d_T is the same as the propagator at the initial position $z = 0$. For the wave function, this means

$$\Psi(x, y, z = d_\mathrm{T}) = \Psi(x, y, z = 0), \tag{2.44}$$

under the condition that the grating structure is periodical according to Eq. (2.39).

2.2.2 Talbot distances

Experimentally, Henry Fox Talbot was the first one to discover this effect in 1836 with visible light and a grating (Talbot, 1836). He observed reappearing interference patterns at only certain distances. But also fractional distances can be observed (Winthrop and Worthington, 1965). Those fractional distances were experimentally determined to occur at

$$d_\mathrm{T} = \eta \cdot \frac{2p^2}{\lambda}, \tag{2.45}$$

where $n = 1, 3, 5...$ is the fractional Talbot order and the factor η being

$$\eta = \begin{cases} n & \text{for an absorption grating,} \\ \frac{n}{4} & \text{for a } \frac{\pi}{2}\text{-phase grating,} \\ \frac{n}{16} & \text{for a } \pi\text{-phase grating.} \end{cases} \tag{2.46}$$

A simulated Talbot carpet for fractional distances for the first period is shown for three different exemplary grating types in Fig. 2.4. For an absorption grating, the reappearing intensity pattern repeats itself at half the Talbot distance (cf. Fig. 2.4 A). An ideal $\frac{\pi}{2}$-shift phase grating has maximum intensity modulation at $\frac{1}{4}d_\mathrm{T}$ and $\frac{3}{4}d_\mathrm{T}$ (cf. Fig. 2.4 B). A π-shift phase grating has multiple occurrences at $\frac{m}{16}d_\mathrm{T}$ with m being an odd integer (cf. Fig. 2.4 C). Importantly, the period of the intensity pattern behind the grating also depends on the induced phase shift. Absorption and $\frac{\pi}{2}$-phase gratings have the same period while π-phase grating periods are halved.

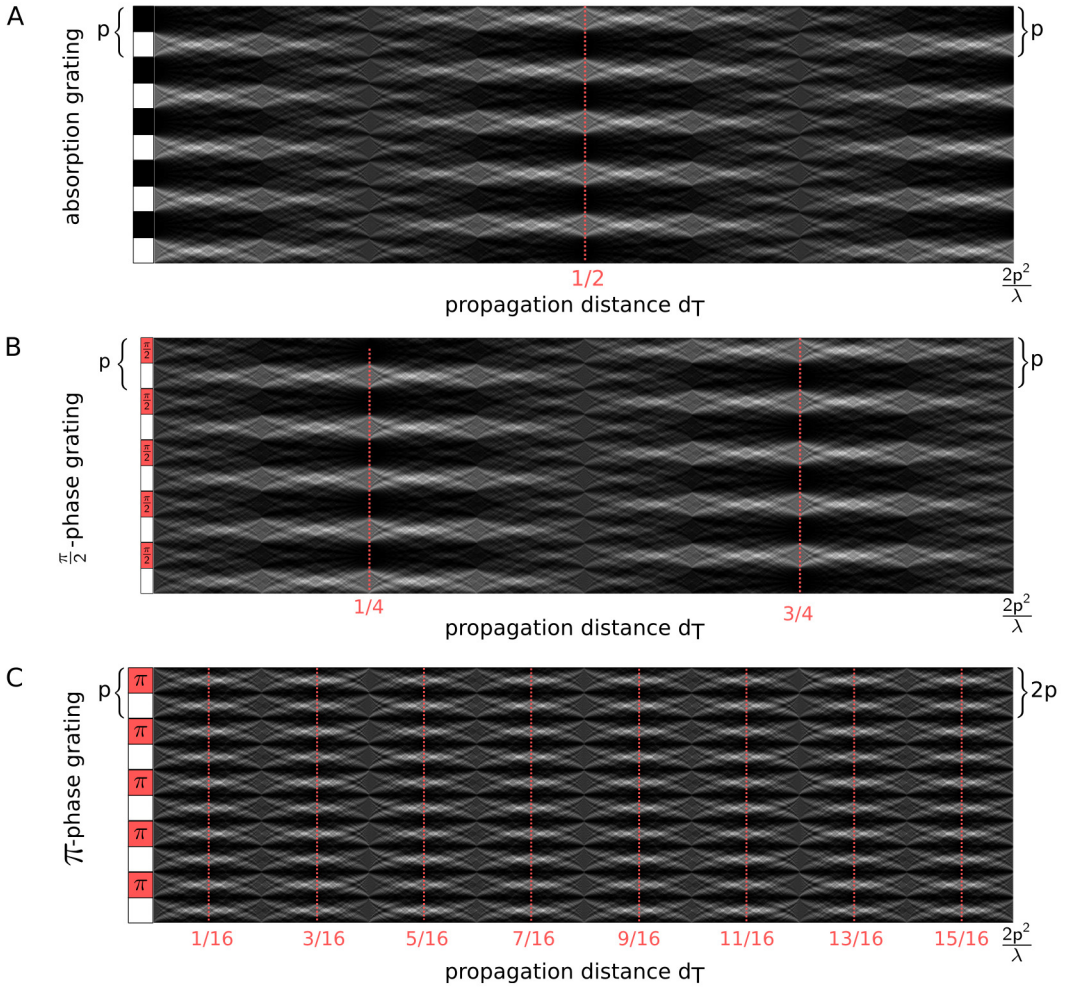

Fig. 2.4 | Talbot carpet of three different grating types. An absorption grating (A), a $\pi/2$-phase grating (B), and a π-phase grating (C) are shown for a full Talbot distance d_T in parallel beam geometry (monochromatic). Fractional Talbot distances can be observed. For the π-phase grating, the resulting period equals half of the initial period.

2.3 X-ray grating interferometry

The idea behind X-ray grating interferometry is to access the phase shift $\Delta\Phi$ of an object caused by changes in the phase shifting part of Eq. (2.23):

$$\Delta\Phi = k \int \delta(\vec{r})\mathrm{d}z. \tag{2.47}$$

In X-ray grating interferometry, the so-called phase grating creates the reoccurring interference pattern at the Talbot distances d_T due to its periodic structure according to Eqs. (2.39) - (2.42). An additional analyzer grating is required to resolve the interference pattern. The latter has to be positioned at the Talbot distance, where the pattern is reoccurring. If the detector has small enough pixel sizes, one can directly resolve the pattern without the need of an analyzer grating. Depending on the periods,

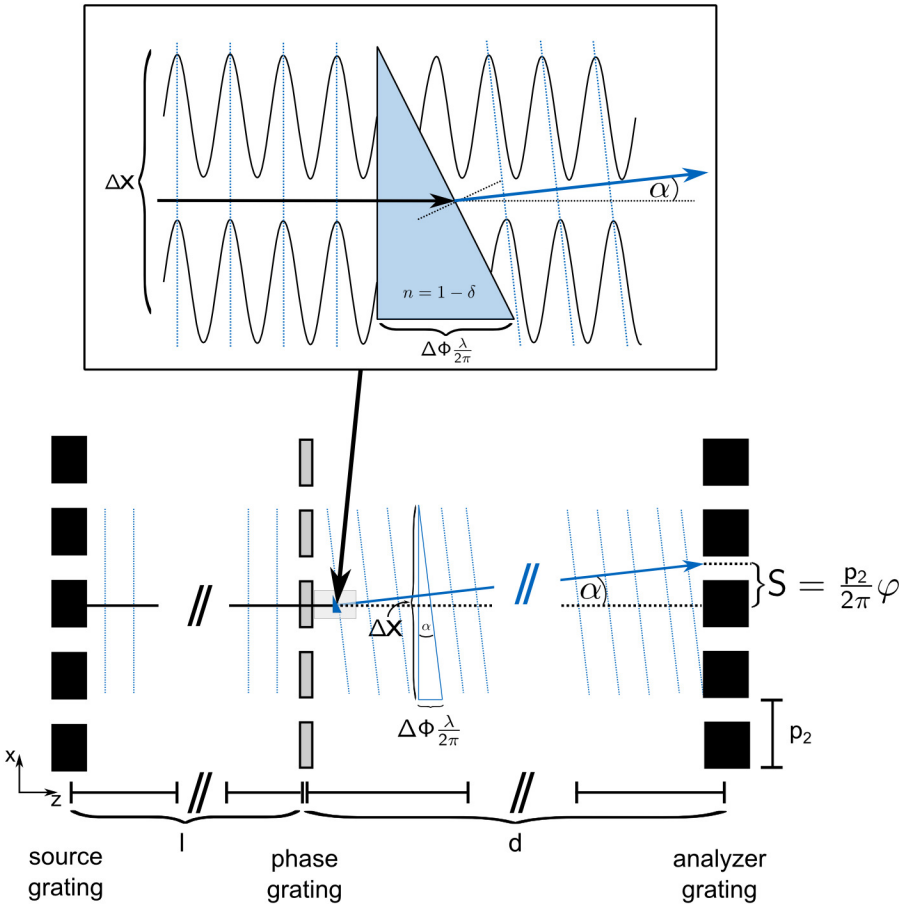

Fig. 2.5 | Interaction at a Talbot-Lau interferometer. Refraction in the sample causes a change of the direction of the wave front α, which is proportional to the difference in optical path $\Delta\Phi/2\pi\lambda$ over a lateral beam distance Δx. The changed wave front propagates to the analyzer grating causing a shift in the interference pattern S. The figure is not to scale.

distances, and the source size, a so-called source grating is required to fulfill coherence requirements (Paganin, 2006; Pfeiffer et al., 2006).

Refraction angle α

Refraction of an object can be described by the refraction angle related to the gradient of the phase:

$$\tan\alpha = \left|\frac{1}{k}\nabla\Phi\right|. \tag{2.48}$$

For simplification, only a two-dimensional description in the x-z-plane is given here. The refraction angle α is also related to a change in the wave front and can be expressed as

$$\tan\alpha = \frac{\lambda}{2\pi}\frac{\Delta\Phi}{\Delta x}, \tag{2.49}$$

as shown in Fig. 2.5. By approximating $\tan\alpha \approx \alpha$ and using

$$\lim_{\Delta x \to 0} \frac{\Delta\Phi}{\Delta x} = \frac{\partial\Phi}{\partial x}, \tag{2.50}$$

one obtains

$$\alpha \approx \frac{1}{k}\frac{\partial\Phi}{\partial x}, \tag{2.51}$$

which describes the relation between α and the gradient of the phase $\nabla_x\Phi$ in one dimension. The refraction angle α causes a lateral shift of the interference pattern S at the position of the analyzer grating. Geometric considerations shown in Fig. 2.5 lead to

$$\tan\alpha = \frac{S}{d}, \tag{2.52}$$

with d being the inter-grating distance between phase and analyzer grating. A purely phase shifting object in the beam leads to a phase shift of the interference pattern φ, which is related to the lateral shift of the interference pattern S by

$$S = \frac{p_2}{2\pi}\varphi, \tag{2.53}$$

with p_2 being the period of the analyzer grating as illustrated in Fig. 2.5. By approximating again $\tan\alpha \approx \alpha$, the combination of the two prior equations Eqs. (2.52) and (2.53) results in the refraction angle in dependency of the setup geometry

$$\alpha \approx \frac{p_2}{2\pi d}\varphi. \tag{2.54}$$

Combining now Eqs. (2.51) and (2.54), one obtains

$$\frac{1}{k}\frac{\partial\Phi}{\partial x} = \frac{p_2}{2\pi d}\varphi. \tag{2.55}$$

Using Eq. (2.47) and including position dependencies, the refractive index decrement $\delta(x)$ is eventually calculated as

$$\delta(x) = \int \delta(x, z')\mathrm{d}z' = \frac{p_2}{2\pi d}\int_0^x \varphi(x')\mathrm{d}x'. \tag{2.56}$$

2.3.1 Image signals

However, this phase shift φ cannot be resolved directly. As already illustrated with Snell's law (cf. Eq. 2.31), the change in refraction angles for X-rays is in the range of $10^{-5} - 10^{-8}$, which is invisible for large pixel sizes of the detector. But also with the analyzer grating with periods typically in the range of $5 - 50\,\mu\mathrm{m}$, resolution of changes in the phase shift is usually hardly possible. To precisely resolve the refraction angle, one uses the phase-stepping procedure (cf. Sec. 3.4.1) (Weitkamp et al., 2005). Thereby, one grating is shifted laterally by at least one grating period.

The phase-stepping allows to determine three different image contrast signals: the attenuation contrast, the differential phase-contrast, and the dark-field contrast

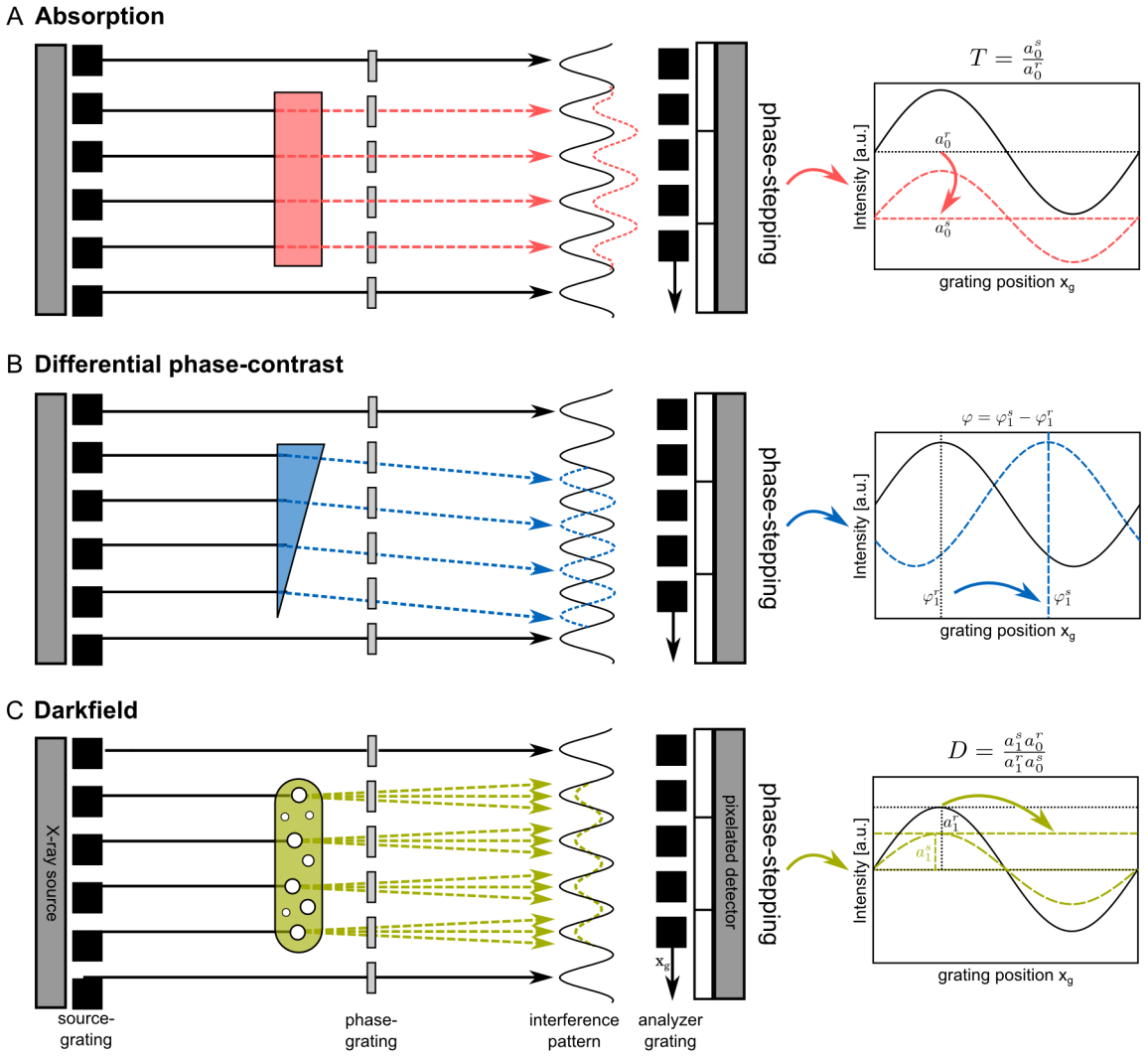

Fig. 2.6 | Contrast signals at Talbot-Lau interferometer. Three different contrast signals are retrieved by the grating interferometer. The attenuation signal is a reduction of the mean intensity a_0 of a purely attenuating object and leads to different offsets of the stepping curve (A). A purely refracting object causes a lateral phase-shift of the interference pattern φ of the stepping curve (B). Multiple scattering of an object neglecting absorption and refraction reduces the amplitude of the interference signal a_1 (C). This is referred to as the dark-field signal. Figure partly adapted from Scherer (2015).

(Weitkamp et al., 2005; Pfeiffer et al., 2008, 2009). A phase-stepping curve is schematically shown in Fig. 2.6 for each of the signals. The measured intensity for M phase steps in dependency of the grating position x_g is

$$I(x, y, x_g) = \sum_i^M a_i \sin\left(\frac{2\pi}{p} x_g + \varphi_i\right), \tag{2.57}$$

which can be approximated to

$$I(x, y, x_\mathrm{g}) \approx a_0 + a_1 \sin(\frac{2\pi}{p} x_\mathrm{g} + \varphi) \tag{2.58}$$

if the visibility is below 50 %, what is usually the case in laboratory Talbot interferometers (Bech, 2009).

Attenuation contrast

The attenuation contrast is the average intensity a_0 of the stepping curve (cf. Fig. 2.6 A). With a sample in the beam, for which a reference curve has to be determined, the transmission signal is

$$T(x, y) = \frac{a_0^\mathrm{s}}{a_0^\mathrm{r}} = \mathrm{e}^{-\int \mu(x,y,z)\mathrm{d}z}, \tag{2.59}$$

with superscript 's' denoting the sample scan and superscript 'r' the reference scan.

Differential phase-contrast

As can be seen in Fig. 2.6 (B), the two stepping curves for the sample and the reference have different phase offsets. The difference between these signals is the differential phase-contrast signal

$$\varphi(x, y) = \varphi^\mathrm{s} - \varphi^\mathrm{r}. \tag{2.60}$$

Visibility and dark-field contrast

Moreover, the relative amplitude a_1 with respect to the mean intensity a_0 defines the visibility V of the interferometer, which is an essential parameter to assess the quality of the interferometer. The visibility is defined by the maximum and minimum intensity

$$V(x, y) = \frac{I_\mathrm{max} - I_\mathrm{min}}{I_\mathrm{max} + I_\mathrm{min}} = \frac{a_1}{a_0}. \tag{2.61}$$

The reduction of the visibility due to scattering is described by the dark-field signal (cf. Fig. 2.6 C)

$$D(x, y) = \frac{a_1^\mathrm{s} a_0^\mathrm{r}}{a_1^\mathrm{r} a_0^\mathrm{s}} = \mathrm{e}^{-\frac{2\pi^2 d^2}{p_2^2} \int \epsilon(x,y,z)\mathrm{d}z}, \tag{2.62}$$

with the linear diffusion coefficient $\epsilon(x, y, z)$ and a setup dependent prefactor $\frac{2\pi^2 d^2}{p_2^2}$. The theoretical basis of the dark-field signal is investigated in Yashiro et al. (2010); Lynch et al. (2011); Jensen et al. (2010); Chabior et al. (2011b); Malecki et al. (2012); Strobl (2014); Prade et al. (2015). The dark-field signal enables to visualize small-angle scattering of structures below the physical pixel size, which are not visible in the absorption signal (cf. Fig. 2.7). The sensitivity of feature sizes in the dark-field signal is moreover described by the autocorrelation length

$$\xi = \frac{d_{\mathrm{S,G_2}} \lambda}{p_2}, \tag{2.63}$$

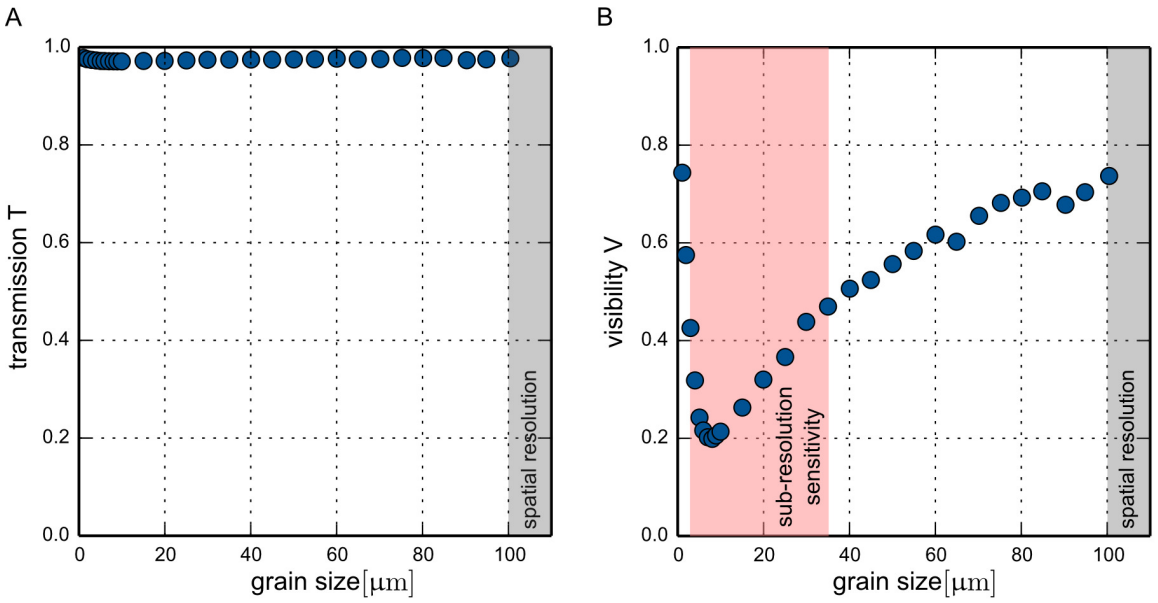

Fig. 2.7 | Comparison of transmission and dark-field signal. In a simulation, the transmission and the dark-field signal of calcium spheres were investigated (Malecki et al., 2012). The total amount of calcium stayed constant, only the number and diameter of the spheres was changed. As it turned out, the transmission signal (A) did not change at all as the integrated attenuation stays constant. In the dark-field signal (B) however, the same signal depends highly on the sphere diameter and number. The maximum signal (visibility reduction) lies around the period of the X-ray analyzer grating. This illustrates the sub-resolution sensitivity of the dark-field signal (red area) in comparison to the spatial resolution of the system. Figure adapted from Scherer (2015).

in dependency of the distance from the object to the analyzer grating d_{S,G_2}, the wavelength λ, and the period of the analyzer grating p_2 (Prade et al., 2015). Similar considerations are used in the description of the angular sensitivity of the phase-contrast signal in Ch. 4.

2.3.2 X-ray Talbot-Lau interferometry

Up to now, one assumed that the beam is monochromatic and one has a point like source size. But coherence requirements have to be included for phase-contrast imaging with polychromatic radiation and extended source sizes of laboratory X-ray sources.

Transverse coherence requirements

The Talbot effect and thus the interference pattern is only visible if the beam is sufficiently coherent (Paganin, 2006; Pfeiffer et al., 2006). This is often not the case if high flux laboratory X-ray sources with larger focal spots are used. If the source size is too large, blur of the source size causes the interference pattern to smear out or even vanish (cf. Fig. 2.8 A).

If one considers an extended source size as a sum of separated line sources in distance ϵ (Bech, 2009), the separation of the line sources at the analyzer grating has to

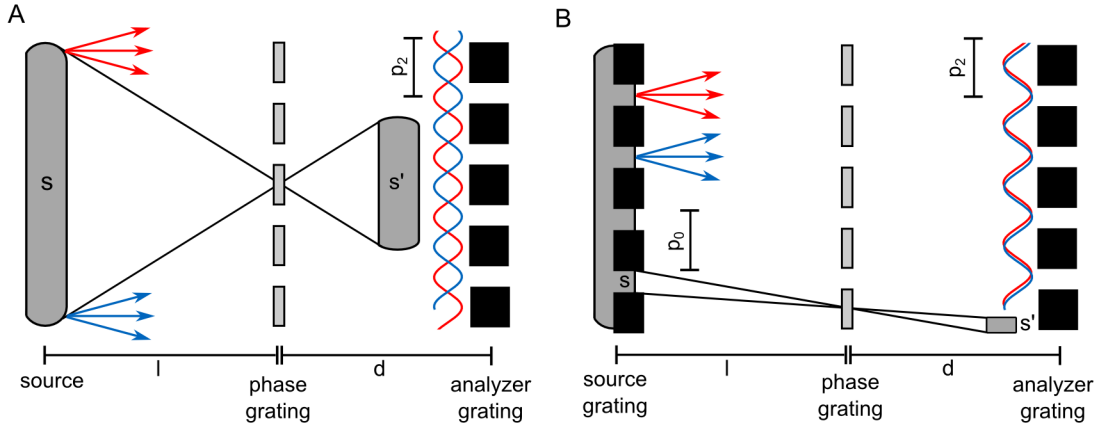

Fig. 2.8 | Illustration of the effect of source-blurring. An extended source causes destructive interference (A), which can be prevented by reducing the projected source size by either large source-to-phase-grating distances l or with the insertion of a source grating (B). The figure is not to scale. Figure partly adapted from Scherer (2015).

be much smaller than the period of the analyzer grating p_2

$$\epsilon \frac{d}{l} \ll p_2. \tag{2.64}$$

Moreover, if the condition $\epsilon d/l = p_2/2$ is fulfilled, the patterns will interfere destructively. This requires a source size s with

$$s \leq \frac{l p_2}{2d}. \tag{2.65}$$

At synchrotron sources with large distances from the phase grating to the source l, this requirement is easily fulfilled. Also with microfocus sources which have a small focal spot of several microns, it is possible to observe the Talbot effect in laboratory environment.
For larger source sizes like with high flux rotating anode sources, one idea to overcome this limitation is to introduce a third grating, the so-called source grating (Pfeiffer et al., 2006). The source grating, which is also an absorption grating like the analyzer grating, divides the extended tube source into multiple thin line sources. With geometrical considerations as illustrated in Fig. 2.8 (B), the period of the source grating p_0 has to be chosen as

$$p_0 = \frac{l}{d} p_2. \tag{2.66}$$

The extended source allows high flux and the source grating provides the necessary partial transverse coherence for the Talbot effect to occur.

Longitudinal coherence requirements

Besides the requirements for transverse coherence due to an enlarged source size, one remaining question is whether the interferometer works with a polychromatic X-ray

source. According to Eq. (2.45), each energy leads to a different Talbot distance. Depending on the spectrum $S(E)$, one chooses a design energy for the phase grating. Photons with higher or lower energy as the design energy of the phase-grating corresponding to the Talbot distance have reduced visibility (Chabior, 2011). Additionally, the phase-grating is designed for a mean energy and the phase-shift for all other energies is different. A superposition of those effects and the choice of distances and duty cycles of the gratings results in the mean visibility. The experimental mean visibility $V(E)$ including its spectral dependency is presented in Sec. 3.6.3. More detailed description of the energy dependent visibility (or spectral acceptance) of the interferometer can be found in Chabior (2011).

2.4 Computed tomography

Computed tomography is a non-destructive X-ray imaging method to determine the interior of an object. With a set of angular projections, one can computationally reconstruct the inner composition of an object. Basically, there are two different methods to reconstruct the data. Filtered backprojection (FBP) is a reconstruction method which is fast and analytically well described. The other type of reconstructions are iterative reconstruction methods. In this work, statistical iterative reconstruction (SIR) is presented next to FBP. Compared to FBP, SIR includes prior knowledge of the sample and statistical information in the reconstruction, allows arbitrary beam geometry, and can handle better missing measurement data. However, the method is rather complex and computationally expensive (Buzug, 2008; Kalender, 2006; Kak and Slaney, 1988).

2.4.1 Filtered backprojection

In filtered backprojection, a set of N sample projections under different angles θ is measured. In the following, parallel beam geometry and a two-dimensional object $f(x, y)$ are assumed. A projection of the object is measured at the rotation angle θ and is defined by the line integral

$$p_\theta(r) = -\ln\left(\frac{I}{I_0}\right) = \int_0^s \mu(s')\mathrm{d}s', \tag{2.67}$$

with the detected signal intensity I relative to the initial intensity I_0 (cf. Fig. 2.9). To account for the exponential dependency in the Lambert-Beer law (cf. Eq. 2.26), the logarithm of the line integral is taken.

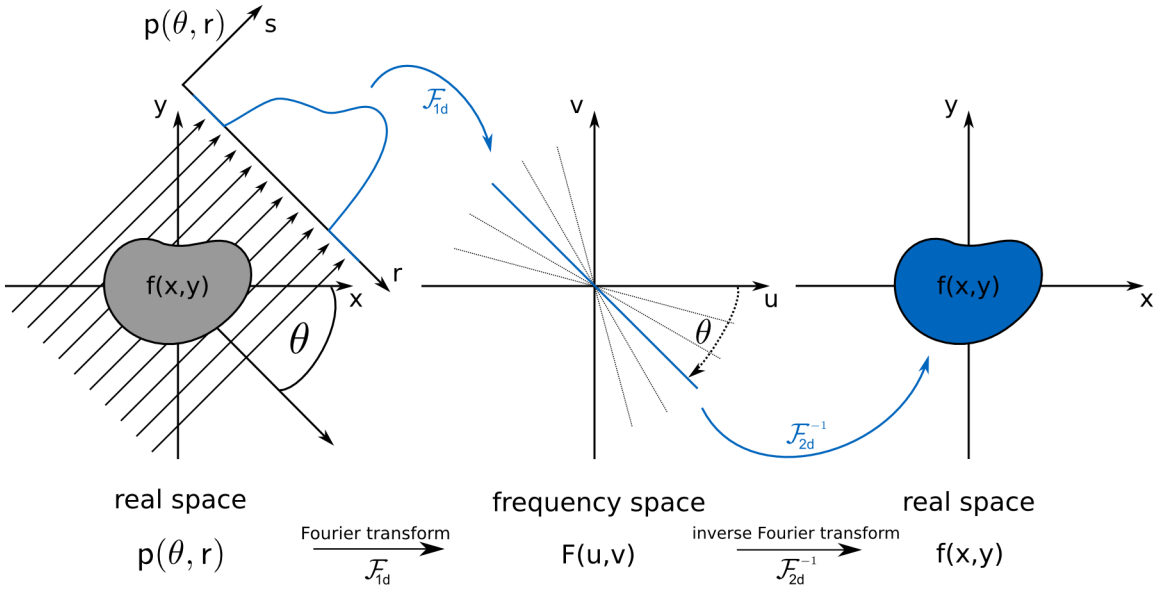

Fig. 2.9 | Fourier slice theorem. The object $f(x, y)$ is measured under the angle θ leading to the projection $p(\theta, r)$. The one-dimensional Fourier transform of a single projection $p(\theta, r)$ corresponds to a slice of the two-dimensional Fourier transform of the object function under the same angle θ. If the two-dimensional Fourier transform is sampled by measuring several projections under different angles, the object function $f(x, y)$ is determined via two-dimensional inverse Fourier transform from $F(u, v)$.

Radon transform

Taking a projection of the object under a certain angle is described by the Radon transform $\mathcal{R}_\theta$ (Radon, 1986)

$$p_\theta(r) = \mathcal{R}_\theta\{f(x,y)\} \tag{2.68}$$

$$= \int_0^d f(r,s)\mathrm{d}s \tag{2.69}$$

$$= \iint_{-\infty}^{\infty} f(x,y)\delta(x\cos\theta - y\sin\theta - r)\mathrm{d}x\mathrm{d}y, \tag{2.70}$$

with the coordinates $r = x\cos\theta - y\sin\theta$, which corresponds to the detector width, and the beam direction for each direction $s = x\sin\theta + y\cos\theta$ as illustrated in Fig. 2.9. The measured set of projections in dependency of the angle θ and the detector width is called sinogram. The idea is now to determine the object function by the inverse Radon function

$$f(x,y) = \mathcal{R}_\theta^{-1}\left\{\int p(\theta,r)\mathrm{d}\theta\right\}. \tag{2.71}$$

However, a direct inversion would be computationally too expensive and would fail in the presence of noise. One idea to reconstruct the data is to use the Fourier slice theorem and filtered backprojection.

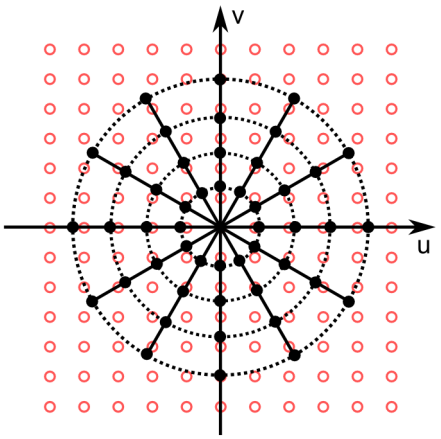

Fig. 2.10 | Radial frequency distribution. The experimental data is measured in polar coordinates (black dots). After Fourier transform of the projections, this leads to increased sampling of lower frequencies in the center and more sparse sampling at higher frequencies. With the use of the Fourier slice theorem, the radial slices are filled by further projections and transformed to Cartesian coordinates u and v represented by the red circles.

Fourier slice theorem

The Fourier slice theorem states that a one-dimensional Fourier transform of a projection $p_\theta(r)$ with respect to r equals a radial slice of the two-dimensional Fourier transform of the object $f(x, y)$ under the same angle θ. The one-dimensional Fourier transform of the projection is then:

$$
\begin{aligned}
P(\theta,\omega) :&= \mathcal{F}_{\mathrm{r}\to\omega}\{p_\theta(r)\} && (2.72)\\
&= \int p_\theta(r) e^{-2\pi i\omega r}\mathrm{d}r && (2.73)\\
&= \int \Big[\iint f(x,y)\delta(x\cos\theta - y\sin\theta - r)\mathrm{d}x\mathrm{d}y\Big] e^{-2\pi i\omega r}\mathrm{d}r && (2.74)\\
&= \iint \Big[\int f(x,y)\delta(x\cos\theta - y\sin\theta - r) e^{-2\pi i\omega r}\mathrm{d}r\Big]\mathrm{d}x\mathrm{d}y && (2.75)\\
&= \iint f(x,y) e^{-2\pi i\omega(x\cos\theta - y\sin\theta)}\mathrm{d}x\mathrm{d}y && (2.76)\\
&= \iint f(x,y) e^{-2\pi i(ux+vy)}\mathrm{d}x\mathrm{d}y\Big|_{u=\omega\cos\theta, v=-\omega\sin\theta} && (2.77)\\
&= \mathcal{F}_{2\mathrm{D}}\{f(x,y)\}(u,v)\Big|_{u=\omega\cos\theta, v=-\omega\sin\theta} && (2.78)\\
&=: F(u=\omega\cos\theta, v=-\omega\sin\theta), && (2.79)
\end{aligned}
$$

with $u = \omega\cos\theta$ and $v = -\omega\sin\theta$.

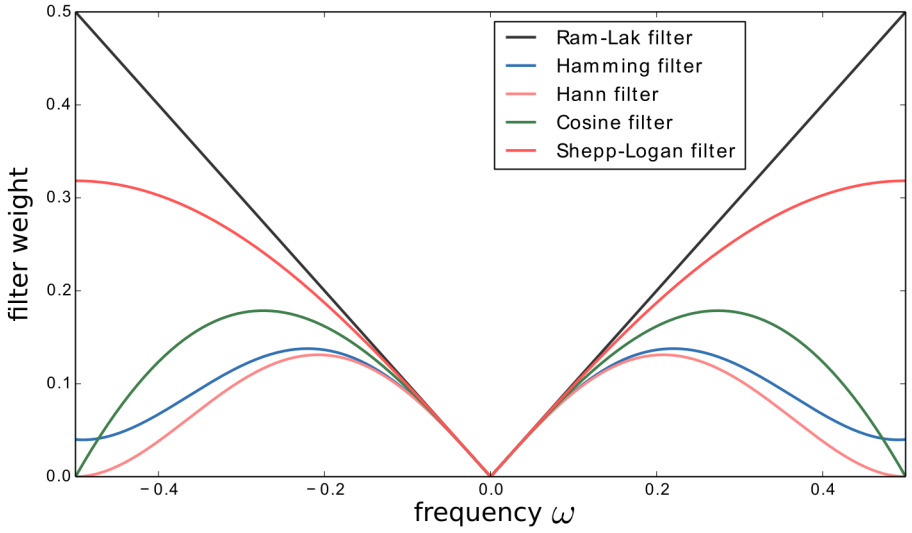

Fig. 2.11 | Different FBP filter functions. Five different FBP filter functions are shown. The Ram-Lak filter is the standard ramp filter originating from coordinate transformation. The other filters have an increasing roll-off towards higher frequencies for noise suppression. The downside is a reduction of spatial resolution.

Filtered backprojection

Filtered backprojection (FBP) is now the process of determining the object function $f(x, y)$ from the measured projections $p(\theta, r)$ exploiting the Fourier slice theorem. The object function $f(x, y)$ can be expressed as the two-dimensional inverse Fourier function

$$f(x,y) = \iint F(u,v) e^{2\pi i(ux+vy)} \mathrm{d}u\mathrm{d}v \tag{2.80}$$

$$= \iint P(\theta,\omega) e^{2\pi i(ux+vy)} \mathrm{d}u\mathrm{d}v \Big|_{u=\omega\cos\theta, v=\omega-\sin\theta} \tag{2.81}$$

$$= \int_0^{2\pi} \int_{-\infty}^{\infty} P(\theta,\omega)|\omega| e^{2\pi i\omega(x\cos\theta - y\sin\theta)} \mathrm{d}\omega\mathrm{d}\theta, \tag{2.82}$$

using the Fourier slice theorem and coordinate transform $\mathrm{d}u\mathrm{d}v = |\omega|\mathrm{d}\omega\mathrm{d}\theta$ obtained by the absolute value of the Jacobian determinant. The Jacobi determinant originates from a coordinate transform from Cartesian to polar coordinates and introduces the factor $|\omega|$ in Eq. (2.80), which is also known as the filter function. In this case, $|\omega|$ is called ramp or Ram-Lak filter. There exist different modifications of this filter to account for CT noise reduction as can be seen in Fig. 2.11. However, this roll-off towards higher frequencies causes a decrease in spatial resolution.

Filtered backprojection with differential data

In this work, not only conventional attenuation data, but also DPC and DFC data is reconstructed. The reconstruction of dark-field contrast (DFC) is handled in the same way as the reconstruction of the attenuation coefficients. For the reconstruction

of the differential phase-contrast (DPC) data however, the so-called Hilbert filter is used (Pfeiffer et al., 2007a):

$$H(\omega) = \frac{1}{2\pi i \operatorname{sgn}(\omega)}, \tag{2.83}$$

which corresponds to the ramp filter with an included integration due to the properties of the Fourier transform. Analysis of FBP reconstruction in combination with GBPC-CT with respect to noise and spatial resolution is investigated in Raupach and Flohr (2011); Köhler et al. (2011); Chen et al. (2011); Weber et al. (2011).

Cone beam geometry

In parallel beam geometry, the extension to three dimensions is straightforward since different slices are independent of each other and can thus be considered separately. However, when dealing with fan or even cone beam geometry, additional weights have to be included in the FBP reconstruction (Feldkamp et al., 1984).

Artifacts and sampling

Several reconstruction artifacts can occur in FBP reconstruction. When dealing with a polychromatic spectrum, beam hardening can lead to a deviating attenuation signal. Moreover, undersampling could deteriorate the image quality, next to metal artifacts also known as beam starvation (Boas and Fleischmann, 2012). According to the Nyquist sampling criterion, the minimum number of projections N for a sufficiently sampled tomographic reconstruction with FBP is given by $N \geq \frac{\pi}{2} n_{\text{pixels}}$ (Kak and Slaney, 1988). In DPC imaging, streak artifacts due to phase-wrapping and gradients in the reconstruction originating from gradients in the DPC projections are common reconstruction artifacts, which are presented in further detail in Sec. 3.4.2 and Ch. 6.

2.4.2 Statistical iterative reconstruction

A different reconstruction technique that emerged with increasing computational capabilities is statistical iterative reconstruction. Especially general purpose graphical processing units (GP-GPUs) allow massive parallelization of the reconstruction processes and thus a reduction of the computational time. The major advantages of statistical iterative reconstruction methods are the ability of implementing statistical models and prior knowledge. Besides, the SIR approach can handle complex geometries and missing data like e.g. lost projections. However, the approach is more complex than the analytical filtered-backprojection (Fessler, 2000).

In iterative reconstruction, the idea is to determine the data $\mathbf{f}$, i.e. the volume of the object to be reconstructed, after measuring experimentally a set of projections $\mathbf{p}$. The relation between the data $\mathbf{f}$ and the projections $\mathbf{p}$ is given by the system matrix A:

$$\mathrm{A}\mathbf{f} = \mathbf{p}. \tag{2.84}$$

As the volume $\mathbf{f}$ is the quantity of interest, inverting this equation leads to the inverse

problem

$$\mathbf{f} = \mathrm{A}^{-1}\mathbf{p}, \tag{2.85}$$

with the inverse matrix A^{-1}.

Several steps are necessary for statistical iterative reconstruction. First, the data has to be discretized similarly to FBP reconstruction. Next, prior knowledge and a combination of forward and data model have to be included. The forward model generates a physical simulation of the expected experiment and the data model calculates the log-likelihood minimization of the difference between measurement data and the forward projection of the calculated data model. The algorithm then tries to find the minimum of the penalized log-likelihood function L, which has to be optimized

$$\mathrm{L} = \left\|\mathrm{A}\mathbf{f} - \mathbf{p}\right\|_{\mathbf{w}}^{2}, \tag{2.86}$$

with w being the statistical weights gained by the experimental statistics. The minimization problem is however ill-conditioned since the optimization results in too much noise due to too many possible solutions (Fessler, 2000).

The addition of a regularizer $\mathrm{R}(\mathbf{f})$ penalizes reconstructed data if the corresponding experimental data implies lower physical probability resulting in

$$\mathrm{L} = \left\|\mathrm{A}\mathbf{f} - \mathbf{p}\right\|_{\mathbf{w}}^{2} + \lambda \mathrm{R}(\mathbf{f}), \tag{2.87}$$

with λ as the regularization strength (or Lagrange multiplier). The quadratic regularizer R_Q is

$$\mathrm{R_Q}(\mathbf{f}) = \sum_i \sum_{j \in \mathcal{N}_i} m_{ij}(f_i - f_j)^2, \tag{2.88}$$

which uses a quadratic weight of neighboring pixels $\mathcal{N}_i$ with respect to pixel i and weights m_{ij} depending on the distance of the voxels. In the realization for the algorithm in the cause of the presented work here, one utilizes the Huber regularizer $\mathcal{R}_{\mathrm{Huber}}$ (Grznar et al., 1997), which is a modified version of the quadratic regularizer:

$$\mathrm{R_{Huber}}(\mathbf{f}, \gamma) = \sum_i \sum_{j \in \mathcal{N}_i} m_{ij} \begin{cases} \frac{(f_i - f_j)^2}{2\gamma^2} & \text{for } |f_i - f_j| \leq \gamma \\ \frac{|f_i - f_j| - \gamma/2}{\gamma} & \text{for } |f_i - f_j| > \gamma, \end{cases} \tag{2.89}$$

with the regularization threshold γ. Depending on γ, small difference pixel values are weighted quadratically (for $|f_i - f_j| \leq \gamma$) and more differing pixel values are weighted linearly (for $|f_i - f_j| > \gamma$), which preserves edge discontinuity (Zhang et al., 2013). An alternative penalizing functions is total variation (TV), which is not considered here (Fessler, 2000).

SIR with differential data

For the implementation of differential data in the SIR algorithm, one needs to add an additional derivative operator ∇ (Köhler et al., 2011; Xu et al., 2012; Nilchian et al., 2013; Hahn, 2014; Hahn et al., 2015). As the data model is then different, the choice of the solver has to be adapted. Empirically, the limited-memory Broyden-Fletcher-Goldfarb-Shanno (L-BFGS) algorithm turned out to be quite robust next to

the non-linear conjugate gradient (NLCG) (Nocedal, 1980). The cost function for DPC data is then

$$\mathrm{L} = \left\| \nabla \mathrm{A}\mathbf{f} - \mathbf{p} \right\|_{\mathbf{w}}^{2} + \lambda \mathrm{R}_{\gamma}(\mathbf{f}). \tag{2.90}$$

The major limitations in iterative reconstruction is the determination of the number of iterations, which can be done with an empirical criterion for convergence, and the choice of optimal parameter determination of the regularizer strength λ and the regularization parameter γ of R_{γ}. The SIR algorithm with differential data is also presented in Ch. 6.

CHAPTER 3

Experimental setup

Short summary

This chapter describes the experimental setup starting with the basic components: the X-ray source, the detector, and the X-ray gratings as displayed in Fig. 3.1. As the focus of this thesis lies on methodical development and optimization, the experimental setup changed continuously over the last years. The experimental working principle of grating interferometry is presented starting from the setup design and alignment of the gratings. Equally important is the processing to extract the attenuation, differential phase-contrast, and dark-field signal as well as postprocessing to increase the quality of the acquired images. Subsequently, the work flow and methods necessary for tomography are illustrated. There, the flat-field selection and interpolation, methods determining the center of rotation, and postprocessing algorithms like bilateral filtering are described, as they are key parts in obtaining high tomographic image quality. A characterization of the setup with respect to the source, detector, spectral acceptance, and spatial resolution finishes this chapter. Various topics covered in the following chapter are presented and complemented in the theses of Willner (2011, 2016); Hipp (2013); Marschner (2013); De Marco (2015); Viermetz (2015).

3.1 X-ray source

There are several ways to generate X-rays. Besides the conventional X-ray tube and its advanced modifications like the rotating anode, there are systems like the liquid metal jet source for generation of X-rays suited for laboratory usage, synchrotron sources, and compact light source systems.

3.1.1 Generation of X-rays

The conventional X-ray tube is an electrode, in which electrons emitted from a heat coil – the cathode – are accelerated by an electric field defined by the acceleration voltage U between anode and cathode. When the electrons hit the target material of the anode, electrons are decelerated in the electric field of the atoms emitting X-rays. This continuous part of X-ray generation is called bremsstrahlung. The maximum energy photons can reach is defined by the acceleration voltage and the electric charge e as $E_{\mathrm{max}} = eU$. Depending on the specific electron energy and anode material, electrons can moreover cause an ejection of bound electrons of the atom if the X-ray energy is at least equal to the binding energy. This electron vacancy is filled by electrons from higher shells. The energy difference of the vacant and the higher shell is emitted as characteristic radiation. The X-ray spectrum from this setup is shown later in this chapter in Fig. 3.10.

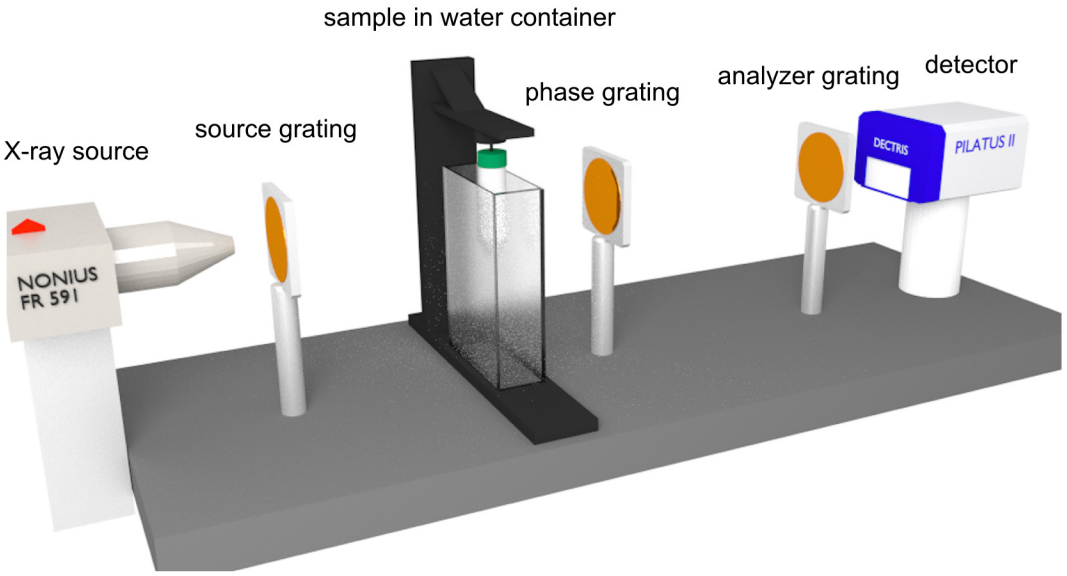

Fig. 3.1 | Schematic laboratory GBPC-CT set-up. The setup consists of the X-ray source, three X-ray gratings, namely the source grating, the phase grating, and the analyzer grating, followed by the Pilatus II detector. The sample, which is immersed in a water container, is put directly in front of the phase grating.

At the liquid metal jet source system (Excillum, Kista, Sweden), electrons hit a liquid metal alloy based on indium and gallium. The achieved focal spot size is quite small and in the range of microfocus X-ray tubes, but with relatively more flux (Thüring et al., 2013). However, the spectrum is largely dominated by the gallium line at 9.2 keV, which is detrimental for imaging thicker objects due to high absorption.

Highly brilliant X-rays are produced specifically at synchrotron facilities. Brilliance describes the photon flux, the beam divergence, and the energy bandwidth. Initially, synchrotron radiation was considered as a parasitic effect when charged particles lost energy due to a deviation of their trajectory caused by bending magnets. In newer synchrotron generations, dedicated periodic arrays of magnets – depending on the type so-called undulators or wigglers – lead to a periodic deviation of the electron trajectory and generate highly brilliant synchrotron radiation.

A novel method to produce X-rays is the compact light source based on the inverse Compton effect. A highly focused laser beam is positioned to collide with electrons in a storage ring. The electrons lose part of their energy to the laser beam increasing its energy into the X-ray regime (Eggl et al., 2016).

3.1.2 Enraf Nonius FR-591 rotating anode

The X-ray source used in this work is an Enraf Nonius FR-591 rotating anode. The maximum voltage in the current available state of the system is 60 kV and the maximum current is 80 mA resulting in a maximum power of 4.8 kW. The target is a molybdenum rotating anode cylinder. For this setup, the established operating parameters are 40 kV and 70 mA due to source stability and mean energy of the spectrum for the setup design. At this energy range, the rotating anode with the molybdenum

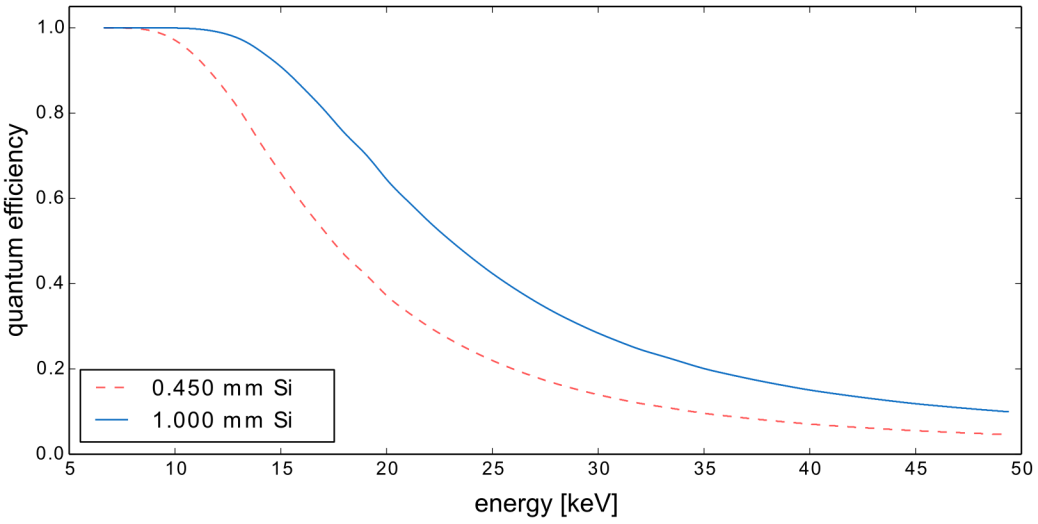

Fig. 3.2 | Simulated quantum efficiency for the Pilatus sensor in dependence of its thickness. The current version of the Pilatus detector has a sensor thickness of 1 mm silicon, the previous version had 450 µm silicon, which provides – as can be observed – only low photon detection above 20 keV.

spectrum provides reasonably high flux (cf. Sec. 3.6.2). The size of the filament is $0.3 \times 3\,\mathrm{mm}^2$ disrespecting an inclination to the anode. In contrast to other laboratory X-ray sources like microfocus sources, rotating anode systems provide stable high flux at the cost of enlarged source sizes. The nominal power per focal spot area for current use is 3.1 $\mathrm{kW/mm}^2$.

3.2 X-ray detectors

There are two major types of digital X-ray imaging detectors, namely integrating and direct counting detectors. Modern integrating detectors use a scintillator screen to transform X-rays into visible light and detect the light with a photo diode combined with a transistor (e.g. CMOS or TFT) or a CCD chip. Integrating detectors are known for their linear signal over a moderate dynamic range and high spatial resolution, but this detector type suffers from readout and dark noise. Direct counting detectors (single-photon counting detectors) – which are able to resolve individual photons in contrast to the integrating detectors – offer a great dynamic range, are energy sensitive, and have in comparison to the indirect counting detectors a box-like point spread function (PSF) as long as charge-sharing does not occur, but the available spatial resolution is limited and the efficiency is in comparison relatively low (Paganin, 2006).

3.2.1 Pilatus II 100K detector

The main detector used in this work is a Dectris Pilatus II 100K (Dectris AG, Baden, Switzerland) single-photon counting detector with a 1 mm thick silicon sensor and 487×195 pixels. The pixel pitch is $172 \times 172\,\mu\mathrm{m}^2$. The active area is $83.8 \times 33.5\,\mathrm{mm}^2$

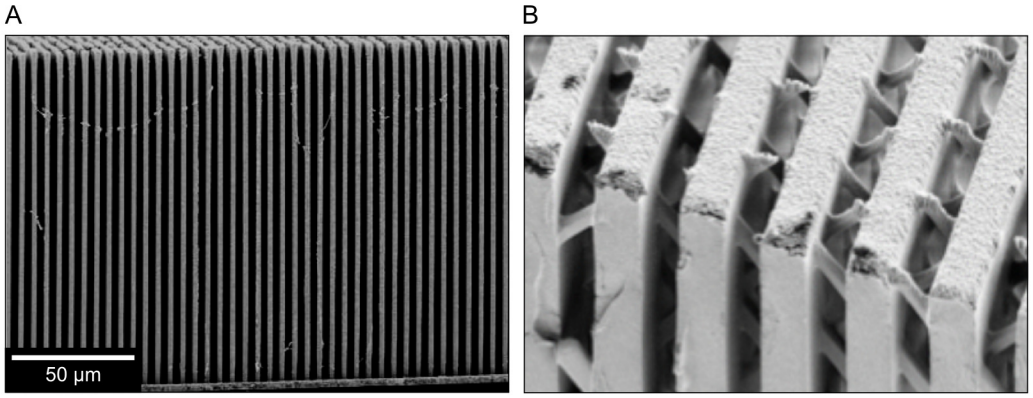

Fig. 3.3 | Scanning electron microscope images of two gratings. Subfigure (A) shows a cross section of a silicon grating. Subfigure (B) displays the gold structure of the sunray design. Images kindly provided by the Institute of Microstructure, Karlsruhe Institute of Technology.

large. The detector chip is a reverse-biased silicon diode array offering 20 bit dynamic range with the ability to count up to 10^6 photons. The readout time is 2.3 ms (Dectris, 2014). The detector comes with one adjustable energy threshold, which can be set between 4 and 18 keV (Broennimann et al., 2006). Here, the threshold is set to 12 keV.

One major limitation of the Pilatus II 100K is the poor quantum efficiency at higher energies (cf. Fig. 3.2). At 30 keV only 35 % of the photons are detected in the 1 mm silicon sensor. In a prior version of the detector, the sensor was only 450 µm thick. Different sensor materials like e.g. cadmium telluride (CdTe) or gallium arsenide (GaAs) would drastically increase the efficiency of the detector for higher energies.

3.3 Gratings

The X-ray gratings are the essential elements forming the X-ray interferometer. The source grating, which is an absorption grating, has to attenuate enough X-rays in the lines to act as a sufficiently coherent source. The phase grating induces a periodic modulation of the wave front caused by a periodical grating structures. There are variations of the interferometer, where the phase grating is replaced by an absorption grating. The analyzer grating is also an absorption grating necessary to resolve the interference pattern on the detector. A scanning electron microscope (SEM) cross section of a silicon grating can be found in Fig. 3.3 (A).

The periods of the gratings have to be in the range of microns to allow reasonable experimental Talbot distances (cf. Eq. 2.45). In combination with high attenuation, the fabrication of especially absorption gratings differs from standard semiconductor lithography due to the deep structures rendering the fabrication technically challenging. It is especially difficult to fabricate large field of views and to provide adapted grating curvature to avoid shadowing necessary for sufficient performance of laboratory interferometers. Tab. 3.1 lists the gratings used in the range of this work.

Tab. 3.1 | Grating table. Gratings no. 1-3 are used in the current configuration. No. 1 is the source grating, no. 2 the phase grating, and no. 3 the analyzer grating. Grating no. 4 was used as previous source grating, grating no. 5 as previous phase grating. Kapton is a type of polyimide, which provides high X-ray transmittance.

no.	type	period [µm	duty cycle	phase shift (design energy)	filling height material	substrate thickness material	size	design
1	absorption	5.4	0.6	N/A	60-70 µm Au	1 mm Kapton	50 x 50 µm^2	sunray
2	phase	5.4	0.55	π (27 keV)	5.2 µm Au	200 µm silicon	50 x 50 µm^2	laser written
3	absorption	5.4	0.65	N/A	60-70 µm Au	500 µm silicon	70 mm diameter	bridge
4	absorption	5.4	0.6	N/A	approx. 70 µm Au	200 µm silicon	50 x 50 µm^2	sunray
5	phase	5.4	0.5	π (27 keV)	8.5 µm Ni	500 µm silicon	50 x 50 µm^2	laser written

3.3.1 Grating fabrication

X-ray grating fabrication is one of the bottlenecks in the process for grating interferometry due to the need of deep absorbing structures. As phase gratings do not require highly absorbing structures, the fabrication requirements are more relaxed. Laser written phase gratings can be fabricated providing large grating areas. However, as this process is not applicable to get high performance absorption gratings, the LIGA (lithography and galvanization) process is employed to get high absorbing structures. The gratings used in this work are fabricated by the Institute of Microstructure (IMT) at the Karlsruhe Institute of Technology (KIT, Karlsruhe, Germany) and by Microworks GmbH (Karlsruhe, Germany).

Phase grating filling height calculation

Besides the calculated period and the choice of duty cycle, the filling height of the structure in the phase grating has to be determined. The setup is designed for a specific design energy matching the spectrum mean energy, phase shift (or setup type), the grating periods, and grating distances. The design energy for the specific phase shift determines the filling height Δh, which be calculated with Eq. (2.47):

$$\Delta\Phi = k \int \delta \mathrm{d}z \tag{3.1}$$

$$= \delta \frac{E}{\hbar c} \Delta h, \tag{3.2}$$

with $\Delta\Phi$ being the phase shift of the phase grating for the design energy E. Depending on the material used for the phase grating structures, the filling height is calculated as

$$\Delta h = \frac{\Delta\Phi}{\delta k} \tag{3.3}$$

$$= \frac{\Delta\Phi k}{2\pi r_0 \rho_\mathrm{e}} \tag{3.4}$$

$$= \frac{\Delta\Phi E}{2\pi\hbar c r_0 \rho_\mathrm{e}}. \tag{3.5}$$

The only quantity necessary is the electron density ρ_e of the filling material besides the design energy and the phase shift. In this work, the design energy was $E = 27\,\mathrm{keV}$

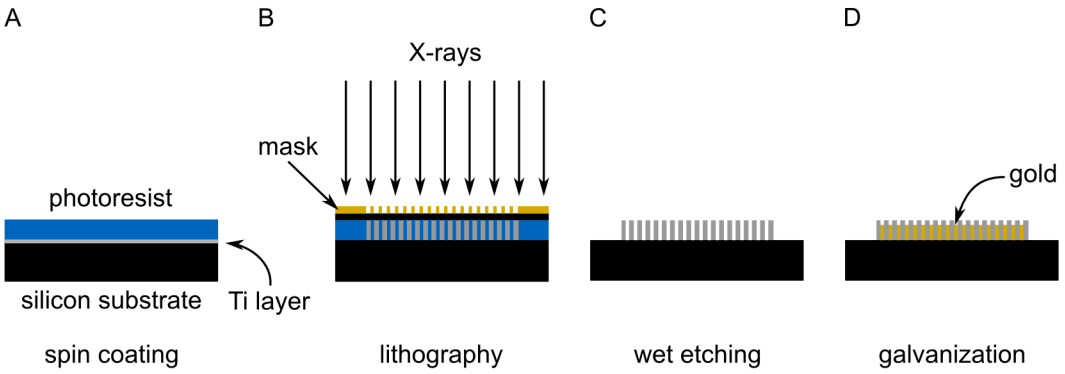

Fig. 3.4 | Illustration of the LIGA process. A silicon wafer is spin-coated with a photoresist (A). Here it is SU-8. A titanium layer for adhesion of the resist is added to the wafer. A mask with the grating structure, which is fabricated with an electron beam writer, is positioned directly on the coated grating and illuminated with X-rays (B). If the sunray design is used the grating is tilted with respect to the X-ray beam for diagonal connecting structures. The photoresist – here being a negative photoresist – is removed by wet etching (C). The remaining structure, which is in the presented case the negative image of the mask, is galvanized and electroplated with gold as a filling material (D).

and the phase shift was $\Delta\Phi = \pi$. The filling materials were either gold or nickel (Au: $467\,\mathrm{e/nm^3}$ and Ni: $256\,\mathrm{e/nm^3}$), as can be seen in Tab. 3.1.

LIGA process

The LIGA process (lithography and galvanization) can be roughly divided into four parts (cf. Fig. 3.4). First, the substrate is coated with a resist (here SU-8) and a titanium layer is sputtered on the silicon wafer necessary for the adhesion of the resist (cf. Fig. 3.4 A). For the lithographic process, the grating structure is provided by a mask, which is generated with an electron beam writer. As deep structures are needed, low energy synchrotron radiation for high penetration depth is used to provide a parallel and intense beam with an energy in the range of 5-10 keV (cf. Fig. 3.4 B). Higher energy would lead to a broadening of the illuminated structure due to scattering. After the irradiation changes the chemical structure only of the illuminated photoresist, the unaltered photoresist is removed by wet etching (cf. Fig. 3.4 C). Eventually, the gold structures are galvanized into the removed structures, as depicted in Fig. 3.4 (D) (Becker et al., 1986; Reznikova et al., 2008).

However, the resulting gold structures with high aspect ratios are deformed by capillary forces. To prevent this deformation, either bridges between the lamellae are included in the design of the grating mask or the so-called sunray design is used. In further detail concerning the sunray design, after the first frontal exposure of the grating, the process is repeated under an inclined exposure direction adding diagonal ray structures. The sunray design improves the grating quality and thus the mean visibility in comparison to the bridge design as the active area of the grating is larger (Kenntner, 2012). A scanning electron microscope cross section of the sunray design is displayed in Fig. 3.3 (B).

3.3.2 Low-absorbing substrates

The additional absorption of the gratings is especially detrimental for imaging at low energies. Silicon, which is the established substrate in lithography, causes substantial attenuation at lower energies (< 30 keV). Although the substrate thickness per grating has been successfully reduced from 500 to 200 µm, further reduction is challenging because of the increased risk of breaking. Therefore, different substrate materials have been investigated. Carbon and Kapton (polyimide) turned out to be favorable substitutes for grating substrates via reducing the additional absorption by the grating substrate. However, as carbon induces scattering, it cannot be used as a phase grating substrate (Koch et al., 2015).

Increasing the field of view

The current size of the active grating area of absorption gratings, which can be fabricated in one process, is limited to 70 mm in diameter. For imaging larger samples, the grating size has to be increased. One idea is stitching smaller tiled gratings with the size of $50 \times 50\,\mathrm{mm}^2$ (Meiser et al., 2016). With sophisticated alignment and reduction of the gaps between the tiles, gratings with the size of $200 \times 200\,\mathrm{mm}^2$ have been achieved. The visibility of each of the tiles turned out to be on a comparable level (Schröter et al., 2017).

Moreover, the cone beam geometry of laboratory setups reduces the flux due to shadowing of the X-ray beam. In detail, if the grating structures are not adapted to the beam shape, the grating lamellae cause position-dependent attenuation and can even be fully absorbed. With mechanical bending according to the radial distance from the source, this effect can be avoided. However, the grating substrate has to be sufficiently flexible for bending, especially for short distances to the source. In this aspect, carbon and Kapton are more favorable than silicon.

3.4 Imaging with a Talbot-Lau interferometer

The design of a Talbot-Lau interferometer depends basically on the sample specifications and the available grating parameters like the period and aspect ratio limited by grating fabrication. First crucial points in setup design are the spectrum and the design energy for the setup depending on the estimated sample attenuation. A spectrum as shown in Fig. 3.10 leads to a mean energy of 27 keV, which is sufficient for biomedical samples with diameter up to several centimeters. Additionally, one has to include beam hardening of the sample and the gratings next to the water container for phase-wrapping reduction.

Another very important point is the choice of the setup geometry. A setup can have equidistant inter-grating distances (symmetric) or asymmetric inter-grating distances. A more compact setup can be realized with an asymmetric setup in comparison to a symmetric setup for the same design energy. Moreover, one has to decide on the type of the phase grating, which defines the Talbot distances and periods of the source and analyzer grating. As the key property of the described setup is high sensitivity and the setup length does not underlie any restrictions, a symmetric design with a phase shift

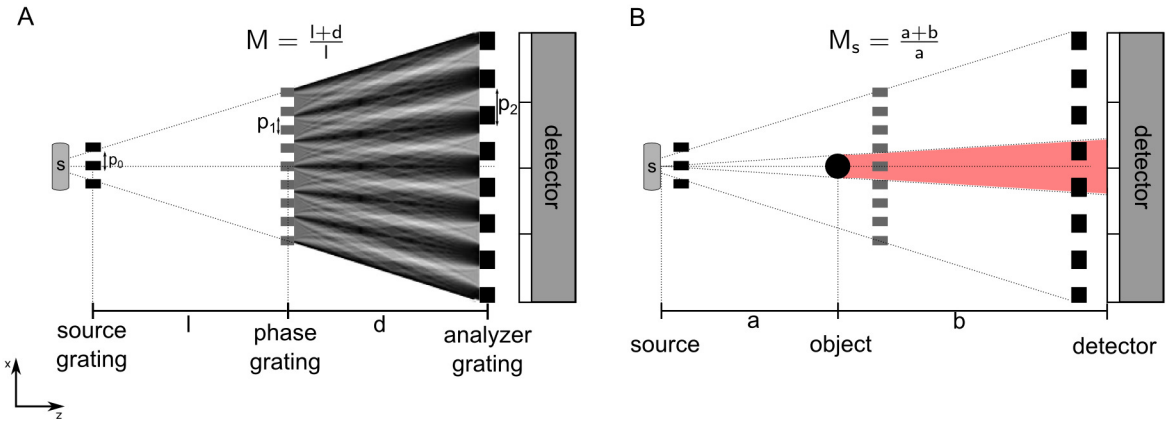

Fig. 3.5 | Talbot carpet and sample magnification. The period of the interference pattern p_2 and the Talbot distance d_T are magnified (A). The sample is magnified depending on its position a leading to the effective pixel size p_eff (B). The figures are not to scale. Figure partly adapted from Bech (2009).

Tab. 3.2 | Geometric parameters of the setup in the latest configuration.

distance	variable	
source to source grating	s	567 mm
source grating to phase grating	l	857 mm
phase grating to analyzer grating	d	857 mm
analyzer grating to detector	f	279 mm
source to sample	a	1309 mm
sample to detector	b	1251 mm

of π is chosen. The angular sensitivity is described in detail in the following chapter (cf. Ch. 4).

Magnification

With cone beam geometry, one has to include also the geometric magnification, which influences the resulting inter-grating distances and the periods of the analyzer and source grating. Also, the periods of the gratings are magnified.

At the setup at hand, the period is $p_1 = 5.4\,\mu\mathrm{m}$, which is limited by grating fabrication and availability. The Talbot distances d_T are defined according to Eqs. (2.45) and (2.46) for parallel beam with a design energy of 27 keV. Due to the magnification M as illustrated in Fig. 3.5 (A), the Talbot distance is magnified to

$$d'_\mathrm{T} = M d_\mathrm{T} = \frac{l + d'_\mathrm{T}}{l} d_\mathrm{T}, \tag{3.6}$$

which can be rearranged to

$$d'_\mathrm{T} = \frac{d_\mathrm{T} l}{l - d_\mathrm{T}}, \tag{3.7}$$

with d'_T being the new Talbot distance. The period of the phase-grating p_1 defines the period of the interference pattern p_2. Additionally, the geometric magnification leads

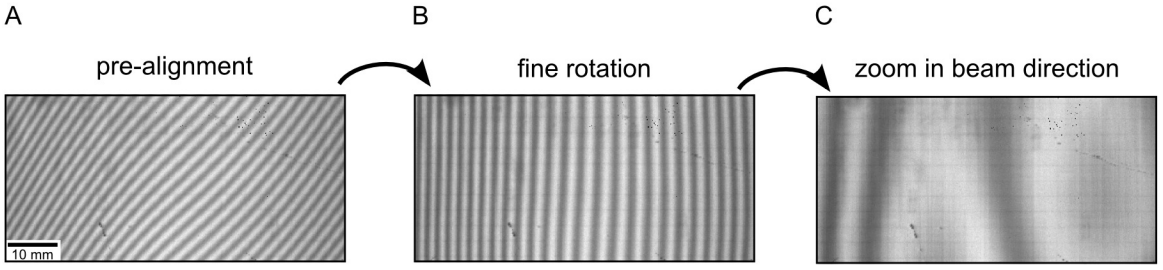

Fig. 3.6 | Grating alignment procedure. The pre-aligned image should look similar to this detector moiré image (A). The direction of the fringes is not parallel to the orientation of the gratings. Therefore, the gratings have to be fine-tuned by rotating one or several gratings around the optical axis (B). Changing the position of the gratings in beam direction increases the size of the moiré fringes (C).

to an increase of the period of the interference pattern

$$p_2' = Mp_2 = \frac{l + d_{\mathrm{T}}'}{l} p_2. \tag{3.8}$$

The specific symmetry of the setup presented in this thesis is symmetrical. Thus, the inter-grating distances and Talbot distances are chosen to $l = d_{\mathrm{T}}'$ leading to $d_{\mathrm{T}}' = 2d_{\mathrm{T}}$ and a magnification of $M = 2$. As the period of the analyzer grating is $p_2 = p_1/2$ for a π-phase grating (cf. Fig. 2.4), the resulting period is

$$p_2' = Mp_1/2 = p_1. \tag{3.9}$$

According to Eq. (2.66) the resulting period of the source grating is then

$$p_0' = \frac{l}{d_{\mathrm{T}}'} p_2' = p_1. \tag{3.10}$$

Therefore, all periods are determined to $p_0', p_1', p_2' = 5.4\,\mu\mathrm{m}$. This corresponds to a Talbot distance of 95 cm for the 3rd Talbot distance. Due to spectral optimization to maximize the mean visibility, the Talbot distance d_{T}' is chosen to equal 85.7 cm. In the following, the chosen Talbot distance d_{T}' will be denoted as d and the periods as p_0, p_1, and p_2 for simplification. The current setup positions are summarized in Tab. 3.2.

Grating alignment

After all three gratings are placed at their respective positions, the gratings have to be aligned. First, due to a heterogeneous beam shape originating in the Heel effect (Buzug, 2008) and to avoid shadowing due to non radial orientation of the gratings, each grating has to be rotated around the vertical axis to reduce shadowing (cf. Sec. 3.3.1). The peak of intensity should be in the center of the detector. Pre-alignment of the grating rotation around the optical axis (y-axis) is helpful to reduce alignment time. A resulting interference image is shown by way of example in Fig. 3.6 (A), in which the interference of the three gratings forms a moiré image. Motorized fine tuning of the grating rotation around the optical axis is performed until

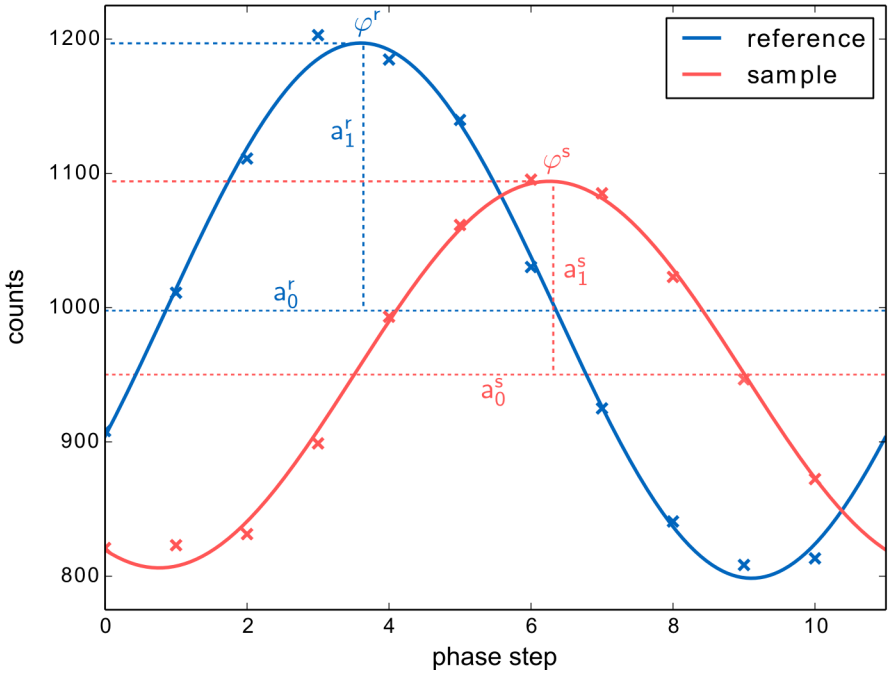

Fig. 3.7 | Simulated phase-stepping curve. This simulated phase-stepping curve shows 11 phase-steps for both sample and reference scan. The parameters for the sinusoidal fit a_0, a_1, and φ_1 are processed with Fast Fourier Transform (FFT) processing.

the moiré fringes are lines parallel to the orientation of the grating lines (cf. Fig. 3.6 B). Aligning the position of the gratings in beam direction leads to the final experimental image (cf. Fig. 3.6 C). Due to cone beam geometry, non-perfect gratings, and limited precision of the alignment, remaining moiré fringes are visible.

With respect to later tomographic applications, the orientation of the grating lines is advised to be parallel to the tomographic axis. The implementation of tilted gratings is described in Ch. 6.

3.4.1 Phase-stepping and processing

The primary idea of grating interferometry is to retrieve the differential phase-contrast and the dark-field signal of an object. Refraction and thus phase shift of the object cause a change of the interference pattern measured as a change of the intensity of the respective pixel $I(x, y)$. However, this shift of the interference pattern is usually much smaller than the detector pixel size, which renders resolving changes in the interference pattern impossible. Moreover, the additional attenuation of the object also changes the intensity of the pixel.

To extract the contribution of the phase shift, a lateral scanning of the interference pattern is performed (Weitkamp et al., 2005). This process is called phase-stepping. Phase-stepping moreover allows to retrieve the sample scattering described by the dark-field image next to the conventional attenuation image (Weitkamp et al., 2005; Pfeiffer et al., 2008). Alternative techniques are single-shot (Bevins et al., 2011; Wu et al., 2013), two-shot (Marschner et al., 2016a, 2017), fringe-scanning (Kottler et al., 2007b), or the direct integration of the phase-stepping in the tomographic reconstruc-

tion, known as intensity-based statistical iterative reconstruction (IB-SIR) (Brendel et al., 2015; Teuffenbach et al., 2017).

The phase-stepping approach was used due to its stability, which is necessary for high sensitivity. A nanoconverter converts movement of a linear motor into lateral movement of the respective gratings with a ratio of 1/100. As already stated in Eq. (2.58), the measured intensity per pixel I is approximated to

$$I(x_\mathrm{g}) \approx a_0 + a_1 \sin(\frac{2\pi}{p} x_\mathrm{g} + \varphi), \tag{3.11}$$

with x_g being the position of the phase-stepper. Due to an extended source the binary gratings produce a sinusoidal intensity shape instead of a triangular shape (Bech, 2009). Fig. 3.7 shows a simulated phase-stepping curve for both sample and reference scan for one pixel. Fig. 3.8 illustrates an exemplary experimental set of reference and sample stepping raw images, the processed individual images, and the final contrast images attenuation (ATC), differential phase shift (DPC), and dark-field scattering (DFC) of the GBPC-CT setup presented in this work.

The number of phase-steps has to be at least three to extract the three contrast signals ATC, DPC, and DFC. In this work, usually 11 phase-steps were used for one grating period, which is an empirical choice leading to sufficiently high resolution of the interference pattern.

FFT processing

There are several processing methods to extract the three image signals. The easiest and fastest way to extract the three contrast signals is Fourier processing, which performs a Fast Fourier Transform (FFT) algorithm of the intensity curve $I(x_\mathrm{g})$ with M phase-steps leading to the complex Fourier frequencies c_j:

$$c_j = \frac{1}{M} \sum_{k=0}^{M-1} I_k \, \mathrm{e}^{2\pi i \cdot j \frac{k}{M}}, \tag{3.12}$$

with the step position $k = x_g/p$ ranging from $0...M-1$ (Chabior, 2011). As discussed earlier, the phase-stepping produces a sinusoidal intensity profile. In terms of a Fourier transform along the different phase steps, the information is encoded in the first frequency component c_1, as this corresponds exactly to a frequency of one cycle per period. The zeroth frequency coefficient c_0 is the offset of the first Fourier coefficient. In theory for Talbot-Lau setups, all other Fourier frequencies should be zero and are therefore neglected in the processing. The image contrast signals are calculated as:

$$a_0 = |c_0|, \tag{3.13}$$

$$\varphi = \arg c_1, \tag{3.14}$$

$$a_1 = 2|c_1|. \tag{3.15}$$

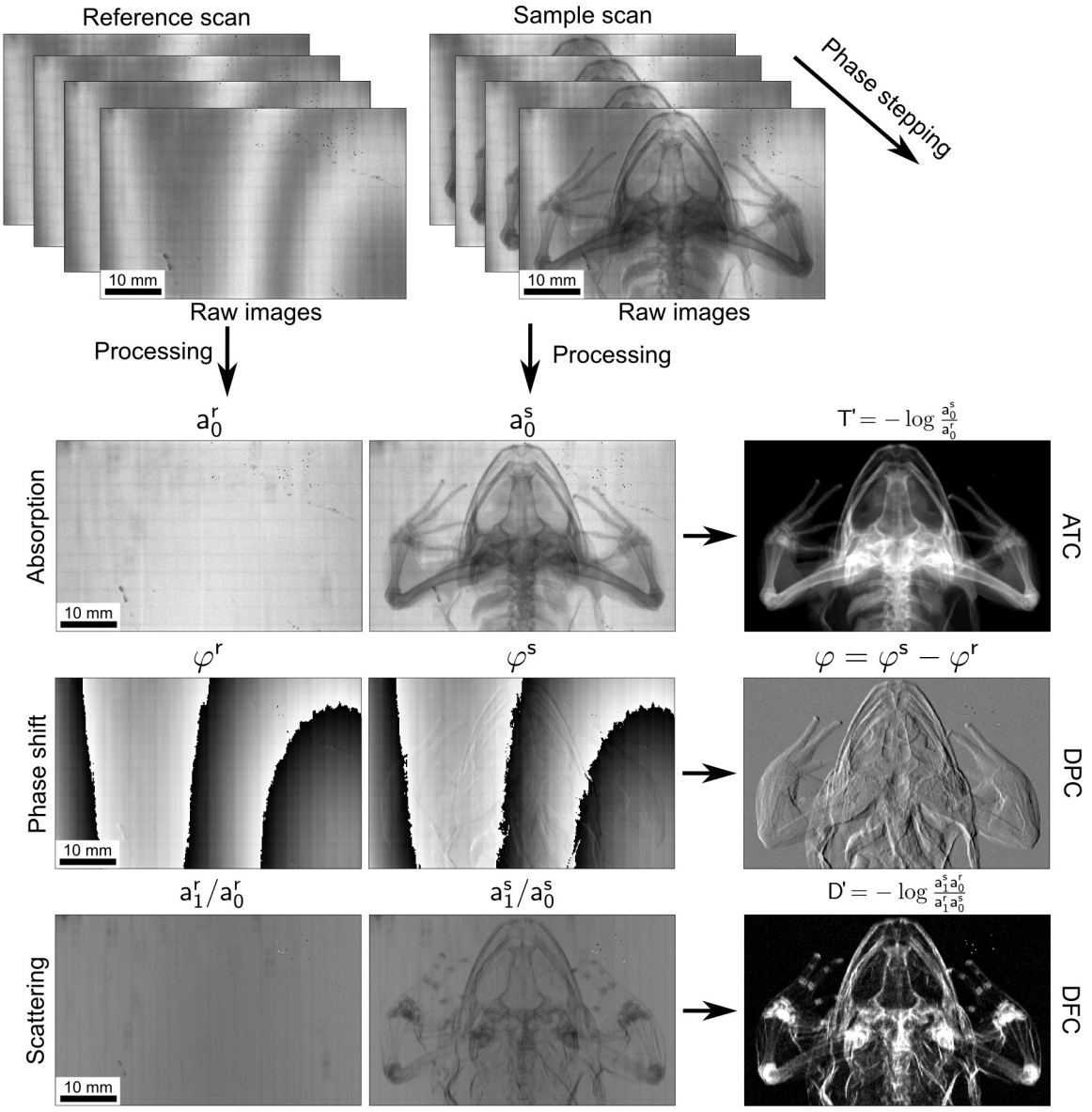

Fig. 3.8 | Experimental phase-stepping and contrast images. Experimental raw stepping images with and without the object are shown on the top. For each of the two stepping series with and without the sample in the beam, the three respective image contrast signals a_0, φ, and a_1/a_0 are retrieved. The processed scattering images are equivalent to the visibility. The resulting image signals ATC, DPC, and DFC are visualized on the right.

Moreover, the visibility being the ratio of the amplitude and the mean value can be calculated as

$$V = \frac{2|c_1|}{|c_0|}, \tag{3.16}$$

as introduced in Eq. (2.61). Thereby, the additional factor 2 in the nominator originates from the complex Fourier transform.

Weighted least-squares processing

A different processing method is weighted least-squares processing, as presented in Hahn (2014). The cost function L, which has to be minimized to retrieve the fit parameters $\mathbf{p}$, equals

$$\mathrm{L} = ||\mathbf{I} - \mathbf{f}(\mathbf{x}_\mathrm{g}; \mathbf{p})||_w^2 \tag{3.17}$$

$$= \sum_{k=0}^{M-1} w_k \left(I_k - f_k((\mathbf{x}_\mathrm{g}; \mathbf{p})\right)^2, \tag{3.18}$$

with $\mathbf{I}$ being the intensity and M the number of phase-steps (De Marco, 2015). The calculation of the weights w is based on Poisson statistics. The sinusoidal model function of the measured intensity is

$$\mathbf{f}(x_\mathrm{g}) = A_0 + A_1 \cos x_\mathrm{g} + B_1 \sin x_\mathrm{g}, \tag{3.19}$$

with x_g being the grating position and A_0, A_1, and B_1 being the fit parameters $\mathbf{p}$ to be determined. The already known image signals can be calculated as

$$a_0 = A_0, \tag{3.20}$$

$$\varphi = \arctan\left(\frac{B_1}{A_1}\right), \tag{3.21}$$

$$a_1 = \sqrt{A_1^2 + B_1^2}. \tag{3.22}$$

As the sinusoidal model in Eq. (3.19) is not linear, this model has to be linearized using trigonometric assumptions (Hahn, 2014). Fitting this linearized model provides additional variances for the parameters A_0, A_1, and B_1, which are obtained by Gaussian error propagation (Hahn, 2014). Those statistical variances σ_T, σ_φ, and σ_D are necessary input weights in statistical iterative reconstruction (SIR) presented in Sec. 2.4.2.

Expectation-maximization processing

The most advanced method used in the range of this work is an expectation-maximization (EM) algorithm. In detail, a cost function is minimized by variation of the model function parameters $\mathbf{p}$ of a statistical model function $f(\mathbf{p})$ to fit to the experimental data $\mathbf{I}$ (De Marco, 2015). In contrast to the weighted least-squares method, the EM-algorithm is additionally able to correct random or systematic changes in the stepping positions. Even missing or unknown steps due to mechanical failure or beam drops can be handled reducing remaining fringes and thus artifacts in the DPC and DFC signal (Marschner et al., 2016b).

Resulting image signals

The resulting three image signals in grating interferometry including reference correction are eventually calculated as

$$T' = -\log \frac{|a_0^{\mathrm{s}}|}{|a_0^{\mathrm{r}}|}, \tag{3.23}$$

$$\varphi = \arg a_1^{\mathrm{s}} - \arg a_1^{\mathrm{r}}, \tag{3.24}$$

$$D' = -\log \frac{|a_1^{\mathrm{s}}|/|a_0^{\mathrm{s}}|}{|a_1^{\mathrm{r}}|/|a_0^{\mathrm{r}}|} = -\log \frac{|a_1^{\mathrm{s}}||a_0^{\mathrm{r}}|}{|a_1^{\mathrm{r}}||a_0^{\mathrm{s}}|}, \tag{3.25}$$

which are visualized in Fig. 3.8. The superscript 's' denotes the sample scan and superscript 'r' the reference scan. In contrast to Eqs. (2.59) and (2.62), the negative logarithm of the transmission signal T and the inverted logarithm of the dark-field signal D is taken.

3.4.2 Ramp and offset correction

Besides the advanced processing methods that are capable of reducing artifacts like beam drops and residual fringes, the differential phase signal often suffers from gradients and offsets. Two approaches are primarily used within the range of this work to improve the DPC image quality.

Three-point-plane and constant offset subtraction

The first approach is the adaptive differential phase recovery method (ADPR), in which a mean gradient of the whole DPC projection $\nabla\varphi(x, y)$, is calculated and then subtracted from the DPC projection

$$\varphi_{\mathrm{corr}}(x, y) = \varphi(x, y) - \arg[\mathrm{e}^{i\nabla\varphi(x,y)}], \tag{3.26}$$

with φ_{corr} being the resulting DPC signal (Tapfer et al., 2012). However, the gradient over the whole DPC projection with a sample in the beam causes an error as the sample is included in the calculation.

A modification of this method is the three point-plane approach, in which three sample free areas at the boarders of the DPC projection are chosen to determine a linear plane in the DPC signal

$$\Delta\varphi(x, y) = a + bx + cy. \tag{3.27}$$

This plane is subtracted from the original DPC signal like in the previous case. The downside of this approach is the need of the sample free areas (Marschner, 2013; De Marco, 2015).

After subtraction of the three-point-plane gradient, an additional mean linear offset has to be subtracted as the gradient does not remove completely the DPC offset. The idea is to enforce $\int \varphi(x', y)\mathrm{d}x' = 0$ meaning that the total phase gradient should equal

zero. This results in

$$\varphi'_{\mathrm{corr}}(x,y) = \varphi_{\mathrm{corr}}(x,y) - \frac{1}{\Delta x}\left\langle \int \varphi_{\mathrm{corr}}(x',y)\mathrm{d}x' \right\rangle_{(x,y)}, \tag{3.28}$$

including averaging in x- and y-direction. The corrections are performed on both reference and sample scan (De Marco, 2015).

Least-squares fit

It is also possible to employ a least-squares fit of the type

$$\mathrm{L} = ||\varphi(x,y) - \Delta\varphi(x,y)||^2. \tag{3.29}$$

The gradient of the DPC signal is thereby defined as

$$\Delta\varphi(x,y) = \sum_{k=0}^{D}\sum_{l=0}^{D} a_{kl}x^k y^l, \tag{3.30}$$

with D being the degree of the polynomial, which was empirically chosen to be 2 (De Marco, 2015; Velroyen, 2015). However, this approach still is not able to handle constant offsets if phase-wrapping occurs. An advanced adaption of this approach including histogram analysis, which shifts the center of the DPC signal to 0, is presented in De Marco (2015).

3.5 Phase-contrast computed tomography

In order to perform phase-contrast computed tomography with a grating interferometer, N projections at different angles are measured. This means that for each tomographic angle, a stepping curve is acquired via taking M phase-steps at each angular position. Additionally, multiple reference scans – so-called flat-fields – without the sample in the beam are taken.

3.5.1 Work flow and optimization

In this work, usually full 360 degree scans were performed due to the cone beam geometry and the need for opposing projections in the tilted approach described later in this work. Furthermore, measurements with the full 360 degrees are beneficial for the determination of the center of rotation.

The number projections N is dependent on the reconstruction method. For FBP, the Nyquist sampling criterion has to be fulfilled (cf. Sec. 2.4.1). In our case with a number of 487 pixels, at least 801 projections were chosen. To improve the quality of the scan with better statistics sometimes even 1201 projections were used.

Before the scan, the rotation axis is aligned in such way that the sample is centered and does not rotate out of the field of view. Moreover, there has to be an area large enough to perform a DPC offset and ramp correction. In order to correct for ring artifacts originating in bad pixels or defect grating areas, a random typewriter

shift of the sample is applied smearing out the artifacts. A two-dimensional random typewriter, which is a movement of the sample in multiple integers of the effective pixel size for each projection angle, turned out to be most promising (Viermetz, 2015). This shift has to be corrected after the processing of the projections for each contrast signal.

The stepping is performed with the nanoconverter over one period of the source grating. In tomographic mode, the phase-stepping is performed in zigzag mode to reduce the motion time.

Flat-fields

For handling non-linear drift of the interference pattern, several flat-field images were taken for high image quality of the DPC and DFC signals. Depending on the number of phase-steps and the exposure time, the sample is moved out of the beam for reference images every 10 to 20 projections. In most of the experiments in this work the period was each 15 angular projections. For each angular projection with the sample in the beam, two neighboring flat-fields are interpolated and weighted corresponding to the temporal relative position of the projection (Viermetz, 2015).

Increasing the exposure time in the flat-field allows to increase the quality of the final projections by reducing the total noise in the DPC image σ_{tot}, as the higher exposure of the flat-field by a factor f leads to

$$\sigma_{\text{tot}} = \sqrt{\sigma_{\text{flat}}^2 + \sigma_{\text{sample}}^2} \tag{3.31}$$

$$= \sqrt{\left(\frac{\sqrt{2}}{V\sqrt{fN}}\right)^2 + \left(\frac{\sqrt{2}}{V\sqrt{N}}\right)^2} \tag{3.32}$$

$$= \sqrt{\frac{1}{f}\left(\frac{\sqrt{2}}{V\sqrt{N}}\right)^2 + \left(\frac{\sqrt{2}}{V\sqrt{N}}\right)^2} \tag{3.33}$$

$$= \sqrt{\left(\frac{1}{f} + 1\right)\sigma_{\text{sample}}^2} \tag{3.34}$$

$$= \sqrt{\frac{1+f}{f}}\sigma_{\text{sample}}, \tag{3.35}$$

with the noise in a DPC image depending on the number of counts N and the visibility V formulated as

$$\sigma = \frac{\sqrt{2}}{V\sqrt{N}}, \tag{3.36}$$

which is derived in Engel et al. (2011). For $f = 1$ the exposure time is the same and the total noise in the DPC image is equivalent to

$$\sigma_{\text{tot}} = \sqrt{2}\sigma_{\text{sample}} = \frac{2}{V\sqrt{N}}. \tag{3.37}$$

For $f = 3$ as used in experiments in this work, this reduces the noise to $\sqrt{4/3} \approx 1.15$

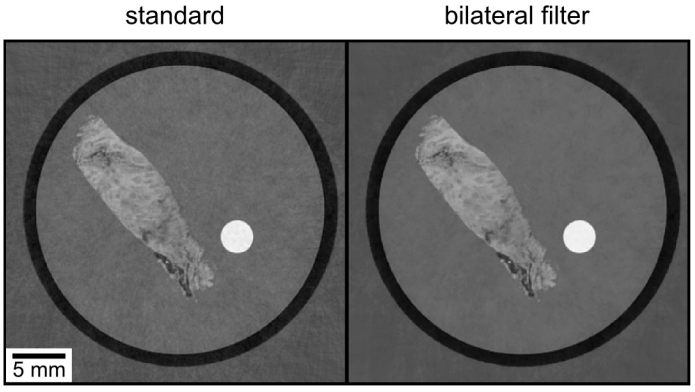

Fig. 3.9 | Bilateral filtering of phase-contrast data. Illustration of the effect of bilateral filtering on the tomographic phase-contrast data of a biomedical sample. The filter induces a noise reduction as can be seen on the right hand side of the figure. The standard deviation and noise of the same are in the PMMA rod (white circle) are 158 ± 4.6 HUp and 158 ± 2.1 HUp. Both data sets were deconvolved as described in Sec. 3.6.4. The phase-contrast values range linearly from -60 to 120 HUp.

compared to $\sqrt{2} \approx 1.41$ signifying a reduction of approximately 20 %.

Center of rotation, tomoconsistency and bilateral filtering

The tomographic center of rotation necessary for reconstruction is determined by comparing two opposing attenuation images. Thereby, the difference between features of projections at e.g. 0 and 180 degrees are compared for each detector line and the center of the difference is determined for each detector line per projection (Donath et al., 2006; Marschner, 2013). A linear fit for all projections leads to the center of rotation. Extending this approach for all detector rows additionally provides the rotation of the tomographic axis.

An advanced method to find the center of rotation is the alignment of the projections by tomographic consistency, which is a method utilizing cross-correlations between the measured projections and the estimated projections acquired from forwardprojecting the initial reconstruction (Guizar-Sicairos et al., 2015).

After tomographic reconstruction, the noise in both attenuation or phase-contrast data can be reduced with the bilateral filtering algorithm based on distance and value weights (Allner et al., 2016). The effect of the bilateral filter is illustrated in Fig. 3.9.

3.6 Specific characterization of the setup

This section presents the specific experimental parameters of the Talbot-Lau interferometer in its final state for grating-based phase-contrast computed tomography. Important parameters are the spectrum, the flux at the detector position, the spectral performance (energy-dependent visibility) of the interferometer, and the spatial resolution of the setup. Explicit noise characteristics are not covered here, but the angular sensitivity related to noise of the setup is in detail discussed in the following chapter (cf. Ch. 4).

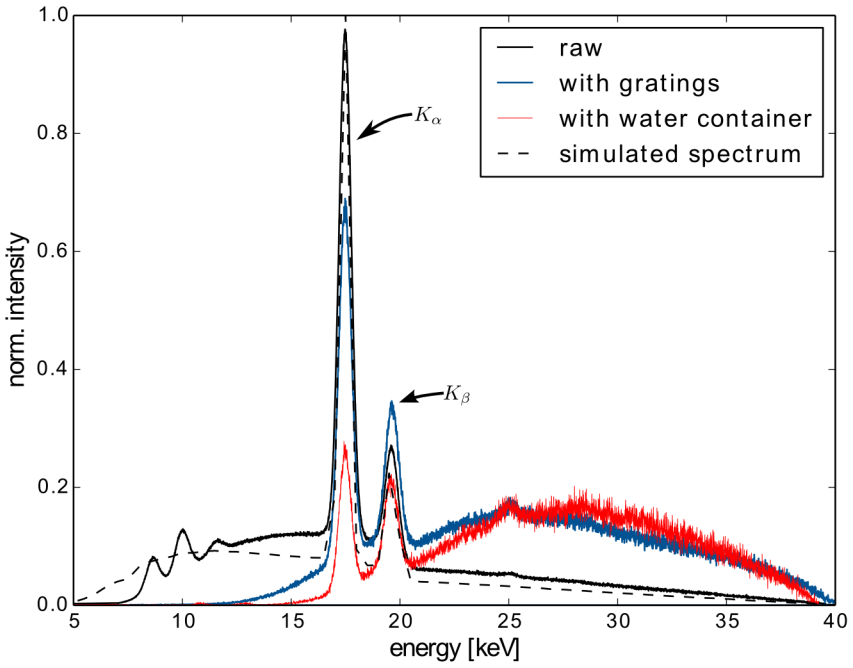

Fig. 3.10 | Spectrum of the FR-591 rotating anode at 40 kVp. The raw spectrum, the spectrum with water container, and the spectrum with the gratings additionally to the water container were measured. The K_α and the K_β lines of molybdenum can be seen at 17.48 and 19.61 keV. The spectrum was determined with an Amptek X-123 XRF detector and corrected for its limited quantum efficiency of the 1 mm thick silicon sensor.

3.6.1 Spectrum

The spectrum of the setup depends mainly on the source acceleration voltage U, which is here 40 kVp, and the anode material molybdenum. Moreover, the spectrum is shaped by all additional components in the beam, namely the three gratings and the water container. The spectrum was measured with an Amptek X-123 XRF detector and is depicted in Fig. 3.10. The spectrum is needed to decide on the design energy of the interferometer.

3.6.2 Flux

The flux of the rotating anode was determined with the Pilatus II 100K detector at its current detector position, which is 2560 mm away from the source, and with the standard operation parameters of the source (40 kVp and 70 mA). Different scenarios are presented: the raw beam, three gratings, and the three gratings with additional 40 mm water.

Since the normalized spectrum $S(E)$ (cf. Fig. 3.10) is known, one can correct the measured flux Φ_{meas} for the reduced quantum efficiency $Q(E) = 1 - \mathrm{e}^{-\mu_{\text{si}}(E)d}$ of the Pilatus detector (cf. Fig. 3.2). The latter was obtained from tabulated attenuation coefficients $\mu_{\text{si}}(E)$ for the silicon sensor of thickness $d = 1$ mm (Nowotny, 1998; Boone

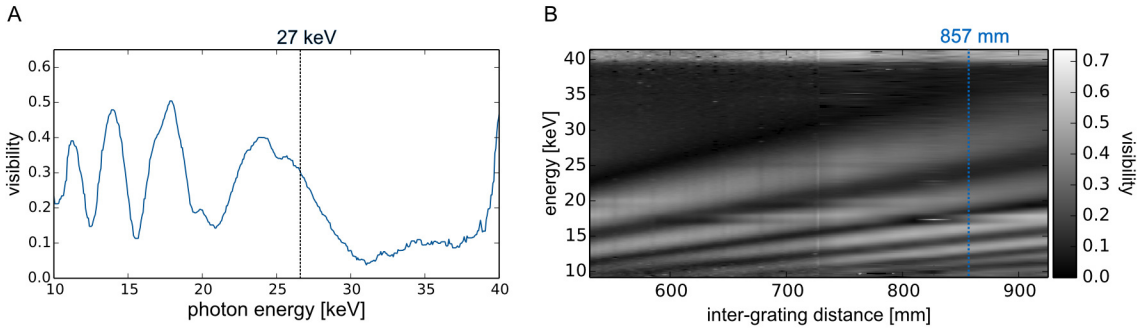

Fig. 3.11 | Energy-dependent visibility. The spectrum was measured at the Talbot distance of the setup $d_{\mathrm{T}} = 85.7\,\mathrm{cm}$ shown in subfigure (A). The energy-dependent visibility for different Talbot distances is depicted in subfigure (B). For different distances the visibility peaks have different positions. One can observe that the peak positions increase linearly with the energy. Figure adapted from Viermetz (2015).

and Chavez, 1996). This leads to the corrected flux of the source:

$$\Phi_{\mathrm{corr}} = \int \frac{S(E)}{Q(E)} \mathrm{d}E \cdot \Phi_{\mathrm{meas}}. \tag{3.38}$$

The experimental results are shown in Tab. 3.3. With the current setup configuration a flux of approximately 520 photons/s/pixel is measured. For the flux at different positions, the flux can be scaled with $1/r^2$, with r being the source-to-detector distance.

3.6.3 Spectral performance of the interferometer

The interferometric visibility is a performance quantity of the grating interferometer. In order to analyze the spectral dependence of the visibility, a phase-stepping curve was determined using the Amptek X-123 XRF detector. This results in the energy-dependent visibility plot visualized in Fig. 3.11 (A). Different visibility peaks can be observed at different energies originating from different energy-dependent Talbot distances and phase-shifts. The resulting mean visibility, which is measured with the Pilatus detector, is thus an integration over all the different visibility contributions for

Tab. 3.3 | Flux of the FR-591 rotating anode. The source was operated with 40 kVp and 70 mA. The detector was 2650 mm away from the source. The grating substrates were 1 mm Kapton, 200 µm silicon, and 500 µm silicon for the source, phase, and analyzer grating, respectively. The water container was 40 mm thick with a combined thickness of 2 mm of the PMMA container.

	flux per pixel [photons/s/pixel]	flux per area [photons/s/mm^2]	corrected flux per pixel [photons/s/pixel]	corrected flux per area [photons/s/mm^2]
pure beam	$(8.7 \pm 0.4) \times 10^4$	$(2.9 \pm 0.1) \times 10^6$	$(1.2 \pm 0.5) \times 10^5$	$(4.0 \pm 0.2) \times 10^6$
beam with gratings	$(4.0 \pm 0.4) \times 10^3$	$(1.4 \pm 0.1) \times 10^5$	$(8.2 \pm 0.8) \times 10^3$	$(2.8 \pm 0.3) \times 10^5$
beam with gratings and 40 mm H_2O	$(5.2 \pm 0.4) \times 10^2$	$(1.8 \pm 0.1) \times 10^4$	$(1.3 \pm 0.1) \times 10^3$	$(4.3 \pm 0.3) \times 10^4$

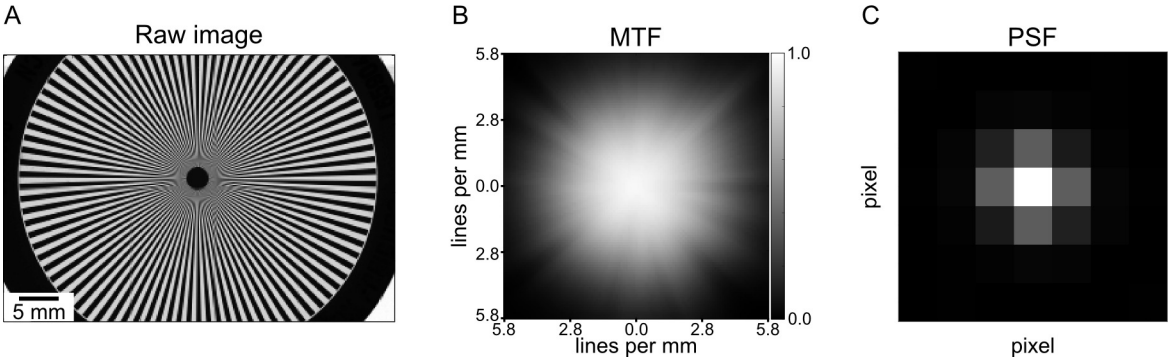

Fig. 3.12 | Determination of the detector PSF. Subfigure (A) shows the raw image of the siemensstar, which was measured directly in front of the detector. Subfigure (B) depicts the modulation transfer function (MTF), which is the Fourier transform of the point spread function (PSF) (C). The siemensstar was measured directly in front of the Pilatus detector.

each energy. As the spectrum of the interferometer $S(E)$ defines the distribution of the energies, the mean visibility is

$$V = \int V(E)S(E)\mathrm{d}E, \tag{3.39}$$

with the condition that the spectrum is normalized with respect to the number of photons $\int S(E)\mathrm{d}E = 1$. As both the XRF spectrometer and the Pilatus detector have a silicon sensor thickness of 1 mm, the effect of the reduced quantum efficiencies cancels out and the mean visibility is not corrected here for quantum efficiency.

An investigation of the energy-dependent visibility for different Talbot distances is depicted in Fig. 3.11 (B). The energy-dependent visibility was measured for different symmetric setup configurations with $d = l$. The source spectrum and the period of the gratings remained constant. Interestingly, the results of this visibility curve allow deviations from the optimum inter-grating distance of 85.7 cm, as long as both distances are equidistant. The mean visibility of this setup at 40 kVp has a range of 28 to 38% depending on the gratings, the grating alignment, and the use of additional filters like the water container.

3.6.4 Spatial resolution

The size of a voxel is determined by the detector pixelsize p_{det} and the magnification of the sample M_{s}. The effective pixel size p_{eff} is

$$p_{\mathrm{eff}} = \frac{p_{\mathrm{det}}}{M_{\mathrm{s}}}, \tag{3.40}$$

with $M_{\mathrm{s}} = (a+b)/a$ being the sample magnification as shown in Fig. 3.5 (B). In three dimensions with isotropic pixel sizes, the effective pixel size corresponds to the voxel size. The spatial resolution, which determines the size of structure that can be resolved, is determined by all optical components in the imaging system. These components have individual point spread functions (PSF). In a standard imaging system, the resulting

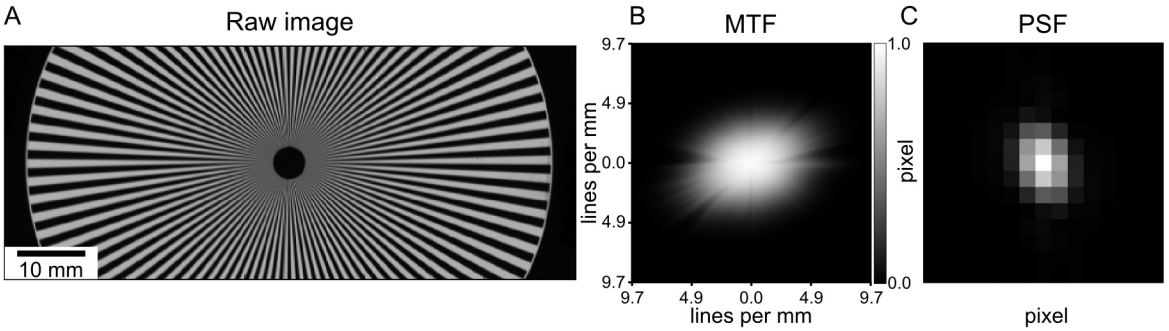

Fig. 3.13 | Influence of the source size. Subfigure (A) shows the raw image of the siemensstar, which was placed 112 cm away from the Pilatus detector to investigate the influence of the source size. Subfigure (B) depicts the corresponding modulation transfer function (MTF), which is the Fourier transform of the point spread function (PSF) (C). The PSF and MTF illustrate the influence of the extended and even anisotropic source size.

image is then a convolution of the total PSF with the object O plus noise

$$\text{Image} = O \star \text{PSF}_{\text{total}} + \text{noise}. \tag{3.41}$$

The total PSF of an imaging system is a convolution of all elements in the beam, which is here

$$\text{PSF}_{\text{total}} = \text{PSF}_{\text{source}} \star \text{PSF}_{\text{detector}} \star \text{PSF}_{\text{gratings}}. \tag{3.42}$$

Determination of the detector PSF

The PSF of the detector was determined with a siemensstar measured directly in front of the detector without the gratings in the beam (cf. Fig. 3.12 A). At this position the effect of the source is negligible and the recorded image leads to the PSF of the detector. As the PSF is not directly accessible with measurements of the siemensstar, one needs to the determine first the modulation transfer function (MTF), which is the Fourier transform of the PSF (cf. Fig. 3.12 B). The manufacturer of the detector guaranteed a box-like PSF of the detector with the size of one pixel (Dectris, 2014), which is consistent with the retrieved PSF (cf. Fig. 3.12 C).

Determination of the source size

The source size of the rotating anode was measured in the same way as the detector PSF (cf. Fig.3.13). Due to the limited field of view, the PSF could only be determined at 112 cm away from the detector. The PSF of the gratings turned out to be approximately 1. With the same result for the detector, the total PSF is hence approximately the PSF of the source

$$\text{PSF}_{\text{total}} \approx \text{PSF}_{\text{source}}. \tag{3.43}$$

For high-resolution imaging, the sample is positioned close to the source to reach high optical magnification. This however increases the impact of the source PSF and deteriorates the achieved spatial resolution.

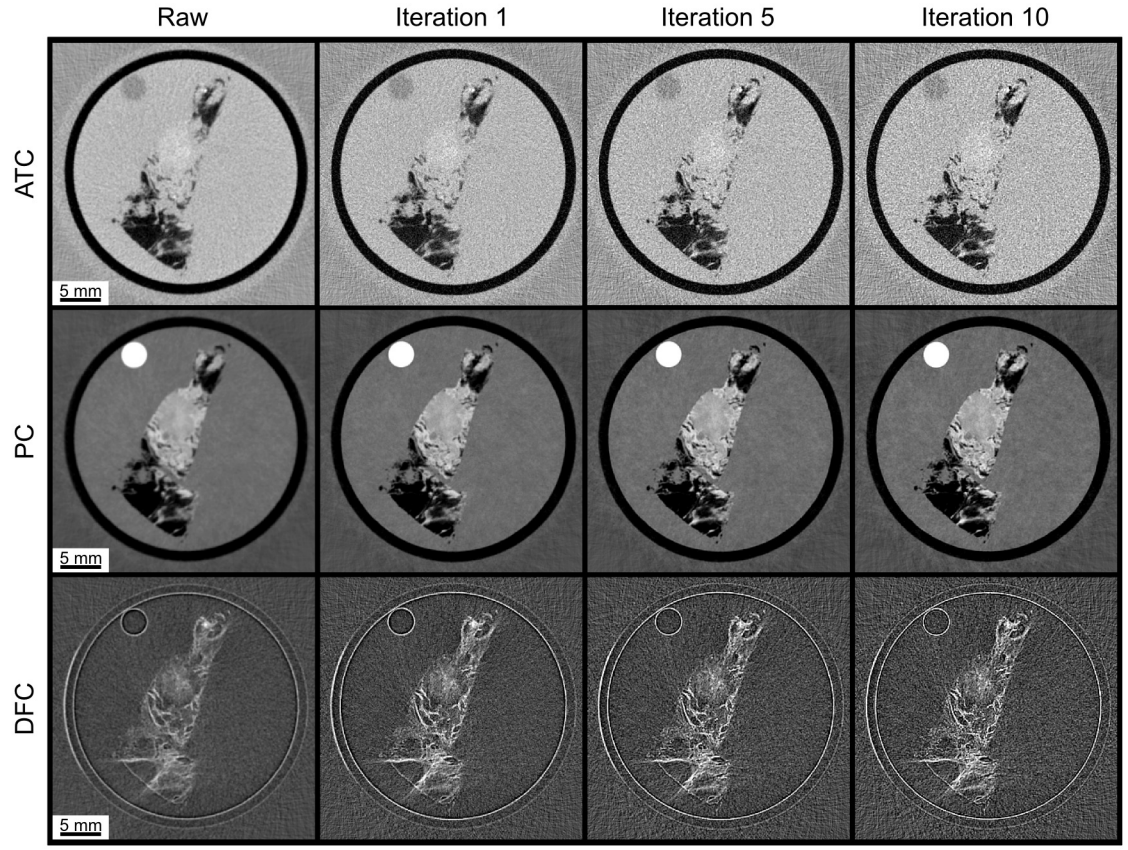

Fig. 3.14 | Exemplary deconvolution images of a ductal carcinoma in situ (DCIS) sample. The image quality increases with the number of iterations at the cost of higher noise (De Marco, 2015). The attenuation values are displayed in a linear range from [-40,200] HU, the phase-contrast values from [-60,120] HUp, and the dark-field values from [-0.004,0.010]. More about the DCIS samples can be found in Sec. 7.2.

Deconvolution

The point spread function of the setup can be used for deconvolution algorithms to increase the spatial resolution of the tomographic data. The idea is to reverse the convolution of the object with the PSF (cf. Eq. 3.41). Whereas a direct inversion of the convolution is not feasible due to the presence of noise, there exist several deconvolution algorithms trying to overcome the loss of information in different ways.

In this work, the Richardson-Lucy algorithm is used as deconvolution algorithm (Richardson, 1972; Lucy, 1974). The iterative algorithm is based on inversion of the convolution

$$O^{(k+1)} = O^{(k)} \frac{\text{Image}}{O^{(k)} \star \text{PSF}} \star \text{PSF}^{\text{T}}, \tag{3.44}$$

with PSF^{T} being the transposed PSF and k being the number of iterations. The effect of the Richardson-Lucy deconvolution on the tomographic data, which was applied to the raw images followed by standard processing and reconstruction, is exemplary shown in Fig. 3.14. It can be observed that the reconstructions appear sharper with increased number of deconvolution iterations k at the cost of increased noise. The

remaining issue is the determination of the maximum number of iterations and the risk of induced artifacts. Further analysis, especially with different algorithms, can be found in De Marco (2015).

Oversampling

Oversampling is a different method to increase the spatial resolution if one does not change the setup components. The method uses sub-pixel shifts of the sample and fits the data into a newly generated image. The comparison of oversampling with the Pilatus detector and a Dectris Eiger detector system with 75 µm pixel size at the GBPC-CT setup at hand is presented in full detail in Viermetz (2015).

3.7 Technical components

The motors are controlled by a Newport XPS controller with eight axes. Most importantly, the three gratings can be rotated around the optical axis. Additionally, the phase grating can be moved in z-direction (direction of the optical axis). It is sufficient that the other alignment motions can be performed manually. The stepping is performed with a Newport LTA-HL linear motor in combination with a nanoconverter developed by the Paul Scherrer Institute (PSI, Villigen, Switzerland), which enables precise and reproducible grating positioning. The sample stages can be moved in two-dimensions in orthogonal direction with respect to the beam direction and rotated around the y-axis for tomographic reconstruction. The whole setup motors are programmed with SPEC (Certified Scientific Software). All used processing and reconstruction algorithms were developed at the Chair of Biomedical Physics.

3.8 Biological samples

If not stated otherwise, the biological samples are measured in 15 or 50 ml Falcon tubes filled with a 4-%-formaldehyde or phosphate buffered saline (PBS) solution. All samples were provided by the corresponding project partner with biological or medical expertise. The corresponding institutes include the Institut für Rechtsmedizin (Ludwig-Maximilians-University Hospital Munich, Germany), the Institute for Diagnostic and Interventional Radiology (Klinikum Rechts der Isar, Technical University of Munich, Germany), the Institute of Clinical Radiology (Ludwig-Maximilians-University Hospital Munich, Germany), and the Institute of Molecular Nutritional Medicine (Else Kröner-Fresenius Center for Nutritional Medicine, Technical University of Munich, Germany). All heart specimens were provided by the Institute for Advancement in Medicine (IIAM). Written informed consent to provide tissue for research purposes had been obtained by the donor or the donor's relatives. The experiments were approved by the local ethics committee (Projectnumber 319/13, Ethikkommission, Fakultät für Medizin, Technical University of Munich, Germany or Ethikkommission of the Ludwig-Maximilian University, Munich) and conducted according to the Declaration of Helsinki of 1975, as revised in 2008.

CHAPTER 4

High-sensitivity phase-contrast imaging

Short summary

Angular sensitivity – or the minimum resolvable refraction angle – of the phase-contrast signal is the essential parameter in GBPC-CT imaging allowing high soft tissue contrast aside from spatial resolution. This chapter covers the investigation on how to achieve experimentally high angular sensitivity with laboratory GBPC-CT. For that, the angular sensitivity is discussed in theory leading to experimental considerations for high sensitivity GBPC-CT setups. The experimental results achieved with the GBPC-CT setup presented in this work are compared to other setups based on literature values. The main results of this chapter are published in Birnbacher et al. (2016).

4.1 Introduction

Sensitivity in grating interferometry can be defined as the minimum resolvable refraction angle in DPC projections (Modregger et al., 2011) based on the refractive index decrement and subsequently on the electron density. Reaching high sensitivity – or more precisely angular sensitivity – is one of the main challenges of grating based phase-contrast computed tomography in order to achieve high soft tissue contrast next to imaging at high spatial resolution and high performance.

Angular sensitivity has already been investigated in Modregger et al. (2011); Thüring et al. (2012); Thüring et al. (2013); Thüring and Stampanoni (2014) and depends primarily on the interferometer configuration including the grating periods, the setup geometry, and the visibility as well as the noise in the DPC projections. Also, the design energy of the setup depending on the X-ray spectrum, the grating duty-cycle, and the inter-grating distances have to be chosen carefully. In general, increasing the angular sensitivity signifies increasing the inter-grating distance between the phase and the analyzer grating and reducing the period of the analyzer grating. Moreover, it is advantageous to reach high angular sensitivity to position the sample as close as possible to the phase grating (Engelhardt et al. (2007); Donath et al. (2009)). Further, one can select the design energy independently from the inter-grating distances enabling a large variety of DPC setups for different applications (Pfeiffer et al., 2006; Engelhardt et al., 2007; Hipp et al., 2014).

High electron density resolution in GBPC-CT data is directly related to high angular sensitivity in DPC projections. However, in order to realize experimentally high sensitivity laboratory GBPC-CT imaging using a polychromatic, incoherent X-ray source, one faces additional challenges mainly in performance and setup design in comparison to results from quasi-monochromatic synchrotron sources. Recently, new developments

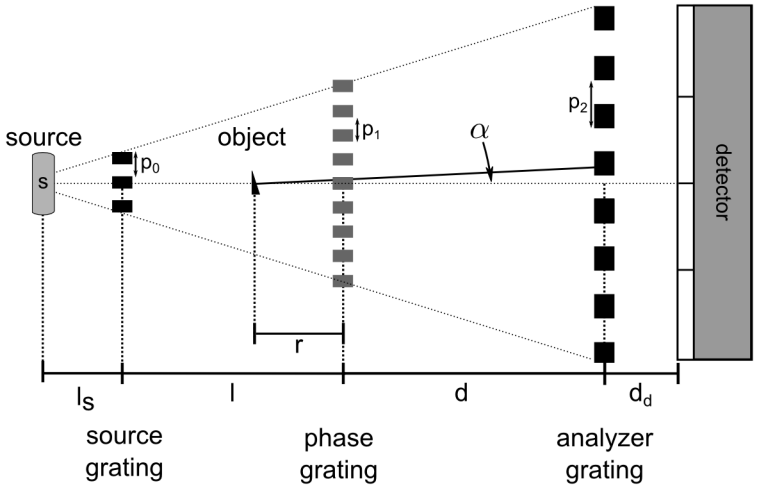

Fig. 4.1 | Schematic of a GBPC-CT setup. From left to right: the X-ray source, the three gratings – source, phase, and analyzer grating with their corresponding periods p_0, p_1, and p_2 – followed by the detector. The source grating is positioned at a distance l_s away from the source and the object is placed at a distance r away from the phase grating. The distance between the detector and the analyzer grating is d_d. The object causes a refraction angle α, which is increased by a factor $(l + r)/l$ taking into account the magnification of α by the distance from the object to the phase grating r (Engelhardt et al., 2007; Donath et al., 2009). The figure is not to scale as in particular the refractive angle and grating periods are much smaller. Figure adapted from Birnbacher et al. (2016).

in grating fabrication (cf. Sec. 3.3.1), the theoretical optimization of the setup design (Thüring and Stampanoni, 2014; Hipp et al., 2014), and more advanced processing algorithms (cf. Sec. 3.4.1) have lead to a substantial rise in quality and stability of DPC imaging, namely in an increase of interferometric visibility and a reduction of noise. Furthermore, studies on quantitative imaging showed that the use of a water container surrounding the sample is necessary, as the imaging results are significantly improved due to reduction of phase-wrapping and beam hardening artifacts (Herzen et al., 2009; Willner et al., 2014; Sarapata et al., 2014).

In this chapter, the design of the GBPC-CT setup presented in this work and how to reach high sensitivity for tomographic scans combining all individual aspects mentioned above is outlined. First, the angular sensitivity in DPC projections is theoretically described. Next, the angular sensitivity of this GBPC-CT setup is determined to provide a comparison to synchrotron facilities and other laboratory PC-CT setups. Eventually, an exemplary GBPC-CT scan of a human cerebellum sample visualizing subtle differences in the refractive index decrement is shown. The reached sensitivity and – in combination with effective energy calibration – electron density resolution is comparable to results from synchrotron sources.

4.2 Angular sensitivity

The goal of GBPC-CT is the visualization of small differences in electron density ρ_e, which allows high soft tissue differentiation. Those differences in electron density or

respectively in the related refractive index decrement δ (cf. Eq. 2.20) are based on the resolution of the gradients in the DPC projections – the lateral phase shift of the interference pattern φ – determined with a Talbot-Lau interferometer. Achieving high DPC contrast means resolving fine differences in φ, which can be described by high signal-to-noise ratio in grating-based phase-contrast.

The signal-to-noise ratio of φ is

$$SNR_{\varphi} = \frac{\varphi}{\sigma_{\varphi}}, \tag{4.1}$$

and can be optimized by increasing the signal φ and reducing the standard deviation σ_{φ}. The DPC signal is however dependent on the setup design as can be seen by the refraction angle as stated in Eq. (2.54)

$$\varphi = \frac{2\pi d}{p_2}\alpha, \tag{4.2}$$

with p_2 being the period of the analyzer grating and d being the inter-grating distance between the phase and the analyzer grating. The refraction angle depends only on the energy and the electron density (cf. Eq. 2.51). This leads to the SNR_{φ} expressed in combination with the refraction angle as

$$SNR_{\varphi} = \frac{\frac{2\pi d}{p_2}\alpha}{\sigma_{\varphi}}, \tag{4.3}$$

which accounts for setup parameters like setup geometry and analyzer grating period and the standard deviation of the phase shift φ.

The DPC sensitivity can be defined as the minimum refraction angle

$$\alpha_{\min} = \frac{p_2}{2\pi d}\sigma_{\varphi}, \tag{4.4}$$

for which a SNR_{φ} of one can be achieved in Eq. (4.3) (Modregger et al., 2011; Thüring et al., 2012; Thüring et al., 2013). The smaller this value is, the smaller refraction angles can be resolved and thus higher angular sensitivity is achieved. This equation expresses explicitly the geometrical dependency and includes the noise in the DPC signal σ_{φ}.

The angular sensitivity $\alpha_{\min}$ depends generally on the geometry of the setup stated in the first term of Eq. (4.4) and the noise behavior in the DPC projections forming the second term. Realizing experimentally high angular sensitivity means reducing the period of the analyzer grating, increasing the Talbot distance d, and reducing the noise of the DPC signal.

Additionally, one has to include a sample dependent reduction of the angular sensitivity as the sample cannot be positioned directly at the position of the phase grating (Engelhardt et al., 2007; Donath et al., 2009), which is illustrated in Fig. 4.1. Therefore, Eq. (4.4) is multiplied with a sample factor f. Taking this into account, the

resulting formula for the minimum refraction angle is

$$\alpha_{\min} = \underbrace{\frac{p_2}{2\pi d}}_{\text{geometry}} \cdot \underbrace{f}_{\text{sample}} \underbrace{\cdot \sigma_\varphi}_{\text{noise}}, \tag{4.5}$$

which expresses the three terms geometry, sample position, and noise.

4.2.1 Geometry

The first term of Eq. (4.5) describes the interferometer geometry and depends on the setup design parameters like phase-shift of the phase grating, design energy, and Talbot order defining the Talbot distance. In order to reach high angular sensitivity, the period of the analyzer grating p_2 has to be decreased and the magnified Talbot distance d increased to reduce $\alpha_{\min}$. For a Talbot-Lau interferometer, the inter-grating distance between phase and analyzer grating d depends on the choice of periods and the Talbot order m, whereas the distance between source and phase grating l is defined by

$$\frac{p_2}{d} = \frac{p_0}{l}, \tag{4.6}$$

with p_0 being the period of the source grating (cf. Sec. 2.3.2). In a different formulation including the total setup length $l + d$, this leads to

$$\frac{p_2}{d} = \frac{1}{l+d}(p_0 + p_2). \tag{4.7}$$

For a Talbot interferometer, this expression is described differently as no source grating is needed (cf. Thüring and Stampanoni (2014)). With limitations on the total setup length and grating period fabrication (cf. Sec. 3.3.1), the symmetric setup configuration with $d = l$ and therefore $p_0 = p_1 = p_2$ as well as π-phase shift is the optimum design choice for a Talbot-Lau interferometer (Donath et al., 2009; Thüring and Stampanoni, 2014).

4.2.2 Sample position

The position of the sample is application specific and depends on the desired magnification and therefore effective pixel size. The already mentioned reduction of the refraction angle due to the distance of the sample to the source grating can be formulated as

$$f(r) = \frac{l+r}{l}, \tag{4.8}$$

with the distance from the sample to the phase grating $r \geq 0$ and the distance from the source grating to the phase grating l (Engelhardt et al., 2007; Donath et al., 2009) as shown in Fig. 4.1. Hence the sample has to be positioned as close as possible to the phase grating for high angular sensitivity. The sample can also placed between the

phase and the analyzer grating resulting in a similar equation:

$$f(r) = \frac{d+r}{d}. \tag{4.9}$$

4.2.3 Noise

Noise in phase-contrast imaging can be expressed according to Poisson statistics as

$$\sigma_\varphi = \frac{\sqrt{2}}{V\sqrt{N}}, \tag{4.10}$$

depending on the interferometric visibility V, which describes the quality of the interferometer, and the total number of counts N (Engel et al., 2011). The angular sensitivity increases, i.e. the minimum resolvable refraction angle decreases, with the visibility V and the number of counts N. The number of detected photons N can be formulated as the counts per pixel

$$N = I_0 \frac{p^2}{s^2} Mt, \tag{4.11}$$

with p being the size of the detector pixel, s being the total distance from the source to the detector, M being the number of steps, and t being the exposure time per phase step. Increasing the total number of counts via larger exposure time or more phase-steps is obvious (Thüring et al., 2012).

Since DPC projections require a reference image without a sample in the beam, the final noise equals a quadratic addition of the individual noise terms

$$\sigma_\varphi^2 = \sigma_{\varphi,\mathrm{s}}^2 + \sigma_{\varphi,\mathrm{r}}^2. \tag{4.12}$$

If the exposure time is the same, Eq. (4.10) is multiplied by an additional factor of $\sqrt{2}$ (Thüring et al., 2012). The effect of higher exposure times of the flat-field reducing the standard deviation $\sigma_{\varphi,\mathrm{r}}$ and thus increasing the sensitivity is described in Sec. 3.5.1.

A different detector with larger pixel size increases the sensitivity, however at the cost of reduced spatial resolution. Decreasing the distance from the source to the detector s for higher flux is compensated by an increase of the intergrating-distance d or decrease in the analyzer period p_2 when using an asymmetric setup design (cf. Eq. (4.5)).

4.2.4 Visibility

The last parameter of Eq. (4.5) in combination with Eq. (4.10) to investigate is the visibility as part of the noise term. Being a central parameter of the interferometer, the visibility has large impact on the setup performance and the noise. Optimum visibility for a Talbot-Lau interferometer can be calculated based on convolution of rectangular gratings with transmission factors τ and duty cycles κ of the gratings. This results in a visibility

$$V = (\frac{4}{\pi}) \cdot V_{\mathrm{SG}}^* \cdot V_{\mathrm{AG}}^*, \tag{4.13}$$

with the subscript 'SG' signifying the source grating and 'AG' meaning the absorption grating as derived in Thüring and Stampanoni (2014). Thereby, the respective visibility is

$$V_i^* = \frac{\kappa(1-\tau)\,\mathrm{sinc}\,\kappa}{\tau+\kappa(1-\tau)}, \tag{4.14}$$

with i being either the source grating ('SG') or the absorption grating ('AG'). This equation results in a maximum visibility in an ideal case with a transmission ratio of $\tau = 0$ and a duty cycle of $\kappa = 0.5$

$$V = 2\left(\frac{2}{\pi}\right)^3 = 0.52, \tag{4.15}$$

for a monochromatic setup case (Thüring and Stampanoni, 2014). For a polychromatic case, the mean visibility depends additionally on the source spectrum, periods, design, and setup type as well as the detector as illustrated in Sec. 3.6.3. A duty cycle of 0.66 was shown to be optimal for a Talbot-Lau type interferometer (Thüring and Stampanoni, 2014). Moreover, the use of a π-grating outperforms $\pi/2$-gratings for higher Talbot orders than 1 with respect to the visibility, as outlined in Chabior (2011), Thüring and Stampanoni (2014), and Hipp et al. (2014).

4.3 Experimental realization of high angular sensitivity

In order to realize experimentally a high sensitivity GBPC-CT setup using a polychromatic source, experimental limitations have to be considered next to the already outlined theoretical aspects. Combining all previous theoretical considerations, the minimum refraction angle is

$$\alpha_{\min} = \frac{p_2}{2\pi d}\frac{l+r}{l}\frac{2}{V\sqrt{N}} \tag{4.16}$$

$$= \frac{p_2}{2\pi d}\frac{l+r}{l}\frac{2}{V\sqrt{I_0\frac{p^2}{s^2}Mt}}. \tag{4.17}$$

Concerning the setup length, a small and compact setup provides increased counts due to a small setup length s. In contrast, the inter-grating distance d should be large. Both effects cancel, which is explicitly shown in Thüring et al. (2012).

However, if the setup does not need to be optimized with respect to time efficiency, a long inter-grating distance d allows to increase the field of view, reduce the relative impact of the sample position, and decrease the effect of shadowing by non-radial grating illumination.

Spectral optimization for high mean visibility values was performed in combination with all setup components. This resulted in a symmetric setup with distances $l = d = 857\,\mathrm{mm}$, which does not correspond to a discrete Talbot distance of the design energy (Hipp et al., 2014). As already indicated the symmetric setup design and the phase shift of π allow high performance at higher Talbot orders and constant periods of all

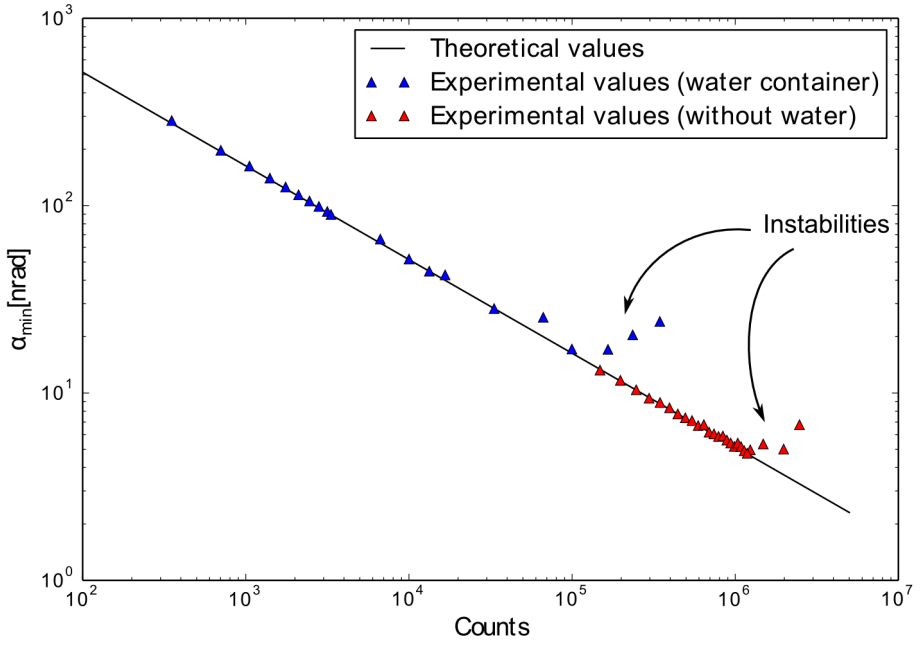

Fig. 4.2 | Double-logarithmic plot of the minimum resolvable refraction angle $\alpha_{\mathbf{min}}$. The blue triangles represent the minimum angular sensitivity with a 40 mm thick water container, the red data points the results without the water container in the beam. The theoretical minimum refraction angle according to Eq. (4.5) is the solid black line. The noise of the lateral phase shift σ_φ was calculated in an area of 190×190 pixels. The mean visibility was 38.7 %. Figure adapted from Birnbacher et al. (2016).

three gratings (Thüring and Stampanoni, 2014).

The periods of all gratings were chosen to 5.4 µm and the corresponding duty cycles to approximately 0.6, both parameters limited by grating fabrication. Two of the gratings were on a 200 µm silicon wafer, which is a lower practical limit for this material because of the danger of breaking. The configuration of the gratings is no. 1, 2, and 4 of Tab. 3.1. The detector efficiency of the single-photon counting detector is lower than integration detectors, however the direct photon counting without additional read-out and electronic noise allows to increase the sensitivity.

4.3.1 Sensitivity in DPC projections

The first experiment determines the experimental angular sensitivity in the DPC projections and compares the results with the theoretical model including explicit noise behavior as shown in Eq. (4.16). The DPC projections were measured in dependency of the counts N with and without water container for investigating the maximum sensitivity limit. Although the angular sensitivity described in Eq. (4.5) is formulated without any theoretical limit, instabilities like thermal or source fluctuations and vibrations pose an experimental boundary. The mean visibility achieved in this configuration of the GBPC-CT setup was 38.7 %.

The data obtained with the water container is shown as blue triangles in Fig. 4.2.

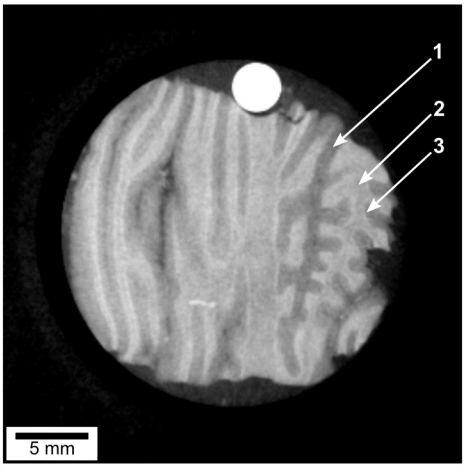

Fig. 4.3 | Exemplary electron density slice of a human cerebellum sample. The electron density resolution based on the high sensitivity reveals subtle differences in the structure of the cerebellum: the stratum moleculare (1), the white matter (2), and the stratum granulosum (3). The displayed values are in the linear range of $338 - 356\,\mathrm{e/nm^3}$. The sample was measured at 40 kVp. For this GBPC-CT scan, 11 phase-steps with 55 s total exposure time per projection and a total of 1200 projections were used. Figure adapted from adapted from Birnbacher et al. (2016).

Starting at about 360 counts, α_{min} decreases linearly in the double-logarithmic plot as theoretically expected. At approximately 1.6×10^5 photons, the values start to increase again due to the already mentioned instabilities like thermal drift and jitter of the gratings (Revol et al., 2010). The highest sensitivity α_{min} with water container is 17 nrad at 1.0×10^5 photons, which is equivalent to 275 s exposure time per DPC projection. As this is too long to perform tomographic scans in a reasonable amount of time, the standard exposure time for tomographic scans is 55 s per DPC projection with a sensitivity of 38 nrad.

In a second set of scans, the angular sensitivity was determined without the water container to increase to number of counts before time-dependent instabilities occurred (cf. red triangles in Fig. 4.2). This increased the flux by a factor of approximately 10. At 1.2×10^6 photons corresponding to 275 s exposure time per DPC projection, the minimum refraction angle α reached its lower limit of 5 nrad. At 55 s total exposure time per projection (2.5×10^5 photons) 10 nrad angular sensitivity were measured. However, without the water container high-quality tomographic scans are not feasible as phase-wrapping occurs and reduces the quality of quantitative imaging. The DPC projections for this experiment were acquired with 11 phase-steps and a polynomial fit and offset correction as described in Sec. 3.4.2 were used.

4.3.2 Sensitivity in tomographic phase-contrast imaging

High angular sensitivity leads to high electron density resolution σ_{ρ_e} when performing tomography. The electron density resolution is determined by the standard deviation

of the refractive index decrement

$$\sigma_{\rho_e} = \frac{E^2}{2\pi\hbar^2 c^2 r_0}\sigma_\delta \tag{4.18}$$

based on Eq. (2.20). How to determine the electron density is described in detail in Ch. 5.

An exemplary biomedical application of GBPC-CT showing the possibilities of high electron density resolution is presented here by a tomographic scan of a human cerebellum specimen (cf. Fig. 4.3). Subtle differences in soft tissue are visualized, as it is possible to delineate the stratum moleculare, the stratum granulosum, and the white matter. This kind of three-dimensional sensitivity has been previously only achieved at synchrotron sources or different imaging modalities like MRI (Pfeiffer et al., 2007a; Schulz et al., 2010, 2012).

The electron density resolution in the cerebellum data was $0.45\,\mathrm{e/nm^3}$ in a volume of $10 \times 10 \times 10$ voxels. A direct determination of the electron density resolution based on the angular sensitivity is not feasible as additional parameters influence the achievable resolution of the refractive index decrement σ_δ when performing a tomographic scan (Raupach and Flohr, 2011; Köhler et al., 2011; Chen et al., 2011). The signal-to-noise ratio (SNR) in the same volume was 1.2×10^3 compared to 3.0 in the attenuation signal. The effective pixel size in this scan was $100 \times 100\,\mu\mathrm{m}^2$. In this experiment the effective energy was 25.6 keV.

4.4 Discussion and conclusion

As can be seen in Fig. 4.2, the best angular sensitivity measured with this state-of-the-art GBPC-CT is 5 nrad, which is unrivaled by any other reported laboratory phase-contrast setup. While this quite long exposure time of 275 s exposure time per DPC projection and the lack of water container limit practical application, the results prove what level of sensitivity can be achieved with a laboratory GBPC-CT setup. The best minimum refraction angle measured with water container is 17 nrad with 275 s exposure time per DPC projection. As direct sensitivity values are rarely provided by literature, a comparison of calculated angular sensitivity limits is compiled in Tab. 4.1. However, the comparison focuses only on the angular sensitivity, since the experimental conditions of referenced setups like exposure time or spatial resolution

Tab. 4.1 | Sensitivity comparison. Parameter comparison between the GBPC-CT setup presented in this study and other grating-based DPC setups reported in literature. d is the inter-grating distance between phase and analyzer grating. Table adapted from Birnbacher et al. (2016).

setup	facility	period p_2	d	sensitivity	exposure time	pixel size
setup without water container	laboratory	5.4 µm	85.7 cm	5 nrad	275 s	172 µm
setup with water container	laboratory	5.4 µm	85.7 cm	38 nrad	55 s	172 µm
reference setup no. 1 (Pfeiffer et al., 2007a)	synchrotron	2.0 µm	36.1 cm	14 nrad	3.2 s	28 µm
reference setup no. 2 (Modregger et al., 2011)	synchrotron	2.4 µm	12.1 cm	67 nrad	2.1 s	7.4 µm
reference setup no. 3 (Revol et al., 2010)	laboratory	3.0 µm	6.9 cm	110 nrad	80.4 s	48 µm
reference setup no. 4 (Thüring et al., 2012)	laboratory	2.4 µm	19.5-32.5 cm	270-300 nrad	128 s	48 µm
reference setup no. 5 (Thüring et al., 2013)	laboratory	2.4 µm	10 cm	250 nrad	128 s	48 µm

are completely different.

Comparison to synchrotron sources

References 1 and 2 are grating interferometer setups operating at a synchrotron source. The sensitivity and spatial resolution of reference 1 is superior in sensitivity and spatial resolution, which originates in the small pixel size in combination with higher flux and the monochromatic performance (Pfeiffer et al., 2007a). The sensitivity of reference setup 2 is lower due to the relatively small inter-grating distance. However, the spatial resolution is with a pixel size of 7.4 µm definitely superior than the presented GBPC-CT setup (Modregger et al., 2011). An increase of the Talbot order and thus the inter-grating distance d or the exposure time, which is quite short in both referenced setups, would most probably lead to higher sensitivity if the dynamic range of the detector is sufficient and the respective gratings are available.

One can state that phase-contrast imaging at synchrotron facilities outperforms laboratory setups in terms of spatial resolution due to the small source size, and in terms of measurement time due to the high flux. But the cone beam geometry in laboratory setups enables measuring large sample due to a potentially increased field of view. The results achieved with this GBPC-CT setup demonstrate that comparably high sensitivity can be achieved in a laboratory environment.

A direct comparison to the electron density resolution is hardly possible as the standard deviation of the refractive index decrement depends on both the measured object and the energy of the experiment. Nonetheless, the electron density resolution achieved with this setup lies with $0.45\,\mathrm{e/nm^3}$ in the range of values calculated from reported measurements at synchrotron facilities ($0.1 - 0.6\,\mathrm{e/nm^3}$) (Pfeiffer et al., 2007a; Zanette et al., 2011, 2013a; Schulz et al., 2010; McDonald et al., 2009).

Comparison to laboratory sources

The results from references 3 – 5 originate from laboratory X-ray sources. The calculated angular sensitivity based on reference 3 is approximately 110 nrad (Revol et al., 2010), which is significantly less sensitive than the present GBPC-CT setup. The referred DPC measurement was performed without a water container and longer exposure time, but smaller pixel size. The main difference however grounds on the differences in geometry. The sensitivity values of references 4 and 5 in Tab. 4.1 were achieved with a very compact setup using a low flux microfocus tube that causes the low sensitivity (Thüring et al., 2012; Thüring et al., 2013). Scaling the distances would lead to an enormous increase in sensitivity.

Edge-illumination or coded aperture is a different phase-contrast technique which can be operated with laboratory X-ray sources. The reported sensitivity values are also defined as the minimum resolvable refraction angle and were 270 nrad, which is attributed to the rather large periods of this method (Diemoz et al., 2014).

Increasing the sensitivity

The performance of high sensitivity in GBPC-CT depends additionally on the spatial resolution and the energy. Both parameters are not expressed in the minimum resolv-

able refraction angle α_{min}. In order to achieve higher spatial resolution, the pixel size could be reduced by selecting a detector with smaller pixel sizes, which decreases the flux per pixel and thus reduces the sensitivity. Alternatively, a sample position closer to the source increases the geometrical magnification. The latter increases the distance to the phase grating and thus reduces the sensitivity according the sample dependent factor stated in Eq. (4.8). Also, the effect of the source blur has to be considered as outlined in Sec. 3.6.4.

The energy dependence of the refractive angle of an object is

$$\alpha \propto \frac{1}{E^2}, \tag{4.19}$$

which means that the angle to be resolved decreases with increasing energy (cf. Eq. 2.20). If the energy is increased, the minimum refraction angle α_{min} is reduced and a refraction angle cannot be resolved anymore. Reducing the energy leads thus to increased sensitivity.

Furthermore, the exposure time for GBPC-CT needs to be at a reasonable level for a broad application of GBPC-CT. X-ray sources with higher power as well as an increase in flux via reduction of the grating substrates and a more efficient sensor of the detector would be beneficial.

While increasing the source power and optimizing the detector efficiency might reduce the exposure times, a reduction of the analyzer period p_2 would provide beneficial impact, however the setup design would have to be adapted. Furthermore, the fabrication of smaller periods at comparable performance is technically challenging. Increasing the distance d would have the same impact on the sensitivity than reducing the analyzer grating period p_2 and would also change the Talbot distance and performance. But the increase in distance would be compensated by reduced counts per pixel if the exposure time stays constant. Further optimizing the visibility would soon reach a limit, as described by Eq. (4.15).

Alternative setup designs like different phase shifts like $3\pi/2$-phase gratings or the choice of an absorption grating instead of a phase grating could be promising ideas to increase the performance especially at higher energies. Moreover, if one wants to achieve good dark-field contrast, high sensitivity is detrimental, especially imaging without water container leads to strong phase-wrapping, which saturates the dark-field signal. The high sensitivity presented in this chapter is necessary for quantitative imaging investigated in the following chapter (cf. Ch. 5).

CHAPTER 5

Quantitative phase-contrast imaging

Short summary

This chapter presents how to realize quantitative GBPC-CT leading to the electron density and the effective atomic number. The refractive index decrement can be transformed into the electron density by energy calibration. Comparison of measured electron density and the attenuation coefficients with literature values showed good agreement for materials with low atomic number. Moreover, one can calculate the effective atomic number by comparing the ratio of the experimentally determined attenuation and electron density values with tabulated cross sections. The results also turned out to be in good agreement with references if a water bath to avoid beam hardening or beam hardening correction is used. The content of this chapter are published in Birnbacher et al. (2018c).

5.1 Introduction

Quantitative imaging in medicine is becoming increasingly important as the need of reproducible, quantitative data emerges with ongoing digitalization (Sardanelli, 2017). In conventional computed tomography (CT), the attenuation coefficient or its alternative representation in Hounsfield units are energy-dependent and therefore of limited comparability. Dual energy computed tomography (DECT) provides a decomposition of data into Compton and photo effect contributions, from which the electron density and the effective atomic number can be calculated. The latter are in general quantities independent of the experimental conditions in contrast to conventional energy-dependent CT (Alvarez and Macovski, 1976; Torikoshi et al., 2003). DECT and related techniques including K-edge or spectral imaging are already used for improved diagnostic imaging of renal stones, gout, fat content quantification in liver (Schlomka et al., 2008; Boll et al., 2009; Hidas et al., 2010; Spek et al., 2016; Leng et al., 2016; Bongartz et al., 2014; Henes et al., 2016; Hur et al., 2014; Hyodo et al., 2017), or for body tissue characterization in radio- and particle therapy (van Abbema et al., 2015).

The electron density and the effective atomic number can also be determined with grating-based phase-contrast computed tomography (GBPC-CT). The electron density is calculated from the refractive index decrement using the beam energy (cf. Eq.2.20). If the experiment is performed with monochromatic synchrotron radiation, the energy is known and the resulting electron density and attenuation coefficients can be verified (Zanette et al., 2011; Willner et al., 2013).

With the translation of GBPC-CT from large-scale synchrotron facilities to laboratory X-ray sources, the range of possible applications is increased and the imaging method is brought closer to industry and medicine (Pfeiffer et al., 2006). But, the

polychromatic nature of laboratory GBPC-CT renders the determination of the quantitative data more complicated. Correct electron density values can be determined with effective energy calibration in combination with a highly sensitive laboratory GBPC-CT setup (Herzen et al., 2009; Qi et al., 2010; Chabior et al., 2011a; Zhou et al., 2013; Willner et al., 2014). Still, the attenuation coefficient remains an energy-dependent quantity.

To access the effective atomic number in a single GBPC-CT scan, two different approaches have been proposed. Qi et al. (2010) use an intensive calibration of a phantom for the determination of the effective atomic number with a fit function. This method provides accurate results, but one needs an additional calibration measurement for each scan differing in parameters like the tube voltage. Additionally, the exponential fit needs highly reliable reference values, which are limited for the effective atomic number (Qi et al., 2010; Spiers, 1946). Willner et al. (2013) proposed to determine the ratio of the Compton scattering part of the linear attenuation coefficient with the total linear attenuation coefficient and compared this result with theoretical cross section data. This approach has already been investigated at a synchrotron source with a monochromatic energy of 82 keV and allowed to determine the effective atomic number.

This chapter discusses the determination of the electron density and the effective atomic number with the already presented experimental laboratory GBPC-CT setup using a polychromatic X-ray source (cf. Ch. 3). First, the energy calibration and retrieved electron density values and attenuation coefficients are presented. For that, a phantom consisting of different materials is measured at 35 kVp and 50 kVp. In order to avoid phase-wrapping and decrease beam hardening effects, the phantom was measured in a water container. The resulting quantitative electron density and absorption coefficients fit well in comparison to theoretical values.

To calculate the effective atomic number, which was performed here for low effective atomic numbers ($Z_{\text{eff}} \leq 8$), the ratio of the experimentally measured electron density values over the attenuation coefficients is compared with tabulated attenuation cross sections using the approach shown in Willner et al. (2013). The effective energy is used to determine the attenuation cross section reducing its dependence on the atomic number. The resulting effective atomic numbers are in good agreement with reference values. Finally, the effect of beam hardening with a phantom immersed in different surrounding liquids was investigated. The differences in electron densities turned out to be small for all three experiments, the same is valid for the differences in effective atomic numbers. However, for low absorbing surrounding liquids like oil additional beam hardening correction had to be applied.

5.2 Theory of quantitative GBPC-CT

5.2.1 Effective energy calibration and electron density calculation

The tomographic reconstruction of the processed ATC and DPC projections leads to both the transmission signal T and the lateral phase-shift of the interference pattern

φ (cf. Eqs. 2.59 and 2.60). The attenuation coefficient can be calculated as

$$\mu_{\mathrm{rel}} = -\frac{\log T}{p_{\mathrm{eff}}}, \tag{5.1}$$

with the effective pixel size p_{eff} and the refractive index decrement determined as

$$\delta_{\mathrm{rel}} = \frac{p_2}{2\pi d}\frac{l+r}{l}\varphi, \tag{5.2}$$

including the sample dependent reduction of the sensitivity defined in Eq. (4.8). As the quantities are measured usually in a water containment, they are denoted with the subscript 'rel'. In order to calculate now absolute quantitative values, energy calibration has to be performed (Herzen et al., 2009).

For calibration of the effective energy, one compares the experimental values of a known material – e.g. the PMMA rod included in the measurements – with the theoretical energy-dependent data. The theoretical energy-dependent differences of PMMA and water are compared with the experimental data. The minimal difference corresponds then to the assigned effective energy, which is performed for both the refractive index decrement δ and the attenuation coefficient μ leading to the effective energies $E_{\mathrm{eff},\delta}$ and $E_{\mathrm{eff},\mu}$.

To determine the absolute attenuation coefficient, the attenuation value of water $\mu_{\mathrm{abs}}(E_{\mathrm{H_2O}})$ has to be added to the measured relative attenuation signal μ_{rel}

$$\mu_{\mathrm{abs}} = \mu_{\mathrm{rel}} + \mu_{\mathrm{H_2O}}(E_{\mathrm{eff},\mu}). \tag{5.3}$$

The absolute refractive index decrement can be accessed in a similar way via adding the refractive index decrement of water $\delta_{\mathrm{H_2O}}(E_{\mathrm{eff},\delta})$ in dependency of the energy

$$\delta_{\mathrm{abs}} = \delta_{\mathrm{rel}} + \delta_{\mathrm{H_2O}}(E_{\mathrm{eff},\delta}). \tag{5.4}$$

The electron density, which is experimentally determined with GBPC-CT, is then

$$\rho_{\mathrm{e}} = \frac{E_{\mathrm{eff},\delta}^2}{2\pi r_0 \hbar^2 c^2}\delta_{\mathrm{abs}}, \tag{5.5}$$

according to Eq. (2.20). Theoretically, the electron density can be calculated if the mass density ρ and composition of the material is known:

$$\rho_{\mathrm{e}} = \rho N_{\mathrm{A}} \frac{\sum w_i Z_i}{\sum w_i A_i}, \tag{5.6}$$

where the weights w_i account for the fraction of electrons of atom i. Z_i is the atomic number, A_i the mass number, and N_{A} Avogadro's number. The electron density of a single atom can be calculated by

$$\rho_{\mathrm{e}} = \rho N_{\mathrm{A}} \frac{Z}{A}. \tag{5.7}$$

or approximated for molecules with negligible hydrogen occurrence to

$$\rho_\mathrm{e} \approx \rho \frac{N_\mathrm{A}}{2}. \tag{5.8}$$

5.2.2 Hounsfield units

In analogy to medical CT, the refractive index decrement can be expressed in phase-contrast Hounsfield units. Conventional Hounsfield units base on the attenuation coefficients, which are normalized to water and air as

$$HU = \frac{\mu - \mu_\mathrm{water}}{\mu_\mathrm{water} - \mu_\mathrm{air}} \cdot 1000, \tag{5.9}$$

with μ being an energy-dependent quantity conventional Hounsfield units are energy-dependent. A similar quantity can be defined for phase-contrast imaging, namely the phase-contrast Hounsfield units

$$HU_\mathrm{p} = \frac{\delta - \delta_\mathrm{water}}{\delta_\mathrm{water} - \delta_\mathrm{air}} \cdot 1000, \tag{5.10}$$

based on the refractive index decrement δ (Donath et al., 2010). Exploiting Eq. (5.5), the phase-contrast Hounsfield units can be expressed by the electron density

$$HU_\mathrm{p} = \frac{\rho_\mathrm{e} - \rho_\mathrm{e,water}}{\rho_\mathrm{e,water} - \rho_\mathrm{e,air}} \cdot 1000, \tag{5.11}$$

which expresses that the phase-contrast Hounsfield unit is a quantity independent of the energy in contrast to the attenuation Hounsfield units. Conventional and phase-contrast Hounsfield units are primarily used in the medical context, as presented e.g. in Ch. 7.

5.2.3 Determination of the effective atomic number

With the electron density and attenuation coefficient at hand, one can determine the effective atomic number Z_eff. In contrast to the electron density, the total attenuation coefficient still depends on both the energy and the atomic number. Assuming a single atom, the total attenuation coefficient is formed by

$$\mu = \rho \frac{N_\mathrm{A}}{A} \sigma_\mathrm{tot}(E, Z), \tag{5.12}$$

with σ_tot being the total cross section. The latter is based on three effects, namely the photoelectric (ph) effect as well as coherent (coh) and incoherent (incoh) scattering

$$\sigma_\mathrm{tot}(E, Z) = \sigma_\mathrm{ph}(E, Z) + \sigma_\mathrm{coh}(E, Z) + \sigma_\mathrm{incoh}(E, Z), \tag{5.13}$$

as outlined in Sec. 2.1.1. If one expands Eq. (5.12) with the atomic number and uses Eq. (5.7), one gets an expression which depends on the electron density, the atomic

number, and the total absorption cross section:

$$\mu = \rho_\mathrm{e} \frac{\sigma_\mathrm{tot}(E, Z)}{Z}. \tag{5.14}$$

Rearranging this expression leads to

$$\frac{\rho_\mathrm{e}}{\mu} = \frac{Z}{\sigma_\mathrm{tot}(E, Z)}, \tag{5.15}$$

with the left side being the ratio of the electron density over the attenuation coefficient, which can be experimentally determined with GBPC-CT. $\sigma_\mathrm{tot}(E, Z)$ can be accessed from tabulated data (McCullough, 1975; Berger et al., 2010; Hubbell, 1969). Now one can calculate the effective atomic number Z_eff with GBPC-CT if one compares the experimental ratio of Eq. (5.15) for compound materials with the interpolated curve of the tabulated data using the effective energy E_eff.

Independent calculation of the atomic number is not trivial (Taylor et al., 2012). However, one can use an empirical formula

$$Z_\mathrm{eff} = \sqrt[2.94]{\sum_i (w_i Z_i)^{2.94}} \tag{5.16}$$

as theoretical reference, where w_i is the total fraction of electrons and Z_i the atomic number of each component of the molecule (Spiers, 1946; Murty, 1965). Different values are given by the XMuDat software, which is used as a second reference (Nowotny, 1998; Boone and Chavez, 1996) and uses a factor of 3.5 as value in Eq. (5.16).

5.3 Results and Discussion

5.3.1 Electron density and absorption coefficients

For determination of the electron density and the attenuation coefficients, tomographic scans of a phantom consisting of five different polymers at two tube voltages 35 kVp

Tab. 5.1 | Electron density values and linear attenuation coefficients of different polymers and water. The data was evaluated from phantom measurements at tube voltages of 35 kVp and 50 kVp (cf. Fig. 5.1). The theoretical reference values can be found in Hubbell (1969); Berger et al. (2010). Table adapted from Birnbacher et al. (2018c).

material	ρ_e (35 kVp) [e/nm^3]	ρ_e (50 kVp) [e/nm^3]	$\rho_\mathrm{e,theo.}$ [e/nm^3]	μ (35 kVp) [1/cm]	$\mu_\mathrm{theo.}$ (25.0 keV) [1/cm]	μ (50 kVp) [1/cm]	$\mu_\mathrm{theo.}$ (34.5 keV) [1/cm]
LDPE	315.5 ± 0.8	316.2 ± 1.9	315.9	0.296 ± 0.010	0.299	0.231 ± 0.006	0.229
Nylon	377.2 ± 0.8	377.1 ± 1.9	376.0	0.418 ± 0.010	0.410	0.295 ± 0.006	0.291
PEEK	405.9 ± 0.9	405.3 ± 1.9	407.3	0.461 ± 0.009	0.457	0.321 ± 0.006	0.322
POM	451.5 ± 1.1	452.7 ± 2.1	452.3	0.607 ± 0.009	0.603	0.392 ± 0.006	0.390
PMMA	385.8 ± 0.9	385.9 ± 2.1	386.4	0.460 ± 0.010	0.459	0.315 ± 0.007	0.314
Water	333.4 ± 0.8	333.5 ± 2.0	334.2	0.509 ± 0.009	0.508	0.314 ± 0.006	0.313

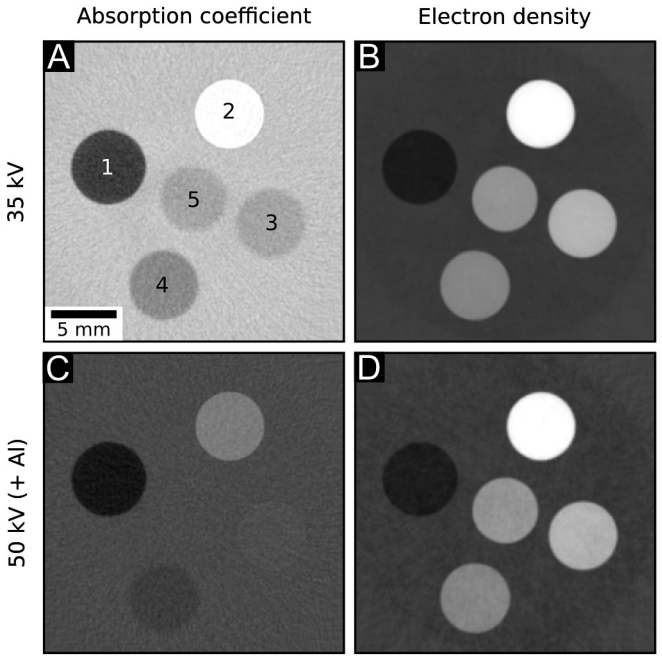

Fig. 5.1 | Results of the phantom measurement at different source spectra. Axial slices of two scans at at 35 kVp and at 50 kVp with an aluminum filter. The phantom consists of five different materials (1: LDPE, 2: POM, 3: PEEK, 4: Nylon, and 5: PMMA) embedded in a water surrounding. The absorption coefficients are displayed on the left and the electron density value on the right. The attenuation coefficient μ is linearly displayed in an interval of $[0.2, 0.6]$ in $1/\mathrm{cm}$ and the electron density ρ_e in an interval of $[300, 450]$ in e/nm^3. Figure adapted from Birnbacher et al. (2018c).

and 50 kVp were performed, the latter with an additional aluminum filter to harden the spectrum. Fig. 5.1 illustrates the corresponding axial slices of the retrieved data. The phantom consists of low-density polyethylene (LDPE), polyoxymethylene (POM), polyetheretherketone (PEEK), Nylon, and polymethylmethacrylate (PMMA), embedded in a water container. In Fig. 5.1 (A) and (C), one observes the different contrast in the attenuation signal, which originates from the energy dependence of the attenuation coefficient. In the attenuation image (C), the contrast between Nylon, PMMA, and the surrounding water is low. The electron density remains however at the same level (cf. Fig. 5.1 B and D). Nylon and PMMA have similar electron density, but both materials can be differentiated in the attenuation signal in Fig. 5.1 (A).

The experimental attenuation coefficients are plotted versus the electron densities in Fig. 5.2 (A) and (B) for both energies to visualize the complementarity of both signals. The distance of the attenuation values to the Compton cross section decreases with increasing energy. Comparing PMMA and PEEK, one can see that the attenuation values are quite similar, especially at 50 kVp.

A quantitative comparison of the obtained data with theoretical values is summarized in Tab. 5.1. The mean and standard deviation of 150×30×30 voxels are compared with the corresponding theoretical values (Hubbell, 1969; Berger et al., 2010). The electron density is calculated according to Eq. (5.6). The effective energies of both scans were determined to $E_{\mathrm{eff},\delta} = 25.7 \pm 0.1\,\mathrm{keV}$ for 35 kVp and $E_{\mathrm{eff},\delta} = 30.0 \pm 0.1\,\mathrm{keV}$ for

50 kVp for the phase-contrast data. For the attenuation contrast data, both effective energies were $E_{\text{eff},\mu} = 25.0 \pm 0.1\,\text{keV}$ for 35 kVp and $E_{\text{eff},\mu} = 34.5 \pm 0.1\,\text{keV}$ for 50 kVp. The composition of the polymers and their mass density are presented in Tab. 5.2. All experimental electron density values with exception of PEEK lie within the range of the standard deviation. The values of PEEK are only slightly off but still below 1% deviation. The same statement can be made for the attenuation coefficients, which show overall good agreement to literature values and other phase-contrast experiments (Sarapata et al., 2014, 2015). The overall electron density resolution is approximately $1.0\,\text{e}/\text{nm}^3$ for the 35 kVp experiment and approximately $2.0\,\text{e}/\text{nm}^3$ for the 50 kVp measurement. Higher total exposure times would increase the electron density resolution (Birnbacher et al., 2016).

5.3.2 Effective atomic number

With the experimental determination of the absorption coefficient and the electron density, it is now possible to extract the effective atomic number Z_{eff} as described by Eq. (5.15). The calculated theoretical values are compared and plotted against the experimental results in Fig. 5.3. The interpolated curves determine the theoretical values for both calibrated effective energies. The experimentally determined ratio of ρ_e/μ is then compared with the interpolated reference data, thereby getting the effective atomic number corresponding to this ratio. The results are summarized in Tab. 5.2. Compared to both provided references, the experimental values lie within the respective standard deviations with exception of LDPE, which is increased. The uncertainty of the calculation of the effective atomic numbers is based on the standard deviation of the attenuation coefficients, the electron density resolution, and the uncertainty of the calibration of the effective energy of 0.1 keV.

In comparison to Ref. 1, the effective atomic numbers deviate slightly (Spiers, 1946). The underlying formula (cf. Eq. 5.16) is however only an empirical approximation and not a ground truth (Taylor et al., 2012). The values provided by Ref. 2 (Nowotny, 1998) were closer to our determined effective atomic numbers for the phantom values.

Tab. 5.2 | Comparison of the determined effective atomic number Z_{eff} with reference values. The theoretical effective atomic numbers of Ref. 1 were calculated from the elemental compositions of the materials according to Eq. (5.16). Ref. 2 is based on Nowotny (1998), the mass density ρ based on the data provided by the manufacturer (Goodfellow Cambridge Ltd.). Nylon is of type 6,6. Table adapted from Birnbacher et al. (2018c).

material	chemical formula	ρ [g/cm^3]	Z_{eff} (ref. 1)	Z_{eff} (ref. 2)	Z_{eff} (25.0 keV)	Z_{eff} (34.5 keV)
LDPE	$[C_2H_4]_n$	0.92	5.44	5.53	5.49 ± 0.10	5.68 ± 0.08
Nylon	$[C_{12}H_{22}N_2O_2]_n$	1.14	6.12	6.21	6.26 ± 0.10	6.26 ± 0.08
PEEK	$[C_{19}H_{12}O_3]_n$	1.30	6.38	6.32	6.38 ± 0.10	6.36 ± 0.08
POM	$[CH_2O]_n$	1.41	6.95	7.03	7.03 ± 0.10	6.98 ± 0.08
PMMA	$[C_5H_8O_2]_n$	1.19	6.47	6.56	6.55 ± 0.10	6.57 ± 0.08
Water	H_2O	1.00	7.42	7.51	7.51 ± 0.10	7.54 ± 0.08

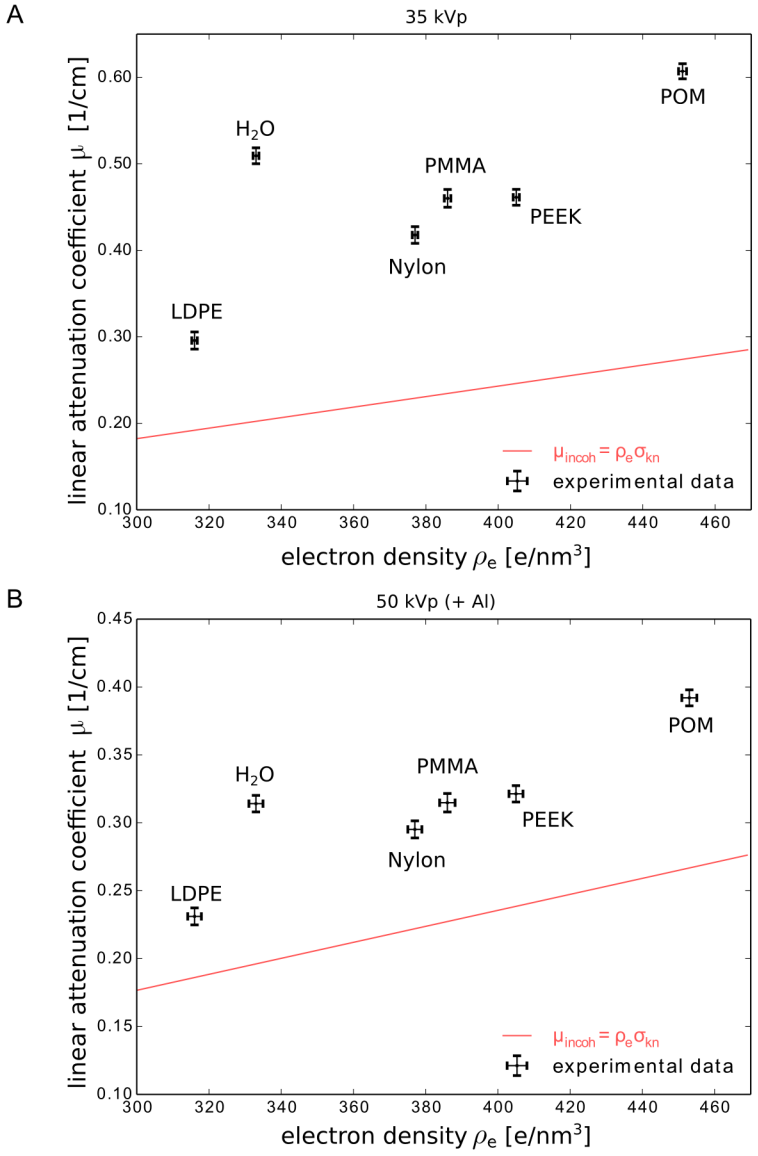

Fig. 5.2 | Total linear attenuation coefficients in dependency of the electron density values. The experimental linear attenuation coefficients μ are plotted against the corresponding electron densities ρ_e obtained from CT measurements at 35 kV (A) and 50 kV (B). Standard deviations are indicated by error bars and the solid line represents the linear attenuation coefficient for Compton scattering μ_{incoh}. Figure adapted from Birnbacher et al. (2018c).

5.3.3 Effect of beam hardening

In a further GBPC-CT experiment, the impact of beam hardening on the quantitative quality of the electron density and effective atomic number was investigated. In order to simulate sufficiently strong beam hardening effects, three different surrounding liquids, namely water, oil, and a 5% sodium chloride (NaCl) solution, were chosen. The measurements were performed at a voltage of 40 kVp, which corresponds to the optimum setup configuration to render the results comparable in best way. The NaCl solution mimics tissue environment with high density like fibrous tissue and the oil

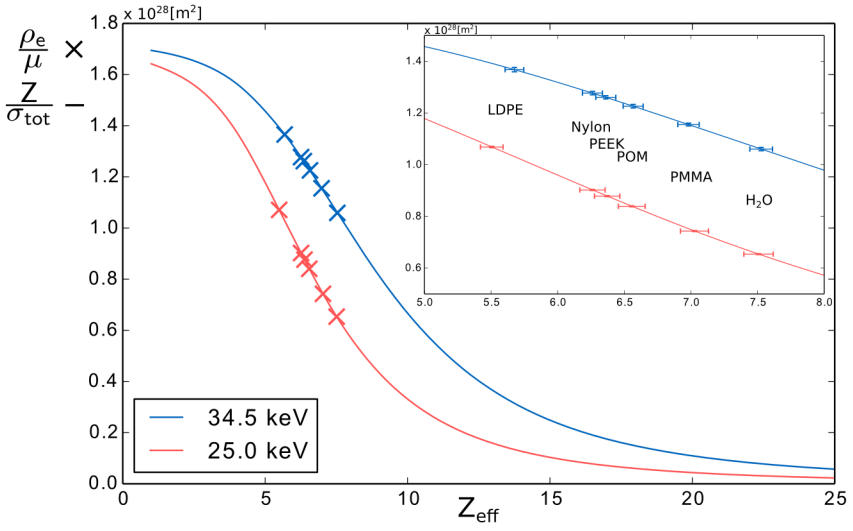

Fig. 5.3 | Determination of the effective atomic number for two different energies. The ratio of the experimentally determined electron density over the linear attenuation coefficient ρ_e/μ of single elements is compared with the interpolated ratio of the atomic number over the total cross section Z/σ_{tot} at two different energies (25.0 keV and 34.5 keV), which were obtained by the effective energy calibration. The colored crosses represent the experimental results from the phantom measurements (cf. Fig. 5.1) plotted against the calculated effective atomic numbers of the respective materials. Figure adapted from Birnbacher et al. (2018c).

is used to represent adipose tissue (Woodard and White, 1986). The phantom itself consists of four Eppendorf tubes filled with water, blood, a 5% water sodium chloride (NaCl) solution, and oil, as the GBPC-CT setup is intended for biomedical research. For calibration, three PMMA rods were added.

Figure 5.4 (A)-(C) shows three different axial slices of the electron density ρ_e and the corresponding slices of the effective atomic number Z_{eff} (cf. Fig. 5.4 D-F), which was determined as described in the previous section (cf. Sec. 5.3.2). The PMMA rods were used to determine an effective energy in all three data sets. The determined effective energies and electron density results are summarized in Tab. 5.3, the effective atomic

Tab. 5.3 | Relative comparison of the electron density of the liquids phantom in dependence of different surrounding liquids at 40 kVp. Results of three phantom measurements with different surrounding liquids. With exception of PMMA and water, no absolute reference values are given (cf. Tab. 5.1). Table adapted from Birnbacher et al. (2018c).

surrounding liquid		water	oil	5 % NaCl
$E_{\text{eff},\mu}$	[keV]	27.2 ± 0.1	27.1 ± 0.1	27.6 ± 0.1
$E_{\text{eff},\delta}$	[keV]	27.0 ± 0.1	26.9 ± 0.1	27.3 ± 0.1
1 - PMMA	[ρ_e in e/nm^3]	386.2 ± 1.0	386.4 ± 1.0	385.9 ± 1.6
2 - blood	[ρ_e in e/nm^3]	354.0 ± 1.0	355.1 ± 0.9	353.7 ± 1.1
3 - water	[ρ_e in e/nm^3]	333.9 ± 1.0	333.8 ± 0.9	334.2 ± 1.0
4 - 5% NaCl	[ρ_e in e/nm^3]	343.0 ± 1.0	344.3 ± 0.8	342.4 ± 1.5
5 - oil	[ρ_e in e/nm^3]	305.9 ± 0.9	305.1 ± 1.0	307.4 ± 1.0

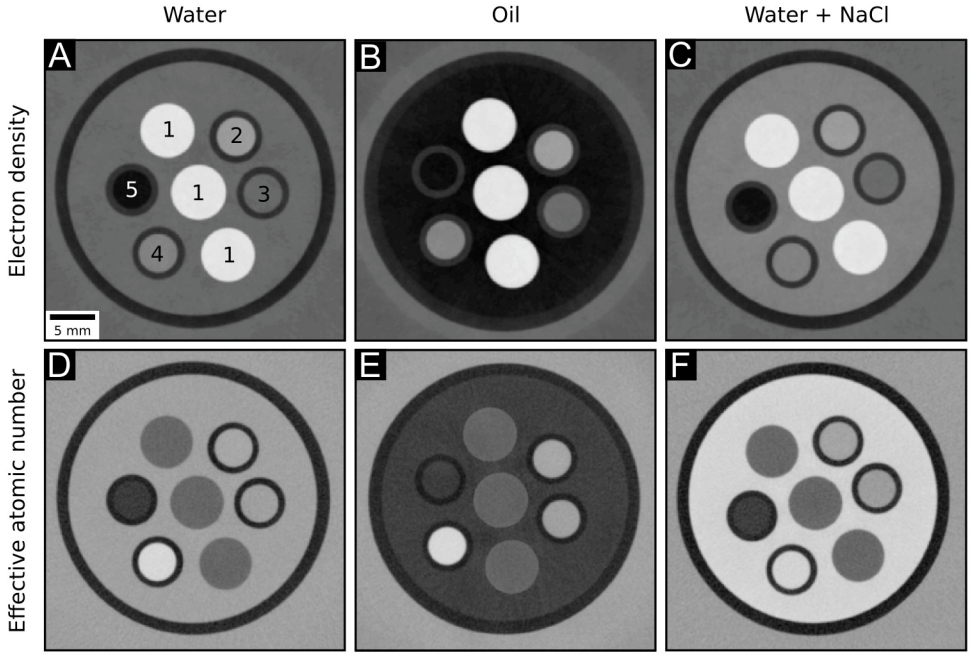

Fig. 5.4 | Beam hardening experiments. Electron density and effective atomic numbers of a phantom measurements with different surrounding liquids are visualized to study the effect of the polychromatic X-ray spectrum on the determination of the effective energy due to beam hardening. The top row represents the electron density, the bottom row the effective atomic numbers. The tube voltage was 40 kVp. Subfigures (A) and (D) show axial slices of the phantom immersed in water, subfigures (B) and (E) the same phantom in oil, and subfigures (C) and (F) the phantom in the 5% NaCl solution. The components and results of the phantom are listed in Tab. 5.3 and 5.4. The electron density ρ_e is displayed linearly in an interval of $[300, 400]$ in $\mathrm{e/nm^3}$ and the effective atomic number Z_eff in an interval of $[5, 9]$. Figure adapted from Birnbacher et al. (2018c).

number Z_eff in Tab. 5.4.

As one would expect due to beam hardening, the effective energy increases slightly from oil (27.1 keV) over water (27.2 keV) to the NaCl solution (27.6 keV). The effective energy of the attenuation contrast $E_{\mathrm{eff},\mu}$ is higher in comparison to the effective energy of the phase-contrast $E_{\mathrm{eff},\delta}$ (cf. Tab. 5.3), which originates in the different dependencies of the signals on e.g. the spectrum, filter, or the setup design for the phase-contrast signal. However, the effective energies for both modalities are quite similar, which can be explained by the way of effective energy determination. The position and the material type are essential for the effective energy determination, which is here the PMMA rod in the center of the tube. Less attenuating materials in the outer part of the tube suffer more from beam hardening. In the case of oil as surrounding liquid, the effect of beam hardening was so strong that polynomial beam hardening correction as presented in Herman (1979) had to be used.

Comparing the electron density results in Tab. 5.3, the absolute values for water and PMMA are in good agreement with reference values (cf. Tab. 5.1) and the relative differences in liquids lie within the range of the noise except for the blood and NaCl in the oil surrounding solution as well as the NaCl in the NaCl surrounding solution.

But the maximum deviation of the electron density is still below 1 %. The electron density resolution determined in the PMMA rods is ranging from 1.0 to 1.6 e/nm^3.

Regarding the effective atomic number, the absolute effective atomic numbers for PMMA and water are in good agreement in comparison to Tab. 5.2. Comparing the different surrounding liquids, all results of the effective atomic number lie within the respective standard deviation except for the NaCl combination. However, beam hardening correction or sufficiently strong filtering from the surrounding liquids water and the NaCl solution was necessary. Otherwise, strong streaks and cupping artifacts would appear and limit the use of the approach.

5.4 Conclusion

In this chapter, the effective atomic number determination with a laboratory GBPC-CT setup with a single tomographic scan is illustrated. The quantitative results of the electron density and the effective atomic number turned out to be reliable in the investigated energy range. The possibility to perform reproducible quantitative tomographic phase-contrast scans was demonstrated and is in good agreement with several preclinical studies (Saam et al., 2013; Hetterich et al., 2014; Grandl et al., 2014; Fingerle et al., 2014). The variation of effective atomic numbers for oil shows that a certain level of filtering of the spectrum or beam hardening correction is necessary to obtain reliable values. The electron density varies only marginally for different surrounding liquids and is not as prone to beam hardening as the attenuation coefficient.

In comparison to related work, one needs only a single calibration for the effective energy. Qi et al. (2010) used multiple material calibration neglecting the coherent part of the cross section σ_{coh}. Moreover, the used exponential fit depends on the quality of reference effective atomic numbers, which can limit the precision of the method. In addition to Willner et al. (2013), this chapter shows that the approach also works with polychromatic X-ray sources. In comparison to DECT, GBPC-CT does not need complex calibration to access the electron density and the effective atomic number. However, GBPC-CT is still at an experimental level and not already clinically implemented like DECT. Furthermore, the polychromatic GBPC-CT experiments shown here have only been investigated for energies up to 50 kVp and for materials with low atomic number ($Z_{\text{eff}} \leq 8$).

Tab. 5.4 | Relative comparison of the effective atomic number of the liquids phantom in dependence of different surrounding liquids at 40 kVp. With exception of PMMA and water, no absolute reference values are given (cf. Tab. 5.2). Table adapted from Birnbacher et al. (2018c).

surrounding liquid		water	oil	5 % NaCl
1 - PMMA	$[Z_{\text{eff}}]$	6.58 ± 0.07	6.55 ± 0.06	6.58 ± 0.08
2 - blood	$[Z_{\text{eff}}]$	7.61 ± 0.06	7.61 ± 0.06	7.58 ± 0.07
3 - water	$[Z_{\text{eff}}]$	7.49 ± 0.08	7.50 ± 0.06	7.47 ± 0.07
4 - 5% NaCl	$[Z_{\text{eff}}]$	8.37 ± 0.07	8.38 ± 0.06	8.30 ± 0.07
5 - oil	$[Z_{\text{eff}}]$	5.92 ± 0.09	5.97 ± 0.08	5.98 ± 0.09

Future work in the direction of quantitative GBPC-CT will include investigation of the electron density and the effective atomic number at higher polychromatic energies increasing the range of application for larger samples. Moreover, the implementation of spectral detectors could allow to improve the performance of the method by reducing beam hardening artifacts and avoid effective energy calibration.

CHAPTER 6

Tilted grating PC-CT

Short summary

This chapter describes the effect of the grating orientation on GBPC-CT imaging with respect to image quality. Thereby, the sensitivity of DPC projections depends on the orientation of the usually one-dimensional grating structures, which can be modified by tilting the gratings. First, two-dimensional phase-integration and subsequent filtered backprojection tomographic reconstruction with tilted gratings is presented. This analytical approach however revealed difficulties occurring at the laboratory GBPC-CT setup used here. A combination of tilted gratings with statistical iterative reconstruction (SIR) is investigated in this chapter to overcome the limitations of the analytical method. The main results of this chapter are published in Birnbacher et al. (2018b).

6.1 Introduction

A method to improve the quality of tomographic data in GBPC-CT is the implementation of tilted gratings. With this approach, the full two-dimensional differential phase-contrast (DPC) information can be utilized to reduce streak artifacts, which are comparable to metal artifacts occurring in conventional computed tomography.

Current gratings are usually line gratings with one-dimensional phase-sensitivity and are only sensitive to changes in the DPC signal perpendicular to the orientation of the grating lines. Different ideas to access the full DPC signal have been proposed. One idea is to utilize two-dimensional phase gratings (Zanette et al., 2010). This approach is limited by the achievable grating fabrication quality and the required two-dimensional phase-stepping procedure. Single-shot methods on the other side imply reduced spatial resolution (Wen et al., 2010; Itoh et al., 2011).

A different method using the line gratings is to perform two DPC scans of an object, which is rotated by $\pi/2$ after the first scan. Subsequent phase-integration of both DPC scans leads to the full two-dimensional phase information (Kottler et al., 2007a; Arnison et al., 2004), which shows artifact reduction and additional direction-sensitive features (Scherer et al., 2014). The resulting phase projections could be used for phase-contrast tomography, but the rotation of the sample or respectively the interferometer is experimentally difficult and causes additional mechanical movement reducing the phase-contrast sensitivity.

Tilting the gratings by $\pi/4$ with respect to the optical axis and performing phase-contrast tomography with additional processing allows to access two-dimensional phase-contrast tomograms. The results, which were first produced at a synchrotron facility, show an overall improvement of the phase-contrast tomogram including reduced streak artifacts (Rutishauser et al., 2011).

Translating this approach from synchrotron to laboratory GBPC-CT setups is of limited feasibility due to the cone beam geometry, as two opposing DPC projections are not matched anymore. Moreover, the necessary rotation of the DPC projections includes additional interpolation steps and the method is not robust to a non-perfectly aligned rotation axis.

A novel approach investigated in this chapter to access the full phase-contrast information is tilting the gratings in combination with a statistical iterative reconstruction (SIR). In more detail, the DPC projections are measured as with conventional GBPC-CT setups as solely the gratings are tilted by $\pi/4$ with respect to the tomographic axis around the optical axis. Instead of the additional processing outlined above in the analytic approach, the SIR algorithm is used with adapted direction of the derivative operator. This is achieved by replacing the horizontal derivative operator with an operator working in diagonal direction. The full 360° DPC projections are reconstructed without any further adaptations.

In the following part of this chapter, the directional dependency of the sensitivity is presented followed by an explanation of the analytical approach using two-dimensional phase-integration and filtered backprojection tomographic reconstruction. Next, the SIR-based GBPC-CT approach with tilted gratings is outlined and the main results are discussed. The achieved results show a significant quality improvement of the phase-contrast tomogram in comparison to the conventional GBPC-CT configuration.

6.2 Sensitivity direction

The refraction angle is in general a two-dimensional quantity and related to the gradient of the phase via $\tan\alpha = \left|\frac{1}{k}\nabla\Phi\right|$, as shown in Sec. 2.3. With the use of line gratings, only a component of the refractive angle or correspondingly of the DPC signal can be retrieved. In order to obtain a DPC signal, at least a component of the DPC signal parallel to the grating lines is needed to induce a lateral phase shift of the interference pattern. Structures oriented perpendicularly to the grating lines cannot be visualized.

The conventional GBPC-CT setup configuration is depicted in Fig. 6.1 (A), where the grating lines are oriented in parallel to the tomographic axis. Regarding the sensitivity direction, an object causes the same signal independently of the tomographic angle, but a purely horizontal structure would be missed. In contrast, the combination of a 45°-tilt of the gratings and tomography enables to measure complementary DPC signals as illustrated in Fig. 6.1 (B).

For better visualization, the DPC signals of a phantom consisting of PMMA (polymethylmethacrylate) rods oriented in vertical, horizontal, and diagonal direction were measured at 0° and 180° sample rotation (cf. Fig. 6.2). In Fig. 6.2 (A) and (B) only vertical components of the phantom can be observed. The vertical and diagonal part of the object are visualized, but the horizontal part is missed. In contrast to that, Fig. 6.2 (C) and (D) present a different situation with the tilted grating configuration. The image content is varying in those DPC projections. The vertical and horizontal components of the phantom are seen at both orientations, as both structures have components parallel grating orientation. However, the diagonal phantom part is missed in Fig. 6.2 (C), since the structure component is perpendicular to the grating orientation,

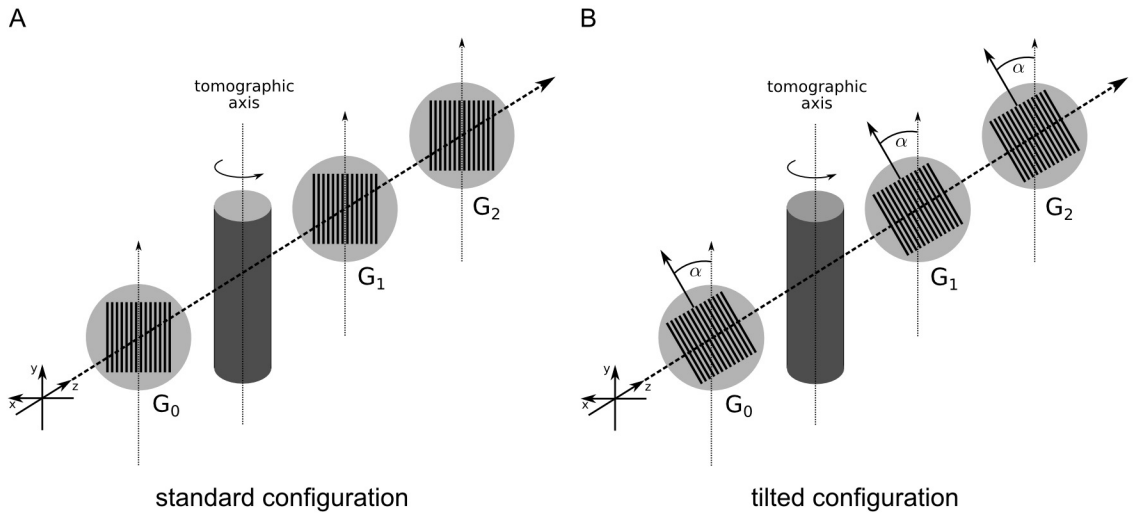

Fig. 6.1 | Laboratory GBPC-CT set-up with different grating orientations. Subfigure (A) shows the conventional Talbot-Lau interferometer with the grating lines in parallel to the tomographic axis. Subfigure (B) shows the tilted grating configuration with a rotation of the grating lines by $\pi/4$ with respect to the optical axis. The sample is indicated as a gray cylinder centered around the tomographic axis. The three gratings are the source grating G_0, the phase grating G_1, and the analyzer grating G_2. X-ray source and detector are not shown in this figure. Figure adapted from Birnbacher et al. (2018b).

and fully visible in Fig. 6.2 (D) because the phantom structure is in parallel to the grating lines. Regarding all projection angles, the DPC information is complementary in the tilted grating approach, whereas in the standard configuration, the directional sensitivity of the DPC signal stays constant.

6.3 Phase integration and filtered backprojection

The analytical method to utilize the full phase-gradient information in tomography is based on two-dimensional phase integration and subsequent filtered backprojection with a standard filter kernel (Rutishauser et al., 2011). A full tomographic scan is performed in tilted grating configuration over a sample rotation of 360°. The processing of the phase-stepping data to obtain DPC projections φ does not differ from the setup configuration with normal grating orientation.

6.3.1 Two-dimensional phase integration

For phase-integration, two opposing DPC projections $\varphi(0)$ and $\varphi(\pi)$ with gradients in diagonal direction are combined to form two DPC projections with gradients in horizontal and vertical direction

$$\varphi_{\mathrm{x}}(0) = \frac{\varphi(0) - \varphi(\pi')}{2\cos\alpha} \tag{6.1}$$

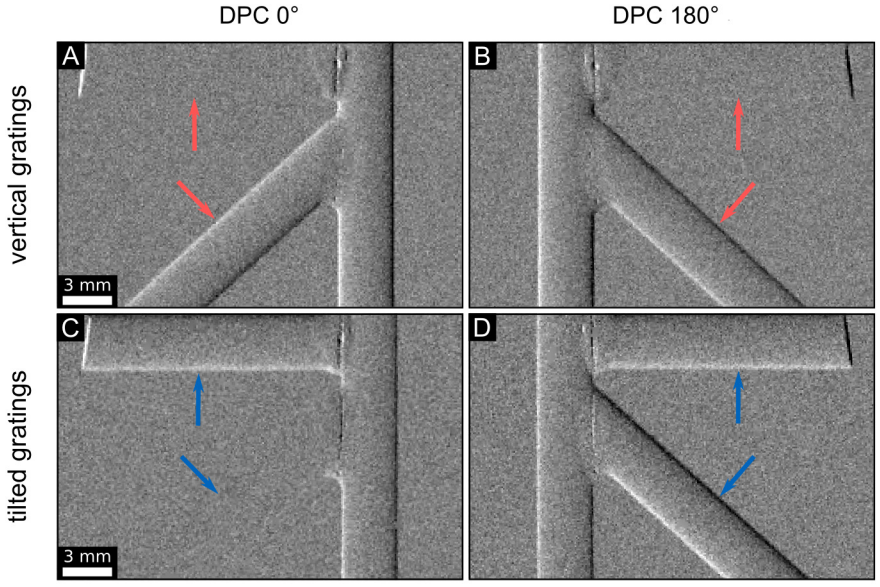

Fig. 6.2 | Experimental DPC projections illustrating the directional dependency of the DPC signal sensitivity. The projections in the top row were measured with the vertical grating configuration, the bottom row with tilted gratings. Subfigures (A) and (C) depict the DPC signal of the phantom at $0°$. Subfigures (B) and (D) show the same sample at $180°$ sample rotation with respect to the tomographic axis. The DPC signal of the full phantom shape is represented by subfigure (D). The colored arrows mark typical differences in sensitivity at the same rotational position arising from the different grating orientation. Both opposing DPC projections $\varphi(0)$ and $\varphi(\pi)$ of the phantom were determined with 11 phase-steps and 5 s exposure time per phase-step. The phantom was immersed in a water container to reduce phase-wrapping artifacts. The gray scale of the lateral phase shift of the interference pattern φ is in the linear range of $[-0.4, 0.4]$. Figure adapted from Birnbacher et al. (2018b).

and

$$\varphi_{\mathrm{y}}(0) = \frac{\varphi(0) + \varphi(\pi')}{2\sin\alpha}, \tag{6.2}$$

with $\varphi(\pi')$ being the horizontally flipped version of $\varphi(\pi)$ (Rutishauser et al., 2011). With two opposing phase-gradients φ_{x} and φ_{y}, one can calculate the two-dimensional phase Φ' using Fourier transform $\mathcal{F}$

$$\Phi'(x,y) = \mathcal{F}^{-1}\left\{\frac{\mathcal{F}\left\{\varphi_{\mathrm{x}} + i\varphi_{\mathrm{y}}\right\}(k,l)}{2\pi i(k+il)}\right\}(x,y), \tag{6.3}$$

where k and l denote the Fourier frequencies (Kottler et al., 2007a). The algorithm used here to reduce edge discontinuity in phase integration via Fast Fourier Transform (FFT) with image mirroring is outlined in Arnison et al. (2004).

The reconstruction of the phase projections over $180°$ is done with conventional filtered backprojection using a Ram-Lak filter. To access the quantitative phase Φ instead of the integrated lateral phase-shift of the interference pattern Φ', one needs to include Eq. (2.55) leading to

$$\Phi(x,y) = \frac{p_2}{\lambda d}\Phi'(x,y), \tag{6.4}$$

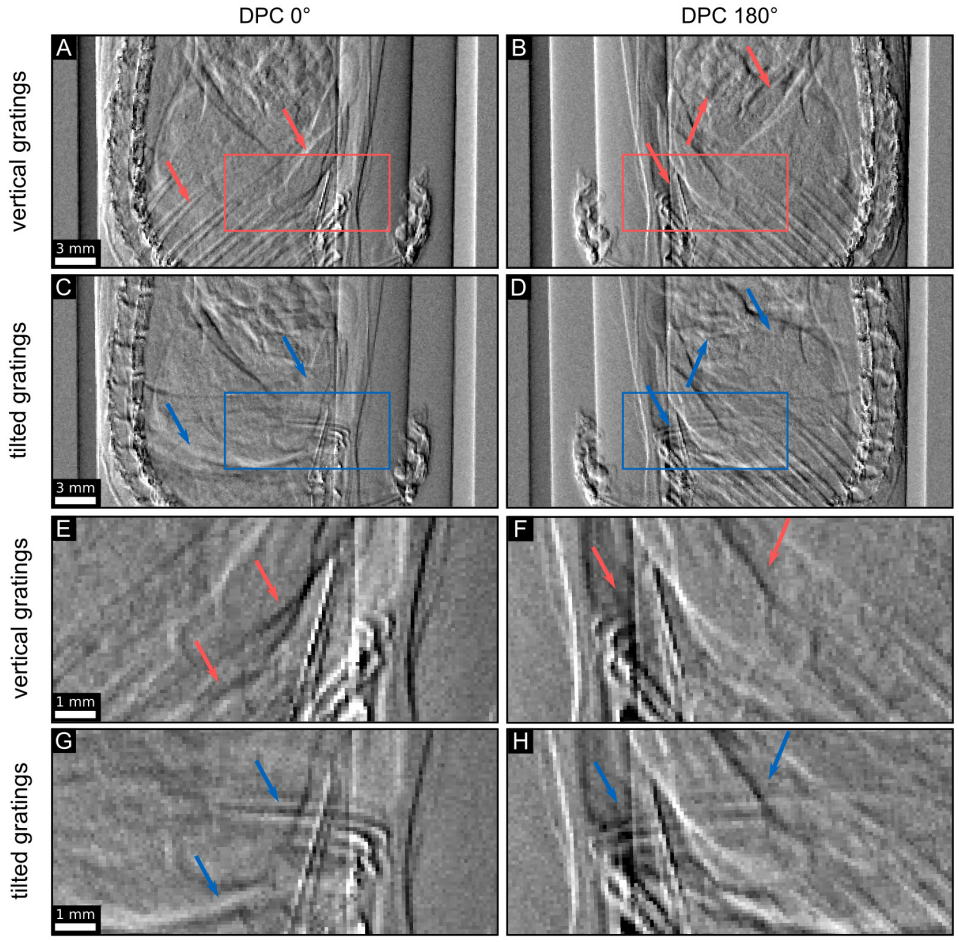

Fig. 6.3 | Comparison of DPC projections with tilted and normal grating orientation of a mouse sample. Subfigures (A) and (C) depict the DPC signal of the mouse at rotation angle $0°$, subfigures (B) and (D) represent the same sample at the opposing $180°$ sample position. The colored arrows mark conspicuous differences at the same rotational position like ribs or intestines. Subfigures (E) - (H) represent magnifications of the respective rectangles in subfigures (A) - (D). The scale of φ is linearly displayed in an interval of $[-0.4, 0.4]$. Figure adapted from Birnbacher et al. (2018b).

with the geometrical parameter d, the analyzer grating period p_2, and the wavelength λ.

6.3.2 Results and discussion

To showcase tilted grating GBPC-CT, a measurement of a mouse sample is presented. The object was measured in two configurations, first with the standard vertical grating configuration as visualized in Fig. 6.1 (A), and with the tilted grating configuration with a tilt angle of $\alpha = \pi/4$ as illustrated in Fig. 6.1 (B). The sample position was unchanged during this experiment as only the gratings were rotated. Moreover, the scan parameters were identical in both cases, namely 11 phase-steps, 5 s exposure time per phase step, and 1200 projection angles. The object was placed in a plastic container filled with formalin solution. For the determination of the DPC projections,

identical processing algorithms were used.

Resulting DPC projections by way of example are depicted in Fig. 6.3. The colored arrows mark visible differences in the different DPC projections. In Fig. 6.3 (A), the ribs are clearly evident, but cannot be resolved in Fig. 6.3 (C) with the tilted configuration. However, Fig. 6.3 (D) provides DPC information in horizontal direction that would be otherwise lost in the conventional configuration (cf. Fig. 6.3 B).

With the tilted projections, it is now possible to calculate the DPC projections with gradient in vertical and horizontal direction as shown in Fig. 6.4 (A) and (B). The DPC projection φ_{x} with tilted gratings should be the same as the DPC projection φ with vertical gratings (cf. Fig. 6.3 A), but the quality of the projections φ_{x} and φ_{y} is limited. The calculated one-dimensional phase-integration of the φ_{x} projection causes pronounced streaks (cf. Fig. 6.4 C). The two-dimensional phase-integration according to Eq. (6.3) allows to reduce significantly the streak artifacts combining both the projections φ_{x} and φ_{y} (cf. Fig. 6.4 D).

The tomographic reconstructions of the one-dimensional phase, the two-dimensional phase – both based on the tilted grating data – and the conventional DPC data with vertical gratings are shown in Fig. 6.5. Comparing the exemplary tomographic slices, the images acquired with tilted gratings have increased blur. However, it is obvious, that the two-dimensional phase-contrast data reduces the streak artifacts in the sagittal slices. In order to investigate if this effect originates from interpolation, the tilted grating phase-contrast signal based only on the φ_{x} data is also shown (cf. Fig. 6.5 B and E). Due to the combination of two opposing DPC projections, the phase reconstruction is performed only over 180°. This can be observed in the streaks in the axial slices of both tilted grating slices marked by the arrows with asterisks (cf. Fig. 6.5 B and C).

Additionally, quantitative values in a volume of $20\times20\times20$ voxels in the PMMA rod, the white disc in Fig. 6.5 (A)-(C), were compared. The mean and standard deviation of the phase in the normal configuration were $(5.12\pm0.07)\times10^{-2}$, for the phase-contrast data in tilted calculated in one-dimension $(4.27\pm0.07)\times10^{-2}$, and $(4.70\pm0.03)\times10^{-2}$ for the tilted phase-contrast data calculated by two-dimensional phase integration.

Difficulties using a laboratory GBPC-CT setup

The analytical approach was demonstrated at a synchrotron facility with parallel beam geometry and showed beneficial results for GBPC-CT (Rutishauser et al., 2011). At the GBPC-CT setup presented in this work however, one has to deal with cone beam geometry. The beam divergence is approximately 11 mrad with 30 mm sample diameter at a distance of 1370 mm away from the source. Sample features at off-center position with respect to the tomographic axis have different magnifications, which renders the matching of the two opposing DPC projections $\varphi(0)$ and $\varphi(\pi)$ inaccurate or even impossible. This is illustrated by the mismatch of the vertical tube edges in the DPC projection φ_{y} of the mouse sample marked by the top right arrow in Fig. 6.4 (B).

The analytical method has moreover increased requirements of the axis alignment accuracy and deviations need to be corrected by rotating the projection axes. The matching of the projections to form the two DPC projections is done with the attenuation images. If the sample attenuation is weak which is often the case in phase-contrast imaging of soft tissue or the sample magnification is too strong, the matching

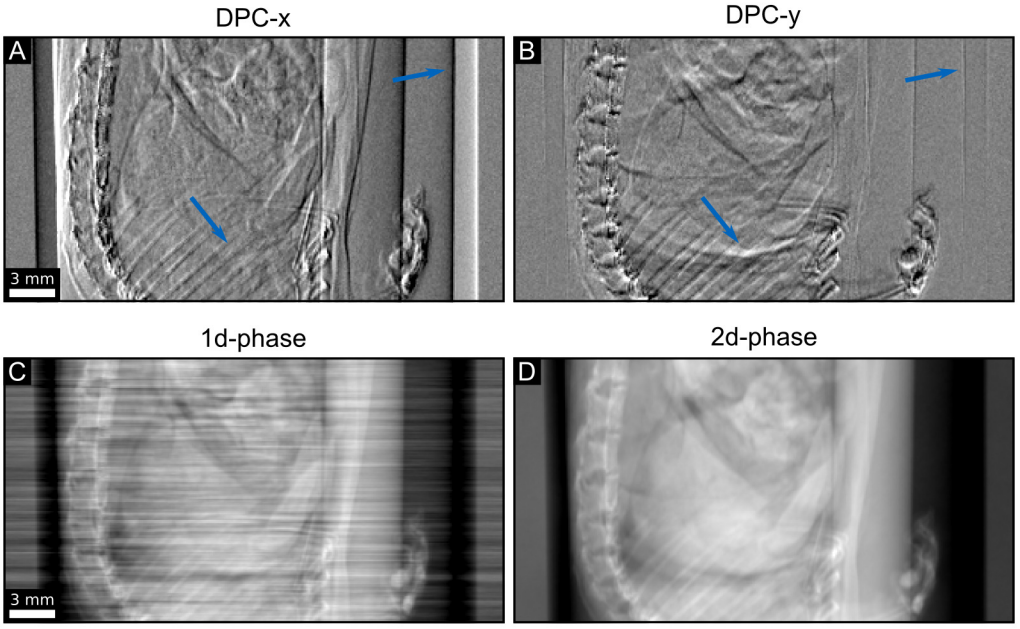

Fig. 6.4 | Tilted gratings DPC and phase projections of a mouse sample. The top row shows the two DPC gradients calculated according to Eqs. (6.1) and (6.2). Subfigure (A) shows the projection φ_x with gradient in x-direction, as can be seen by the vertical structures. Subfigure (B) visualizes the projection φ_y with gradient in vertical direction. Using one-dimensional phase-integration leads to the phase-projection in subfigure (C). Performing two-dimensional phase-integration (cf. Eq. 6.3) of the DPC projections with gradients in vertical and horizontal direction leads to subfigure (D). The scale of φ is linearly displayed in an interval of $[-0.6, 0.6]$, the phase Φ' in a linear range of $[-6.0, 6.0]$.

algorithm is prone to fail. The matching of the mouse sample was only possible due to the good attenuation of the bones and the edges of the Falcon tube. Matching of the PMMA rod as depicted in Fig. 6.2 to form the projections φ_x and φ_y in contrast was not possible. Also, a rotation of the projection reduces the spatial resolution due to interpolation caused by the numerical rotation.

An additional practical problem is the limitation of the phase data to 180 degrees, which reduces the accuracy of the determination of the center of rotation necessary for reconstruction and reducing the quality of the quantitative data. A reduction of noise could however be observed.

6.4 Statistical iterative reconstruction approach

The combination of statistical iterative reconstruction with tilted gratings is possible by adapting the derivative direction of the SIR algorithm for DPC imaging. The SIR algorithm is based on a maximum a-posteriori using statistical properties of the projection data and enforcing prior knowledge, as described in Sec. 2.4.2. In detail, the cost function as stated in Eq. (2.87) is minimized

$$\mathrm{L} = \left\| \nabla \mathrm{A}\mathbf{f} - \mathbf{p} \right\|_{\mathbf{w}}^2 + \lambda \mathrm{R}_\gamma(\mathbf{f}), \tag{6.5}$$

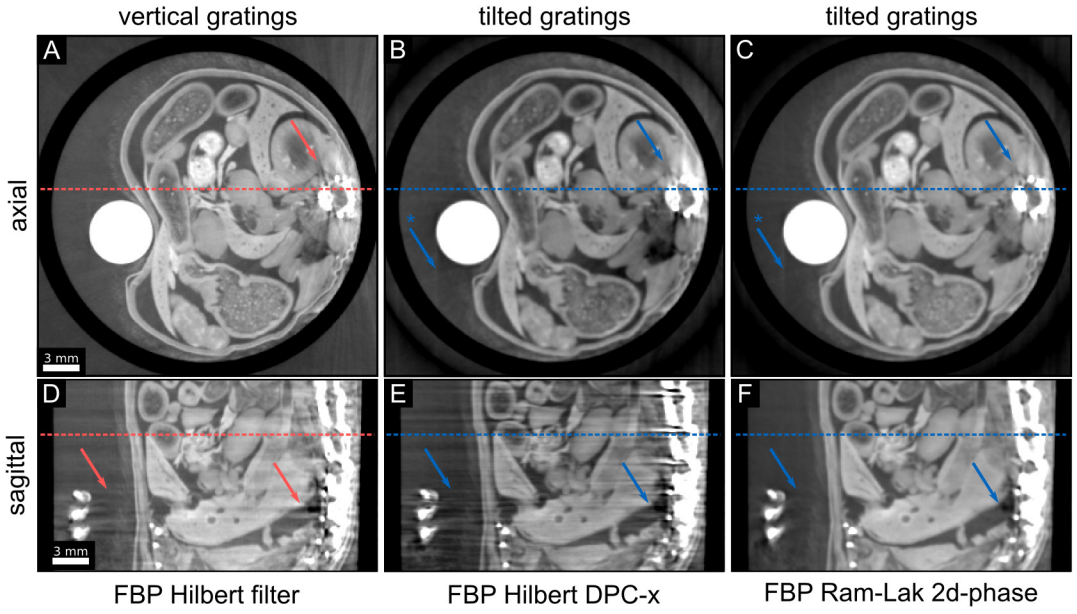

Fig. 6.5 | Comparison of phase-contrast tomograms with tilted and normal grating orientation using the analytical approach. The left column represents conventional phase-contrast results with vertical grating orientation, the other two columns show data measured with tilted grating orientation. The dashed lines represent the corresponding axial or sagittal slices, the arrows mark specific differences in the data. The phase Φ is displayed in a linear range of $[-0.01, 0.03]$.

with $\mathbf{p}$ being the retrieved DPC projections, A being the forward projection system matrix, and $\mathbf{f}$ being the reconstructed tomographic volume. The variances of the projection data $\mathbf{w}$ are calculated by least-squares processing of the raw projections (Hahn et al., 2015) and $\lambda \mathrm{R}_\gamma(\mathbf{f})$ represents the Huber regularization with parameters λ and γ constraining the ill-posed reconstruction problem. In this work, the derivative operator ∇ for the conventional SIR algorithm with horizontal DPC gradient direction is chosen to be a convolution of the data with

$$\nabla_{\mathrm{horiz}} = \begin{bmatrix} -1 & +1 \end{bmatrix}. \tag{6.6}$$

The diagonal derivative operator ∇_{diag} for the two possible tilted grating configurations with an angle of $\alpha = \pm\pi/4$ is the so-called Roberts cross operator formulated as

$$\nabla_{\mathrm{diag}} = \frac{1}{\sqrt{2}} \begin{bmatrix} 0 & +1 \\ -1 & 0 \end{bmatrix} \quad \text{and} \quad \frac{1}{\sqrt{2}} \begin{bmatrix} +1 & 0 \\ 0 & -1 \end{bmatrix}. \tag{6.7}$$

In principle, other tilt angles can be utilized, but the optimum signal complementarity is achieved at $\alpha = \pi/4$. In this reconstruction procedure, a limited-memory Broyden-Fletcher-Goldfarb-Shanno (L-BFGS) algorithm is employed (Nocedal, 1980; Okazaki and Nocedal, 2010) until the difference of 20 consecutive iterations was less than 1×10^{-3}, as used in Sun et al. (2015). The regularization threshold parameter γ was fixed in both reconstructions ($\gamma = 10^{-3}$) to enforce a comparable edge-sharpness and the regularization strength λ was adapted individually ($\lambda_{\mathrm{vertical}} = 1.5 \times 10^{-1}$ and

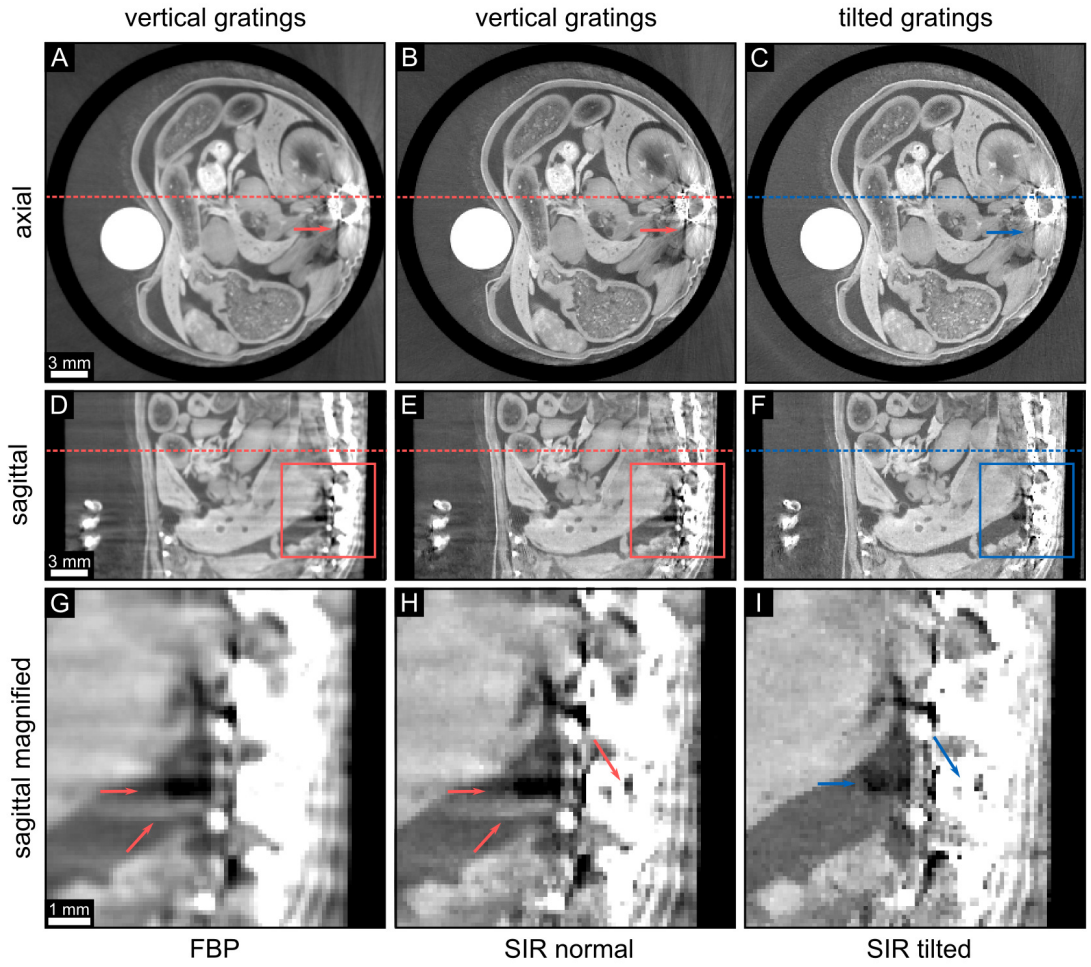

Fig. 6.6 | Comparison of phase-contrast tomograms with tilted and normal grating orientation and different reconstruction methods. Exemplary tomographic slices of the same mouse sample from Fig. 6.5 are shown. The left column shows the conventional FBP reconstruction of the GBPC-CT data with vertical gratings in axial (A) and sagittal slices (D) and (G). The middle column visualizes the same data set reconstructed with the SIR algorithm with vertical gratings. The right column depicts the adapted SIR data set compatible to tilted grating orientation. Magnification of the marked rectangles in the sagittal slices of subfigures (D),(E), and (F) is depicted in the bottom row. There, the arrows mark particular differences in the corresponding sagittal slices. The dashed lines indicate the corresponding axial or sagittal slice. All phase-contrast values Φ are ranged in a linear scale of $[-0.01, 0.03]$. Figure adapted from Birnbacher et al. (2018b).

$\lambda_{\text{tilted}} = 3.0 \times 10^{-3}$) to reach an overall comparable noise level in the image. Both regularization parameters were chosen empirically.

6.4.1 Results and discussion

In order to compare the FBP and the SIR algorithm, the DPC projections with the standard grating configuration were reconstructed with filtered backprojection using the Hilbert filter (cf. left column in Fig. 6.6) and the SIR algorithm with the horizontal gradient ∇_{horiz} (cf. middle column in Fig. 6.6). Both data sets show similar horizontal

streaks in sagittal view. The input data for both reconstructions was identical.

The tilted grating SIR tomographic data of the measurement with tilted gratings is depicted in the right column in Fig. 6.6. Comparing all axial slices, visible differences in the axial slices include less pronounced streaks emerging from the mouse spine in the tilted phase-contrast data (cf. Fig. 6.6 A-C). In the sagittal slices however, the differences are more distinct as the horizontal streaks from the mouse spine are strongly reduced in the tilted data set (cf. Fig. 6.6 D-F). Magnifications of the areas framed in Fig. 6.6 (D)-(F) are displayed in the bottom row of Fig. 6.6 and illustrate the differences even more. The colored arrows mark exemplary differences between the sagittal slices. In Fig. 6.6 (I), the data is smooth and almost artifact free in contrast to the additional bright or dark structures in the non-tilted phase-contrast slice (cf. Fig. 6.6 G and H).

The empirical determination of the regularization parameters in iterative reconstruction limits the feasibility of a noise analysis as the regularization strength λ was chosen individually. But the noise of the phase-contrast signal Φ was calculated with the same parameter γ for both SIR reconstructions in a volume of $20 \times 20 \times 20$ voxels in the PMMA rod, the white circle in Fig. 6.6 (A)-(C). For the normal configuration the noise was 6.93×10^{-4} and for the tilted configuration the noise value was 6.86×10^{-4}. The average phase-contrast signal Φ in the same volume as before equals 5.13×10^{-2} for the FBP, 5.14×10^{-2} for the normal SIR, and 5.22×10^{-2} for the tilted SIR reconstruction. This signifies that the GBPC-CT data remains quantitatively reliable when the tilted grating approach is applied. Slight differences in quantitative values, which improve the quality of the quantitative data, can be explained by the reduced streak artifacts and the non-identical input data. The gained phase-contrast signal Φ, the refractive index decrement δ, and the electron density ρ_e can be determined as described in Ch. 5.

In Fig. 6.7 (A) and (C), the difference images between the SIR and the FBP tomograms in vertical configuration allow to assess the effect of SIR in comparison to FBP. The resulting differences are small and mainly limited to sharpness at the edges. The difference images in Fig. 6.7 (B) and (D) visualize strong streaks between SIR of vertical and tilted grating configuration. Interestingly, no additional significant features could be observed in the slices when comparing tilted with non-tilted data. Solely minor differences at feature borders can be observed (cf. Fig. 6.7). The reason for this lies in the cone beam perspective. In the case of vertical grating orientation, the cone beam perspective of horizontal features changes for different tomographic angles allowing to detect also vertical components of the horizontal features. In comparison to the tilted-grating configuration, horizontal features are also not missed completely. Additionally, the sample does not provide purely horizontal features. In the case of parallel beam geometry, additional features should be observed when comparing tilted and non-tilted grating configuration Rutishauser et al. (2011).

6.5 Conclusion

Tilting the gratings by $\pi/4$ around the optical axis in combination with GBPC-CT improves the quality of phase-contrast tomograms as the extent of streak artifacts is considerably reduced. The experimental realization is simple since only the gratings

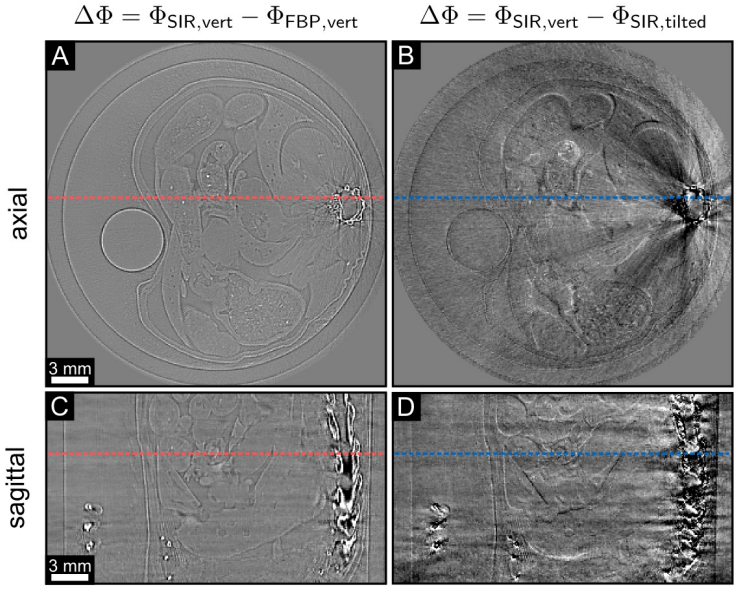

Fig. 6.7 | Difference images between different phase-contrast tomograms. The left column shows the differences between the FBP and the SIR algorithm with vertical gratings in axial (A) and sagittal view (C). The right column shows the differences of the phase-contrast tomograms of the vertical and the tilted grating configuration with SIR, both in axial (B) and sagittal view (D). The slices are the same as depicted in Fig. 6.6. The dashed lines indicate the corresponding axial or sagittal slice. All phase-contrast values Φ are ranged in a linear scale of $[-0.01, 0.01]$. Figure adapted from Birnbacher et al. (2018b).

have to be rotated. The measurement schematic and processing does not differ from GBPC-CT with normal grating orientation, especially the duration of the tomographic scan is unchanged.

Statistical iterative reconstruction offers several benefits in contrast to FBP. The iterative approach uses statistical information and is robust when projections are corrupt signifying a possible reduction of necessary projections (Hahn, 2014). The implementation of the diagonal derivative operator into the SIR framework is straightforward if the framework already exists. Solely the diagonal derivative operator has to be replaced by the horizontal derivative operator. The major disadvantage of tilted SIR is the longer reconstruction time in comparison to FBP and the empirical reconstruction parameter determination.

In contrast to the analytical tilted gratings method described in Rutishauser et al. (2011), no additional processing introducing interpolation is necessary. Moreover, the iterative approach works in cone beam geometry as often occurring in laboratory environment.

Other methods for streak artifact reduction use phase-unwrapping with energy resolving detectors (Epple et al., 2013, 2015) or an iterative bone-artifact removal algorithm (Hahn et al., 2015). The reduction of streak artifacts on an experimental level is however more robust.

Additionally, the use of tilted gratings with advanced iterative reconstruction methods like intensity-based SIR (Brendel et al., 2015) would be possible. Furthermore, the modified SIR algorithm can be employed at other one-dimensional phase-contrast

imaging techniques with differential character like analyzer based or diffraction enhanced imaging (Bravin et al., 2012). Tilting the gratings is also beneficial for dark-field imaging, which is investigated in Sharma et al. (2017).

CHAPTER 7

Biomedical applications of GBPC-CT

Short summary

This chapter presents exemplary results from biomedical GBPC-CT studies, which were performed with the described laboratory setup as part of this thesis. Next to a general overview, three specific ex-vivo studies are selected for further presentation in more detailed medical context to highlight the potential for preclinical GBPC-CT applications. The first ex-vivo study shows GBPC-CT results of samples containing intraductal carcinoma in situ (DCIS). The GBPC-CT images of this breast cancer type allow to visualize the extension of the carcinoma and the enlarged ducts by the three-dimensional nature of the method. The results of this chapter, which are in good correlation with histology, are to be published in Hellerhoff et al. (2018). The second study illustrates the potential of GBPC-CT imaging of renal cell carcinomas (RCC) for high soft tissue contrast without using contrast agents. The GBPC-CT results were compared with clinical CT and MRI next to histology to assess potential clinical performance. Moreover, the high GBPC-CT sensitivity allowed quantitative characterization of RCCs. The results of this study are published in Braunagel et al. (2017). The last exemplary study shown here focuses on the grating-based dark-field CT (GBDF-CT) signal of coronary arteries with atherosclerotic plaque containing microcalifications. Microcalcifications, which are associated with high risk plaques, cannot be visualized with conventional radiography, clinical CT, or MRI. However, the dark-field signal enables the detection of microcalcifications, although the size of the calcifications is below the spatial resolution. The results of this study are published in Hetterich et al. (2017). All GBPC-CT study results presented here were conducted under similar settings, as explained in detail in Ch. 3. In the following chapter, results, figures, tables, and text parts have been or are to be published in the corresponding references. More information on the study design and additional methods can be found in the respective references.

7.1 Overview of biomedical preclinical GBPC-CT studies

First biomedical grating interferometry studies were performed at synchrotron sources and showed that GBPC-CT provides excellent soft tissue contrast in comparison to attenuation contrast (Momose, 2003; Weitkamp et al., 2005). Several biomedical GBPC-CT samples were investigated including brain (Schulz et al., 2010), breast cancer (Sztrókay et al., 2012b), renal ischemia (Velroyen et al., 2014), and atherosclerotic plaque specimens (Saam et al., 2013; Hetterich et al., 2013).

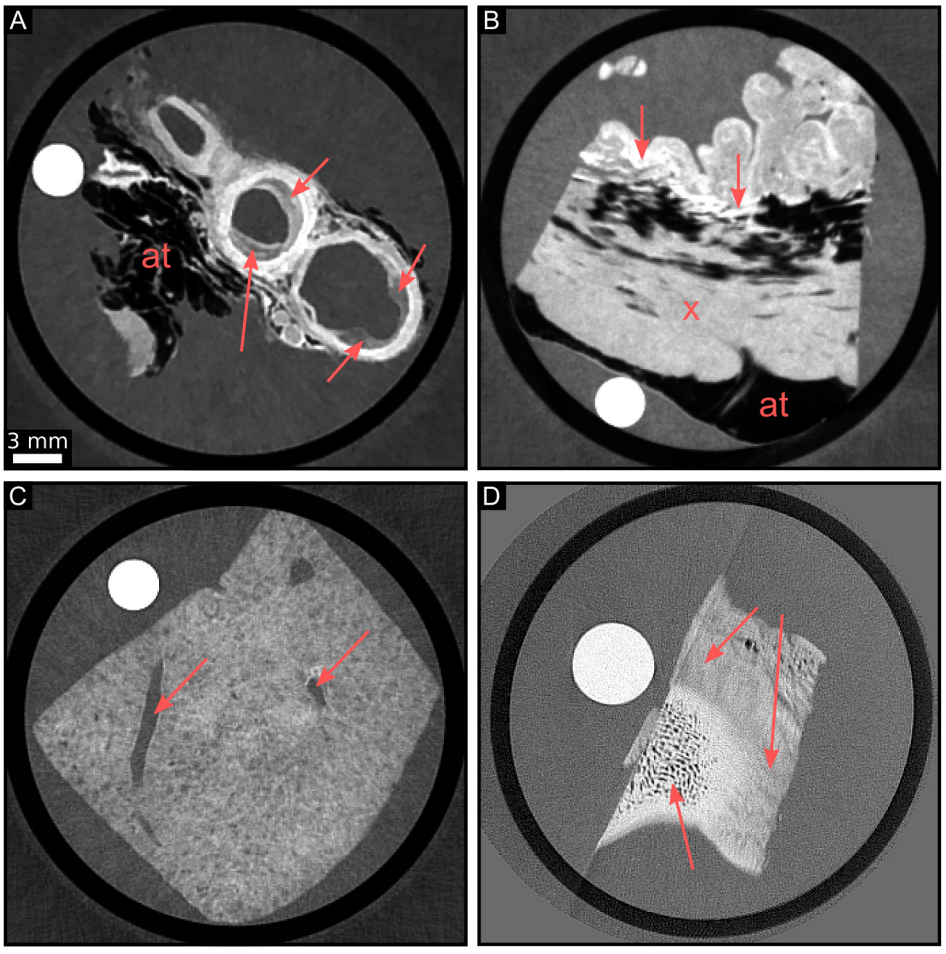

Fig. 7.1 | Phase-contrast slices of different ex-vivo GBPC-CT studies by way of example. A carotid artery phase-contrast slice (A) shows dilated vessel walls (arrows) indicating high-risk atherosclerotic plaque. Adipose tissue next to the vessel is marked with 'at'. Subfigure (B) presents a myocardial infarct sample similar to the ones investigated in Notohamiprodjo et al. (2017). The bright lines in the center indicated with arrows mark fibrosis due to myocardial infarct. The 'x' represents the heart muscle. Subfigure (C) depicts a fibrotic liver sample including vessels (arrow) related to Herzen et al. (2014). Small fibrotic cysts are spread over the whole sample. Subfigure (D) visualizes a cartilage sample as investigated in Jungmann et al. (2018). The top arrows point to areas of cartilage. The bottom arrow marks trabecular bone structures. The phase-contrast data is displayed in a linear range of [-113,138] HUp for subfigures (A) - (C) and [-100,150] HUp for subfigure (D).

With the possibility to apply GBPC-CT in a laboratory environment (Pfeiffer et al., 2006) and with all optimizing steps to realize this high sensitivity GBPC-CT as outlined in the previous chapters, it is possible to perform a large variety of biomedical ex-vivo studies of human and murine samples.

Atherosclerotic plaque can be visualized by differences in vessel walls as shown in Fig. 7.1 (A) (Hetterich et al., 2014, 2015b,a; Habbel et al., 2017; Hetterich et al., 2017). Myocardial infarcts can be depicted with significant increase in contrast and depiction of the fibrous infarct scar (Notohamiprodjo et al., 2017) (cf. Fig. 7.1 B).

GBPC-CT can be used for imaging of pathologies like renal cysts (Fingerle et al., 2014) or liver lesions (Herzen et al., 2014), which manifests in fibrous areas (cf. Fig. 7.1 C). Electron density differences originating in cartilage degeneration can be observed, as visible in Fig. 7.1 (D) (Jungmann et al., 2018). Furthermore, breast carcinoma (Grandl et al., 2014; Willner et al., 2014), or pancreatic adeonocarcinoma (Tapfer et al., 2013) can be measured with increased soft tissue contrast in comparison to the attenuation contrast. It is even possible to image subtle soft tissue differences like brain structures (Birnbacher et al., 2016; Viermetz et al., 2017) (cf. Fig. 4.3).

Besides, quantitative GBPC-CT allows to perform soft tissue decomposition in water, lipid, and protein (Willner et al., 2016). Based on those results, the use of GBPC-CT for imaging of pathological fluids revealed an increased differentiation possibility (Richter et al., 2017). Additionally, the impact of formalin on quantitative phase-contrast data was investigated in Willner et al. (2015).

In an ex-vivo study in the area of diabetes research, the electron density distribution of brown adipose tissue (BAT) within mice of different age was determined with GBPC-CT as part of this thesis (Birnbacher et al., 2018a). Brown adipose tissue could not only be visualized similar to prior results (Eggl et al., 2015), the quantitative characterization leads to a more detailed decomposition of fat and mitochondria (cf. Fig. 7.2).

Three exemplary GBPC-CT studies, which were performed in collaboration with radiology research partners as part of this thesis, are presented in the following sections to emphasize the potential of biomedical GBPC-CT application. This includes three-dimensional visualization of breast cancer samples (cf. Sec. 7.2), quantitative imaging without contrast agent of renal cell carcinomas (cf. Sec. 7.3), and dark-field tomography – or grating-based dark-field computed tomography (GBDF-CT) – to visualize microcalcifications below the physical pixel size in atherosclerotic plaque samples (cf. Sec. 7.4).

7.2 Assessment of intraductal carcinoma in situ

7.2.1 Introduction

Intraductal carcinoma in situ (DCIS) represents approximately 20 % of diagnosed breast cancers in mammography screening. The extent of DCIS is commonly underestimated as the tumor grows discontinuous or appears only with partial calcification. Since systemic therapy is rarely recommended, the diagnostic focus lies on the correct determination of the tumor margins for surgery (Houssami and Morrow, 2014). Thereby, it is highly important that the DCIS resection in conservative primary surgery is complete to avoid subsequent surgery and to reduce the risk of recurrent disease (Butler-Henderson et al., 2014a,b; Edwards et al., 2016; Van Zee et al., 2015). This leads to established wide resection margins, which are determined with interoperative specimen radiography. State-of-the-art diagnostic means is two-view digital radiography. However, the sensitivity of this method for DCIS diagnosis is currently limited (Schmachtenberg et al., 2012). In contrast, pathological methods like intraoperative frozen sections and imprint cytology provide better diagnostic sensitivity, but perform worse with respect to long duration of the method and a limitation of

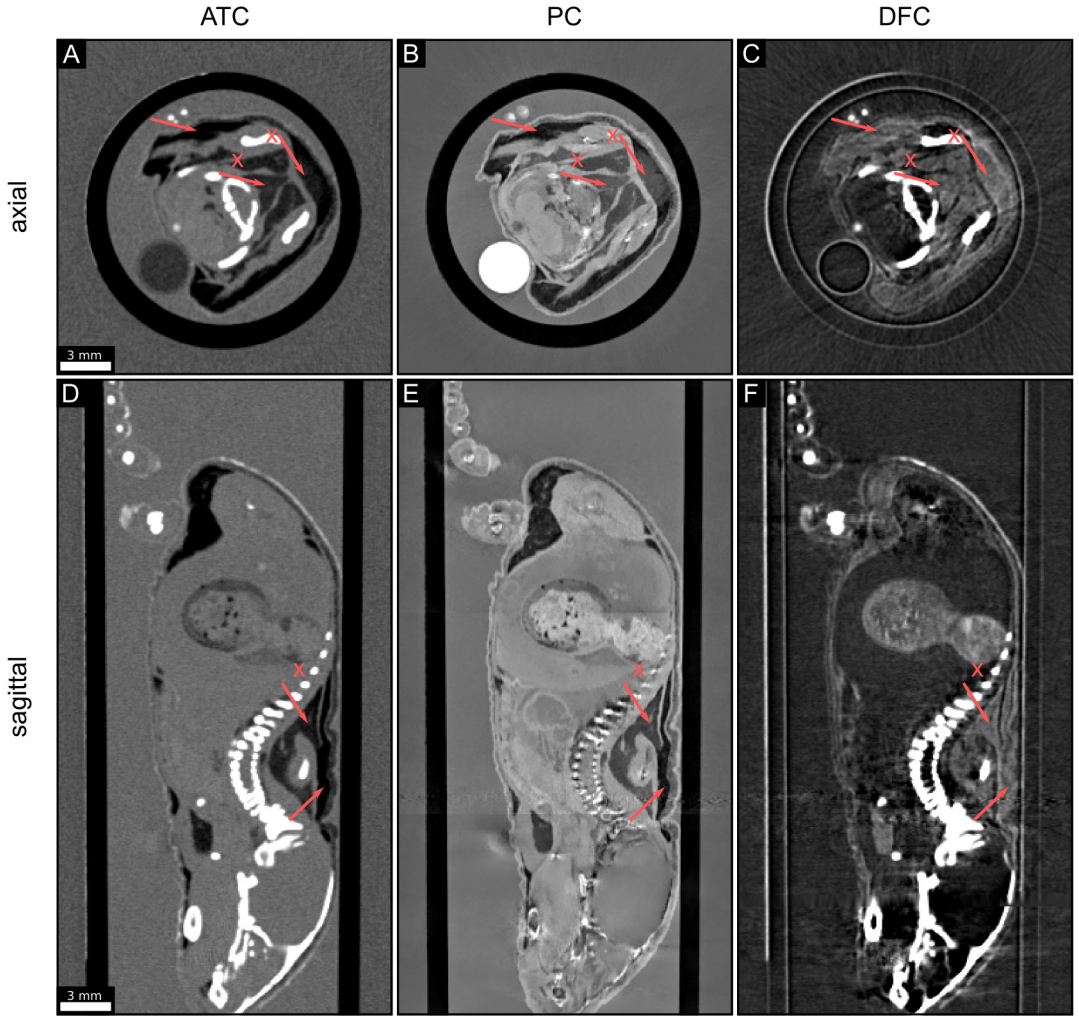

Fig. 7.2 | Exemplary GBPC-CT images visualizing brown adipose tissue of a mouse. Axial and horizontal slices of the three contrast modalities are shown. Subfigures (A) and (D) show the attenuation image in different orientations. White adipose tissue of the scapular fat is marked with an arrow, brown adipose tissue is additionally marked with an 'x'. Subfigures (B) and (E) represent the phase-contrast image. The two types of fat can clearly be differentiated. For illustration purpose, the corresponding dark-field images are included in subfigures (C) and (F), where the contrast gain in fat differentiation with the current setup configuration is low. The attenuation data is displayed in a linear range of [-200,400] HU, the phase-contrast data is displayed in a linear range of [-70,120] HUp, and the dark-field data in a linear range of [-0.002, 0.010]. The data was measured with tilted gratings (cf. Ch. 6) and the phase-contrast data was filtered bilaterally (cf. Sec. 3.5).

the extent and number of samples (Harness et al., 2014). Currently, several different X-ray based imaging techniques are investigated for intraoperative margin assessment and specimen radiography (Schulz-Wendtland et al., 2013; Urano et al., 2015).

With the development of diverse phase-contrast techniques at synchrotron facilities, initial mammography studies showed promising results with respect to soft tissue contrast (Pani et al., 2004; Dreossi et al., 2008; Keyriläinen et al., 2010; Castelli et al., 2011; Auweter et al., 2014). The translation of grating interferometry from synchrotron

to lab sources allowed to directly compare phase-contrast mammograms with conventional clinical mammography (Pfeiffer et al., 2006; Stampanoni et al., 2011; Scherer et al., 2014; Hauser et al., 2014; Köhler et al., 2015; Gromann et al., 2016). In the course of further research, the dark-field signal turned out to be even more beneficial than the DPC signal as for example the visualization of sub-pixel microcalcifications is possible (Grandl et al., 2015; Scherer et al., 2015b).

Phase-contrast CT studies of breast specimens realized at synchrotron sources showed enhanced soft tissue contrast and differentiability of fine structures compared to absorption-based imaging (Zhao et al., 2012; Sztrókay et al., 2012a; Jian et al., 2015; Nesterets et al., 2015; Longo et al., 2016). Using GBPC-CT of breast samples with synchrotron radiation provided similar results as specific microscopic structures of DCIS could be visualized in PC-CT but not in absorption CT (Sztrókay et al., 2012b). The successful correlation of GBPC-CT data with histopathology as a reference standard suggests that the visualization of ductal walls of dilated intramammary ducts allows the identification of areas of DCIS (Sztrókay et al., 2012b).

In contrast to phase-contrast mammography, there are only few studies which investigate laboratory phase-contrast CT of breast samples. In two ex-vivo studies, laboratory GBPC-CT of large breast tumors showed improved spatial resolution and permitted diagnostically relevant identification of three-dimensional tissue sections (Grandl et al., 2013, 2014).

This section presents selected results of a feasibility study investigating DCIS structure differentiation with laboratory GBPC-CT. Two different tumors divided in several samples were measured with this GBPC-CT setup and compared with histology as standard of reference. The focus lies on the determination of the extent of the ducts of different ex-vivo samples containing invasive ductal carcinoma and DCIS. The resulting phase-contrast data is compared to the attenuation data and histopathology. Additional methodical details of this study aside from GBPC-CT can be found in Hellerhoff et al. (2018).

7.2.2 Results

In this section, three samples of one exemplary breast tumor are presented. The attenuation and phase-contrast data is intrinsically matched and was best correlated with histopathological slices based on characteristic macroscopic features including the distribution of adipose tissue for direct comparison. Besides the GBPC-CT setup parameters as presented in Ch. 3, the raw detector data was deconvolved using the Richardson-Lucy algorithm with an experimentally determined point-spread function (cf. Sec. 3.6.4). Thereby, the number of iterations was 10.

Histology of all three samples revealed a diffusely growing DCIS in combination with multifocal invasive carcinoma of non-specific type (NST, formerly invasive ductal carcinoma). Figures 7.3 - 7.6 show representative slices of the three different samples.

The absorption-based image of sample 1 shows only limited contrast of ductal walls, intraductal carcinoma, and invasive carcinoma, as only the adipose tissue can be visualized (cf. Fig. 7.3 A). The phase-contrast image allows a clear identification of the compact invasive tumor and surrounding ductal structures due to different electron density values (cf. Fig 7.3 B). The ducts containing DCIS are delineated by bright duct

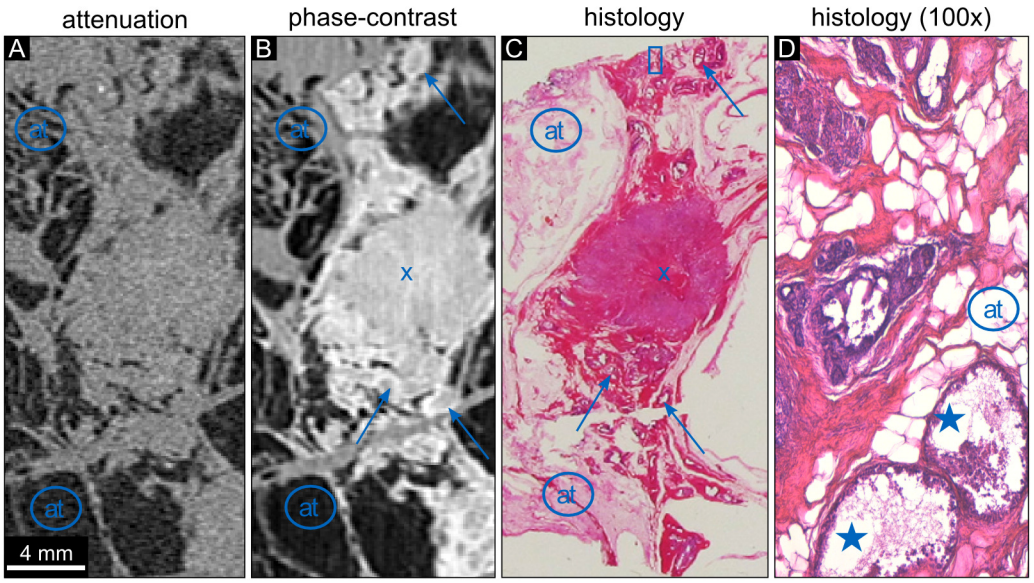

Fig. 7.3 | Attenuation, phase-contrast, and histology images of DCIS sample 1. The absorption based image (A) reveals only adipose tissue (at) appearing dark. The tumor tissue cannot be differentiated. The attenuation data is displayed in a linear range of [-60,60] HU. The phase-contrast image (B) of the same region shows a round shaped invasive part of the tumor (marked with 'x') and surrounding DCIS. The bright delineation of duct walls in dilated ducts containing DCIS can be observed (arrows). The phase-contrast data is displayed in a linear range of [-100,100] HUp. The corresponding histopathological slice (C) (HE staining) shows an invasive ductal cancer (violet, marked with 'x') surrounded by DCIS and dilated mammary ducts (pink). The arrows indicate dilated ducts with intraductal carcinoma. The tumor area is embedded in an area of adipose tissue (at). Magnification of the histopathological slice (D) indicated by the rectangle in subfigure (C) visualizes dilated ducts (violet). An atypical epithelium that fills up completely or partially the lumen of the ducts can be observed. The DCIS areas marked by the asterisks depict central necrosis. Figure to be published in Hellerhoff et al. (2018).

walls (cf. arrows). The histopathological image visualizes a clearly, round shaped invasive ductal carcinoma with high cellularity and intraductal cellular components in immediate proximity (cf. Fig. 7.3 C). The surrounding DCIS areas are marked by way of example with arrows and can be identified by violet vessel walls originating in the epithelial layer. In the magnified slice of the rectangle in the top in Fig. 7.3 (C), one can identify DCIS areas as closely packed polymorphic tumor cells within the lumen and hyperchromatic nuclei (cf. Fig.7.3 D). Compared to the high magnification view of optical microscopy, the diagnostically relevant DCIS features within areas of dilated intramammary ducts cannot be identified in the phase-contrast signal due to the limited resolution.

The absorption image of sample 2 does not reveal any contrast except for adipose tissue (at) (cf. Fig. 7.4 A). In comparison, the phase-contrast image depicts two areas of dilated ducts and fibrosis connected by a thin tissue strand and allows clear visualization of the bright walls (cf. Fig. 7.4 B). The corresponding histological slice visualizes the widespread distribution of dilated ducts in various directions (cf. arrows). The triangular tissue structure extending into the adipose tissue marked with an asterisk

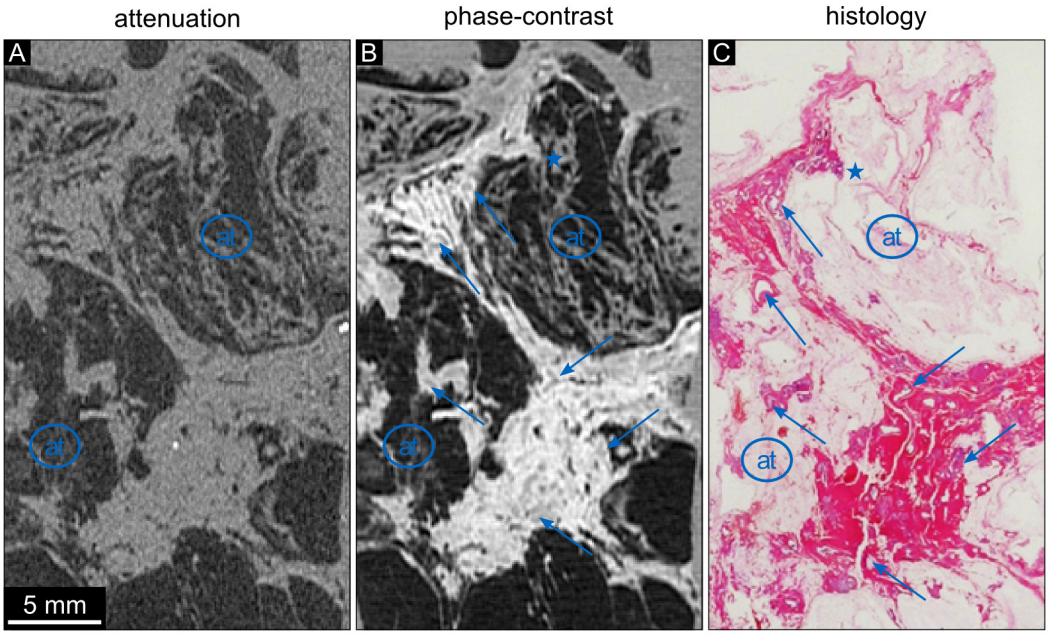

Fig. 7.4 | Attenuation, phase-contrast, and histology images of DCIS sample 2. The absorption based image (A) visualizes low contrast of all structures except for adipose tissue (at). The attenuation data is displayed in a linear range of [-60,60] HU. The phase-contrast image (B) of the same region corresponding to (A) shows dilated ducts delineated with a bright wall. Exemplary ducts are marked by arrows. The phase-contrast data is displayed in a linear range of [-100,100] HUp. The corresponding histological slice (C) (HE staining) contains areas of fibrous tissue with violet ductal structures in different directions. The triangular tissue structure in the upper part of the slice represents an area of low grade DCIS (asterisk), which can also be seen in the phase-contrast image (B). Magnification of the histology slices is presented in Fig. 7.5. Figure to be published in Hellerhoff et al. (2018).

represents an area of low grade DCIS (cf. Fig. 7.4 C). The same area can be observed in the phase-contrast image (cf. Fig. 7.4 B). Magnification of the histopathological slice of sample 2 shows the extent of the vessel marked by the asterisk (cf. Fig. 7.5 A), the epithelial layer, and the duct filled with atypical epithelium in 100-fold magnification (cf. Fig. 7.5 B). In the 200-fold magnification even necrosis is visible (cf. Fig. 7.5 C). This level of detail cannot be reached with GBPC-CT, however the contrast of ductal vessels can be clearly depicted.

The attenuation image of sample 3 reveals adipose tissue and vessels (cf. Fig. 7.6 A, arrow and asterisk). Moreover, the attenuation signal shows an area containing calcifications marked by the rectangular frame. However, the soft tissue component of the DCIS area could not be further identified in the absorption based image. The vessel delineation is more pronounced in a superior way in the phase-contrast image (cf. Fig 7.6 B). The corresponding histology slice shows calcifying DCIS and the tissue structure in high detail (cf. Fig. 7.6 C). A cluster of microcalcifications can be observed in both modalities, but not in the histological slice at this magnification.

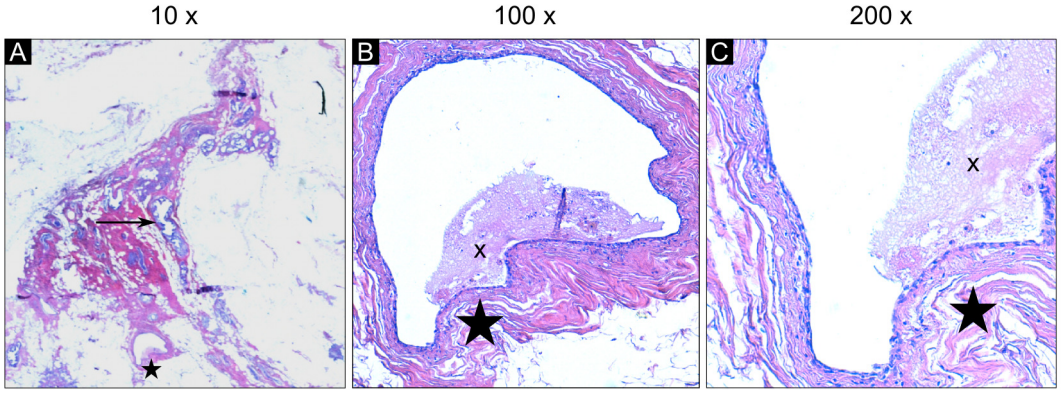

Fig. 7.5 | Histology slices of DCIS sample 2 in detailed magnification. In 10-fold magnification (A), the details of the duct marked by the asterisk cannot be visualized. The arrow marks an exemplary DCIS structure. The 100-fold magnification (B) shows the epithelial structure of the duct. The 200-fold magnification (C) depicts the epithelial monolayer and the necrosis in the duct marked by the 'x' in more detail. Figure to be published in Hellerhoff et al. (2018).

7.2.3 Discussion and conclusion

The main result of this section is the three-dimensional visualization of ductal walls with laboratory grating-based phase-contrast CT. The illustration of the ductal walls is diagnostically relevant as they represent an indication for the extent of DCIS in dilated inflammatory form, which is challenging in breast diagnostics (Schmachtenberg et al., 2012; Sztrókay et al., 2012b).

As shown with the exemplary samples, the GBPC-CT images could depict areas of dilated ducts suspicious for DCIS. A clear differentiation of both invasive carcinoma and surrounding areas of intraductal carcinoma was also possible. The phase-contrast data outperforms the corresponding attenuation signal with respect to image contrast, which reveals solely adipose tissue and microcalcifications. These observations were confirmed by matching the phase-contrast and attenuation data with histology, in which single dilated ducts, intraductal bleeding, and distinct vessels were identified. However, identification and classification of DCIS areas and epithelial hyperplasia is limited to histopathological inspection. Pathognomonic features of DCIS like atypical epithelial growth, mitoses, and nuclear size can only be revealed by histopathological staining and light microscopy with higher magnification factors. Since these features are essential for the differentiation of dilated ducts between sclerosing adenosis or malignant intraductal epithelial growth, phase-contrast will not be able to replace histological work-up, at least at the current level of resolution.

Specimen radiography with dark-field and phase-contrast imaging is beneficial, especially with respect to diagnostics of microcalcifications, but also provides only limited possibility of DCIS margin assessment (Scherer et al., 2016b). The major advantage of GBPC-CT in contrast to histopathologic sections or specimen radiography is its full three-dimensional capability allowing a more precise margin assessment over the whole sample especially for non-calcifying DCIS extending the invasive tumor. In this respect, phase-contrast CT is able to deliver essential histological landmarks to identify suspicious areas within a sample to navigate the placement of histological sections.

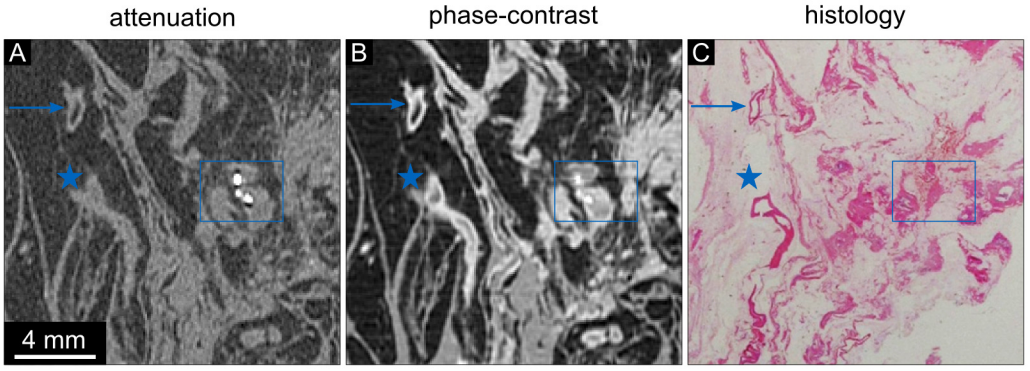

Fig. 7.6 | Attenuation, phase-contrast, and histology images of DCIS sample 3. The absorption based image (A) clearly depicts microcalcifications, but low contrast of the vessel wall and no contrast of the soft tissue component of the DCIS area. The attenuation data is displayed in a linear range of [-60,60] HU. The phase-contrast image (B) presents a clear depiction of the vessel wall (asterisk). The calcifying DCIS region shows moderate soft tissue contrast. The phase-contrast data is displayed in a linear range of [-100,100] HUp. The histological section (C) (HE stained) of sample 3 reveals a tubular structure in the left part of the section representing a vessel with a tortous segment in the lower border of the section (asterisk). Areas of calcifying DCIS are visible in the right part of the section (frame). Figure to be published in Hellerhoff et al. (2018).

Current limitations for intraoperative specimen GBPC-CT are the disproportional duration of a measurement rendering the current approach not feasible for preclinical application and further performance optimization of the method like the use of more efficient detectors or an X-ray source with higher flux is needed. Additionally, higher spatial resolution is essential to bring GBPC-CT for specimen tomography to clinical application.

7.3 Imaging evaluation of renal cell carcinoma subtypes

7.3.1 Introduction

Renal cell carcinomas (RCC) account for approximately 2 - 3 % of all adult cancers worldwide (Rini et al., 2009). The most common subtypes of sporadic RCC are clear cell (ccRCC) with 70-85 %, papillary (pRCC) with 7-15 %, and chromophobe RCC (chrRCC) with 5-10 % (Escudier et al., 2014). The prognosis, metastatic rate, and response to targeted therapies differ for each RCC subtype (Lam et al., 2005).

While most renal lesions are detected with ultrasound (US) or non-enhanced computed tomography (CT), they often present without clinical symptoms. Differentiation of renal lesions is limited due to low resolution of US or the low contrast in non-enhanced CT (Young et al., 2013). Detection and discrimination of different RCC subtypes can be improved using contrast agents in multiphasic CT (Young et al., 2013; Kim et al., 2002; Pierorazio et al., 2013) or magnetic resonance imaging (MRI) (Sun et al., 2009; Pedrosa et al., 2007). In CT, iodine-based contrast agents can cause

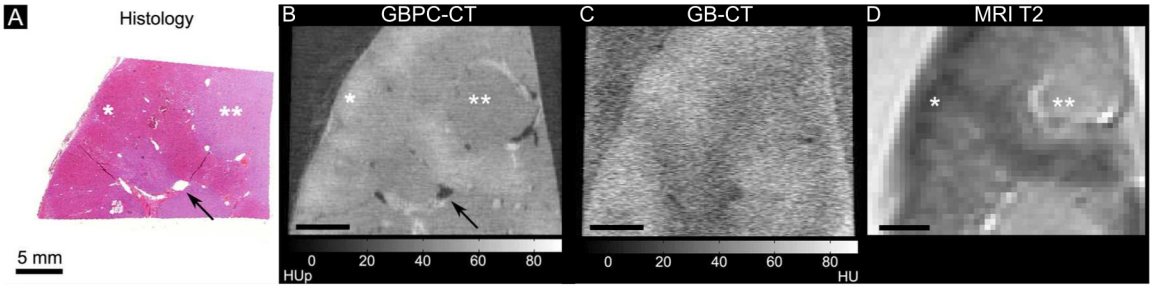

Fig. 7.7 | Histological slice (coronal slice) and corresponding grating-based phase-contrast CT(GBPC-CT), grating-based attenuation-contrast CT (GB-CT), and T2-w magnetic resonance images of a normal human kidney sample. The histopathological slice (A) was stained with HE staining. The cortex (*) and the medulla (**) are depicted as well as renal vessels (arrow). Good visual agreement is achieved between histology the corresponding grating-based phase-contrast CT slice (B), where the same features can be observed. The absorption image (C) (GB-CT), simultaneously achieved with the GBPC-CT setup, shows limited soft tissue contrast. T2-w magnetic resonance imaging (MRI T2) (D) provides similar soft tissue contrast than the GBPC-CT image in subfigure (B), however at reduced spatial resolution. Figure adapted from Braunagel et al. (2017).

acute renal failure, anaphylactic reactions, or thyrotoxic crisis. Using MRI contrast media based on gadolinium can cause nephrogenic systemic fibrosis. Preoperative histological diagnosis is based on percutaneous renal biopsies, but potential post biopsy complications lead to limited acceptance (Lebret et al., 2007).

Grating-based phase-contrast computed tomography (GBPC-CT) showed in several studies an increase in soft tissue contrast in comparison to conventional attenuation images without the use of contrast agents. Differences in renal carcinoma should become visible in GBPC-CT if differences in electron density occur.

In this section, the potential of GBPC-CT imaging for tumor architecture visualization without the use of contrast agent is presented. Different RCC subtypes and healthy kidney samples were characterized qualitatively and quantitatively in GBPC-CT in comparison to the simultaneously acquired attenuation-based CT (GB-CT), clinical CT, and MRI. The results were correlated with histopathology as the standard of reference. Additional methodical details of this study aside from the GBPC-CT setup can be found in Braunagel et al. (2017).

7.3.2 Results

Normal kidney parenchyma

GBPC-CT imaging of a normal human kidney sample allowed qualitative and quantitative differentiation between cortex (54±4 HUp) and medulla (44±3 HUp). Good visual correlation to T2w-MRI and histological slices was achieved (cf. Fig. 7.7). Moreover, vessels could be clearly distinguished from kidney parenchyma. In GB-CT (cf. Fig. 7.7 C) and clinical CT (not shown) a discrimination between cortex or medulla was not possible.

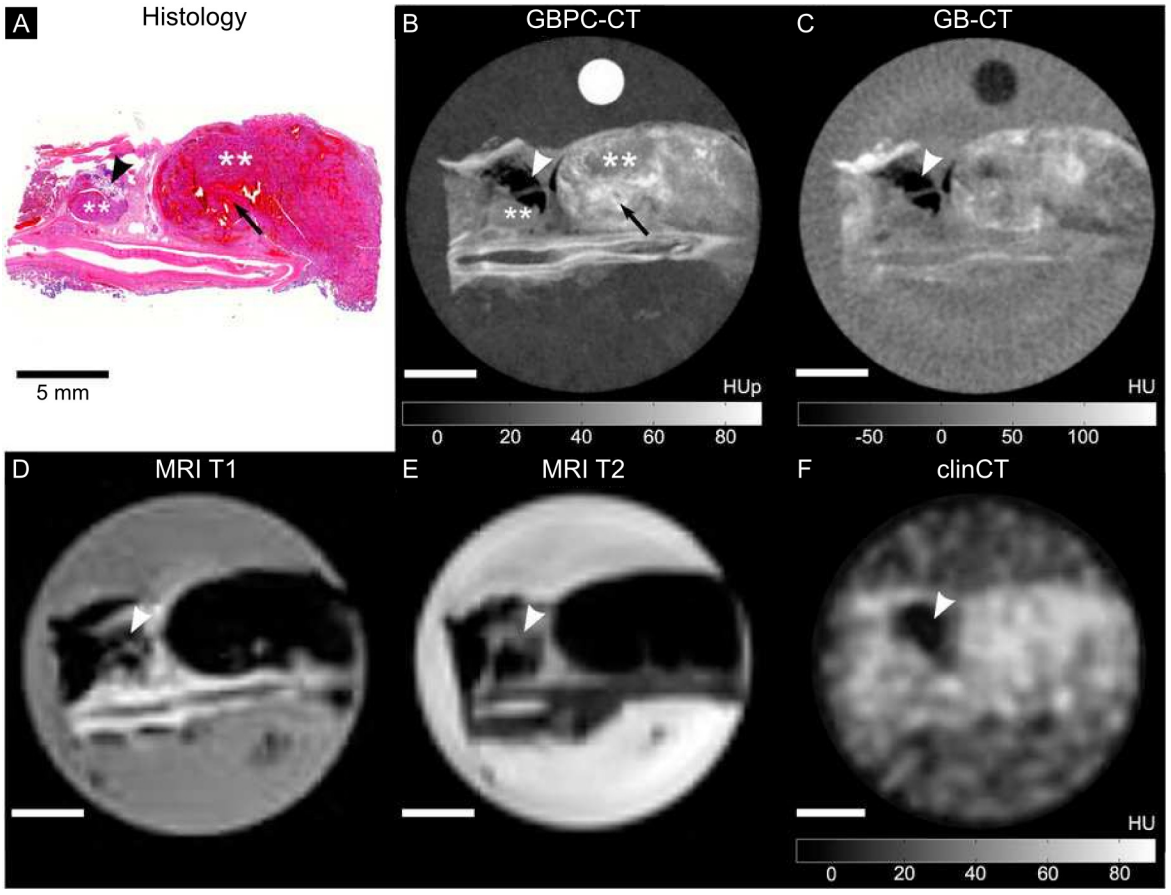

Fig. 7.8 | Histology, phase-contrast CT, grating-based and clinical CT, and MRI images of a clear cell renal cell carcinoma (ccRCC) sample. The histological slice with HE-staining (A) shows a large and a small tumor nodule (**). Diffuse intratumoral bleeding is marked by the arrow. The arrowhead points to an area containing adipose tissue. The tumor boundaries and the extended vessel can be seen at the bottom. The GBPC-CT slice (B) is in good correlation to histology as similar features can be observed. Attenuation images (C) and (F) allow only to detect fat and areas with hyperdensity. The MRI images (D and E) show reduced structure visualization in contrast to the GBPC-CT images as only tumor components like intratumoral bleeding are visible due to susceptibility artifacts. Figure adapted from Braunagel et al. (2017).

Qualitative analysis of renal cell carcinomas

Qualitative GBPC-CT image analysis of ccRCCs, pRCCs, and chrRCCs allowed a reliable tumorous tissue differentiation from normal renal cortex (cf. Fig. 7.8 - 7.10). Thereby, tumorous tissue had a visually lower phase-contrast signal, atypical cortical or medullar structure, and absent normal vessels in comparison to normal kidney tissue. The tumor areas could be detected in GBPC-CT and MRI with a sensitivity of 100 % diagnosed by trained radiologists and verified by histology (cf. Braunagel et al. (2017)). Tumor boundaries could be clearly differentiated from normal kidney tissue in good visual agreement with histological slices. Attenuation-based CT images were significantly less sensitive for detection and discrimination of tumor areas from normal parenchyma (GB-CT: 50 %; clinical CT: 40 %). Moreover, clear tumor boundary delineation was not possible in the attenuation images (cf. Fig. 7.8 - 7.10).

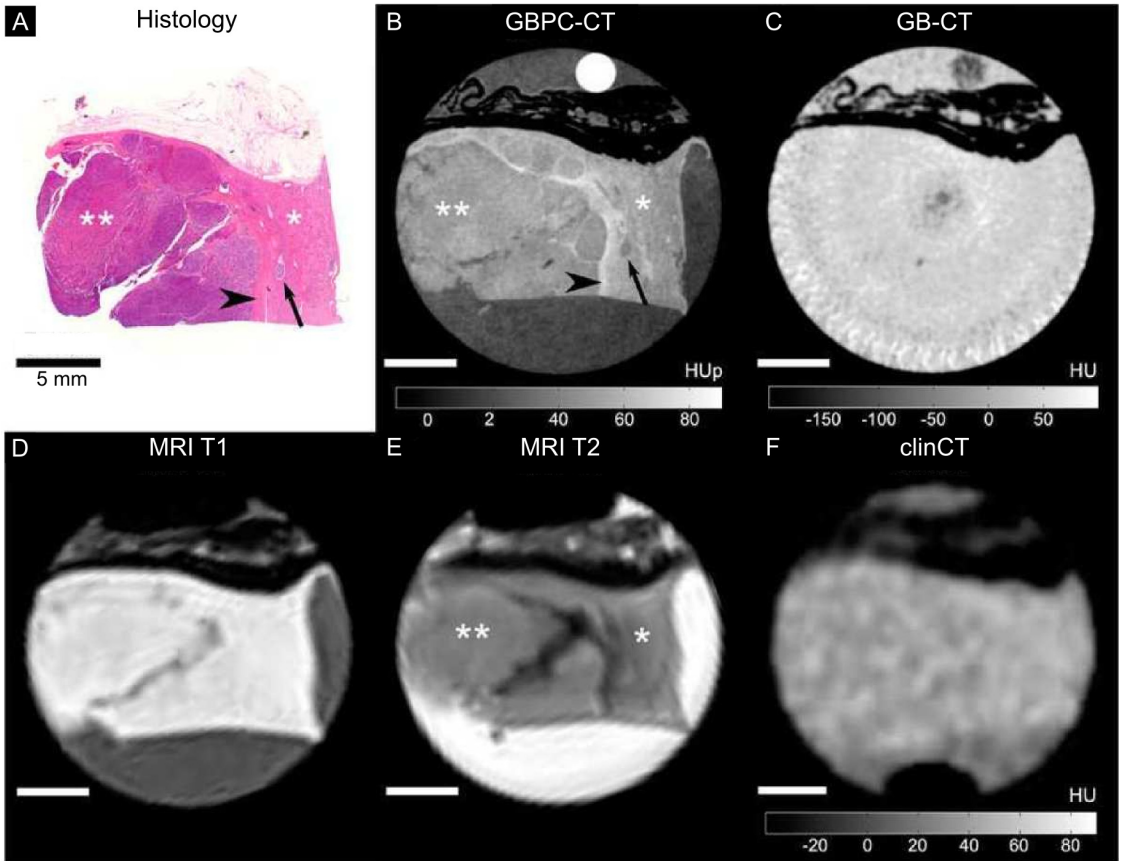

Fig. 7.9 | Histology, phase-contrast CT, grating-based and clinical CT, and MRI images of a papillary renal cell carcinoma (pRCC) sample. The histological slice (A) allows a clear discrimination of the normal cortex (*) and the homogeneous tumor area (**). One can observe additionally the pseudocapsule surrounding the tumor (arrowhead) and a micrometastasis in the cortex (arrow) as well as small linear fibrous strands. The GBPC-CT slice (B) is perfectly matched to the histological slice and allows a clear discrimination of the normal and tumorous cortex. In grating-based CT (GB-CT) (C) and clinical CT (F), only perirenal fat was visible (hypodense) as soft tissue components could not be differentiated. The MR images (D and E) show less pronounced discrimination of tumor and normal kidney tissue than the phase-contrast image (B). Figure adapted from Braunagel et al. (2017).

Soft tissue components could be visualized with high sensitivity in GBPC-CT (cf. Tab. 7.1 and Fig. 7.11). Microbleeding and diffuse hemorrhage showed an increased GBPC-CT signal with a wide distribution throughout the tumorous tissue. Fibrous strands and pseudocapsules were represented as contrast-rich bands in the tumorous tissue and in the surrounding tumor boundaries (cf. Fig. 7.11). In comparison, these tissue components could not be observed with GB-CT and clinical CT (cf. Tab. 7.1). Areas containing necrosis had higher and areas showing hyalinization had lower phase-contrast signal values in comparison to tumorous tissue (cf. Fig. 7.11). The detection rate of GBPC-CT was lower than histology, but still better than GB-CT, MRI, and clinical CT (cf. Tab. 7.1).

It was clearly possible to visualize the small dot-like appearing microcalcifications in GBPC-CT. Larger calcifications showed high signal values with small surrounding

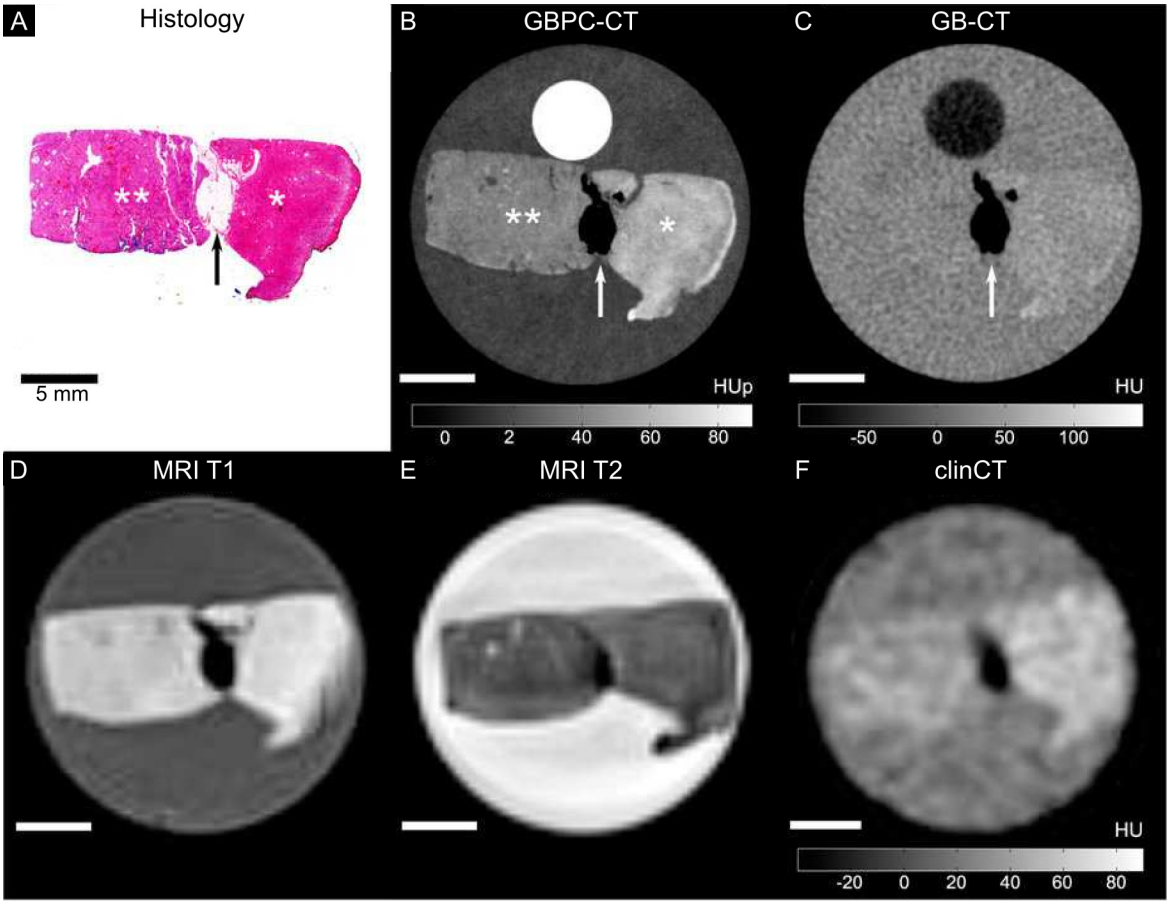

Fig. 7.10 | Histology, phase-contrast CT, grating-based and clinical CT, and MRI images of a chromophobe renal cell carcinoma (chRCC) sample. The histopathological slice (A) shows a clear detection of normal kidney (*) and the homogeneous tumor areas (**). In the middle of the image, a stripe of fat with low signal (arrow) is clearly depicted. The phase-contrast slice (B) shows significantly higher values for the normal and lower values for the tumorous area. In comparison, grating-based CT (GB-CT) (C), clinical CT (F), and MRI (D and E) could only provide a marginal visible difference between normal and tumorous tissue. Figure adapted from Braunagel et al. (2017).

artifacts due to phase-wrapping in GBPC-CT and an excellent visualization in GB-CT and a lower detection rate in clinical CT (cf. Tab. 7.1). Fat depositions could be observed in all imaging modalities (cf. Fig. 7.8 - 7.10).

In good correlation with histopathology, most ccRCCs (75 %) had a heterogeneous appearance in GBPC-CT including hyalinization, necrotic areas, local and diffuse hemorrhage, small calcifications, sinusoidal tumor vessels, and cystic changes. The pRCC and chrRCC subtypes were more homogeneous (71 % and 100 %, respectively) with linear, contrast-rich bands in the low-signal tumor tissue corresponding to fibrous strands and pseudocapsules, and displayed fewer calcifications than the ccRCC specimens. In the chrRCC samples, diffuse hemorrhage, hyalinization, necrosis, or cystic changes could not be seen in GBPC-CT.

In contrast, no intratumoral tissue components like fibrous strands, pseudocapsules, or microbleedings could be observed with GB-CT and clinical CT (cf. Tab. 7.1). A

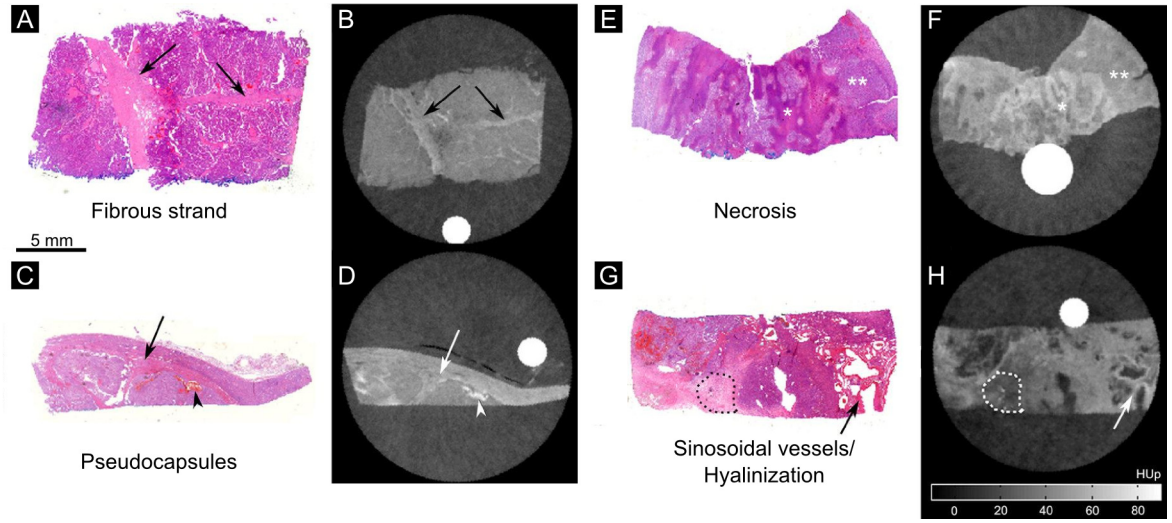

Fig. 7.11 | Visual comparison between histological slices and GBPC-CT images. Histological slices with HE-staining (A,C,E,G) show a good visual correlation with phase-contrast images (B,D,F,H). Different tumor tissue components (arrows) include fibrous strands (A,B), pseudocapsule (arrow) and hemorrhage (arrowhead) (C,D), diffuse necrotic areas with higher signal (*) and tumor tissue with lower phase-contrast signal (**) (E,F) as well as sinusoidal vessels (arrow) and hyalinization (dotted line) (G,H). Figure adapted from Braunagel et al. (2017).

good part of the ccRCC samples showed hypodense and inhomogeneous tissue with large calcifications (3/8) and diffuse hemorrhage (2/8) in clinical CT and GB-CT. The other samples appeared as hyperdense tissues without a possible differentiation from normal kidney tissue. Homogeneous hypodense tissues were detected in pRCC and chrRCC subtypes in GB-CT (4/7 and 2/5, respectively) and clinical CT (3/7 and 2/5, respectively) with large calcifications in one chrRCC sample.

Quantitative analysis of renal cell carcinomas

In GBPC-CT, a quantitative differentiation between tumorous tissue of ccRCC (n=8), pRCC (n=7), and chrRCC (n=5) specimens and normal renal cortex (n=6) was possible. However, renal medulla and tumorous tissue as well as the subtypes ccRCC,

Tab. 7.1 | Detection of different tumor components in GBPC-CT, GBCT, clinical CT, and MRI compared with histopathological findings. * Small susceptibility artifacts in susceptibility weighted images (SWI), ** large hypointense areas. Table adapted from Braunagel et al. (2017).

	GBPC-CT/hist	GB-CT/hist	clinical CT/hist	MRI/hist
Fibrous strands	15/15	0/15	0/15	4/15
Pseudocapsule	8/9	0/9	0/9	6/9
Calcification	9/17	17/17	4/17	*
Microbleeding	10/11	0/11	0/11	*
Diffuse hemorrhage	5/5	3/5	2/5	5**/5
Hyalinization	6/8	6/8	2/8	6/8
Necrosis	2/3	0/3	0/3	1/3

pRCC, and chrRCC could not be differentiated quantitatively (cf. Braunagel et al. (2017)).

Moreover, several tumor tissue components could be quantitatively analyzed in GBPC-CT due to significantly different phase-contrast values. Hemorrhage provided a significantly higher phase-contrast signal (80±9 HUp) than pseudocapsule (66±8 HUp), fibrotic strands (57±5 HUp), and necrosis (54±5 HUp). In comparison, the phase-contrast values of hyalinization areas had a lower signal intensity. Calcifications showed the highest phase-contrast values with 280±199 HUp and fat the lowest with -60±10 HUp. In contrast to MRI, where calcifications and microbleedings could not be differentiated due to susceptibility artifacts, GBPC-CT allowed for a solid discrimination between hemorrhage (80±9 HUp) and larger calcifications (>290 HUp) with small artifacts.

7.3.3 Discussion and conclusion

This ex-vivo GBPC-CT feasibility study illustrates that qualitative and quantitative discrimination of normal kidney tissue from renal cell carcinoma subtypes is possible in contrast to absorption-based CT. GBPC-CT showed improved visualization of soft tissue, tumor tissue architecture, and enhanced discrimination between normal kidney and tumorous kidney tissue. This outcome is in good agreement with a recent GBPC-CT study performed with synchrotron radiation showing improved assessment of normal and ischemic renal parenchyma in murine kidneys (Velroyen et al., 2014). In comparison to literature, quantitative phase-contrast values for cortex and medulla of healthy human renal samples were increased (Willner et al., 2015; Woodard and White, 1986), most likely due to formalin fixation over a relatively long period (Willner et al., 2015). With respect to visual and quantitative differentiation of fine intratumoral structures, GBPC-CT was in good agreement to histopathology and turned out to be superior in comparison to MRI and unenhanced absorption-based CT. Nonetheless, histology provides a much higher spatial resolution than GBPC-CT, clinical CT, or MRI, and even first enables diagnosis of RCC subtypes.

GBPC-CT results of ccRCC samples had a more heterogeneous appearance including diffuse hemorrhages, hyalinization, necrosis, and sinusoidal vessels in contrast to pRCC and chrRCC specimens compared to histology. GBPC-CT data of pRCC samples allowed improved detection of fibrous strands, pseudocapsules, and microbleedings as well as diffuse hemorrhage and cystic changes. The chRCC data appeared as homogeneous tumors containing fibrous strands and microbleeding without depicted hyalinization or necrosis. However, a quantitative differentiation between the RCC subtypes was not possible.

In clinical routine, the detection and characterization of renal lesions in unenhanced CT is difficult as the method provides only low soft tissue contast (Young et al., 2013). Contrast-enhanced multiphasic CT and MRI images are clinically used to diagnose RCC and to define the subtype (Kim et al., 2002; Pedrosa et al., 2007). As both approaches CT and MRI face potential limitations with respect to the use of contrast agents, GBPC-CT may improve diagnostics without the use of contrast agents, although there are still various challenges to be addressed.

The major limitation of this GBPC-CT study is its preclinical setting. Addition-

ally, the RCC samples in this study were measured without contrast media in the reference GB-CT, clinical CT, and MRI scans, which most likely reduces the sensitivity. Also, the spatial resolution of GBPC-CT in this study was much higher than a dose-compatible resolution typically used in clinical imaging. However, such a high resolution has no limitation for a histopathological workup scan.

Scaling GBPC-CT towards a clinical scenario is technically challenging. Especially, larger pixel sizes for dose compatibility would dissolve the boundary differentiation between healthy and tumorous tissue. Potential benefits could include imaging without contrast agents and the differentiation of malignant tumors with benign renal lesions like angiomyolipomas or oncocytomas.

A preclinical biomedical use of GBPC-CT as described in the previous section (cf. Sec. 7.2) would be possible. One could gain additional information for ex-vivo tumor analysis after partial or total nephrectomy before histological workup, which is in contrast a destructive process. Moreover, the three-dimensional visualization is highly beneficial and could improve histopathological analysis. Furthermore, GBPC-CT could be used for quantitative tumor tissue characterization in ex-vivo imaging studies, as previously shown for pancreatic cancer on animal models (Tapfer et al., 2013).

7.4 Dark-field imaging in coronary atherosclerosis

7.4.1 Introduction

The occurrence of calcifications is an important phenomenon in the development of atherosclerotic plaque. Macrocalcifications are the result of long-term subsiding vessel wall inflammation and are likely to be found in generally stable plaque stages. In contrast, microcalcifications are more often found in areas of active inflammation, such as lipid-rich necrotic cores or fibrous caps, and might be an interesting target in the assessment of plaque vulnerability (Vengrenyuk et al., 2006). For example, ex-vivo studies have shown that microcalcifications increase local tissue stress and cause fibrous cap rupture (Hutcheson et al., 2014). However, while it is usually possible to detect macrocalcifications, microcalcifications are too small to be detected in clinical CT.

The dark-field signal, which is simultaneously acquired next to the attenuation and phase-contrast signal in grating-interferometry (cf. Sec. 2.3), allows to visualize small-angle scattering with sub-pixel resolution structures (Malecki et al., 2012; Wolf et al., 2014). The small-angle scattering occurs predominantly in areas with multiple electron density fluctuations destroying locally the interferometric coherence in X-ray grating-interferometry. Results of several preclinical studies of dark-field radiography showed that the dark-field signal is highly sensitive for microcalcifications in breast tissue (Michel et al., 2013; Scherer et al., 2016a) or in kidney stones (Scherer et al., 2015b).

In this presentation of an ex-vivo study performed within the range of this thesis, the potential of X-ray grating-based dark-field CT (GBDF-CT) for recognizing calcifications in human coronary atherosclerotic plaque is investigated. The dark-field signal is supposed to be highly sensitive to calcifications and especially microcalcifications in comparison to both phase- and attenuation signals. Therefore, several coronary artery

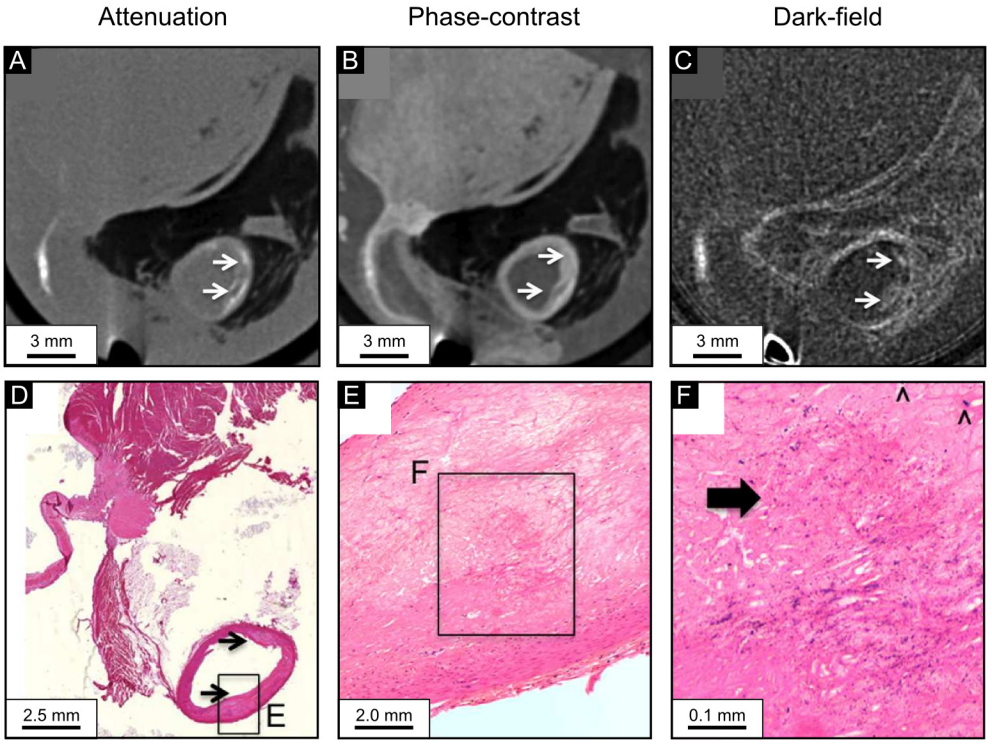

Fig. 7.12 | Exemplary slice of the left circumflex artery with high signal intensity in the dark-field image and no signal intensity in attenuation and phase-contrast signals. Subfigures (A), (B), and (C) show axial slices of GBPC-CT in three image modalities attenuation (A), phase-contrast (B), and dark-field (C). Subfigures (D), (E), and (F) represent the corresponding HE-stained histology sections, where (E) and (F) are magnified views. The highly intense dark-field signal is visible at the boundary of the vessel (C). The presence of microcalcifications in the areas of high dark-field signal is visualized in the histopathological magnification images. The arrowheads in subfigure (F) point to normal cell nuclei and the thick arrow indicates an area with multiple microcalcifications. Adipose tissue is depicted by low signal intensity in attenuation and phase-contrast (small arrows), whereas the dark-field signal values are high in the same area. Lipid rich tissue can be observed in the same regions in the histological slices. Figure adapted from Hetterich et al. (2017).

samples were measured with this laboratory GBPC-CT setup and were compared with histology, which serves as the standard of reference. The methodical details of this study can be found in Hetterich et al. (2017).

7.4.2 Results

Fifteen coronary specimens were obtained from five donor hearts. Histopathology, dark-field, phase, and attenuation contrast data was retrieved in 283 cross-sections. Ten cases of isolated high signal intensity in dark-field imaging were found (3.5 %). According to attenuation and dark-field imaging, there were 162 cross sections (57.2 %) containing macrocalcifications and 111 cross sections (39.2 %) without macrocalcifications.

In histopathology, microcalcifications occurred in all specimens (10/10) with iso-

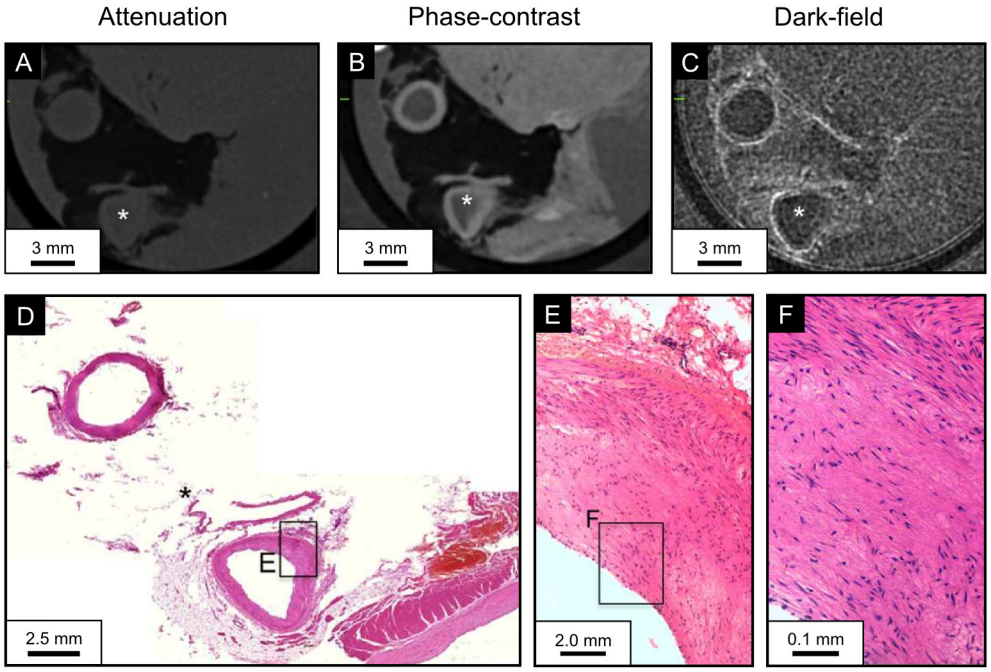

Fig. 7.13 | Exemplary slice of the left circumflex artery (vessel *) as negative control with no enhanced signal intensity in attenuation, phase-contrast, and dark-field. Subfigures (A), (B), and (C) show axial slices of GBPC-CT in three image modalities attenuation (A), phase-contrast (B), and dark-field (C). Subfigures (D), (E), and (F) represent the corresponding HE-stained histology sections, where (E) and (F) are magnified views. A small eccentric plaque without lipid core is depicted in the histological slice. No microcalcifications can be observed in the magnification slices. The small eccentric plaque and other anatomical structures are best visible in the phase-contrast signal. Figure adapted from Hetterich et al. (2017).

lated high dark-field signal (cf. Fig. 7.12). In the slices with no intensity in all three image modalities representing negative control specimens, histology showed neither micro- nor macrocalcifications (0/10) (cf. Fig. 7.13). In the positive control specimens with high signal in all three image contrast, macrocalcifications were also found in histopathology (cf. Fig. 7.14). In 9 out of 10 cases (90 %), histology confirmed microcalcifications in vicinity of macrocalcifications. In 8 of these 9 cases (89 %), the dark-field signal showed high intensity values in areas that did not provide contrast in the phase and attenuation modality. Microcalcifications were often revealed in relation to plaques consisting predominantly of fibrous and adipose tissue. No example of microcalcifications inside a fibrous cap was found, possibly due to the limited specimen number in this study.

7.4.3 Discussion and conclusion

This ex-vivo study demonstrates that GBDF-CT is able to visualize microcalcifications in coronary artery plaques with increased sensitivity in comparison to X-ray attenuation and phase-contrast methods with the same pixel size. Dark-field CT could become an interesting ex-vivo tool to obtain complementary information about plaque morphology and to further assess plaque vulnerability. With respect to clinical in-vivo

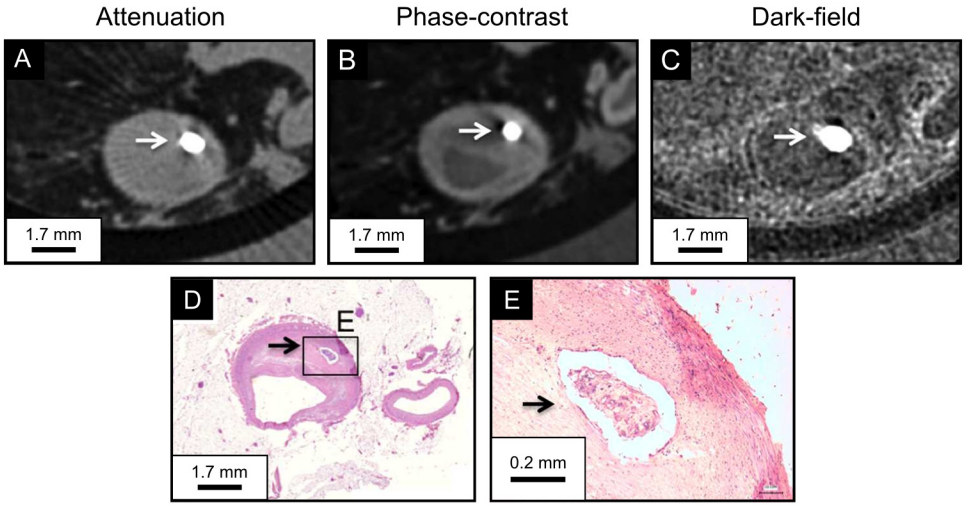

Fig. 7.14 | Exemplary slice of the left anterior descending artery as positive control with high signal intensity in all three modalities. Subfigures (A), (B), and (C) show axial slices of GBPC-CT in three image modalities attenuation (A), phase-contrast (B), and dark-field (C). Subfigures (D) and (E) represent the corresponding HE-stained histology sections, with subfigure (E) being a magnified view. The arrow marks the respective region containing macrocalcifications. The signal intensity is high in all three imaging modalities. The calcifications are presented with higher signal in the dark-field and attenuation images than in the phase-contrast slice. Figure adapted from Hetterich et al. (2017).

applications, further studies are necessary to investigate the results and diagnostic benefits.

Physiologically, the composition and anatomy of atherosclerotic plaques is important to assess the risk for cardiovascular incidents such as myocardial infarction or stroke (Naghavi, 2003a,b). Characteristic risk features are large lipid rich necrotic core, thin overlying fibrous cap, surface defects, and intraplaque hemorrhage. Calcification used to count as a sign for plaque stability, however it has been shown that the role of calcifications is more complex. Although macrocalcifications contribute indeed to plaque stabilization, microcalcifications with a size of less than 60 µm can destabilize the plaque. Microcalcifications are the result of matrix vesicles being released by smooth muscle cells and macrophages within atherosclerotic plaques. These matrix vesicles include calcium binding proteins, which lead to the formation of microcalcifications. The inclusion of relatively hard particles within the soft tissue of the fibrous cap leads to stress in the vessel with subsequent plaque rupture (Hutcheson et al., 2014).

GBPC-CT is capable of differentiating plaque composition due to improved soft tissue contrast (Saam et al., 2013; Hetterich et al., 2013, 2014). Since the dark-field signal is simultaneously acquired alongside the phase-contrast signal in grating interferometry, both signals can provide additional and complementary information on plaque morphology. Although there have not been yet reported any further GBDF-CT studies on atherosclerotic plaque, the results of this study are concordant with similar dark-field radiography studies of breast imaging (Michel et al., 2013; Scherer et al., 2016a). In those studies, the dark-field signal revealed scattering of calcifications on a

micrometer scale.

Since only standard histology was used, ultra small microcalcifications could potentially have been lost due to washing in histopathological sample preparation and are not accessible in this evaluation. However, it has been shown that very small calcifications with sizes less than 5 µm do not increase the risk for plaque rupture and can be neglected with respect to risk evaluation (Kelly-Arnold et al., 2013).

The GBPC-CT setup used for this study is designed and optimized for small biomedical samples at high-sensitivity. As dose optimization and scaling to higher energies are not feasible with this setup, the conclusions discussed in this study are only valid for ex-vivo imaging. Additionally, the rather small number of specimens (15 arteries, 10 cross sections with dark-field signal and no sign of calcifications in other modalities) suggests that further studies with an increased number of specimens are necessary to draw more substantial conclusions.

The three-dimensional visualization of microcalcifications within high risk atherosclerotic plaque would be highly diagnostically relevant and promising if GBDF-CT was translated into clinical application. Clinical in-vivo visualization of microcalcifications is currently difficult. Nuclear medicine techniques using 18F-fluoride PET (positron emission tomography) have recently allowed to visualize the calcification process indirectly by functional molecular imaging of metabolic processes (Chen and Dilsizian, 2013; Joshi et al., 2014). With respect to that, the experimental results of this study suggest that GBDF-CT allows to detect microcalcifications directly at an early stage of their formation and could provide the potential for in-vivo visualization of microcalcifications if the technique could be translated into clinical application.

CHAPTER 8

Conclusions and outlook

8.1 Summary of results

The main results presented in this work were achieved with a laboratory grating-based phase-contrast computed tomography setup with an incoherent, polychromatic X-ray source and are namely
1. The realization of high angular sensitivity GBPC-CT leading to high phase-contrast resolution enabling high soft tissue contrast (cf. Ch. 4),
2. The realization of quantitative measurements leading to the electron density and the effective atomic number (cf. Ch. 5),
3. The increase in image quality by the implementation of tilted gratings reducing the extent of streak artifacts and improving the phase-contrast data (cf. Ch. 6), and
4. The application of GBPC-CT in several biomedical studies for quantitative phase-contrast imaging at high soft tissue resolution (cf. Ch. 7).

High sensitivity GBPC-CT

High angular sensitivity is defined by the minimum resolvable refraction angle. With the demonstrated angular sensitivity values of 5 nrad, it could be demonstrated that high sensitivity is not only limited to synchrotron facilities, but can also be achieved with polychromatic laboratory GBPC-CT setups. The realization of high sensitivity is done by geometrical and statistical considerations. A large inter-grating distance as well as a small period of the analyzer grating are necessary on the one hand. On the other hand, high interferometric visibility and large number of counts are of similar importance to increase the minimum resolvable refraction angle. Thereby, the visibility depends on the setup design like the inter-grating distances and periods as well as grating absorption quality, duty cycle, and type of the phase grating. Additionally, sufficient beam stability has to be provided by the source and vibrations have to be reduced to avoid experimental sensitivity limits. Due to the sensitivity optimization of this GBPC-CT setup, the visualization of subtle soft tissue differences of brain tissue was possible in a laboratory environment, which has been limited to synchrotron facilities.

Quantitative GBPC-CT

High angular sensitivity leads to high electron density resolution in combination with effective energy calibration. As a main result, the achieved electron density resolution lies below 0.5 e/nm^3. Moreover, the effective atomic numbers can be determined by comparing the ratio of the electron density and the simultaneously measured attenuation coefficient with tabulated total cross section data. The results are in good agreement with reference values, as long as the effect of beam-hardening is minimized

by sufficient filtering or beam hardening correction has to be applied. Both the effective atomic number and the electron density are absolute quantities independent of the used energy, which increases the comparability of the imaging signals.

Tilted grating GBPC-CT

The tilted grating method reduces the extent of streak artifacts and improves significantly the quality of GBPC-CT data. Especially at high sensitivity GBPC-CT setups, phase-wrapping occurs easily. Cone-beam geometry usually occurring in laboratory GBPC-CT setups prevents implementing two-dimensional phase-integration. The approach presented here employs the tilt of the gratings by $\pi/4$ around the optical axis in combination with statistical iterative reconstruction. In more detail, the horizontal derivative operator was exchanged with one working in diagonal direction. The retrieved full three-dimensional phase information can the be utilized to reduce the extent of streak artifacts and acquire more homogeneous phase-contrast data. The presented approach allows the use of cone-beam geometry and simplifies the technique in contrast to the analytical realization using direct phase-integration and additional processing.

Biomedical applications of GBPC-CT

A series of different preclinical GBPC-CT ex-vivo studies was successfully investigated to support high-resolution and high-sensitivity application of GBPC-CT. Among others, GBPC-CT of breast specimens containing intraductal carcinoma in situ allowed improved three-dimensional visualization of the tumor extent and the diagnostically relevant dilated ducts. The quantitative characterization of renal carcinoma is superior in GBPC-CT in comparison to clinical imaging methods like MRI and clinical CT without the application of contrast agents. However, in both studies the spatial resolution is still limited and histology is needed to determine the cancer subtype. The use of GBDF-CT of coronary atherosclerotic plaque allowed to detect microcalcifications associated with high risk plaque, since the dark-field signal enables the visualization of structures below the physical pixel size.

8.2 Further development of GBPC-CT

The current setup configuration at high sensitivity is ideal for imaging soft tissue samples at unprecedented electron density resolution realized with laboratory GBPC-CT. However, the general direction of further development of grating-based phase-contrast and dark-field computed tomography goes towards high-resolution ex-vivo phase-contrast imaging in preclinical imaging settings and towards clinical application.

8.2.1 Preclinical application of GBPC-CT

GBPC-CT offers several aspects rendering the method highly interesting for preclinical research as shown in the chapter presenting the biomedical applications (cf. Ch. 7).

GBPC-CT studies of diagnostically relevant samples allowed for three-dimensional tissue visualization and provided quantitative tissue characterization. In order to increase the application range of preclinical GBPC-CT studies, the spatial resolution has to be increased. The ideal resolution level for three-dimensional phase-contrast histology would be below 1 µm to be on a cellular level comparable to histology (Zanette et al., 2013b).

The current GBPC-CT setup presented in this thesis allows for phase-contrast imaging at effective pixel sizes of 80 -100 µm, which corresponds in this case approximately to the spatial resolution. Higher resolution of 28 µm was achieved with the oversampling approach in combination with a different detector, a Dectris Eiger detector with a pixel size of 75 µm. The method is however extremely time-consuming (Viermetz, 2015). Increasing the spatial resolution via geometric magnification is in contradiction to the realization of high sensitivity due to the increased distance from the phase grating to the sample or the necessary change in the setup design, respectively (cf. Ch. 4). Also, the effect of source blurring caused by the focal spot size of the X-ray source increases. Therefore, a different detector, which is both photon-counting and has a higher resolution than the used one here, would only be beneficial if at the same time a different X-ray source with decreased focal spot is employed.

In further detail, decreasing the focal spot of the X-ray source with constant power per area would improve the current setup. Microfocus tubes provide the small spot size, but cannot provide the same level of stable high flux as rotating anode systems. Additionally, higher flux would decrease the still long exposure times and thus increase the applicability of the method.

Although the angular sensitivity is at a high level, it could still be increased to reach higher electron density resolution. For that, the inter-grating distance should be kept large and the periods small. An interesting idea to reach smaller periods is presented in Miao et al. (2015, 2016a,b) allowing ultra high sensitivity using submicron grating periods. Further, the effect of shadowing for compact GBPC-CT setup has to be reduced by improved bendable gratings. Also, the efficiency of the detector and the interferometric visibility could still be increased. Moreover, as the energy dependence of the refractive index decrement is proportional to $1/E^2$, higher electron density resolution would be reached if one shifted the GBPC-CT experiment to lower energies, which means imaging smaller samples.

If fast imaging application is needed, one could implement motionless phase-stepping via deflecting the electron beam of the X-ray tube (Harmon et al., 2015) or intensity-based SIR (IB-SIR) without phase-stepping (Brendel et al., 2015; Teuffenbach et al., 2017).

8.2.2 Towards clinical application

As it turned out, GBPC-CT has many challenges to address if clinical implementation is desired, especially with respect to dose and grating performance at higher energies. Technically, the grating fabrication with high aspect ratios and a stable implementation into a rotating CT scanner is definitely difficult and further improvement of the grating performance at higher energies is needed. Besides, the Compton effect becomes the main interaction process with increasing energy. This leads to a conver-

gence of the attenuation and the phase-contrast signal reducing the complementarity (cf. Sec. 2.1.1). Also, phase-wrapping at the skin-air interface remains an issue, at least for high sensitivity GBPC-CT. Spectral detectors could however reduce the effect of phase-wrapping.

One potential tomographic application could be GBPC-CT of the breast. Dedicated CT systems for breast imaging are in current development (Kalender et al., 2011). The implementation of gratings in such a system could be feasible and provide excellent soft tissue contrast. The needed increase in energy is moderate with approximately $50 - 60\,\mathrm{kVp}$ and the breast contains only soft tissue.

Dark-field imaging

As shown in the introduction, dark-field radiography is highly promising for clinical applications. Dark-field mammography enabled improved visualization of different tumor structures like spiculations and hyperdense tumor foci or revealed microcalcifications (Stampanoni et al., 2011; Grandl et al., 2015; Scherer et al., 2015a, 2016b). Another active field of research is dark-field radiography for chronic obstructive pulmonary diseases, which revealed significantly improved diagnostics, as presented in Bech et al. (2013); Yaroshenko et al. (2013); Meinel et al. (2014); Yaroshenko et al. (2015, 2016); Hellbach et al. (2015, 2016, 2017); Scherer et al. (2017). With the realization of an X-ray grating interferometer operating at higher energies, as shown by dark-field imaging of a living pig (Gromann et al., 2017), clinical implementation of dark-field imaging is within reach.

Furthermore, the search for new contrast agents in combination with dark-field imaging is highly interesting. As conventional contrast agents can have large side-effects like iodine in CT or gadolinium in MRI, the performance of dark-field contrast agents like microbubbles is investigated and could have huge clinical impact (Velroyen et al., 2015). Next to the potential in medical diagnostic application, the dark-field signal is more suitable for clinical realization than the phase-contrast signal with respect to technical realization and dose. As the dark-field signal visualizes structures below the physical pixel size, larger pixel sizes and thus a dose reduction is possible. The sensitivity condition is relaxed allowing larger grating periods and smaller grating distances. Additionally, a water container is not necessary.

Although this setup is not optimized for GBDF-CT, diagnosing athersosclerotic plaques containing microcalcifications was possible and moreover could be scaled in principle to clinical parameters as motivated in simulations in Hetterich et al. (2017). Similar results are to be expected for GBDF-CT for breast diagnostics. The unique potential in GBDF-CT of the breast would lie in the three-dimensional characterization of microcalcifications, which are –as aleady stated – related to the malignancy of breast cancer (Scherer et al., 2016b).

Bibliography

S. Allner, T. Koehler, A. Fehringer, L. Birnbacher, M. Willner, F. Pfeiffer, and P. B. Noël. Bilateral filtering using the full noise covariance matrix applied to X-ray phase-contrast computed tomography. *Physics in Medicine and Biology*, 61(10): 3867–3856, 2016.

J. Als-Nielsen and D. McMorrow. *Elements of Modern X-ray Physics*. John Wiley & Sons, Chichester, 2011.

R. E. Alvarez and A. Macovski. Energy-selective reconstructions in X-ray computerised tomography. *Physics in Medicine and Biology*, 21(5):733, 1976.

M. R. Arnison, K. G. Larkin, C. J. R. Sheppard, N. I. Smith, and C. J. Cogswell. Linear phase imaging using differential interference contrast microscopy. *Journal of Microscopy*, 214(1):7–12, 2004.

S. D. Auweter, J. Herzen, M. Willner, S. Grandl, K. Scherer, F. Bamberg, M. F. Reiser, F. Pfeiffer, and K. Hellerhoff. X-ray phase-contrast imaging of the breast—advances towards clinical implementation. *The British Journal of Radiology*, 87(1034): 20130606, 2014.

M. Bech. *X-ray imaging with a grating interferometer*. PhD thesis, University of Copenhagen, 2009.

M. Bech, A. Tapfer, A. Velroyen, A. Yaroshenko, B. Pauwels, J. Hostens, P. Bruyndonckx, A. Sasov, and F. Pfeiffer. In-vivo dark-field and phase-contrast X-ray imaging. *Scientific Reports*, 3(1), 2013.

E. Becker, W. Ehrfeld, P. Hagmann, A. Maner, and D. Münchmeyer. Fabrication of microstructures with high aspect ratios and great structural heights by synchrotron radiation lithography, galvanoforming, and plastic moulding (LIGA process). *Microelectronic Engineering*, 4(1):35 – 56, 1986.

M. Berger, J. Hubbell, S. Seltzer, J. Chang, J. Coursey, R. Sukumar, D. Zucker, and K. Olsen. XCOM: Photon cross section database (version 1.5)., 2010.

N. Bevins, J. Zambelli, K. Li, Z. Qi, and G.-H. Chen. Multicontrast X-ray computed tomography imaging using Talbot-Lau interferometry without phase stepping. *Medical Physics*, 39(1):424–428, 2011.

L. Birnbacher, M. Willner, A. Velroyen, M. Marschner, A. Hipp, J. Meiser, F. Koch, T. Schröter, D. Kunka, J. Mohr, and et al. Experimental realisation of high-sensitivity laboratory X-ray grating-based phase-contrast computed tomography. *Scientific Reports*, 6(1), 2016.

L. Birnbacher, S. Maurer, K. Scheidt, J. Herzen, F. Pfeiffer, and T. Fromme. Electron density of adipose tissues determined by phase-contrast computed tomography provides a measure for mitochondrial density and fat content. *Frontiers in Physiology*, 9:707, 2018a.

L. Birnbacher, M. Viermetz, W. Noichl, S. Allner, A. Fehringer, M. Marschner, M. Willner, M. von Teuffenbach, K. Achterhold, P. B. Noël, T. Koehler, F. Pfeiffer, and J. Herzen. Tilted grating phase-contrast computed tomography using statistical iterative reconstruction. *Scientific Reports*, 8(6608), 2018b.

L. Birnbacher, M. Willner, M. Marschner, F. Pfeiffer, D. Muenzel, and J. Herzen. Accurate electron density and effective atomic number determination with polychromatic grating-based phase-contrast computed tomography. *Optics Express*, 26 (12):15153–15166, 2018c.

F. E. Boas and D. Fleischmann. CT artifacts: causes and reduction techniques. *Imaging in Medicine*, 4(2):229–240, 2012.

D. T. Boll, N. A. Patil, E. K. Paulson, E. M. Merkle, W. N. Simmons, S. A. Pierre, and G. M. Preminger. Renal stone assessment with dual-energy multidetector CT and advanced postprocessing techniques: Improved characterization of renal stone composition — pilot study. *Radiology*, 250(3):813–820, 2009.

T. Bongartz, K. N. Glazebrook, S. J. Kavros, N. S. Murthy, S. P. Merry, W. B. Franz, C. J. Michet, B. M. Akkara Veetil, J. M. Davis, T. G. Mason, and et al. Dual-energy CT for the diagnosis of gout: An accuracy and diagnostic yield study. *Annals of the Rheumatic Diseases*, 74(6):1072–1077, 2014.

U. Bonse and M. Hart. An X-ray interferometer. *Applied Physics Letters*, 6(8):155–156, 1965.

J. M. Boone and A. E. Chavez. Comparison of X-ray cross sections for diagnostic and therapeutic medical physics. *Medical Physics*, 23(12):1997–2005, 1996.

M. Braunagel, L. Birnbacher, M. Willner, M. Marschner, F. De Marco, M. Viermetz, S. Notohamiprodjo, K. Hellbach, S. Auweter, V. Link, and et al. Qualitative and quantitative imaging evaluation of renal cell carcinoma subtypes with grating-based X-ray phase-contrast CT. *Scientific Reports*, 7:45400, 2017.

A. Bravin, P. Coan, and P. Suortti. X-ray phase-contrast imaging: From pre-clinical applications towards clinics. *Physics in Medicine and Biology*, 58(1):R1–R35, 2012.

B. Brendel, M. von Teuffenbach, P. B. Noël, F. Pfeiffer, and T. Koehler. Penalized maximum likelihood reconstruction for x-ray differential phase-contrast tomography. *Medical Physics*, 43(1):188–194, 2015.

C. Broennimann, E. F. Eikenberry, B. Henrich, R. Horisberger, G. Huelsen, E. Pohl, B. Schmitt, C. Schulze-Briese, M. Suzuki, T. Tomizaki, and et al. The PILATUS 1M detector. *Journal of Synchrotron Radiation*, 13(2):120–130, 2006.

K. Butler-Henderson, A. H. Lee, N. P. Lenzo, and R. I. Price. Epidemiology of ductal carcinoma in situ in Western Australia: Implications for surgical margins and management. *Breast Cancer*, 22(6):641–647, 2014a.

K. Butler-Henderson, A. H. Lee, R. I. Price, and K. Waring. Intraoperative assessment of margins in breast conserving therapy: A systematic review. *The Breast*, 23(2): 112–119, 2014b.

T. Buzug. *Computed tomography: From photon statistics to modern cone-beam CT.* Springer-Verlag Berlin Heidelberg, 2008.

E. Castelli, M. Tonutti, F. Arfelli, R. Longo, E. Quaia, L. Rigon, D. Sanabor, F. Zanconati, D. Dreossi, A. Abrami, and et al. Mammography with synchrotron radiation: First clinical experience with phase-detection technique. *Radiology*, 259(3):684–694, 2011.

M. Chabior. *Contributions to the characterization of grating-based X-ray phase-contrast imaging.* PhD, Technische Universität Dresden, 2011.

M. Chabior, T. Donath, C. David, O. Bunk, M. Schuster, C. Schroer, and F. Pfeiffer. Beam hardening effects in grating-based X-ray phase-contrast imaging. *Medical Physics*, 38(3):1189–1195, 2011a.

M. Chabior, T. Donath, C. David, M. Schuster, C. Schroer, and F. Pfeiffer. Signal-to-noise ratio in X-ray dark-field imaging using a grating interferometer. *Journal of Applied Physics*, 110(5):053105, 2011b.

D. Chapman, W. Thomlinson, R. E. Johnston, D. Washburn, E. Pisano, N. Gmu::r, Z. Zhong, R. Menk, F. Arfelli, and D. Sayers. Diffraction enhanced X-ray imaging. *Physics in Medicine and Biology*, 42(11):2015–2025, 1997.

G.-H. Chen, J. Zambelli, K. Li, N. Bevins, and Z. Qi. Scaling law for noise variance and spatial resolution in differential phase contrast computed tomography. *Medical Physics*, 38(2):584–588, 2011.

W. Chen and V. Dilsizian. Targeted PET/CT imaging of vulnerable atherosclerotic plaques: Microcalcification with sodium fluoride and inflammation with fluorodeoxyglucose. *Current Cardiology Reports*, 15(6), 2013.

P. Cloetens, W. Ludwig, J. Baruchel, J.-P. Guigay, P. Pernot-Rejmánková, M. Salomé-Pateyron, M. Schlenker, J.-Y. Buffière, E. Maire, and G. Peix. Hard X-ray phase imaging using simple propagation of a coherent synchrotron radiation beam. *Journal of Physics D: Applied Physics*, 32(10A):A145–A151, 1999.

A. H. Compton. A quantum theory of the scattering of X-rays by light elements. *Physical Review*, 21(5):483–502, 1923.

C. David, B. Nöhammer, H. H. Solak, and E. Ziegler. Differential X-ray phase contrast imaging using a shearing interferometer. *Applied Physics Letters*, 81(17):3287–3289, 2002.

T. J. Davis, D. Gao, T. E. Gureyev, A. W. Stevenson, and S. W. Wilkins. Phase-contrast imaging of weakly absorbing materials using hard X-rays. *Nature*, 373: 595–598, 1995.

F. De Marco. *Optimizing data processing for grating-based X-ray phase-contrast computed tomography.* Master thesis, Technical University of Munich, 2015.

. Dectris. *PILATUS 100K-S detector system: Technical specification and operating procedure.* Dectris Ltd., Baden, Switzerland, 2014.

P. C. Diemoz, M. Endrizzi, C. K. Hagen, C. Rau, A. Bravin, R. D. Speller, I. K. Robinson, and A. Olivo. Edge illumination X-ray phase-contrast imaging: nanoradian sensitivity at synchrotrons and translation to conventional sources. *Journal of Physics: Conference Series*, 499:012006, 2014.

T. Donath, F. Beckmann, and A. Schreyer. Automated determination of the center of rotation in tomography data. *Journal of the Optical Society of America A*, 23(5): 1048, 2006.

T. Donath, M. Chabior, F. Pfeiffer, O. Bunk, E. Reznikova, J. Mohr, E. Hempel, S. Popescu, M. Hoheisel, M. Schuster, J. Baumann, and C. David. Inverse geometry for grating-based X-ray phase-contrast imaging. *Journal of Applied Physics*, 106(5), 2009.

T. Donath, F. Pfeiffer, O. Bunk, C. Grünzweig, E. Hempel, S. Popescu, P. Vock, and C. David. Toward clinical X-ray phase-contrast CT. *Investigative Radiology*, page 1, 2010.

D. Dreossi, A. Abrami, F. Arfelli, P. Bregant, K. Casarin, V. Chenda, M. Cova, R. Longo, R.-H. Menk, E. Quai, and et al. The mammography project at the SYRMEP beamline. *European Journal of Radiology*, 68(3):S58–S62, 2008.

S. B. Edwards, I. M. Leitman, A. J. Wengrofsky, M. J. Giddins, E. Harris, C. B. Mills, S. Fukuhara, and S. Cassaro. Identifying factors and techniques to decrease the positive margin rate in partial mastectomies: Have we missed the mark? *The Breast Journal*, 22(3):303–309, 2016.

E. Eggl, S. Schleede, M. Bech, K. Achterhold, R. Loewen, R. D. Ruth, and F. Pfeiffer. X-ray phase-contrast tomography with a compact laser-driven synchrotron source. *Proceedings of the National Academy of Sciences*, 112(18):5567–5572, 2015.

E. Eggl, M. Dierolf, K. Achterhold, C. Jud, B. Günther, E. Braig, B. Gleich, and F. Pfeiffer. The Munich compact light source: initial performance measures. *Journal of Synchrotron Radiation*, 23(5):1137–1142, 2016.

K. J. Engel, D. Geller, T. Köhler, G. Martens, S. Schusser, G. Vogtmeier, and E. Rössl. Contrast-to-noise in X-ray differential phase contrast imaging. *Nuclear Instruments and Methods in Physics Research, Section A: Accelerators, Spectrometers, Detectors and Associated Equipment*, 648(SUPPL. 1):202–207, 2011.

M. Engelhardt, J. Baumann, M. Schuster, C. Kottler, F. Pfeiffer, O. Bunk, and C. David. High-resolution differential phase contrast imaging using a magnifying projection geometry with a microfocus X-ray source. *Applied Physics Letters*, 90 (22):90–92, 2007.

F. M. Epple, G. Potdevin, P. Thibault, S. Ehn, J. Herzen, A. Hipp, F. Beckmann, and F. Pfeiffer. Unwrapping differential X-ray phase-contrast images through phase estimation from multiple energy data. *Optics Express*, 21(24):29101, 2013.

F. M. Epple, S. Ehn, P. Thibault, T. Koehler, G. Potdevin, J. Herzen, D. Pennicard, H. Graafsma, P. B. Noel, and F. Pfeiffer. Phase unwrapping in spectral X-ray differential phase-contrast imaging with an energy-resolving photon-counting pixel detector. *IEEE Transactions on Medical Imaging*, 34(3):816–823, 2015.

B. Escudier, C. Porta, M. Schmidinger, F. Algaba, J. J. Patard, V. Khoo, T. Eisen, and A. Horwich. Renal cell carcinoma: ESMO clinical practice guidelines for diagnosis, treatment and follow-up. *Annals of Oncology*, 25(suppl 3):iii49–iii56, 2014.

L. A. Feldkamp, L. C. Davis, and J. W. Kress. Practical cone-beam algorithm. *Journal of the Optical Society of America A*, 1(6):612, 1984.

J. A. Fessler. *Tomography handbook of medical imaging, volume 2. Medical image processing and analysis: Statistical image reconstruction methods for transmission.* SPIE, Bellingham, 2000.

A. A. Fingerle, M. Willner, J. Herzen, D. Münzel, D. Hahn, E. J. Rummeny, P. B. Noël, and F. Pfeiffer. Simulated cystic renal lesions: Quantitative X-ray phase-contrast CT—An in vitro phantom study. *Radiology*, 272(3):739–748, 2014.

R. Fitzgerald. Phase-sensitive X-ray imaging. *Physics Today*, 53(7):23–26, 2000.

S. H. Gage. Modern dark-field microscopy and the history of its development. *Transactions of the American Microscopical Society*, 39(2):95–141, 2009.

S. Grandl, M. Willner, J. Herzen, D. Mayr, S. D. Auweter, A. Hipp, F. Pfeiffer, M. Reiser, and K. Hellerhoff. Evaluation of phase-contrast CT of breast tissue at conventional X-ray sources – presentation of selected findings. *Zeitschrift für Medizinische Physik*, 23(3):212–221, 2013.

S. Grandl, M. Willner, J. Herzen, A. Sztrókay-Gaul, D. Mayr, S. D. Auweter, A. Hipp, L. Birnbacher, M. Marschner, M. Chabior, and et al. Visualizing typical features of breast fibroadenomas using phase-contrast CT: An ex-vivo study. *PLOS ONE*, 9 (5):e97101, 2014.

S. Grandl, K. Scherer, A. Sztrókay-Gaul, L. Birnbacher, K. Willer, M. Chabior, J. Herzen, D. Mayr, S. D. Auweter, F. Pfeiffer, and et al. Improved visualization of breast cancer features in multifocal carcinoma using phase-contrast and dark-field mammography: An ex vivo study. *European Radiology*, 25(12):3659–3668, 2015.

L. B. Gromann, D. Bequé, K. Scherer, K. Willer, L. Birnbacher, M. Willner, J. Herzen, S. Grandl, K. Hellerhoff, J. I. Sperl, and et al. Low-dose, phase-contrast mammography with high signal-to-noise ratio. *Biomedical Optics Express*, 7(2):381, 2016.

L. B. Gromann, F. De Marco, K. Willer, P. B. Noël, K. Scherer, B. Renger, B. Gleich, K. Achterhold, A. A. Fingerle, D. Muenzel, and et al. In-vivo X-ray dark-field chest radiography of a pig. *Scientific Reports*, 7(1), 2017.

J. Grznar, D. E. Booth, and P. Sebastian. A robust smoothing approach to statistical process control. *Journal of Chemical Information and Computer Sciences*, 37(2): 241–248, 1997.

M. Guizar-Sicairos, J. J. Boon, K. Mader, A. Diaz, A. Menzel, and O. Bunk. Quantitative interior X-ray nanotomography by a hybrid imaging technique. *Optica*, 2(3): 259, 2015.

C. Habbel, H. Hetterich, M. Willner, J. Herzen, K. Steigerwald, S. Auweter, U. Schüller, J. Hausleiter, S. Massberg, M. Reiser, and et al. Ex vivo assessment of coronary atherosclerotic plaque by grating-based phase-contrast computed tomography. *Investigative Radiology*, 52(4):223–231, 2017.

D. Hahn. *Statistical iterative reconstruction for X-ray phase contrast computed tomography*. PhD thesis, Technical University of Munich, 2014.

D. Hahn, P. Thibault, A. Fehringer, M. Bech, T. Koehler, F. Pfeiffer, and P. B. Noøel. Statistical iterative reconstruction algorithm for X-ray phase-contrast CT. *Scientific Reports*, 5(1), 2015.

K. J. Harmon, H. Miao, A. A. Gomella, E. E. Bennett, B. A. Foster, P. Bhandarkar, and H. Wen. Motionless electromagnetic phase stepping versus mechanical phase stepping in x-ray phase-contrast imaging with a compact source. *Physics in Medicine and Biology*, 60(8):3031–3043, 2015.

J. K. Harness, A. E. Giuliano, B. A. Pockaj, and E. Downs-Kelly. Margins: A status report from the annual meeting of the american society of breast surgeons. *Annals of Surgical Oncology*, 21(10):3192–3197, 2014.

N. Hauser, Z. Wang, R. A. Kubik-Huch, M. Trippel, G. Singer, M. K. Hohl, E. Roessl, T. Köhler, U. van Stevendaal, N. Wieberneit, and et al. A study on mastectomy samples to evaluate breast imaging quality and potential clinical relevance of differential phase contrast mammography. *Investigative Radiology*, 49(3):131–137, 2014.

K. Hellbach, A. Yaroshenko, F. G. Meinel, A. O. Yildirim, T. M. Conlon, M. Bech, M. Mueller, A. Velroyen, M. Notohamiprodjo, F. Bamberg, and et al. In vivo dark-field radiography for early diagnosis and staging of pulmonary emphysema. *Investigative Radiology*, 50(7):430–435, 2015.

K. Hellbach, A. Yaroshenko, K. Willer, T. Pritzke, A. Baumann, N. Hesse, S. Auweter, M. F. Reiser, O. Eickelberg, F. Pfeiffer, and et al. Facilitated diagnosis of pneumothoraces in newborn mice using X-ray dark-field radiography. *Investigative Radiology*, 51(10):597–601, 2016.

K. Hellbach, A. Yaroshenko, K. Willer, T. M. Conlon, M. B. Braunagel, S. Auweter, A. O. Yildirim, O. Eickelberg, F. Pfeiffer, M. F. Reiser, and et al. X-ray dark-field radiography facilitates the diagnosis of pulmonary fibrosis in a mouse model. *Scientific Reports*, 7(1), 2017.

K. Hellerhoff, L. Birnbacher, S. Grandl, J. Herzen, M. Marschner, M. Willner, D. Mayr, S. Auweter, M. F. Reiser, F. Pfeiffer, and A. Sztrókay-Gaul. Assessment of intraductal carcinoma in situ (DCIS) using grating-based X-ray phase-contrast CT at conventional X-ray sources: an experimental ex-vivo study. *PLOS ONE (accepted)*, 2018.

J. Henes, M. Fuld, E. Fishman, M. Horger, and J. Fritz. Dual-energy computed tomography of the knee, ankle, and foot: Noninvasive diagnosis of gout and quantification of monosodium urate in tendons and ligaments. *Seminars in Musculoskeletal Radiology*, 20(01):130–136, 2016.

G. T. Herman. Correction for beam hardening in computed tomography. *Physics in Medicine and Biology*, 24(1):81–106, 1979.

J. Herzen, T. Donath, F. Pfeiffer, O. Bunk, C. Padeste, F. Beckmann, A. Schreyer, and C. David. Quantitative phase-contrast tomography of a liquid phantom using a conventional X-ray tube source. *Optics Express*, 17(12):10010, 2009.

J. Herzen, M. S. Willner, A. A. Fingerle, P. B. Noël, T. Köhler, E. Drecoll, E. J. Rummeny, and F. Pfeiffer. Imaging liver lesions using grating-based phase-contrast computed tomography with bi-lateral filter post-processing. *PLOS ONE*, 9(1):e83369, 2014.

H. Hetterich, S. Fill, J. Herzen, M. Willner, I. Zanette, T. Weitkamp, A. Rack, U. Schüller, M. Sadeghi, R. Brandl, and et al. Grating-based X-ray phase-contrast tomography of atherosclerotic plaque at high photon energies. *Zeitschrift für Medizinische Physik*, 23(3):194–203, 2013.

H. Hetterich, M. Willner, S. Fill, J. Herzen, F. Bamberg, A. Hipp, U. Schüller, S. Adam-Neumair, S. Wirth, M. Reiser, and et al. Phase-contrast CT: Qualitative and quantitative evaluation of atherosclerotic carotid artery plaque. *Radiology*, 271(3):870–878, 2014.

H. Hetterich, N. Webber, M. Willner, J. Herzen, L. Birnbacher, A. Hipp, M. Marschner, S. D. Auweter, C. Habbel, U. Schüller, and et al. AHA classification of coronary and carotid atherosclerotic plaques by grating-based phase-contrast computed tomography. *European Radiology*, 26(9):3223–3233, 2015a.

H. Hetterich, M. Willner, C. Habbel, J. Herzen, V. S. Hoffmann, S. Fill, A. Hipp, M. Marschner, U. Schüller, S. Auweter, and et al. X-ray phase-contrast computed tomography of human coronary arteries. *Investigative Radiology*, 50(10):686–694, 2015b.

H. Hetterich, N. Webber, M. Willner, J. Herzen, L. Birnbacher, S. Auweter, U. Schüller, F. Bamberg, S. Notohamiprodjo, H. Bartsch, J. Wolf, M. Marschner, F. Pfeiffer, and T. Saam. Dark-field imaging in coronary atherosclerosis. *European Journal of Radiology*, 94:38–45, 2017.

G. Hidas, R. Eliahou, M. Duvdevani, P. Coulon, L. Lemaitre, O. N. Gofrit, D. Pode, and J. Sosna. Determination of renal stone composition with dual-energy CT: In vivo analysis and comparison with X-ray diffraction. *Radiology*, 257(2):394–401, 2010.

A. Hipp. *Highly sensitive grating interferometry using a polychromatic X-ray-source.* Diploma thesis, Technical University of Munich, 2013.

A. Hipp, M. Willner, J. Herzen, S. Auweter, M. Chabior, J. Meiser, K. Achterhold, J. Mohr, and F. Pfeiffer. Energy-resolved visibility analysis of grating interferometers operated at polychromatic X-ray sources. *Optics Express*, 22(25):30394, 2014.

R. Hooke. *Micrographia or Some physiological descriptions of minute bodies made by magnifying glasses: with observations and inquiries thereupon.* Printed by Jo. Martyn and Ja. Allestry, printers to the Royal Society, 1665.

N. Houssami and M. Morrow. Margins in breast conservation: A clinician's perspective and what the literature tells us. *Journal of Surgical Oncology*, 110(1):2–7, 2014.

J. H. Hubbell. Photon cross sections, attenuation coefficients, and energy absorption coefficients from 10 keV to 100 GeV. *Technical reports, NSRDS-NBS*, 1969.

B. Y. Hur, J. M. Lee, W. Hyunsik, K. B. Lee, I. Joo, J. K. Han, and B. I. Choi. Quantification of the fat fraction in the liver using dual-energy computed tomography and multimaterial decomposition. *Journal of Computer Assisted Tomography*, 38 (6):845–852, 2014.

J. D. Hutcheson, N. Maldonado, and E. Aikawa. Small entities with large impact. *Current Opinion in Lipidology*, 25(5):327–332, 2014.

T. Hyodo, M. Hori, P. Lamb, K. Sasaki, T. Wakayama, Y. Chiba, T. Mochizuki, and T. Murakami. Multimaterial decomposition algorithm for the quantification of liver fat content by using fast-kilovolt-peak switching dual-Energy CT: Experimental validation. *Radiology*, 282(2):381–389, 2017.

H. Itoh, K. Nagai, G. Sato, K. Yamaguchi, T. Nakamura, T. Kondoh, C. Ouchi, T. Teshima, Y. Setomoto, and T. Den. Two-dimensional grating-based X-ray phase-contrast imaging using Fourier transform phase retrieval. *Optics Express*, 19(4):3339, 2011.

T. H. Jensen, M. Bech, O. Bunk, T. Donath, C. David, R. Feidenhans'l, and F. Pfeiffer. Directional X-ray dark-field imaging. *Physics in Medicine and Biology*, 55(12): 3317–3323, 2010.

W. Jian, M. Wu, H. Shi, L. Wang, L. Zhang, and S. Luo. Signs analysis and clinical assessment: Phase-contrast computed tomography of human breast tumours. *PLOS ONE*, 10(4):e0124143, 2015.

N. V. Joshi, A. T. Vesey, M. C. Williams, A. S. V. Shah, P. A. Calvert, F. H. M. Craighead, S. E. Yeoh, W. Wallace, D. Salter, A. M. Fletcher, and et al. 18F-fluoride positron emission tomography for identification of ruptured and high-risk coronary atherosclerotic plaques: A prospective clinical trial. *The Lancet*, 383(9918): 705–713, 2014.

P. Jungmann, D. Karampinos, P. Foehr, L. Birnbacher, M. Viermetz, R. Burgkart, T. Baum, F. Lohoefer, M. Wildgruber, F. Schilling, M. Willner, M. Marschner, P. B. Noël, E. J. Rummeny, F. Pfeiffer, and J. Herzen. Grating-based X-ray phase-contrast imaging for high-resolution quantitative assessment of cartilage: An experimental feasibility study with 3T MRI, 7T MRI and biomechanical correlation. *Osteoarthritis and Cartilage (submitted)*, 2018.

A. Kak and M. Slaney. *Principles of computerized tomographic imaging*. IEEE Press, 1988. ISBN 9780879421984.

W. A. Kalender. X-ray computed tomography. *Physics in Medicine and Biology*, 51 (13):R29–R43, 2006.

W. A. Kalender, M. Beister, J. M. Boone, D. Kolditz, S. V. Vollmar, and M. C. C. Weigel. High-resolution spiral CT of the breast at very low dose: Concept and feasibility considerations. *European Radiology*, 22(1):1–8, 2011.

A. Kelly-Arnold, N. Maldonado, D. Laudier, E. Aikawa, L. Cardoso, and S. Weinbaum. Revised microcalcification hypothesis for fibrous cap rupture in human coronary arteries. *Proceedings of the National Academy of Sciences*, 110(26):10741–10746, 2013.

J. Kenntner. *Herstellung von Gitterstrukturen mit Aspektverhältnis 100 für die Phasenkontrastbildgebung in einem Talbot-Interferometer*. PhD thesis, Karlsruher Institut für Technologie (KIT), 2012.

J. Keyriläinen, A. Bravin, M. Fernández, M. Tenhunen, P. Virkkunen, and P. Suortti. Phase-contrast X-ray imaging of breast. *Acta Radiologica*, 51(8):866–884, 2010.

J. K. Kim, T. K. Kim, H. J. Ahn, C. S. Kim, K.-R. Kim, and K.-S. Cho. Differentiation of subtypes of renal cell carcinoma on helical CT scans. *American Journal of Roentgenology*, 178(6):1499–1506, 2002.

O. Klein and Y. Nishina. Über die Streuung von Strahlung durch freie Elektronen nach der neuen relativistischen Quantendynamik von Dirac. *Z. Phys.*, 52(11-12): 853 – 869, 1929.

F. J. Koch, T. J. Schröter, D. Kunka, P. Meyer, J. Meiser, A. Faisal, M. I. Khalil, L. Birnbacher, M. Viermetz, M. Walter, and et al. Note: Gratings on low absorbing substrates for X-ray phase contrast imaging. *Review of Scientific Instruments*, 86 (12):126114, 2015.

T. Köhler, K. Jürgen Engel, and E. Roessl. Noise properties of grating-based X-ray phase contrast computed tomography. *Medical Physics*, 38(S1):S106–S116, 2011.

C. Kottler, C. David, F. Pfeiffer, and O. Bunk. A two-directional approach for grating based differential phase contrast imaging using hard x-rays. *Optics Express*, 15(3): 1175, 2007a.

C. Kottler, F. Pfeiffer, O. Bunk, C. Grünzweig, and C. David. Grating interferometer based scanning setup for hard x-ray phase contrast imaging. *Review of Scientific Instruments*, 78(4):043710, 2007b.

T. Köhler, H. Daerr, G. Martens, N. Kuhn, S. Löscher, U. van Stevendaal, and E. Roessl. Slit-scanning differential X-ray phase-contrast mammography: Proof-of-concept experimental studies. *Medical Physics*, 42(4):1959–1965, 2015.

J. Lam, O. Shvarts, J. Leppert, R. Figlin, and A. Belldegrun. Renal cell carcinoma 2005: New frontiers in staging, prognostication and targeted molecular therapy. *The Journal of Urology*, 173(6):1853–1862, 2005.

T. Lebret, J. E. Poulain, V. Molinie, J. M. Herve, Y. Denoux, A. Guth, A. Scherrer, and H. Botto. Percutaneous core biopsy for renal masses: Indications, accuracy and results. *The Journal of Urology*, 178(4):1184–1188, 2007.

S. Leng, A. Huang, J. M. Cardona, X. Duan, J. C. Williams, and C. H. McCollough. Dual-energy CT for quantification of urinary stone composition in mixed stones: A phantom study. *American Journal of Roentgenology*, 207(2):321–329, 2016.

R. Longo, F. Arfelli, R. Bellazzini, U. Bottigli, A. Brez, F. Brun, A. Brunetti, P. Delogu, F. Di Lillo, D. Dreossi, and et al. Towards breast tomography with synchrotron radiation at Elettra: First images. *Physics in Medicine and Biology*, 61(4): 1634–1649, 2016.

L. B. Lucy. An iterative technique for the rectification of observed distributions. *The Astronomical Journal*, 79:745, 1974.

S. K. Lynch, V. Pai, J. Auxier, A. F. Stein, E. E. Bennett, C. K. Kemble, X. Xiao, W.-K. Lee, N. Y. Morgan, and H. H. Wen. Interpretation of dark-field contrast and particle-size selectivity in grating interferometers. *Applied optics*, 50(22):4310–4319, 2011.

A. Malecki, G. Potdevin, and F. Pfeiffer. Quantitative wave-optical numerical analysis of the dark-field signal in grating-based X-ray interferometry. *Europhysics Letters*, 99(4):48001, 2012.

M. Marschner. *Data processing in grating-based X-ray phase-contrast computed tomography: Workflow automation and noise studies.* Diploma thesis, Technical University of Munich, 2013.

M. Marschner, L. Birnbacher, K. Mechlem, W. Noichl, A. Fehringer, M. Willner, K. Scherer, J. Herzen, P. Noël, and F. Pfeiffer. Two-shot X-ray dark-field imaging. *Optics Express*, 24(23):27032, 2016a.

M. Marschner, M. Willner, G. Potdevin, A. Fehringer, P. B. Noël, F. Pfeiffer, and J. Herzen. Helical X-ray phase-contrast computed tomography without phase stepping. *Scientific Reports*, 6(1), 2016b.

M. Marschner, L. Birnbacher, M. Willner, M. Chabior, J. Herzen, P. B. Noël, and F. Pfeiffer. Revising the lower statistical limit of X-ray grating-based phase-contrast computed tomography. *PLOS ONE*, 12(9):e0184217, 2017.

E. C. McCullough. Photon attenuation in computed tomography. *Medical Physics*, 2 (6):307–320, 1975.

S. A. McDonald, F. Marone, C. Hintermüller, G. Mikuljan, C. David, F. Pfeiffer, and M. Stampanoni. Advanced phase-contrast imaging using a grating interferometer. *Journal of Synchrotron Radiation*, 16(4):562–572, 2009.

F. G. Meinel, A. Yaroshenko, K. Hellbach, M. Bech, M. Müller, A. Velroyen, F. Bamberg, O. Eickelberg, K. Nikolaou, M. F. Reiser, and et al. Improved diagnosis of pulmonary emphysema using in vivo dark-field radiography. *Investigative Radiology*, 49(10):653–658, 2014.

J. Meiser, M. Willner, T. Schröter, A. Hofmann, J. Rieger, F. Koch, L. Birnbacher, M. Schüttler, D. Kunka, P. Meyer, and et al. Increasing the field of view in grating based X-ray phase contrast imaging using stitched gratings. *Journal of X-ray Science and Technology*, 24(3):379–388, 2016.

H. Miao, A. A. Gomella, K. J. Harmon, E. E. Bennett, N. Chedid, S. Znati, A. Panna, B. A. Foster, P. Bhandarkar, and H. Wen. Enhancing tabletop X-ray phase contrast imaging with nano-fabrication. *Scientific Reports*, 5(1), 2015.

H. Miao, L. Chen, M. Mirzaeimoghri, R. Kasica, and H. Wen. Cryogenic etching of high aspect ratio 400-nm pitch silicon gratings. *Journal of Microelectromechanical Systems*, 25(5):963–967, 2016a.

H. Miao, A. Panna, A. A. Gomella, E. E. Bennett, S. Znati, L. Chen, and H. Wen. A universal moiré effect and application in X-ray phase-contrast imaging. *Nature Physics*, 12(9):830–834, 2016b.

T. Michel, J. Rieger, G. Anton, F. Bayer, M. W. Beckmann, J. Durst, P. A. Fasching, W. Haas, A. Hartmann, G. Pelzer, and et al. On a dark-field signal generated by micrometer-sized calcifications in phase-contrast mammography. *Physics in Medicine and Biology*, 58(8):2713–2732, 2013.

P. Modregger, B. R. Pinzer, T. Thüring, S. Rutishauser, C. David, and M. Stampanoni. Sensitivity of X-ray grating interferometry. *Optics express*, 19(19):18324–18338, 2011.

A. Momose. Phase-sensitive imaging and phase tomography using X-ray interferometers. *Optics express*, 11(19):2303–2314, 2003.

A. Momose, T. Takeda, Y. Itai, and K. Hirano. Phase–contrast X–ray computed tomography for observing biological soft tissues. *Nature Medicine*, 2(4):473–475, 1996.

A. Momose, S. Kawamoto, I. Koyama, Y. Hamaishi, K. Takai, and Y. Suzuki. Demonstration of X-ray Talbot interferometry. *Japanese Journal of Applied Physics*, 42 (Part 2, No. 7B):L866–L868, 2003.

D. B. Murphy and M. W. Davidson. *Fundamentals of light microscopy and electronic imaging*. John Wiley & Sons, Chichester, 2013.

R. C. Murty. Effective atomic numbers of heterogeneous materials. *Nature*, 207(4995): 398–399, 1965.

M. Naghavi. From vulnerable plaque to vulnerable patient: A call for new definitions and risk assessment strategies: Part I. *Circulation*, 108(14):1664–1672, 2003a.

M. Naghavi. From vulnerable plaque to vulnerable patient: A call for new definitions and risk assessment strategies: Part II. *Circulation*, 108(15):1772–1778, 2003b.

Y. I. Nesterets, T. E. Gureyev, S. C. Mayo, A. W. Stevenson, D. Thompson, J. M. C. Brown, M. J. Kitchen, K. M. Pavlov, D. Lockie, F. Brun, and et al. A feasibility study of X-ray phase-contrast mammographic tomography at the Imaging and Medical beamline of the Australian Synchrotron. *Journal of Synchrotron Radiation*, 22 (6):1509–1523, 2015.

M. Nilchian, C. Vonesch, P. Modregger, M. Stampanoni, and M. Unser. Fast iterative reconstruction of differential phase contrast X-ray tomograms. *Optics Express*, 21 (5):5511, 2013.

J. Nocedal. Updating quasi-Newton matrices with limited storage. *Mathematics of Computation*, 35(151):773–773, 1980.

G. Nomarski. Nouveau dispositif pour l'observation en contraste de phase différentiel. *Journal de Physique et Le Radium*, 16, 1955.

S. Notohamiprodjo, N. Webber, L. Birnbacher, M. Willner, M. Viermetz, J. Herzen, M. Marschner, D. Mayr, H. Bartsch, T. Saam, and et al. Qualitative and quantitative evaluation of structural myocardial alterations by grating-based phase-contrast computed tomography. *Investigative Radiology*, page 1, 2017.

R. Nowotny. XMuDat: photon attenuation data on PC. Tech. Rep. IAEA-NDS-195, International Atomic Energy Agency, Vienna, Austria, `https://www-nds.iaea.org/publications/iaea-nds/iaea-nds-0195.htm.`, 1998. [Online; accessed 21-June-2017].

N. Okazaki and J. Nocedal. Liblbfgs: a library of limited-memory broyden-fletcher-goldfarb-shanno (l-bfgs). *URL http://www.chokkan.org/software/liblbfgs*, 2010.

D. M. Paganin. *Coherent X-ray optics.* Oxford science publications, 2006.

S. Pani, R. Longo, D. Dreossi, F. Montanari, A. Olivo, F. Arfelli, A. Bergamaschi, P. Poropat, L. Rigon, F. Zanconati, and et al. Breast tomography with synchrotron radiation: preliminary results. *Physics in Medicine and Biology*, 49(9):1739–1754, 2004.

I. Pedrosa, M. T. Chou, L. Ngo, R. H. Baroni, E. M. Genega, L. Galaburda, W. C. DeWolf, and N. M. Rofsky. MR classification of renal masses with pathologic correlation. *European Radiology*, 18(2):365–375, 2007.

F. Pfeiffer, T. Weitkamp, O. Bunk, and C. David. Phase retrieval and differential phase-contrast imaging with low-brilliance X-ray sources. *Nature Physics*, 2(4):258–261, 2006.

F. Pfeiffer, O. Bunk, C. David, M. Bech, G. Le Duc, A. Bravin, and P. Cloetens. High-resolution brain tumor visualization using three-dimensional X-ray phase contrast tomography. *Physics in Medicine and Biology*, 52(23):6923–6930, 2007a.

F. Pfeiffer, C. Kottler, O. Bunk, and C. David. Hard X-ray phase tomography with low-brilliance sources. *Physical Review Letters*, 98(10):108105, 2007b.

F. Pfeiffer, M. Bech, O. Bunk, P. Kraft, E. F. Eikenberry, C. Brönnimann, C. Grünzweig, and C. David. Hard-X-ray dark-field imaging using a grating interferometer. *Nature materials*, 7(2):134–137, 2008.

F. Pfeiffer, M. Bech, O. Bunk, T. Donath, B. Henrich, P. Kraft, and C. David. X-ray dark-field and phase-contrast imaging using a grating interferometer. *Journal of Applied Physics*, 105(10):102006, 2009.

F. Pfeiffer, J. Herzen, M. Willner, M. Chabior, S. Auweter, M. Reiser, and F. Bamberg. Grating-based X-ray phase contrast for biomedical imaging applications. *Zeitschrift für Medizinische Physik*, 23(3):176–185, 2013.

P. M. Pierorazio, E. S. Hyams, S. Tsai, Z. Feng, B. J. Trock, J. K. Mullins, P. T. Johnson, E. K. Fishman, and M. E. Allaf. Multiphasic enhancement patterns of small renal masses ($\leq$4 cm) on preoperative computed tomography: Utility for distinguishing subtypes of renal cell carcinoma, angiomyolipoma, and oncocytoma. *Urology*, 81(6):1265–1272, 2013.

F. Prade, A. Yaroshenko, J. Herzen, and F. Pfeiffer. Short-range order in mesoscale systems probed by X-ray grating interferometry. *EPL (Europhysics Letters)*, 112 (6):68002, 2015.

Z. Qi, J. Zambelli, N. Bevins, and G.-H. Chen. Quantitative imaging of electron density and effective atomic number using phase contrast CT. *Physics in Medicine and Biology*, 55(9):2669–2677, 2010.

J. Radon. On the determination of functions from their integral values along certain manifolds. *IEEE Transactions on Medical Imaging*, 5(4):170–176, 1986.

R. Raupach and T. G. Flohr. Analytical evaluation of the signal and noise propagation in X-ray differential phase-contrast computed tomography. *Physics in Medicine and Biology*, 56(7):2219–2244, 2011.

V. Revol, C. Kottler, R. Kaufmann, U. Straumann, and C. Urban. Noise analysis of grating-based X-ray differential phase contrast imaging. *Review of Scientific Instruments*, 81(7):073709, 2010.

E. Reznikova, J. Mohr, M. Boerner, V. Nazmov, and P.-J. Jakobs. Soft X-ray lithography of high aspect ratio SU8 submicron structures. *Microsystem Technologies*, 14 (9):1683–1688, 2008.

W. H. Richardson. Bayesian-based iterative method of image restoration. *Journal of the Optical Society of America*, 62(1):55, 1972.

V. Richter, M. S. Willner, J. Henningsen, L. Birnbacher, M. Marschner, J. Herzen, M. A. Kimm, P. B. Noël, E. J. Rummeny, F. Pfeiffer, and et al. Ex vivo characterization of pathologic fluids with quantitative phase-contrast computed tomography. *European Journal of Radiology*, 86:99–104, 2017.

B. I. Rini, S. C. Campbell, and B. Escudier. Renal cell carcinoma. *Lancet*, 373(9669): 1119–1132, 2009.

W. C. Röntgen. Über eine neue Art von Strahlen. *Annalen der Physik*, 300(1):12–17, 1898.

S. Rutishauser, T. Donath, C. David, F. Pfeiffer, F. Marone, P. Modregger, and M. Stampanoni. A tilted grating interferometer for full vector field differential X-ray phase contrast tomography. *Optics Express*, 19(25):24890, 2011.

T. Saam, J. Herzen, H. Hetterich, S. Fill, M. Willner, M. Stockmar, K. Achterhold, I. Zanette, T. Weitkamp, U. Schüller, S. Auweter, S. Adam-Neumair, K. Nikolaou, M. F. Reiser, F. Pfeiffer, and F. Bamberg. Translation of atherosclerotic plaque phase-contrast CT imaging from synchrotron radiation to a conventional lab-based X-ray source. *PLOS ONE*, 8(9):e73513, 2013.

A. Sarapata, M. Chabior, C. Cozzini, J. I. Sperl, D. Bequé, O. Langner, J. Coman, I. Zanette, M. Ruiz-Yaniz, and F. Pfeiffer. Quantitative electron density characterization of soft tissue substitute plastic materials using grating-based X-ray phase-contrast imaging. *Review of Scientific Instruments*, 85(10):103708, 2014.

A. Sarapata, M. Willner, M. Walter, T. Duttenhofer, K. Kaiser, P. Meyer, C. Braun, A. Fingerle, P. B. Noël, F. Pfeiffer, and J. Herzen. Quantitative imaging using high-energy X-ray phase-contrast CT with a 70 kVp polychromatic X-ray spectrum. *Optics Express*, 23(1):523, 2015.

F. Sardanelli. Trends in radiology and experimental research. *European Radiology Experimental*, 1(1), 2017.

K. Scherer. *Grating-based X-ray phase-contrast mammography*. PhD thesis, Technical University of Munich, 2015.

K. Scherer, L. Birnbacher, M. Chabior, J. Herzen, D. Mayr, S. Grandl, A. Sztrókay-Gaul, K. Hellerhoff, F. Bamberg, and F. Pfeiffer. Bi-directional X-ray phase-contrast mammography. *PLOS ONE*, 9(5):e93502, 2014.

K. Scherer, E. Braig, K. Willer, M. Willner, A. A. Fingerle, M. Chabior, J. Herzen, M. Eiber, B. Haller, M. Straub, H. Schneider, E. J. Rummeny, P. B. Noël, and F. Pfeiffer. Non-invasive differentiation of kidney stone types using X-ray dark-field radiography. *Scientific Reports*, 5:9527, 2015a.

K. Scherer, K. Willer, L. Gromann, L. Birnbacher, E. Braig, S. Grandl, A. Sztrókay-Gaul, J. Herzen, D. Mayr, K. Hellerhoff, and et al. Toward clinically compatible phase-contrast mammography. *PLOS ONE*, 10(6):e0130776, 2015b.

K. Scherer, L. Birnbacher, K. Willer, M. Chabior, J. Herzen, and F. Pfeiffer. Correspondence: Quantitative evaluation of X-ray dark-field images for microcalcification analysis in mammography. *Nature Communications*, 7:10863, 2016a.

K. Scherer, E. Braig, S. Ehn, J. Schock, J. Wolf, L. Birnbacher, M. Chabior, J. Herzen, D. Mayr, S. Grandl, and et al. Improved diagnostics by assessing the micromorphology of breast calcifications via X-ray dark-field radiography. *Scientific Reports*, 6(1), 2016b.

K. Scherer, A. Yaroshenko, D. A. Bölükbas, L. B. Gromann, K. Hellbach, F. G. Meinel, M. Braunagel, J. v. Berg, O. Eickelberg, M. F. Reiser, and et al. X-ray dark-field radiography - In-vivo diagnosis of lung cancer in mice. *Scientific Reports*, 7(1), 2017.

A. Schierbeek. *Measuring the invisible world: the life and works of Antoni van Leeuwenhoek*. Abelard-Schuman, 1959.

J. P. Schlomka, E. Roessl, R. Dorscheid, S. Dill, G. Martens, T. Istel, C. Bäumer, C. Herrmann, R. Steadman, G. Zeitler, and et al. Experimental feasibility of multi-energy photon-counting K-edge imaging in pre-clinical computed tomography. *Physics in Medicine and Biology*, 53(15):4031–4047, 2008.

C. Schmachtenberg, F. Engelken, T. Fischer, U. Bick, A. Poellinger, and E. Fallenberg. Intraoperative specimen radiography in patients with nonpalpable malignant breast lesions. *RoeFo - Fortschritte auf dem Gebiet der Roentgenstrahlen und der bildgebenden Verfahren*, 184(07):635–642, 2012.

T. J. Schröter, F. J. Koch, D. Kunka, P. Meyer, S. Tietze, S. Engelhardt, M. Zuber, T. Baumbach, K. Willer, L. Birnbacher, and et al. Large-area full field X-ray differential phase-contrast imaging using 2D tiled gratings. *Journal of Physics D: Applied Physics*, 50(22):225401, 2017.

G. Schulz, T. Weitkamp, I. Zanette, F. Pfeiffer, F. Beckmann, C. David, S. Rutishauser, E. Reznikova, and B. Müller. High-resolution tomographic imaging of a human cerebellum: comparison of absorption and grating-based phase contrast. *Journal of The Royal Society Interface*, 7(53):1665–1676, 2010.

G. Schulz, C. Waschkies, F. Pfeiffer, I. Zanette, T. Weitkamp, C. David, and B. Müller. Multimodal imaging of human cerebellum - merging X-ray phase microtomography, magnetic resonance microscopy and histology. *Scientific Reports*, 2, 2012.

R. Schulz-Wendtland, G. Dilbat, M. Bani, P. Fasching, K. Heusinger, M. Lux, C. Loehberg, B. Brehm, M. Hammon, M. Saake, and et al. Full field digital mammography (FFDM) versus CMOS technology, specimen radiography system (SRS) and tomosynthesis (DBT) - Which system can optimise surgical therapy? *Geburtshilfe und Frauenheilkunde*, 73(05):422–427, 2013.

Y. Sharma, F. Schaff, M. Wieczorek, F. Pfeiffer, and T. Lasser. Design of acquisition schemes and setup geometry for anisotropic X-ray dark-field tomography (AXDT). *Scientific Reports*, 7(1), 2017.

A. Snigirev, I. Snigireva, V. Kohn, S. Kuznetsov, and I. Schelokov. On the possibilities of X-ray phase contrast microimaging by coherent high-energy synchrotron radiation. *Review of Scientific Instruments*, 66(12):5486–5492, 1995.

A. Spek, F. Strittmatter, A. Graser, P. Kufer, C. Stief, and M. Staehler. Dual energy can accurately differentiate uric acid-containing urinary calculi from calcium stones. *World Journal of Urology*, 34(9):1297–1302, 2016.

F. W. Spiers. Effective atomic number and energy absorption in tissues. *The British Journal of Radiology*, 19(218):52–63, 1946.

M. Stampanoni, Z. Wang, T. Thuering, C. David, E. Roessl, M. Trippel, R. A. Kubik-Huch, G. Singer, M. K. Hohl, and N. Hauser. The first analysis and clinical evaluation of native breast tissue using differential phase-contrast mammography. *Investigative Radiology*, 46(12):801–806, 2011.

M. Strobl. General solution for quantitative dark-field contrast imaging with grating interferometers. *Scientific Reports*, 4(1), 2014.

M. R. M. Sun, L. Ngo, E. M. Genega, M. B. Atkins, M. E. Finn, N. M. Rofsky, and I. Pedrosa. Renal cell carcinoma: Dynamic contrast-enhanced MR imaging for differentiation of tumor subtypes—Correlation with pathologic findings. *Radiology*, 250(3):793–802, 2009.

T. Sun, N. Sun, J. Wang, and S. Tan. Iterative CBCT reconstruction using Hessian penalty. *Physics in Medicine and Biology*, 60(5):1965–1987, 2015.

A. Sztrókay, P. C. Diemoz, T. Schlossbauer, E. Brun, F. Bamberg, D. Mayr, M. F. Reiser, A. Bravin, and P. Coan. High-resolution breast tomography at high energy: A feasibility study of phase contrast imaging on a whole breast. *Physics in Medicine and Biology*, 57(10):2931–2942, 2012a.

A. Sztrókay, J. Herzen, S. D. Auweter, S. Liebhardt, D. Mayr, M. Willner, D. Hahn, I. Zanette, T. Weitkamp, K. Hellerhoff, and et al. Assessment of grating-based X-ray phase-contrast CT for differentiation of invasive ductal carcinoma and ductal carcinoma in situ in an experimental ex vivo set-up. *European Radiology*, 23(2): 381–387, 2012b.

H. F. Talbot. Facts relating to optical science. *Philosophical Magazine and Journal of Science*, pages 401–407, 1836.

A. Tapfer, M. Bech, A. Velroyen, J. Meiser, J. Mohr, M. Walter, J. Schulz, B. Pauwels, P. Bruyndonckx, X. Liu, A. Sasov, and F. Pfeiffer. Experimental results from a preclinical X-ray phase-contrast CT scanner. *Proceedings of the National Academy of Sciences of the United States of America*, 109(39):15691–6, 2012.

A. Tapfer, R. Braren, M. Bech, M. Willner, I. Zanette, T. Weitkamp, M. Trajkovic-Arsic, J. T. Siveke, M. Settles, M. Aichler, and et al. X-ray phase-contrast CT of a pancreatic ductal adenocarcinoma mouse model. *PLOS ONE*, 8(3):e58439, 2013.

M. L. Taylor, R. L. Smith, F. Dossing, and R. D. Franich. Robust calculation of effective atomic numbers: The Auto-Zeff software. *Medical Physics*, 39(4):1769–1778, 2012.

M. v. Teuffenbach, T. Koehler, A. Fehringer, M. Viermetz, B. Brendel, J. Herzen, R. Proksa, E. J. Rummeny, F. Pfeiffer, and P. B. Noël. Grating-based phase-contrast and dark-field computed tomography: A single-shot method. *Scientific Reports*, 7 (1), 2017.

T. Thüring and M. Stampanoni. Performance and optimization of X-ray grating interferometry. *Philosophical transactions. Series A, Mathematical, physical, and engineering sciences*, 372(2010):20130027, 2014.

T. Thüring, P. Modregger, S. Hämmerle, S. Weiss, J. Nüesch, and M. Stampanoni. Sensitivity in X-ray grating interferometry on compact systems. *AIP Conference Proceedings*, 1466(1):293–298, 2012.

T. Thüring, S. Hämmerle, S. Weiss, J. Nüesch, J. Meiser, J. Mohr, C. David, and M. Stampanoni. Compact hard X-ray grating interferometry for table top phase contrast micro CT. *Proc. SPIE*, 8668:866813–866817, 2013.

T. Thüring, T. Zhou, U. Lundström, A. Burvall, S. Rutishauser, C. David, H. M. Hertz, and M. Stampanoni. X-ray grating interferometry with a liquid-metal-jet source. *Applied Physics Letters*, 103(9):091105, 2013.

M. Torikoshi, T. Tsunoo, M. Sasaki, M. Endo, Y. Noda, Y. Ohno, T. Kohno, K. Hyodo, K. Uesugi, and N. Yagi. Electron density measurement with dual-energy X-ray CT using synchrotron radiation. *Physics in Medicine & Biology*, 48(5):673, 2003.

M. Urano, N. Shiraki, T. Kawai, T. Goto, Y. Endo, N. Yoshimoto, T. Toyama, and Y. Shibamoto. Digital mammography versus digital breast tomosynthesis for detection of breast cancer in the intraoperative specimen during breast-conserving surgery. *Breast Cancer*, 23(5):706–711, 2015.

J. K. van Abbema, M.-J. van Goethem, M. J. W. Greuter, A. van der Schaaf, S. Brandenburg, and E. R. van der Graaf. Relative electron density determination using a physics based parameterization of photon interactions in medical DECT. *Physics in Medicine and Biology*, 60(9):3825–3846, 2015.

K. J. Van Zee, P. Subhedar, C. Olcese, S. Patil, and M. Morrow. Relationship between margin width and recurrence of ductal carcinoma in situ. *Annals of Surgery*, 262 (4):623–31, 2015.

A. Velroyen. *X-ray phase-contrast and dark-field imaging of small animals: Contrast enhancement and in vivo Imaging.* PhD thesis, Technical University of Munich, 2015.

A. Velroyen, M. Bech, I. Zanette, J. Schwarz, A. Rack, C. Tympner, T. Herrler, C. Staab-Weijnitz, M. Braunagel, M. Reiser, and et al. X-ray phase-contrast tomography of renal ischemia-reperfusion damage. *PLOS ONE*, 9(10):e109562, 2014.

A. Velroyen, M. Bech, A. Tapfer, A. Yaroshenko, M. Müller, P. Paprottka, M. Ingrisch, C. C. Cyran, S. D. Auweter, K. Nikolaou, and et al. Ex vivo perfusion-simulation measurements of microbubbles as a scattering contrast agent for grating-based X-ray dark-field imaging. *PLOS ONE*, 10(7):e0129512, 2015.

Y. Vengrenyuk, S. Carlier, S. Xanthos, L. Cardoso, P. Ganatos, R. Virmani, S. Einav, L. Gilchrist, and S. Weinbaum. A hypothesis for vulnerable plaque rupture due to stress-induced debonding around cellular microcalcifications in thin fibrous caps. *Proceedings of the National Academy of Sciences*, 103(40):14678–14683, 2006.

M. Viermetz. *Optimization of a high sensitivity X-ray phase-contrast computed tomography setup.* Master thesis, Technical University of Munich, 2015.

M. Viermetz, L. Birnbacher, A. Fehringer, M. Willner, P. B. Noel, F. Pfeiffer, and J. Herzen. High resolution laboratory grating-based X-ray phase-contrast CT. *Medical Imaging 2017: Physics of Medical Imaging*, 2017.

C. Vonesch, F. Aguet, J.-L. Vonesch, and M. Unser. The colored revolution of bioimaging. *IEEE Signal Processing Magazine*, 23(3):20–31, 2006.

T. Weber, P. Bartl, F. Bayer, W. Haas, T. Michel, and G. Anton. Noise in X-ray grating-based phase-contrast imaging. *Med Phys.*, 38(7):4133–40., 2011.

T. Weitkamp, A. Diaz, C. David, F. Pfeiffer, M. Stampanoni, P. Cloetens, and E. Ziegler. X-ray phase imaging with a grating interferometer. *Optics Express*, 13(16):6296, 2005.

H. H. Wen, E. E. Bennett, R. Kopace, A. F. Stein, and V. Pai. Single-shot X-ray differential phase-contrast and diffraction imaging using two-dimensional transmission gratings. *Optics Letters*, 35(12):1932, 2010.

R. J. Wheeler. Wikipedia.org - Dark-field microscopy. `https://en.wikipedia.org/wiki/Dark-field_microscopy#/media/File:Paper_Micrograph_Dark.png/`, 2010.

D. R. White. An analysis of the Z-dependence of photon and electron interactions. *Physics in Medicine and Biology*, 22(2):219, 1977.

S. W. Wilkins, T. E. Gureyev, D. Gao, A. Pogany, and A. W. Stevenson. Phase-contrast imaging using polychromatic hard X-rays. *Nature*, 384(6607):335–338, 1996.

P. Willmott. *An introduction to synchrotron radiation.* John Wiley & Sons, Ltd, 2011.

M. Willner. *Development of a system for X-ray phase-contrast imaging.* Diploma thesis, Friedrich-Alexander-Universität Erlangen and Technical University of Munich, 2011.

M. Willner. *Quantitative phase-contrast computed tomography for biomedical X-ray imaging at conventional sources.* PhD thesis, Technical University of Munich, 2016.

M. Willner, M. Bech, J. Herzen, I. Zanette, D. Hahn, J. Kenntner, J. Mohr, A. Rack, T. Weitkamp, and F. Pfeiffer. Quantitative X-ray phase-contrast computed tomography at 82 keV. *Optics Express*, 21(4):4155, 2013.

M. Willner, J. Herzen, S. Grandl, S. Auweter, D. Mayr, A. Hipp, M. Chabior, A. Sarapata, K. Achterhold, I. Zanette, T. Weitkamp, A. Sztrókay, K. Hellerhoff, M. Reiser, and F. Pfeiffer. Quantitative breast tissue characterization using grating-based X-ray phase-contrast imaging. *Physics in Medicine and Biology*, 59(7):1557–1571, 2014.

M. Willner, G. Fior, M. Marschner, L. Birnbacher, J. Schock, C. Braun, A. A. Fingerle, P. B. Noël, E. J. Rummeny, F. Pfeiffer, and J. Herzen. Phase-contrast Hounsfield units of fixated and non-fixated soft-tissue samples. *PLOS ONE*, 10(8):e0137016, 2015.

M. Willner, M. Viermetz, M. Marschner, K. Scherer, C. Braun, A. Fingerle, P. Noël, E. Rummeny, F. Pfeiffer, and J. Herzen. Quantitative three-dimensional imaging of lipid, protein, and water contents via X-ray phase-contrast tomography. *PLOS ONE*, 11(3):e0151889, 2016.

J. T. Winthrop and C. R. Worthington. Theory of Fresnel images I. Plane periodic objects in monochromatic light. *Journal of the Optical Society of America*, 55(4): 373, 1965.

J. Wolf, A. Malecki, J. Sperl, M. Chabior, M. Schüttler, D. Bequé, C. Cozzini, and F. Pfeiffer. Fast one-dimensional wave-front propagation for X-ray differential phase-contrast imaging. *Biomedical Optics Express*, 5(10):3739, 2014.

H. Q. Woodard and D. R. White. The composition of body tissues. *The British Journal of Radiology*, 59(708):1209–1218, 1986.

Z. Wu, K. Gao, Z. Wang, X. Ge, J. Chen, D. Wang, Z. Pan, K. Zhang, P. Zhu, and Z. Wu. A new method to retrieve phase information for equiangular fan beam differential phase contrast computed tomography. *Medical Physics*, 40(3):031911, 2013.

Q. Xu, E. Y. Sidky, X. Pan, M. Stampanoni, P. Modregger, and M. A. Anastasio. Investigation of discrete imaging models and iterative image reconstruction in differential X-ray phase-contrast tomography. *Optics Express*, 20(10):10724, 2012.

A. Yaroshenko, F. G. Meinel, M. Bech, A. Tapfer, A. Velroyen, S. Schleede, S. Auweter, A. Bohla, A. O. Yildirim, K. Nikolaou, and et al. Pulmonary emphysema diagnosis with a preclinical small-animal X-ray dark-field scatter-contrast scanner. *Radiology*, 269(2):427–433, 2013.

A. Yaroshenko, K. Hellbach, A. O. Yildirim, T. M. Conlon, I. E. Fernandez, M. Bech, A. Velroyen, F. G. Meinel, S. Auweter, M. Reiser, and et al. Improved in vivo assessment of pulmonary fibrosis in mice using X-ray dark-field radiography. *Scientific Reports*, 5(1), 2015.

A. Yaroshenko, T. Pritzke, M. Koschlig, N. Kamgari, K. Willer, L. Gromann, S. Auweter, K. Hellbach, M. Reiser, O. Eickelberg, and et al. Visualization of neonatal lung injury associated with mechanical ventilation using X-ray dark-field radiography. *Scientific Reports*, 6(1), 2016.

W. Yashiro, Y. Terui, K. Kawabata, and A. Momose. On the origin of visibility contrast in X-ray Talbot interferometry. *Opt. Express*, 18(16):16890, 2010.

J. R. Young, D. Margolis, S. Sauk, A. J. Pantuck, J. Sayre, and S. S. Raman. Clear cell renal cell carcinoma: Discrimination from other renal cell carcinoma subtypes and oncocytoma at ,ultiphasic multidetector CT. *Radiology*, 267(2):444–453, 2013.

I. Zanette, T. Weitkamp, T. Donath, S. Rutishauser, and C. David. Two-dimensional X-ray grating interferometer. *Physical Review Letters*, 105(24):2–5, 2010.

I. Zanette, T. Weitkamp, S. Lang, M. Langer, J. Mohr, C. David, and J. Baruchel. Quantitative phase and absorption tomography with an X-ray grating interferometer and synchrotron radiation. *Physica Status Solidi (A) Applications and Materials Science*, 208(11):2526–2532, 2011.

I. Zanette, S. Lang, A. Rack, M. Dominietto, M. Langer, F. Pfeiffer, T. Weitkamp, and B. Müller. Holotomography versus X-ray grating interferometry: A comparative study. *Applied Physics Letters*, 103(24):244105, 2013a.

I. Zanette, T. Weitkamp, G. Le Duc, and F. Pfeiffer. X-ray grating-based phase tomography for 3D histology. *RSC Advances*, 3(43):19816, 2013b.

F. Zernike. Phase-contrast, a new method for microscopic observation of transparent objects. *Physica*, 9:974–986, 1942.

F. Zernike. How I discovered phase contrast. *Science*, 121:345–349, 1955.

H. Zhang, S. Zhang, D. Hu, D. Zeng, Z. Bian, L. Lu, J. Ma, and J. Huang. Threshold choices of Huber regularization using global- and local-edge-detecting operators for X-ray computed tomographic reconstruction. *2013 35th Annual International Conference of the IEEE Engineering in Medicine and Biology Society (EMBC)*, pages 2352–2355, 2013.

Y. Zhao, E. Brun, P. Coan, Z. Huang, A. Sztrokay, P. C. Diemoz, S. Liebhardt, A. Mittone, S. Gasilov, J. Miao, and et al. High-resolution, low-dose phase contrast X-ray tomography for 3D diagnosis of human breast cancers. *Proceedings of the National Academy of Sciences*, 109(45), 2012.

T. Zhou, U. Lundström, T. Thüring, S. Rutishauser, D. H. Larsson, M. Stampanoni, C. David, H. M. Hertz, and A. Burvall. Comparison of two X-ray phase-contrast imaging methods with a microfocus source. *Optics Express*, 21(25):30183, 2013.

Abbreviations

ATC ..... attenuation contrast
BI-RADS .... breast imaging reporting and data system
CT ..... computed tomography
COPD ..... chronic obstructive pulmonary disease
DCIS ..... intraductal carcinoma in situ
DECT ..... dual energy computed tomography
DFC ..... dark-field contrast
DPC ..... differential phase-contrast
EM ..... expectation maximization
FBP ..... filtered backprojection
FFT ..... fast Fourier transform
GB-CT ..... grating-based attenuation contrast computed tomography
GBDF-CT ... grating-based dark-field computed tomography
GBPC-CT ... grating-based phase-contrast computed tomography
GI ..... grating interferometry
HE ..... hematoxylin and eosin (staining)
HU ..... Hounsfield units for attenuation imaging
HUp ..... Hounsfield units for phase-contrast imaging
NST ..... none-specific type (invasive breast cancer)
MRI ..... magnetic resonance imaging
PC ..... phase-contrast
PCI ..... phase-contrast imaging
PC-CT ..... phase-contrast computed tomography
PET ..... positron emission tomography
PMMA ..... polymethylmethacrylate
RCC ..... renal cell carcinoma
SIR ..... statistical iterative reconstruction

Symbols

A ..... atomic mass number
α ..... refraction angle
a_i ..... real Fourier coefficient
β ..... imaginary part of the refractive index
c_i ..... complex Fourier coefficient
d ..... inter-grating distance between phase and analyzer grating
δ ..... refractive index decrement
E ..... energy
E_{eff} ..... effective energy
I ..... intensity
k ..... wave vector
l ..... inter-grating distance between source and phase grating
λ ..... wavelength
M ..... magnification
μ ..... attenuation coefficient
n ..... complex index of refraction
ν ..... frequency
ω ..... angular frequency
p_i ..... period of grating i
φ ..... lateral phase shift of the interference pattern (DPC signal)
Ψ ..... wave function
ρ_{e} ..... electron density
ρ ..... mass density
S ..... lateral shift of the interference pattern
σ_φ ..... standard deviation in the DPC projection
σ_{ph} ..... photoelectric cross section
σ_{coh} ..... coherent scattering cross section
σ_{incoh} ..... incoherent scattering cross section
σ_{tot} ..... total scattering cross section
θ ..... rotation angle
x_{g} ..... grating position
Z ..... atomic number
Z_{eff} ..... effective atomic number

List of publications and scientific presentations

First-authored publications

L. Birnbacher, M. Willner, A. Velroyen, M. Marschner, A. Hipp, J. Meiser, F. Koch, T. Schröter, D. Kunka, J. Mohr, F. Pfeiffer, and J. Herzen. Experimental realisation of high-sensitivity laboratory X-ray grating-based phase-contrast computed tomography. *Scientific Reports* 6, 24022, 2016.

L. Birnbacher, M. Viermetz, W. Noichl, S. Allner, A. Fehringer, M. Marschner, M. von Teuffenbach, M. Willner, K. Achterhold, P. B. Noël, T. Koehler, J. Herzen, and F. Pfeiffer. Tilted grating phase-contrast computed tomography using statistical iterative reconstruction. *Scientific Reports* 8, 6608, 2018.

L. Birnbacher, M. Willner, M. Marschner, D. Pfeiffer, F. Pfeiffer, and J. Herzen. Accurate electron density and effective atomic number determination with polychromatic grating-based phase-contrast CT. *Optics Express* 26(12):15153-15166, 2018.

L. Birnbacher, S. Maurer, K. Scheidt, J. Herzen, F. Pfeiffer, T. Fromme. Electron density of adipose tissues determined by phase-contrast computed tomography provides a measure for mitochondrial density and fat content. *Frontiers in Physiology* 9, 707, 2018.

Shared first-authored publications

K. Hellerhoff, L. Birnbacher, A. Sztrókay, S. Grandl, M. Willner, M. Marschner, D. Mayr, S. Auweter, M.F. Reiser, F. Pfeiffer, and J. Herzen. Assessment of intraductal carcinoma in situ (DCIS) using grating-based X-ray phase-contrast CT at conventional X-ray sources: An experimental ex-vivo study. *PLOS ONE (accepted)*, 2018.

Co-authored publications

S. Allner, T. Koehler, A. Fehringer, L. Birnbacher, M. Willner, F. Pfeiffer, and P. B. Noël. Bilateral filtering using the full noise covariance matrix applied to X-ray phase-contrast computed tomography. *Physics in Medicine and Biology*, 61(10):3867–3856, 2016.

E. Braig, L. Birnbacher, F. Schaff, L. Gromann, A. Fingerle, J. Herzen, E. Rummeny, P. B. Noël, F. Pfeiffer, D. Münzel. Simultaneous wood and metal particle detection on dark-field radiography. *European Radiology Experimental*, 2(1), 2018.

M. Braunagel, L. Birnbacher, M. Willner, M. Marschner, F. De Marco, M. Viermetz, S. Notohamiprodjo, K. Hellbach, S. Auweter, V. Link, and et al. Qualitative and quantitative imaging evaluation of renal cell carcinoma subtypes with grating-based X-ray phase-contrast CT. *Scientific Reports*, 7:45400, 2017.

F. De Marco, M. Marschner, L. Birnbacher, P. B. Noël, J. Herzen, and F. Pfeiffer. Analysis and correction of bias induced by phase stepping jitter in grating-based X-ray phase-contrast imaging. *Optics Express*, 26(10):12707, 2018.

S. Grandl, M. Willner, J. Herzen, A. Sztrókay-Gaul, D. Mayr, S. D. Auweter, A. Hipp, L. Birnbacher, M. Marschner, M. Chabior, and et al. Visualizing typical features of breast fibroadenomas using phase-contrast CT: An ex-vivo study. *PLOS ONE*, 9(5):e97101, 2014.

S. Grandl, K. Scherer, A. Sztrókay-Gaul, L. Birnbacher, K. Willer, M. Chabior, J. Herzen, D. Mayr, S. D. Auweter, F. Pfeiffer, and et al. Improved visualization of breast cancer features in multifocal carcinoma using phase-contrast and dark-field mammography: an ex vivo study. *European Radiology*, 25(12):3659–3668, 2015.

L. B. Gromann, D. Bequé, K. Scherer, K. Willer, L. Birnbacher, M. Willner, J. Herzen, S. Grandl, K. Hellerhoff, J. I. Sperl, and et al. Low-dose, phase-contrast mammography with high signal-to-noise ratio. *Biomedical Optics Express*, 7(2):381, 2016.

H. Hetterich, N. Webber, M. Willner, J. Herzen, L. Birnbacher, A. Hipp, M. Marschner, S. D. Auweter, C. Habbel, U. Schüller, and et al. AHA classification of coronary and carotid atherosclerotic plaques by grating-based phase-contrast computed tomography. *European Radiology*, 26(9):3223–3233, 2015.

H. Hetterich, N. Webber, M. Willner, J. Herzen, L. Birnbacher, S. D. Auweter, U. Schüller, F. Bamberg, S. Notohamiprodjo, H. Bartsch, J. Wolf, M. Marschner, M. F. Reiser, F. Pfeiffer, T. Saam. Dark-field Imaging in coronary atherosclerosis. *European Journal of Radiology*, 94:38–45, 2017.

F. J. Koch, T. J. Schröter, D. Kunka, P. Meyer, J. Meiser, A. Faisal, M. I. Khalil, L. Birnbacher, M. Viermetz, M. Walter, and et al. Note: Gratings on low absorbing substrates for X-ray phase contrast imaging. *Review of Scientific Instruments*, 86(12): 126114, 2015.

M. Marschner, L. Birnbacher, K. Mechlem, W. Noichl, A. Fehringer, M. Willner, K. Scherer, J. Herzen, P. Noël, and F. Pfeiffer. Two-shot X-ray dark-field imaging. *Optics Express*, 24(23):27032, 2016.

M. Marschner, L. Birnbacher, M. Willner, M. Chabior, J. Herzen, P. Noël, and F. Pfeiffer. Revising the lower statistical limit of X-ray grating-based phase-contrast computed tomography *PLOS ONE*, 12(9):e0184217, 2017.

J. Meiser, M. Willner, T. Schröter, A. Hofmann, J. Rieger, F. Koch, L. Birnbacher, M. Schüttler, D. Kunka, P. Meyer, A. Faisal, M. Amberger, T. Duttenhofer, T. Weber, A. Hipp, S. Ehn, M. Walter, J. Herzen, J. Schulz, F. Pfeiffer, and J. Mohr. Increasing

the field of view in grating based X-ray phase contrast imaging using stitched gratings. *Journal of X-ray Science and Technology*, 24(3):379–388, 2016.

S. Notohamiprodjo, N. Webber, L. Birnbacher, M. Willner, J. Herzen,S. D. Auweter, V. Viermetz, D. Mayr, H. Bartsch, M. Marschner, M. F. Reiser, F. Pfeiffer, T. Saam, H. Hetterich. Qualitative and quantitative evaluation of structural myocardial alterations by grating-based phase-contrast computed tomography. *Investigative Radiology*, (epub), 2017.

V. Richter, M. S. Willner, J. Henningsen, L. Birnbacher, M. Marschner, J. Herzen, M. A. Kimm, P. B. Noël, E. J. Rummeny, F. Pfeiffer, and et al. Ex vivo characterization of pathologic fluids with quantitative phase-contrast computed tomography. *European Journal of Radiology*, 86:99–104, 2017.

M. Ruiz-Yaniz, I. Zanette, A. Sarapata, L. Birnbacher, M. Marschner, M. Chabior, M. Olbinado, F. Pfeiffer, and A. Rack. Hard X-ray phase-contrast tomography of non-homogeneous specimens: grating interferometry versus propagation-based imaging. *Journal of Synchrotron Radiation*, 23(5):1202–1209, 2016.

K. Scherer, L. Birnbacher, M. Chabior, J. Herzen, D. Mayr, S. Grandl, A. Sztrókay-Gaul, K. Hellerhoff, F. Bamberg, and F. Pfeiffer. Bi-directional X-ray phase-contrast mammography. *PLOS ONE*, 9(5):e93502, 2014.

K. Scherer, K. Willer, L. Gromann, L. Birnbacher, E. Braig, S. Grandl, A. Sztrókay-Gaul, J. Herzen, D. Mayr, K. Hellerhoff, and et al. Toward clinically compatible phase-contrast mammography. *PLOS ONE*, 10(6):e0130776, 2015.

K. Scherer, L. Birnbacher, K. Willer, M. Chabior, J. Herzen, and F. Pfeiffer. Correspondence: Quantitative evaluation of X-ray dark-field images for microcalcification analysis in mammography. *Nature Communications*, 7:10863, 2016.

K. Scherer, E. Braig, S. Ehn, J. Schock, J. Wolf, L. Birnbacher, M. Chabior, J. Herzen, D. Mayr, and et al. Improved diagnostics by assessing the micromorphology of breast calcifications via X-ray dark-field radiography. *Scientific Reports*, 6(1), 2016.

T. J. Schröter, F. J. Koch, D. Kunka, P. Meyer, S. Tietze, S. Engelhardt, M. Zuber, T. Baumbach, K. Willer, L. Birnbacher, and et al. Large-area full field X-ray differential phase-contrast imaging using 2D tiled gratings. *Journal of Physics D: Applied Physics*, 50(22):225401, 2017.

M. Willner, G. Fior, M. Marschner, L. Birnbacher, J. Schock, C. Braun, A. A. Fingerle, P. B. Noël, E. J. Rummeny, F. Pfeiffer, and et al. Phase-contrast Hounsfield units of fixated and non-fixated soft-tissue samples *PLOS ONE*, 10(8):e0137016, 2015.

Oral presentations

Mar. 2014 – DPG-Frühjahrstagung – *Current state of the art of grating-based laboratory X-ray phase-contrast computed tomography*, Mainz, Germany

Sep. 2014 – MAP Kolloquium – *Phase-contrast imaging of renal cell carcinomas, LMU Klinikum Großhadern*, München, Germany

Mar. 2015 – DPG -Frühjahrstagung – *Tilted-grating X-ray phase-contrast computed tomography*, Wuppertal, Germany

Sep. 2015 – XNPIG – *Tilted grating laboratory phase-contrast computed tomography*, Bethesda, Maryland, USA

Jan. 2016 – IMXP – *Tilted grating laboratory phase-contrast computed tomography using statistical iterative reconstruction*, Garmisch-Partenkirchen, Germany

Mar. 2017 – KNMF User Meeting – *Dark-field imaging in coronary atherosclerosis*, Karlsruhe, Germany

Poster presentations

Jan. 2013 – IMXP – *A compact Talbot-Lau-interferometer for mammography applications*, Garmisch-Partenkirchen, Germany

Jan. 2014 – IMXP – *Characterization of renal stones with grating-based phase-contrast imaging*, Garmisch-Partenkirchen, Germany

Oct. 2014 – XRM – *High-sensitivity X-ray phase-contrast computed tomography with laboratory sources*, Melbourne, Australia

Mar. 2015 – IMXP & XNPIG – *High sensitivity X-ray phase-contrast computed tomography*, Garmisch-Partenkirchen, Germany

Jan. 2018 – IMXP – *Accurate determination of the effective atomic number with polychromatic grating-based phase-contrast computed tomography*, Garmisch-Partenkirchen, Germany

Mar. 2018 – KNMF User Meeting – *Accurate determination of the effective atomic number with polychromatic grating-based phase-contrast computed tomography*, Karlsruhe, Germany

Acknowledgments

This thesis would not have been possible without the help and support of my supervisors, colleagues, and friends.

In over five years' work in the Chair of Biomedical Physics, I got the chance to learn incredibly much and work in a unique atmosphere, which is something that propagates from the management of this group to each individual member. Not only for this opportunity to work in this group, but also for all the advice, support, and motivation, I want to thank you sincerely, Franz.

Thank you, Julia, for all your endless advice, support, pushing, motivation, paper, abstract & thesis corrections, the fabulous beamtime in Hamburg, and the one or other (maybe more) dinner, party, beer, or Mexikaner.

Marian, it was extremely helpful for me to have you as my advisor and predecessor at the Miriam setup. Thanks for the great work and working atmosphere with all your support with the different projects, which would not have been possible your continuous effort. Phasenkontrast macht auch ohne dich keinen Sinn.

Kai, it was fun working with you, not only at the mammography project. Thanks for your supervision and help during my diploma project. Let's see what comes next.

Special thanks to Mathias, who helped with all the processing and reconstruction issues. Without you many parts of this work would not have been possible. Also thanks for the mutual support, beam times and conferences, as well as all the extracurricular activities.

I thank my master student Manuel for his astonishing work he did at the setup.

Thank you Martin, for all your amazing support with the detectors, SPEC, unix, data storage. It was just never ending help.

I want to thank you, Kathi, for your help with the brown fat mice project.

Thanks to Christian for his work with the different detector characterizations.

Merci Josef and Christian, for your great help with the new rotating anode.

Moreover, Fabio, thanks for all his work with the high-level processing, the deconvolution, flat-field selection. Also for the fabulous long distance kidney reconstruction support from Zurich.

I want to thank Peter Noël for his support and advice with the medical projects.

Thanks to Michael Chabior for his support during my early time in this group.

Thanks to my USA trip crew Florian, Friedrich, and Christoph, as well as Maite, Mathias, and Wolfgang. Thank you Maite, Mathias, Irene, and Regine for the fabulous ESRF beamtimes.

Thanks to you, Konsti, for the Hamburg beamtime and the work together at the rotating anode.

Thank you Dieter and Ulrike for your high quality cultural and social efforts. The dinners, Biergarten, and theaters were quite the events.

Thank you Klaus for your help with organizational issues and for continuously helping with the rotating anode and radiation safety.

Thanks to Nelly for endless help with managing all the bureaucracy and providing me with pens.

Special thanks for the office guys, with whom I spent a lot of time Mathias, Basti, Andreas, Max, Marco, Astrid, Wolfgang, and Lorenz. And from the neighboring office Basti, Korbinian, Eva, Thorsten, Björn, Kai, Michael, Josef, and Maite.

Thanks to everyone from E17 for not only enduring security instructions, group meetings, or more or less tedious talks, but more for coffee, lunch, cake, Beer & BBQ, Christmas parties, conferences, and the seminar days. That includes Basti and Basti, Dieter and Dieter, Manuel and Manuel, Manuela and Manuela, Simone and Simone, Astrid, Arne, Maite, Madleen, Martin, Michael, Karin, Eva, Thorsten, Korbinian, Björn, Bene, Regine, Benedikt, Christoph, Konsti, Klaus, Barbara, Pidassa, Florian, Friedrich, Ronja, Pierre, Irene, Veronica, Kaye, Marie, Josef, Lukas, Markus, Larissa, Joni, Johannes, Andre, Nico, Marco P., Jessie, Daniel, Alex, Mark, and everybody else. Thanks to the boulder, Schafkopf, running, soccer, and party crew for keeping me sufficiently distracted and motivated. Special thanks to Thomas B. and Laura M.

Many thanks to the colleagues working with me in diverse collaborations: Thomas Köhler, Daniela Pfeiffer, Sigrid Auweter, Nicole Webber, Holger Hetterich, Tobias Saam, Susanne Grandl, Karin Hellerhoff, Margarita Braunagel, Susan Notohamiprodjo, and Tobias Fromme. This work would not have been possible with the excellent collaboration and help from the people from the KIT Institute for Microstructure namely Tobias Schröter, Frieder Koch, Jan Meiser, Pascal Meyer, Danays Kunka, and Jürgen Mohr as well as Joachim Schulz and his team from Microworks.

Thanks to Alen Bregic for his help from the workshop.

Special thanks to Egon Lenker for repeatedly surviving the Miriam setup.

I thank the Dr. Johannes-Heidenhain-Stiftung for their generous support during my

studies.

Thanks to everyone proofreading this thesis including Wolfgang, Max, Lorenz, Eva, Basti A., and Julia.

Last but not least, I want to thank my dearest friends and family Toni, Matthias, Vroni, Leo, Lena, Frizzi, Fritzi, Mum & Dad, and eventually thanks to you, Anni.